Hydrogenation of Carbon Dioxide in the Gas- and Liquid-Phase over Cu-based Catalysts

Dissertation

Zur Erlangung des akademischen Grades eines
Doktors der Naturwissenschaften
- Dr. rer. nat. -

vorgelegt von
Jil-Lorean Gieser
geboren in Duisburg

Fakultät für Chemie der Universität Duisburg-Essen

Tag der mündlichen Prüfung: 07.12.2023

Prüfungskommission:

Prof. Dr. Malte Behrens (Erster Gutachter)
Prof. Dr. Corina Andronescu (Zweite Gutachterin)
Prof. Dr. Georg Jansen (Vorsitzender)

DOI: 10.17185/duepublico/81346
URN: urn:nbn:de:hbz:465-20240109-120420-5

Danksagung

Eine globale Pandemie und daraus resultierende monatelange Lieferverzögerungen, ein Wechsel des Professors an eine andere Uni im hohen Norden, dadurch bedingt eine Aufspaltung der Gruppe, ein Krieg mitten in Europa, ein digitaler Angriff auf die Uni mit allen seinen Konsequenzen - das sind mehr Herausforderungen als in eine Doktorandenzeit passen, sollte man meinen. Aller Umstände zum Trotz haltet ihr die fertige Doktorarbeit nun in den Händen. Dafür muss ich vielen Leuten danken, ohne deren Hilfe das nicht denkbar gewesen wäre:

Zunächst bedanke ich mich bei Prof. Dr. Malte Behrens für die freundliche Aufnahme in seinen Arbeitskreis. Auf seine Unterstützung und konstruktive Kritik konnte ich mich stets verlassen und mir wurde Raum für die Einbringung persönlicher Ideen gegeben.

Prof. Dr. Corina Andronescu danke ich für die Übernahme des Zweitgutachtens und für die harmonische Zusammenarbeit mit ihr und ihrer Gruppe in den geteilten Laboren des NETZ-Gebäudes.

Allen Mitgliedern des IMPRS RECHARGE danke ich für die gute Zusammenarbeit und die kleinen Pausengespräche, die meinen Horizont nicht nur auf wissenschaftlicher Ebene erweitert haben. Ein großer Dank geht an Rita Groever, die unser Graduiertenprogramm stets mit viel Engagement organisiert hat. Ich bedanke mich außerdem bei dem Sprecher Prof. Dr. Frank Neese, durch den ich in dieses Programm aufgenommen werden konnte, das mich finanziell und auf wissenschaftlicher Basis unterstützt hat.

Dem Team des SPP2080 Konsortiums danke ich für die gute Zusammenarbeit.

Der gesamten Arbeitsgruppe Behrens (sowohl in Essen als auch in Kiel) danke ich für die schöne, wenn auch viel zu kurze Zeit, die wir miteinander verbracht haben. Danke für alle Messungen, die ihr für mich durchgeführt und all die Dinge, die ihr mir beigebracht habt. Vielen Dank an meinen Duisburger Bürokollegen Maik, der es durch seine pessimistische Art immer wieder schaffte, mich optimitisch zu stimmen. BeMo danke ich für die Einweihung in die Kunst der Chemisorption und seine vielen Anekdoten. Ein Danke geht auch an Sharif, der uns in Duisburg engagiert mit guten Ratschlägen zur Seite stand und immer eien Lösung parat hatte. Anna und Patrik danke ich für die herzliche Aufnahme in das Kieler Hydrier-Team, durch die ich trotz 500 km Entfernung immer bestens informiert war.

An dieser Stelle sei auch allen wissenschaftlichen Mitarbeitern in Essen gedankt: Dietrich Tönnes für XRD Messungen, Robin Meya und Beate Römer für die Mikroanalytik sowie Kateryna Loza und Tobias Bochmann für SEM-Messungen.

Alina Jakubowski vom MPI CEC danke ich für ihre aufgeschlossene und hilfsbereite Art. Ohne deinen Einsatz für mich zur Nutzung des GC-MS wäre meine Autoklaven-Analytik wirklich schwierig gewesen. Auch Annika Gurowski danke ich für die Hilfe bei den Messungen.

Uwe Rettig und dem gesamten Team der Duisburger Werkstatt danke ich für den Anlagenaufbau, für den handwerklichen Input bei verschiedensten Projektplanungen und für den einen oder anderen beigebrachten handwerklichen Trick.

Was würden wir im NETZ-Gebäude nur ohne Stefan Behrensmeyer machen? Er war der stets verlässliche erste Ansprechpartner, wenn es mal wieder tropfte, pfiff, klemmte oder einfach nicht tat, was es soll. Danke für deine Hilfsbereitschaft, deine unkomplizierte Art, kreative und schnell umgesetzte Lösungsvorschläge und auch das Management der vielen Gaslieferungen für unsere Gruppe.

Danke auch an das Team des Chemikalienlagers in Duisburg: Wolfgang Giese, Torsten Werner und Christian Bohlmann.

Susanne Moser und Sabine Bollmann danke ich dafür, dass sie sich stets um die vielen Bestellungen, Anträge und weiteren organisatorischen Dinge gekümmert haben.

Dem AK Schulz möchte ich für das tolle Miteiander während meiner ersten Zeit in Essen danken und den Amigos des AK Andronescu für die spätere Zeit in Duisburg.

Ohne den öcher Social Mittwoch (sowie kiloweise Pick Ups und Eis vom Delzepich) hätte ich es nicht durch die anstrengenden Klausurphasen geschafft und gar nicht mit der Promotion beginnen können. Vielen Dank, dass ihr mir geholfen habt, nicht am nächsten Nobis falsch abzubiegen und mich bis heute begleitet. Ein besonderer Dank gebührt Hans und Paulina für das Korrekturlesen dieser Arbeit.

Meine verehrten Ritter und Ladys der Tafelrunde: Danke, dass ihr seit all den Jahren für mich da seid! Ohne euren Einfluss hätte ich vermutlich niemals mit dem Studieren angefangen und wäre schon mal gar nicht dafür von Zuhause ausgezogen.

Meiner Familie danke ich für die Hilfe, das Vertrauen, den Rückhalt und die Liebe, die sie mir nicht erst seit meinem Auszug nach Aachen gegeben und geschenkt hat. Nach ziemlich genau zehn Jahren geht das studentische Kapitel meines Lebens zuende. Ich hoffe, ich habe eure Unterstüzung gut genutzt und konnte euch ein wenig stolz machen.

Schließlich danke ich meinem Partner Marco, dem noch nie ein Weg für mich zu weit war. Du hast meine Wut, meine Angst und meine Tränen zuhause meist als Erster mitbekommen, wenn es mal wieder nicht nach Plan lief. Und immer wieder hast du mich aufgebaut, mir Mut gemacht und mich zum Lächeln gebracht. Dafür danke ich dir sehr.

Abstract

The energy transition is one of the most pressing challenges of the 21st century. Due to depleting fossil feedstocks and and the environmental changes that go along with their usage, there is a huge need for renewable energy resources. Yet they are known to be volatile. The development of an efficient energy storage therefore is a coupled task to accomplish the transition.

Saving energy in chemical bonds gained growing attention within the last years. A potential molecule for the large-scale application is methanol. Already today, millions of tons are produced annually. However, fossil-based synthesis gas is commonly used in most production plants. In addition, a high process temperature and low per-pass conversion makes the synthesis energy-demanding. Yet to use methanol in an ecologically benign and circular way, it needs to be produced from CO_2 and green hydrogen only. Therefore, CO_2 is used as the sole carbon source for experiments conducted in the scope of this thesis.

Two process parameters are picked in this work and looked at in detail in order to improve the methanol synthesis and adapt it to the use of sole CO_2. The first one is the choice of catalyst. Layered double hydroxides (LDHs) based on Cu were selected as a precursor phase and the performance of resulting catalysts in the CO_2 hydrogenation is rated regarding conversion and selectivity in comparison to catalysts based on a malachite precursor. Although this phase is rarely found in the conventional catalyst, it offers the advantage of a flexible metal composition and is easily obtainable by co-precipitation. The composition is varied both in terms of the Cu content and the use of the promoters Zn, Al and Ga. Routine measurements such as X-ray diffraction, infrared spectroscopy, optical emission spectrometry and nitrogen physisorption are used to analyze the synthesized materials. Next to that, more advanced characterization methods are applied for an in-depth study of the activated catalysts. By a series of N_2O and H_2 chemisorption steps, the exposed Cu surface areas are determined which are proportional to the number of active sites. Additionally, the extent of strong metal-support interaction (SMSI) can be estimated by identifying the amount of partially reduced Zn. By *in situ* X-ray diffractograms of reduced samples and hydrogen temperature-programmed reductions, the (micro-)structure of the catalysts in the active state is further analyzed.

The second process parameter is the presence of an additional liquid phase in order to alter the reaction mechanism. In the alcohol-assisted liquid-phase reaction, an alcohol is used as an active solvent or co-catalyst, respectively. Formic acid is an intermediate in this and it forms an ester with the alcohol. This ester is then further hydrogenated to the desired methanol and the alcohol is retrieved. Due to the ester intermediate, the reaction temperature can be decreased below 160 °C. A number of LDH-derived materials is employed to elaborate requirements for the catalyst characteristic for the alcohol-assisted reaction. By a subsequent comparison of the product distribution and methanol yield, the suitability of the alcohol-assisted process as an alternative to the industrial gas-phase reaction is evaluated.

Zusammenfassung

Die Energiewende ist eine der drägendsten Herausforderungen des 21. Jahrhunderts. Wegen schwindender fossiler Rohstoffe und Veränderungen der Umwelt, die mit ihrer Verwendung einhergehen, gibt es eine enorme Notwendigkeit für erneuerbare Energien. Sie sind jedoch bekannt dafür, unbeständig zu sein. Daher ist die Entwicklung einer effizienten Energiespeicherung eine an die Energiewende gekoppelte Aufgabe.

In den letzten Jahren hat das Speichern von Energie in Form von chemischen Bindungen steigende Aufmerksamkeit erhalten. Ein potenzielles Molekül für die großtechnische Anwendung ist Methanol. Schon heute werden Millionen Tonnen jährlich produziert. Gewöhnlicherweise wird in den Produktionsanlagen aber Synthesegas auf fossiler Basis verwendet. Außerdem machen eine hohe Prozesstemperatur und ein geringer Umsatz pro Durchlauf die Synthese energieintensiv. Um Methanol umweltfreundlich und in einem Kreislauf zu benutzen, muss es hingegen ausschließlich aus CO_2 und grünem Wasserstoff hergestellt werden. Für die Experimente, die im Rahmen dieser Dissertation durchgeführt werden, wird daher CO_2 als einzige Kohlenstoffquelle eingesetzt.

Zwei Prozessparameter werden in dieser Arbeit ausgewählt und im Detail untersucht, um die Methanolsynthese zu verbessern und sie an die Verwendung von CO_2 anzupassen. Ersterer ist die Wahl des Katalysators. Cu-basierte Hydrotalkite (LDHs) wurden als Prekursorphase ausgewählt und die Leistung der resultierenden Katalysatoren in der CO_2 Hydrierung hinsichtlich Umsatz und Selektivität im Vergleich zu Katalysatoren auf Basis eines Malachit-Prekursors beurteilt. Obwohl diese Phase selten im klassischen Katalysator verwendet wird, bietet sie den Vorteil einer flexiblen Metallzusammensetzung und kann leicht durch Co-Fällung erhalten werden. Die Zusammensetzung wird bezüglich des Cu-Gehalts und der Verwendung von Zn, Al und Ga als Promotoren variiert. Routinemessungen wie Röntgenbeugung, Infrarotspektroskopie, optische Emissionsspektrometrie und Stickstoffphysisorption werden zur Analyse der synthetisierten Materialien verwendet. Darüber hinaus werden fortgeschrittene Charakterisierungsmethoden eingesetzt für eine detaillierte Untersuchung der aktivierten Katalysatoren. Durch eine Sequenz von N_2O und H_2 Chemisorptionen kann die freiliegende Kupferoberfläche bestimmt werden, welche proportional zur Anzahl aktiver Zentren ist. Zusätzlich kann die Stärke der Metall-Träger-Wechselwirkung (SMSI) durch Bestimmung der Menge an partiell reduziertem Zink eingeschätzt werden. Durch *in situ* Diffraktogramme der reduzierten Proben und Wasserstoff-temperatur-programmierte Reduktionen wird die (Mikro-)Struktur der Katalysatoren im aktivierten Zustand näher untersucht.

Der zweite Prozessparameter is die Anwesenheit einer zusätzlichen Flüssigphase, um den Reaktionsmechanismus zu verändern. In der Alkohol-unterstützten Flüssigphasenreaktion wird ein Alkohol als aktives Lösungsmittel bzw. Co-Katalysator verwendet. Ameisensäure ist ein Intermediat in dieser Reaktion und bildet mit dem Alkohol einen Ester. Dieser Ester wird dann weiter zum gewünschten Methanol hydriert unter Rückgewinnung des Alkohols. Die Reaktionstemperatur kann durch den Ester als Intermediat auf unter 160 °C reduziert werden. Eine Reihe von LDH-basierten Materialien wird verwendet, um Anforderungen an den Katalysator auszuarbeiten, welche charakteristisch für die Alkohol-unterstützte Reaktion sind. Durch einen anschließenden Vergleich der Produktverteilung und Methanolausbeute wird das Potential des Alkohol-unterstützten Prozesses als Alternative zur industriellen Gasphasenreaktion beurteilt.

Preface

This thesis is the result of my research as a doctoral candidate in the group of Professor Malte Behrens. From February 2019 to March 2023, I worked at the Faculty of Chemistry of the University of Duisburg-Essen on the carbon dioxide conversion to methanol. The project contained a wide scope of research, from catalyst synthesis and analysis over the setup of a new liquid-phase reactor to process parameter variation and tuning. A collaboration with the Kondratenko group at the Leibniz Institute for Catalysis in Rostock enabled our group to perform gas phase reactions as well. For the synthesis part, I especially focused on copper catalysts derived from a laydered double hydroxide (LDH) structure and analyzed the influence of the nominal copper content, addition of promoters and calcination conditions.

In Section 1, I explain my motivation for this research and explain why it is important at the current time. In Section 2, the most important devices and setups used in this work are described. Section 3 of this thesis deals with the performance of LDH-derived catalysts in the gas phase methanol synthesis. A special focus is on the impact of the calcination temperature prior to catalysis. Section 4 addresses the influence of the nominal copper content and promoters on the catalytic performance in the liquid phase methanol synthesis. In Section 5, the performance of selected catalysts in the liquid phase synthesis are compared to the gas-phase performance.

Each aforementioned section is intended to be used as a publication and hence written in a manuscript style. They can be seen as independent reports and thus, some information might repeat. Nonetheless, they are formatted consistently and share one reference list.

In addition, I was a member of the International Max Planck Research School on Reactive Structure Analysis for Chemical Reactions (IMPRS-RECHARGE) of the Max Planck Institute for Chemical Energy Conversion in Mülheim an der Ruhr. It enabled me to discuss my latest results in a peer group, to attend lecture series on analytic methods, participate in soft skill courses and to use the analytical instruments of the institute.

List of Abbreviations

1-but	1-butanol
2-but	2-butanol
a	Specific activity of a surface species
A_{Cu}	Number of Cu atoms per surface area[1]
AA	Acetic acid
AAS	Atomic Absorption Spectroscopy
AcAld	Acetaldehyde
β	Heating rate
calc	Calcined
cat	Catalyst
EA	Ethyl acetate
EDX mapping	Energy dispersive X-ray mapping
EF	Ethyl formate
EtOH	Ethanol
f_{N2O}	Stochiometric factor[2]
FA	Formic acid
GC	Gas chromatography
H_2-TA	Hydrogen transient adsorption
H_2-TPD	Hydrogen temperature-programmed desorption
H_2-TPR	Hydrogen temperature-programmed reduction (also called TPR)
HT-CO_3^{2-}	High-temperature carbonate
ICDD	International Centre for Diffraction Data
ICP-OES	Iductively coupled plasma optical emission spectrometry
ICSD	Inorganic Crystal Structure Database
IR	Infrared
λ	Wavelength
LDH	Layered Double Hydroxide (synonymously used to hydrotalcite)
m_{cat}	Mass of catalyst
M	Molar mass

MeOH	Methanol
MF	Methyl formate
MMO	Mixed metal oxides
MS	Mass spectrometer
n	Amount of product
$\dot{n}_{\mathrm{CO2,conv}}$	Molar flow of converted CO_2
N_2O-RFC	Nitrous oxide reactive frontal chromatography
N_{A}	Avogadro constant
$\bar{\nu}$	Wavenumber
p	Pressure
PXRD	Powder X-ray diffraction (also called XRD)
r	Methanol formation rate
ρ	Density
rpm	Rotations per minute
rWGS	Reversed water gas shift reaction
S	Selectivity
S_{BET}	Specific surface area, determined by Brunauer-Emmett-Teller equation
S_{Cu}	Copper surface area (also called $S_{\mathrm{Cu-only}}$)
$S_{\mathrm{Cu\&Zn\delta+}}$	Combined surface area of metallic copper and partially reduced Zn
SEM	Scanning electron microscopy
SI	Supporting Information
SMSI	Strong metal-support interaction
Syngas	Synthesis gas (in this work: mixture of H_2 and CO_2)
t	time
T	Temperature
TCD	Thermal conductivity detector
TEOS	Tetraethyl orthosilicate
TPR	Temperature-programmed reduction (also called H_2-TPR)
$\dot{V}$	Volume flow
V_{H2}	Volume of consumed hydrogen
V_{norm}	Molar volume at standard conditions 20 °C and 1.013 bar

V_P	Pore volume
WGS	Watergas shift reaction
x	Mole fraction
X	Conversion
XCAD	External catalyst addition device
XRD	X-ray diffraction (also called PXRD)
Y	Yield
$\mathrm{Zn}^{\delta+}$	Partially reduced Zn

Table of Contents

1. Motivation

The world as we know it today was built based on fossil resources. We need them to heat our homes, fuel our cars, produce electricity and as a feedstock to fabricate all kinds of materials for our daily lives. Yet is is known for decades that tremendous amounts of CO_2 and further greenhouse gases are released by their usage which greatly damages our climate. In addition, the energy and raw material demand is increasing due to a growing world population, but the fossil resources are depleting.[3–6]
There is a huge need for a shift to renewable resources to stop the climate change and overcome evanescent feedstocks. The European Union thus aims for a climate neutrality until 2050, meaning a CO_2 net-emission free economy.[7,8] Moreover, up today 195 parties ratified the Paris Agreement of 2015 which sets the goal to limit the global warming to less than 2 °C.[9,10] The most prominent sustainable resources are nuclear, hydro, wind and solar power. However, due to the constant requirement of isotope-enriched uranium, also nuclear power has to tackle the problem of a diminishing feedstock.[11,12] In contrast, hydro, wind and solar power are inexhaustible and have been investigated for decades now. They have established as green alternatives for the power production and because of advances in technology, they can also compete from a economically point of view.[13–15]
Drawbacks accompanied by the use of renewable resources are the fluctuating power supply and the difficult applicability as a transportable energy source apart from static power grids. Both show the necessity of an effective energy storage.[16] In the transportation sector, fuels are being replaced by batteries to use electric energy instead of a fossil one.[3,17] The German government set a goal of 15 million electric cars by 2030.[18] However, batteries are not applicable for aviation and shipping as their energy density per mass and per volume is too low compared to kerosene and heavy oil.[19,20]
An alternative to batteries is the storage of energy in a chemical bound state. Green hydrogen became the most important energy carrier to carry out the energy transition. It is carbon-free and obtainable from water splitting, hence there is an almost unlimited source of raw material available on earth. When extracting the saved chemical energy, water will be the sole, environmentally benign product.[19–22] Moreover, hydrogen can be implemented in the most important and energy consuming industrial processes. For example, those are the ammonia synthesis which is needed to fabricate fertilizers,[23,24] or for a sustainable production of steel.[25,26] However, even in a compressed state this gas has a low volumetric energy density. A high flammability and large explosion range have to be added to the disadvantages, making it challenging to

store and handle.[22,27] The problems can be overcome by storing hydrogen in a chemical bound state, preferentially in the liquid state. Such liquid hydrogen carriers are ammonia[28,29] or renewable fuels, also called e-fuels.[20,30,31]

A simple renewable fuel that can be obtained from hydrogen and CO_2 in one step is the alcohol methanol.[32–35] Suggestions were made to set up a methanol economy to tackle the energy crisis. Different to hydrogen, methanol is a liquid with a higher energy density and less hazards. It can replace gasoline in combustion motors or be used in direct methanol fuel cells. The current gasoline distribution infrastructure could be adopted without the need of much reconstruction. Methanol serves as a energy storage and can also be used mobile, independent from a static electricity grid. In addition, it can serve as a feedstock to synthesize hydrocarbons and its many follow-up products. In this way, it has the potential to substitute fossil resources both as a energy feedstock and raw material and help mankind to overcome the fossil era.[36–40]

Methanol is industrially produced since the 1920s from fossil fuels and since the 1960s, copper based catalysts are used. These are - with only minor changes - employed until today.[41–43] Nonetheless, research is still ongoing to improve the process and the catalyst regarding conversion per cycle, selectivity and energy demand. The catalyst synthesis conditions were found to be crucial for the later performance. This influence of the preparation is also known as the chemical memory.[44,45] From a scientific point of view, single-phase precursors and precisely defined catalysts are especially important as they allow for structure-activity relationships.[46,47]

For this thesis, the phase of layered double hydroxides was chosen as precursor phase. With copper as the main component, the effect of different promoters and their amount in this specific phase on the activity and selectivity towards methanol will be investigated. In addition, the influence of thermal treatment will be analyzed. The LDH-based catalysts will be implemented in the industrial gas-phase synthesis process. Thereafter, they will be tested in a non-commercial liquid-phase process and their performance in the two processes will be compared. Finally, the suitability of LDH-based materials as potential catalysts for the methanol production will be evaluated.

2. Setups and Methods

2.1. OptiMax Synthesis Reactor

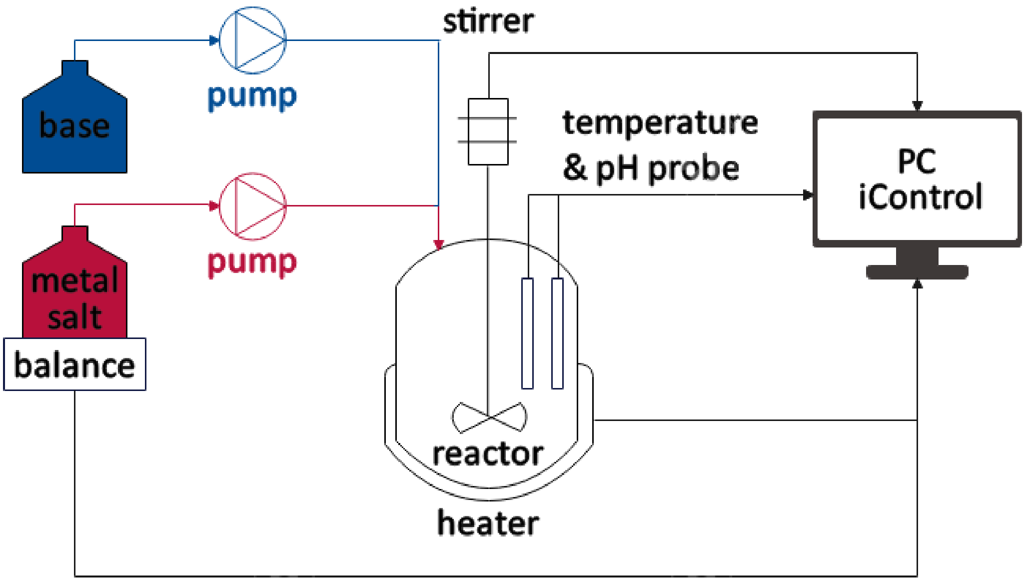

Figure 2.1.: Schematic drawing of the OptiMax synthesis reactor. Cables are drawn in black and tubes in blue and red, respectively.

The OptiMax 1001 from Mettler Toledo is a workstation that allows the preparation of catalyst precursors under defined and automated conditions. The setup used for this thesis was equipped with a 1 l reactor and a water-cooled heating jacket. The inside of the reactor included a blade stirrer, a pH and temperature probe, a hose for inert gas introduction (not used in this thesis) and a gas outlet connected to a bubbler. Additionally, two dosing fingers were mounted on the reactor head. A metal salt solution and a base solution were fed through them by two peristaltic pumps. The metals precipitated as hydroxides, oxides or carbonates, depending on the applied base solution, pH and temperature. The amount of dosed metal salt was determined by a balance. The balance, the pumps, the probes, the stirrer and the heater were connected to a PC. By the iControl software, a program was defined in which various parameters could be set. For example, the materials for this thesis were prepared with a metal salt dosing rate of 75 g within 30 min at 25 °C and a stirrer speed of 300 rpm at a pH of 8. Subsequently, the dosing and pH control was shut off and the material was allowed to age for 1 h under continuous stirring. As all parameters except the concentrations of the two solutions were automatically controlled by the software, a reproducible catalyst synthesis was achieved.

2.2. Belcat-B

The Belcat-B from BEL JAPAN, Inc. (Haradanaka Toyonaka, Japan) is a chemisorption instrument equipped with a thermal conductivity detector (TCD). A screenshot of the user interface is shown in Figure 2.2. The Belcat-B has two different gas streams, Flow 1 and Flow 2. By switching the valves 4WAV1 and 6WAV4, either an inert gas or reactive gas can be passed through the U-shaped quarz glass reactor with an inner diameter of 4 mm and outer diameter of 6 mm. The reactor is positioned in an oven and the temperature is measured inside the reactor with a K-type thermocouple. Before filling in a sample, quarz wool is put in the reactor to prevent flushing and spreading of the sample throughout the machine by the gas stream. A solvent trap filled with a molecular sieve can be put online by valve 4WMV1 to protect the TCD from harmful solvents. In the experiments performed for this thesis, water is the only liquid product formed. By an additional mixbox, the reactive gas (Flow 2) can be further diluted or switched completely by adjusting the flow rates of Flow 2, Mix 1 and Mix 2. The flows are controlled by mass flow controllers (MFCs). During the time of this research, the outlet gas (vent 1) was attached to an Omnistar GSD 320 mass spectrometer from Pfeiffer Vacuum (MS).

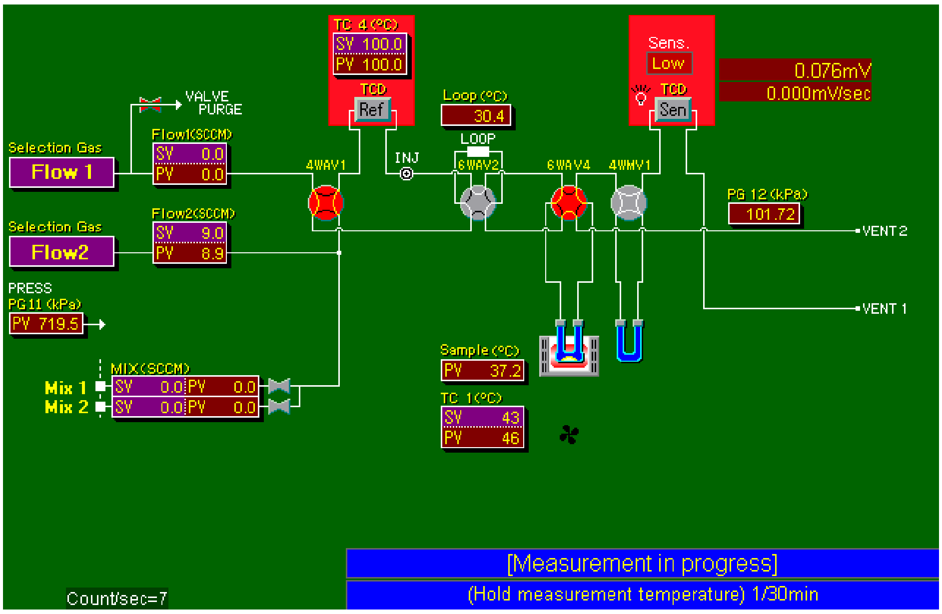

[Measurement in progress]

(Hold measurement temperature) 1/30min

Count/sec=7

Figure 2.2.: User interface of the Belcat-B. The labels "Flow 1", "Flow 2", "Mix 1" and "Mix 2" were added on this screenshot for clarity.

In the context of this work, hydrogen temperature-programmed reductions (H_2-TPR), Nitrous oxide reactive frontal chromatography (N_2O-RFC) and hydrogen transient adsorptions (H_2-TA) were conducted on this setup. To track the H_2-TPR, the TCD was used. Prior to measurements, the TCD was calibrated by reducing different amounts of copper oxide in a TPR and correlate the mass with the integral of the TCD signal. For the analysis of H_2-TA and N_2O-RFC, the MS was used. Prior to each analysis cycle (consisting of a first H_2-TA, first N_2O-RFC, second H_2-TA and second N_2O-RFC), it was calibrated for H_2, N_2 and N_2O. Mass to charge ratios m/z of 1, 2, 4, 14, 16, 18, 28, 30, 32, 40 and 44 were recorded to track the concentrations of H_2, He, N_2 and N_2,O quantitatively and O_2, H_2O and Ar qualitatively. Before each measurement, the lines were purged with He for at least 10 min to avoid a contamination with reactive gas of the previous measurement.

2.3. Slurry-Phase Reactor

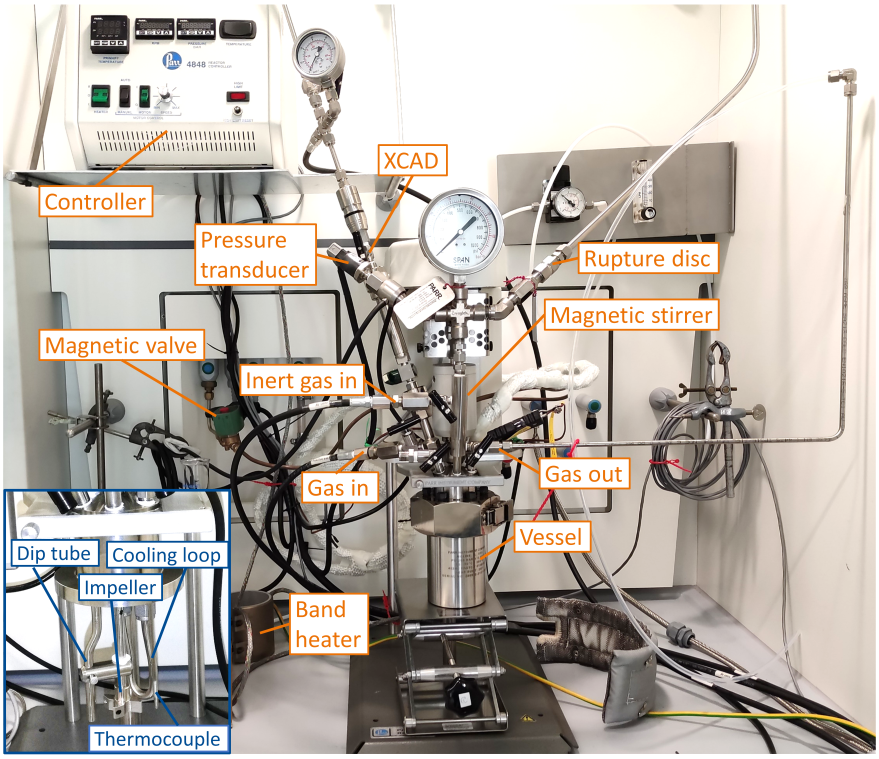

Figure 2.3.: Labeled picture of the used autoclave setup. The inset framed in blue shows the interior parts of the reaction vessel.

For the methanol synthesis reaction in the liquid phase, a 300 ml bench top fixed head 4560 mini reactor equipped with a 4848 controller from the Parr Instrument Company was used. Inside the reactor, a thermocouple in a thermosleeve and a gas entrainment impeller were installed. *Via* the holes in the shaft and in the stirring blades, the impeller could generate a slurry phase by extensive mixing of the gas and liquid phase. The magnetic stirrer that operated the impeller was positioned on the fixed head and could rotate up to 1700 rpm. In addition, a dip tube was mounted in the reactor, enabling both sampling of liquid samples and introducing gas. Finally, a cooling loop controlled by a magnetic valve enabled fast cooling of the reaction mixture. Moreover, a pressure transducer, a rupture disc, a gas outlet, a pressure gauge and a 5 ml external catalyst addition device (XCAD) were attached to the fixed head. The reaction volume was heated by a band heater placed around the 300 ml vessel. The band heater, magnetic valve of the cooling loop, thermocouple, pressure transducer, magnetic stirrer and a PC were connected to the controller to enable an automated temperature and stirring control and to digitally record the temperature, pressure and stirring speed. The maximum operating conditions of this reactor were 350 °C and 200 bar.

Samples were taken before, during and after a reaction. Before taking the actual sample, the sampling loop was purged by taking and discarding about 1 - 2 ml of reaction volume. Only after that about 1 ml of reaction volume was collected as a sample. The samples were analyzed by GC-MS (gas chromatograph GC 2010 Plus with a MS-QP 2020 mass spectrometer from Shimadzu, equipped with a CP-Wax 52 CB column from Agilent). For further details on the instrument and method see experimentals in Subsection 4.5). Prior to catalytic evaluation, two error estimations were done. For the error estimation of the GC-MS instrument, 5 µl of methanol (target product) were dissolved in 1 ml ethanol (solvent in the slurry phase reaction) and the mixture was measured three times in a row. The single mass $m/z = 31$ was used for the detection and latter quantification of methanol. The error was calculated by dividing the standard deviation by the mean value of the three measurement runs. The results are shown in Table 2.1.

Table 2.1.: Error estimation of the GC-MS instrument and of the process with regard to the target product methanol. The area detected for the single mass $m/z = 31$ was used.

error source	area run 1	area run 2	area run 3	error
Instrument	1655052	1573074	1602454	2.6 %
Process	567494	614750	559812	5.1 %

An error of 2.6 % was determined for the instrument. This is a reasonable value and allows a qualitative comparison of the catalytic performance in the liquid phase. The error might arise from the manual integration of the peaks to obtain the areas. Moreover, to analyze the process error, a reaction was repeated three times with the same conditions (temperature, pressure, syngas mixture, catalyst loading, type of catalyst, stirring speed, volume of ethanol, number of samples taken and duration). An error of 5.1 % was determined. As the GC was used to determine the process error, it is more accurately described as a combined instrument and process error. A few reasons come into consideration for this error. The most significant one might be the catalyst amount. Prior to each reaction, the catalyst was reduced and transferred into a glovebox. Inside the box, 1.00 g of reduced catalyst were filled into the external catalyst addition device (XCAD). However, the used balance only had two significant digits and the second digit slightly fluctuated because of the fluctuating pressure inside the box. In addition, a small but varying amount of catalyst remained in the XCAD. This could be observed indirectly by the few grains of catalyst flushed out of the XCAD when cleaning it. Another reason might be the initial pressure of syngas dosed into the reactor. Though the same pressure of 50 bar was always targeted, this value varied from 49 to 52 bar as the syngas was added manually. Moreover, the volume drained from the reactor for sampling might have varied as well. As the sampling is a manual process, deviations in the volume can occur, although it was tried to follow a uniform protocol. The error will be taken into consideration for all liquid phase experiments shown in this thesis.

3. Impact of the Calcination Temperature on LDH-derived Copper Catalysts for Methanol Synthesis

3.1. Abstract

A layered double hydroxide with the composition $Cu_{0.5}Zn_{0.17}Al_{0.33}(OH)_2(CO_3)_{0.17} \cdot m\,H_2O$ was prepared and calcined at two temperatures derived from TG-MS measurements. Calcination of the crystalline precursor at 330 °C led to the formation of an almost amorphous material that still contained carbonate, while a poorly crystalline material was obtained at 600 °C. Most of the high-temperature carbonate decomposed by the thermal treatment at 600 °C, but a small residue could still be detected by different methods. In a series of H_2-TA and N_2O-RFC chemisorption experiments, we determined the specific surface areas of combined metallic Cu and reduced Zn surface sites as well as the individual Cu or Zn surface area. The higher calcination temperature of 600 °C revealed to have a positive impact of the BET surface area, the specific Cu surface area and the activity of the material in the CO_2 hydrogenation to methanol. Compared to an industrial-type reference catalyst, the LDH-derived materials show a slightly lower absolute activity. However, their intrinsic activities outperform the reference by a factor of more than two.

3.2. Introduction

Methanol is a highly demanded chemical with annual production of over 106 million tons in 2021. It has a very broad application range in chemical industry and can either be used as a solvent directly or for the production of various value-added products, e.g. acetic acid, methyl methacrylate, silicons, olefins and formaldehyde. These intermediates are further converted into plastics, paints, adhesives and insulators and amongst other things, are used for automotive manufacturing, construction materials and medical equipment. In recent years, methanol was also discussed as an efficient hydrogen storage material. As a transportation fuel, it can be used in direct methanol fuel cells or combustion engines for a net-carbon free circular CO_2 economy.[36,38,48,49] Methanol is nowadays mostly synthesized in the low-pressure gas-phase process at temperatures of 230 to 280 °C and pressures of 50 to 100 bar. The applied synthesis gas consists of CO and H_2 with low amounts of CO_2. A $Cu/ZnO/Al_2O_3$ catalyst is commonly used in industry and it is synthesized by co-precipitation of mixed metal solutions. A metal distribution of Cu:Zn = 70:30 with 5 to 10 % Al is usually applied.[34,49–51] Mild calcination of the precipitated hydroxy carbonate precursor leads to intensely mixed metal oxides. Treatment with H_2 reduces the CuO to elemental Cu in the form of highly dispersed nanoparticles. This recipe for the industrial methanol synthesis catalyst was optimized empirically. However, the hydroxy carbonate precursor consists of different phases like zincian malachite and rosasite $(Cu,Zn)_2(CO_3)(OH)$, aurichalcite $(Cu,Zn)_5(CO_3)_2(OH)_6$ and layered double hydroxides with the general composition $(Cu,Zn)_{1-x}Al_x(OH)_2(CO_3)_{x/2} \cdot m\,H_2O$ (x = 0.2 - 0.33). It is assumed that these phases contribute differently to the catalyst in terms of microstructure and catalytic properties. Thus, a catalyst comprised of this mixture is hard to characterize. To fully understand the high activity of the industrial catalyst, the different phases can be looked at individually.[46,51–53] This work will focus on the layered double hydroxide phase.

Layered double hydroxides (LDHs) are also known as hydrotalcites and are derived from the mineral brucite $Mg(OH)_2$. The Mg^{2+} cations in this mineral are octahedrally coordinated by hydroxyls and form two-dimensional layers. The layers are held together by weak van-der-Vaals interactions of the hydroxyls. When substituting a fraction of the bivalent Mg by a trivalent cation, the excess positive charge needs to be compensated by an anion. This anion is intercatalated between the cationic layers. Additionally, water molecules are present in this interlayer and they strongly connect the cationic layers by hydrogen bonds with the hydroxyl groups. For a CuZnAl LDH, the cations will homogeneously distribute in the octahedrally coordinated hydroxy layer. Hence, they are finely dispersed within a single phase. The high dispersion can be maintained upon calcination and reduction when choosing appropriate conditions. However, LDHs are not obtainable with the metal ratios of the industrial catalyst due to the low trivalent metal content (mostly Al) of only up to 10 %. In contrast to that, at least 20 % of trivalent cations are needed to avoid byphase formation in LDHs, especially with Cu^{2+} being present in a Jahn-Teller distorted octahedra that destabilizes the hydrotalcite structure.[53–55]

The use of an CuZnAl LDH for methanol synthesis has been analyzed by Kühl *et al.*[54] They showed that by calcination of the hydrotalcite at 330 °C, a mixture of CuO particles and a $ZnAl_2O_4$ spinel is obtained. A kinetic model was introduced by them to describe the reduction mechanism of CuO. Higher reduction temperatures are needed for the LDH-based catalyst compared to a conventional methanol catalyst and a pronounced shoulder toward the lower temperature side is found in the reduction profile. The presence of the shoulder was ascribed to a two-step reduction process. Kühl *et al.*

state that finely dispersed CuO particles are strongly bound to the spinel matrix by O^{2-} or CO_3^{2-} anions. These strong bonds need to be broken before a phase separation of the reducible Cu^{2+} from the irreducible spinel can occur. The formation of a metastable Cu_2O intermediate is delayed because of the strong bonding and it causes the shoulder in the reduction profile. A subsequent full reduction of Cu_2O to metallic copper occurs more easily, leading to a sharp peak in the profile. Thus, a higher reduction temperature can be ascribed to a high dispersion of Cu. In line to that, Schumann *et al.* also concluded that the shoulder in the reduction profile of a conventional methanol catalyst can either be ascribed to the reduction of finely dispersed CuO, or to the presence of a so-called high-temperature carbonate (HT-CO_3^{2-}) which retards the reduction of CuO.[56] Mass spectrometry of the effluent gas in their TPR experiments revealed the formation of CO_2, which further suggests the presence of a thermally stable carbonate species in the calcined sample.

Bems *et al.* studied the presence of the high-temperature carbonate in binary CuZn catalysts in detail.[45] They analyzed the evolved gas during thermogravimetric measurements and found a high-temperature decomposition step coupled exclusively to CO_2 formation in the temperature range of 440 to 480 °C. It was proposed that the decomposition of this HT-CO_3^{2-} is kinetically hindered as it is occluded at the phase boundary of CuO and ZnO. Similar to Kühl *et al.*, they further stated that the HT-CO_3^{2-} acts as a glue between these two phases and as a growth inhibitor for the oxidic crystallites. Thus, at a calcination temperature of 300 to 350 °C typically applied for copper-based catalysts, the thermal decomposition of the materials is incomplete. Velu *et al.* proposed that the HT-CO_3^{2-} is occluded at the phase boundaries of resulting CuO and ZnO and stabilized by the formation of an oxycarbonate.[57] For a set of malachite-derived catalysts, Baltes *et al.* showed a correlation between HT-CO_3^{2-} containing samples and a high activity in methanol synthesis.[44] The highest activity was found for catalysts calcined at 300 °C. They presumed that the formation of highly active sites was facilitated during reduction by the present carbonates.

The specific copper surface area S_{Cu} is a commonly applied measure for the catalytic activity of copper-based catalysts. It can be determined by different techniques, like hydrogen transient adsorption (H_2-TA), hydrogen temperature-programmed desorption (H_2-TPD) or nitrous oxide reactive frontal chromatography (N_2O-RFC). The latter one was introduced by Chinchen *et al.* as a fast and easy method to copper surface areas in supported catalysts.[58] However, it was later found by Fichtl *et al.* that the areas determined by this method are overestimated in the presence of Zn in the catalyst.[59] They proposed that the N_2O does not selectively probe Cu surface sites, but also oxygen defects at the interface of Cu and Zn. The defects are introduced by partially reduced Zn ($Zn^{\delta+}$) and they are an expression of the so-called strong metal-support interaction (SMSI).[60,61] It was shown by TEM imaging that for Cu catalysts with a Zn-containing support, the Zn will form an overlayer and partially cover the Cu particles during reductive activation. Chatterjee *et al.* examined the (S)MSI of Cu catalysts on various supports and discovered that the areas determined by N_2O-RFC are systematically overestimated compared to the areas obtained from H_2-TPD if reducible supports like ZnO, TiO_2 or CeO_2 are present.[2] Moreover, Kuld *et al.* demonstrated that the extent of the overestimation is a function of the hydrogen partial pressure applied during reduction.

In this study, we will present the synthesis, characterization and catalytic activity of LDH-based catalysts with the nominal composition of Cu:Zn:Al = 50:17:33. Two calcination temperatures of 600 and 330 °C were chosen to evaluate the effect of the thermal treatment and the high-temperature carbonate on the catalytic properties in the CO_2 hydrogenation to methanol and compared to the uncalcined material. Moreover, H_2-TA and N_2O-RFC will be used to determine the number of Cu^0 and $Zn^{\delta+}$ surface sites and to estimate the extent of the SMSI.

3.3. Results & Discussion

3.3.1. Co-Precipitation and Calcination

The synthesis of a LDH precursor was performed in a semi-automatic lab reactor and the precipitation conditions were precisely controlled and recorded. The temperature, pH and stirring speed was kept constant by a computer program. It also controlled the dosing of the basic precipitant and metal salt solution to maintain a constant pH during precipitation. The protocol is shown in Figure 3.13 in the SI. After aging, washing and drying, the material was ground. This as-prepared LDH is denoted no-calc. Because of the limited yield of LDH per synthesis in our reactor and the high material consumption for all characterization methods, reproductions had to be used for some of the methods. As the synthesis of no-calc is straightforward, reproductions could be synthesized with ease. A comparison of no-calc and two reproductions by several methods is given in Table 3.3 and Figure 3.14 in the SI. A part of no-calc was thermally decomposed at 330 °C and 600 °C. These materials are denoted 330-calc and 600-calc, respectively. The calcination temperatures were chosen after thermogravimetric analysis of no-calc (see Figure 3.1).

In the mass spectrometry-coupled thermogravimetry (TG-MS) of no-calc, a two-step mass loss can be observed. In the first step, a mass loss of about 25 % is accompanied by water and CO_2 evolution. The water signal has a maximum at about 110 °C and a broad shoulder towards higher temperatures. The maximum can be related to adsorbed water on the surface and interlayer water, whereas the shoulder originates from dehydroxylation of the hydroxide anions. CO_2 is detected simultaneously in the temperature range of 80 to 320 °C. It originates from the decomposition of the carbonate anions in the interlayer.[54,62] A second distinct mass loss step occurs around 600 °C. It coincides with a maximum in CO_2 evolution. This circumstance is known in literature for copper-containing materials and ascribed to the high-temperature carbonate (HT-CO_3^{2-}).[45,57] At 1000 °C, the mass loss reaches 31.5 %. The calcination temperature of 330 °C was chosen for a resulting material that does not contain any more hydroxyl groups and the 600-calc material should represent a sample that does contain no more HT-CO_3^{2-}.

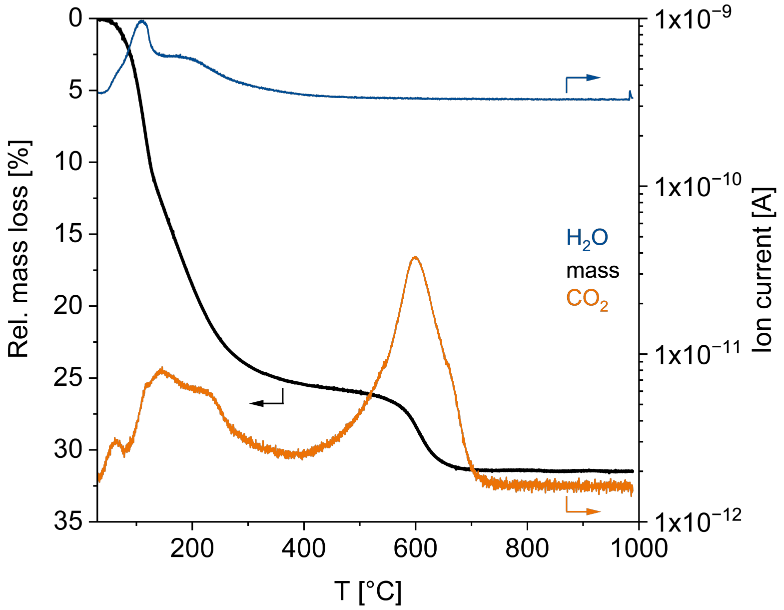

Figure 3.1.: Thermogravimetric analysis of no-calc in 21 % O_2 in Ar (β = 2 °C min^{-1}). The evolution of H_2O was detected by m/z = 18 and evolution of CO_2 by m/z = 44 by mass spectrometry in the effluent gas. The peak near 1000 °C in the water signal is an artifact from the device.

Powder diffraction patterns of no-calc, 330-calc and 600-calc are shown in Figure 3.2. The co-precipitation resulted in a material that exhibits relatively broad reflections, which indicates the formation of small crystallite domains. The positions are in good agreement with the pattern (ICDD 37-0629) reported for a hydroxycarbonate with a metal ratio of Cu:Zn:Al = 3:3:2 (compared to about 3:1:2 for the present no-calc). Upon calcination at 330 °C, the hydrotalcite structure decomposes and a material with very low crystallinity emerges. One very broad reflection at about 35° 2θ implies the presence of CuO. At higher calcination temperatures of 600 °C, the material is still quite amorphous, but few broad reflections hint at a mixture of CuO and a $ZnAl_2O_4$ spinel. Although it is not expected from the metal ratio, a $CuZn_2O_4$ spinel could have formed either. As the reflections for both spinels are very close to each other and partially coinciding, no assignment can be made based on the XRD pattern. Hence, the presence of only one type of spinel or the co-existence of both spinels is possible. In a previous calcination series up to 1000 °C, a reflection narrowing with increasing temperature could be found and the reflections clearly assigned to CuO and a spinel (see Figure 3.15 in the SI).

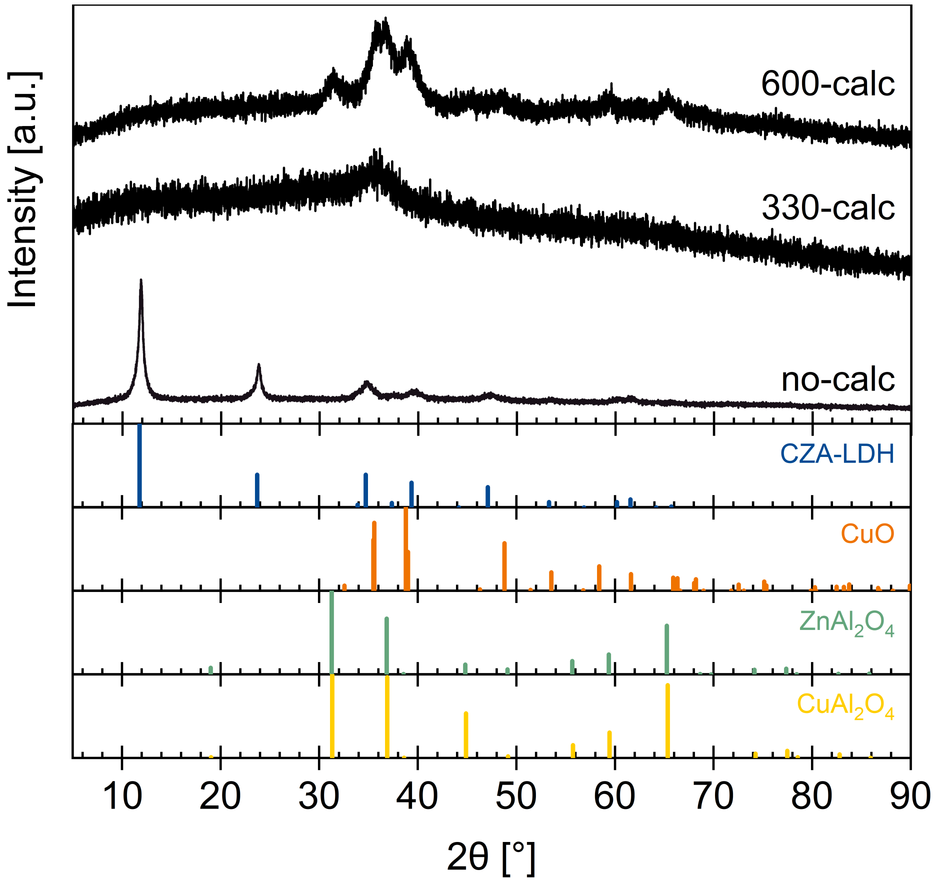

Figure 3.2.: XRD powder patterns of the as-prepared and calcined material. References for a CuZnAl LDH (blue), CuO (orange), $ZnAl_2O_4$ (green) and $CuAl_2O_4$ (yellow) are shown as bars.

Table 3.1 shows the metal ratios of the three synthesized materials. It was aimed for a nominal composition of Cu:Zn:Al = 50:17:33 to reach a molar 1:1 mixture of CuO and spinel upon calcination. In the LDH precursor no-calc, the molar amounts fairly match the target values. The Cu amount is a little higher than expected and the Al amount slightly lower. The metal ratios should not change during calcination, as it is assumed that only carbonates, water and hydroxyls evaporate meanwhile. The values of 330-calc match well with the ones of no-calc. On the other hand, the Cu amount of 600-calc increased by about 4 mol % and the Al amount decreased by that value. It is not clear why Al depleted from the sample. Atomic absorption spectroscopy (AAS) was used as an alternative method to determine the metal ratios. Although the values slightly vary from the ones found by ICP-OES, the depletion of Al could be confirmed from 31.5 % in no-calc to 26.4 % in 600-calc. From the XRD patterns it is known that the Al forms a spinel together with Zn during thermal decomposition. In case of a phase segregation of the spinel, both the Zn and Al amount would deplete in the sample, which is the case for the AAS results. On the other hand, the Zn amount is lowered by only 0.5 % according to ICP-OES. Here, the formation and segregation of a XRD amorphous Al_2O_3 phase seems to be more likely. In both cases, an enrichment of Cu took place during the calcination at 600 °C. This has to be taken into account for the discussion of the catalytic activity per Cu surface site later on.

Table 3.1.: Mole fractions x(M) of Cu, Zn and Al determined by ICP-OES and AAS.

	ICP-OES results [mol %]			AAS results [mol %]		
sample	x(Cu)	x(Zn)	x(Al)	x(Cu)	x(Zn)	x(Al)
no-calc	52.8	16.9	29.5	52.8	15.7	31.5
330-calc	52.4	16.8	30.0	52.8	15.4	31.8
600-calc	56.6	16.3	26.3	61.1	12.5	26.4
Target	50.0	16.7	33.3	50.0	16.7	33.3

Infrared spectroscopy gives an insight to the molecules present in the interlayers of the LDH-derived materials and to the interactions of the layers and interlayer molecules (see Figure 3.3). In the uncalcined sample no-calc, water can be detected by its bending mode at 1633 $\mathrm{cm^{-1}}$ and by a very broad band around 3400 $\mathrm{cm^{-1}}$ caused by OH stretching.[63,64] The stretching occurs both in interlayer water and and layer hydroxy groups. The ν_3 antismymmetric stretching of carbonate causes a strong band at 1348 $\mathrm{cm^{-1}}$. The frequency is clearly shifted compared to the free anion that has its band maximum at 1415 $\mathrm{cm^{-1}}$.[65] A shift in frequency can be caused by strong hydrogen bonding with both interlayer water and layer hydroxy groups. The band around

855 cm^{-1} can be attributed to the ν_2 out-of-plane strechting of carbonate and the band at 564 cm^{-1} to metal-OH deformations.[53,62][62]

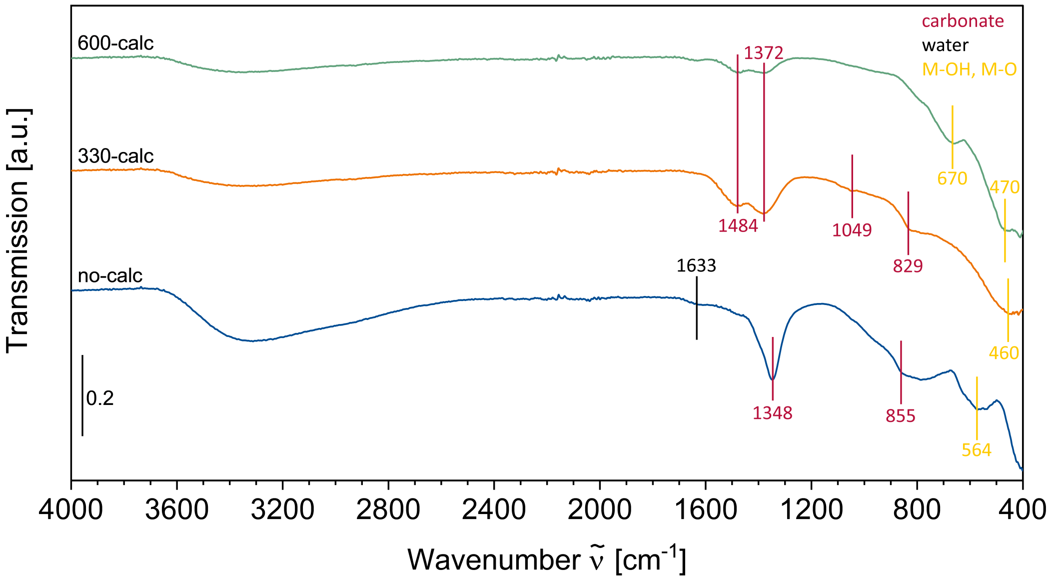

Figure 3.3.: Infrared spectra of the catalysts measured in transmission mode.

For the calcined samples, no more water bending is observable and the OH stretching band becomes much weaker compared to no-calc. From TG-MS it was expected that the water is fully evaporated and the layers dehydroxylated when calcining the LDH at temperatures higher than 300 °C. Hence, no more OH stretching should be detectable at all. The still present bands might be caused by an incomplete dehydroxylation during calcination. However, no high-temperature hydrate was reported as in the case of carbonate, making this option unlikely, especially in the case of 600-calc. Another reason might be that the dehydration is a reversible process. Stanimirova *et al.* showed that a MgNiAl LDH dried at 160 °C reversibly rehydrated back to the initial hydrotalcite structure in air, even at low humidity.[66] After drying at higher temperatures of 260 °C, the initial structure could not be recovered, but still the interlayer thickness grew in air and water was re-incorporated in it. In the present case, the samples were stored in closed containers in air. Hence water could have diffused into the containers and rehydrated the samples, either by rehydration of the interlayers or by water adsorption on the outer surface. The ν_3 band of carbonate shifted less compared to no-calc and it split into two bands positioned at 1484 cm^{-1} and 1372 cm^{-1}. Due to the drastically decreased amount of water in the interlayers, fewer and weaker hydrogen bonds are formed. The splitting occurs as the D_{3h} symmetry is lowered.[63,66] A rearrangement of the carbonate ions in the interlayer toward a monodentate or bidentate coordination to the hydroxy groups was suggested as a reason,[62,64] or even the incorporation of carbonate into the cationic layer.[66] The (normally IR inactive) ν_1 mode of carbonate becomes visible as well at 1049 $\mathrm{cm^{-1}}$ in the spectrum of 330-calc because of the lowered symmetry. In 600-calc, the bands attributed to carbonate are much weaker compared to 330-calc. From the thermogravimetric measurement, it was concluded that the high-temperature carbonate is fully released from the material by calcination at 600 °C. However, the bands did not vanish completely, meaning that a certain amount of carbonate is left in the sample. The IR spectrum of 600-calc thus proves that some extremely stable carbonates exist in this sample series. As no further CO_2 was detected until the end of the TG-MS, it can be concluded these HT-CO_3^{2-} are stable even up to 1000 °C. Further bands in the spectra of the calcined samples can be assigned to M-O vibrations. Bands at 460 $\mathrm{cm^{-1}}$ and 470 $\mathrm{cm^{-1}}$ in 330-calc and 600-calc, respectively, can be ascribed to CuO and the band at 679 $\mathrm{cm^{-1}}$ to the $ZnAl_2O_4$ spinel.

Residues of carbonate in 600-calc are further confirmed by elemental analysis (EA, see Figure 3.16 in the SI). The mass fractions of carbon and hydrogen determined by EA were normalized by the sum of metals identified by AAS. The ratios of C and H are the highest in no-calc with 4.0 % and 5.7 %, respectively. The carbon stems from both interlayer and loosely bound carbonates, while hydrogen originates from interlayer water and hydroxyl groups. Upon calcination at 330 °C, dehydration and dehydroxylation leads to a decrease of the H ratio to 0.7 %. On the other hand, the C ratio only slightly decreases as the HT-CO_3^{2-} is still present in 330-calc. In 600-calc, the C and H ratio both decreased below 0.5 %. The decomposition of the HT-CO_3^{2-} led to the drop in the C fraction, but a residue remains (0.4 %). As discussed above, it was expected from TG-MS measurements that the water is fully evaporated when calcining the LDH at temperatures higher than 300 °C. Contrarily, hydrogen was detected in both calcined samples. Although the H ratio in 330-calc is considerably lower than in no-calc, it is only half as high in 600-calc. The platelet morphology is destroyed after calcination at 600 °C (also see SEM images in Figure 3.4), hence no more interlayer is present to be rehydrated. That is why water can only be readsorbed on the outer surface of 600-calc and the H ratio is lower compared to 330-calc, in which interlayer rehydration can still occur additionally to an adsorption on the outer surface.

3.3.2. Catalyst Characterization

The microstructures of the three samples were analyzed by reproductions *via* scanning electron microscopy (see Figure 3.4). no-calc formed hexagonal platelets which are typical for hydrotalcite materials.[52,53] Broken hexagons can be attributed to prior mortaring of all samples right after synthesis. The platelet diameter determined from the images is about 100 to 200 nm and the thickness 25 nm. Energy dispersive X-ray (EDX) mapping of the LDH illustrates a homogeneous distribution of the cations, enabled by a uniform incorporation into the hydrotalcite structure. Upon calcination at 330 °C, the high dispersion of the metal ions was maintained, leading to atomically mixed metal oxides (MMOs). EDX mapping is shown in Figure 3.17 and Figure 3.18 in the SI. The platelet shape was also retained during the thermal treatment. In contrast to that, the particle shape of 600-calc has clearly changed during calcination at 600 °C. The edges are not as defined as in no-calc and 330-calc and the platelets seem slightly agglomerated.

For all characterizations shown from here on, aggregate size fractions of 125 to 250 µm were used. They were prepared by pressing and sieving and also applied in the catalytic experiments. The microstructure of the materials was further analyzed by N_2 physisorption and the results are summarized in Figure 3.5. no-calc reached a surface area S_{BET} of 40.1 $\mathrm{m^2\,g^{-1}}$. The area is somewhat lower than the 64 $\mathrm{m^2\,g^{-1}}$ reported for a sample with similar metal ratio and synthesis route.[53] A reason could be the previous pressing and sieving of the sample and the use of a certain sieve fraction only. We observed that S_{BET} is significantly lowered by pressing and sieving, e.g. we determined a value of 51.9 $\mathrm{m^2\,g^{-1}}$ for the unsieved sample of no-calc. However, the values subsequent to pressing and sieving are more relevant for connecting the characterization results with the catalytic data. The isotherms and surface areas obtained for the unsieved samples are shown in Figure 3.19 in the SI.

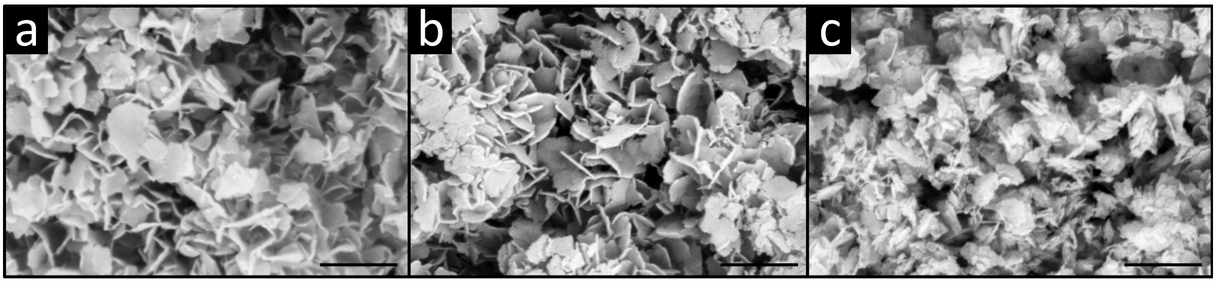

Figure 3.4.: Scanning electron microscopy images of a) no-calc, b) 330-calc and c) 600-calc. Black bars indicate 400 nm.

The adsorption-desorption isotherm of no-calc is a type IV(a) isotherm typical for mesoporous adsorbents. It has a hysteresis loop of mixed type H3 and H4. The H3 loop is usually associated with plate-like particles and matches the platelet shape of no-calc found by SEM imaging. However, the hysteresis is relatively broad, similar to a H4 loop. This broadening compared to a H3 loop is usually caused by small pores or micropores. Hence, the void between the platelets of no-calc can be interpreted as mesopores and additionally, smaller pores are present within the platelets. S_{BET} did not change significantly after calcination at 330 °C. However, the hysteresis became narrower and steeper compared to no-calc and can be characterized as a mere H3 loop. Thus, less smaller pores are present in this material and the pores have a more uniform size. After thermal treatment at 600 °C, the surface area increased to 59.1 $\mathrm{m^2\,g^{-1}}$. This result is surprising as it contradicts the visual impression of 600-calc obtained by SEM imaging and the general expectation of sintering with temperature increase. The shape is similar to 330-calc and can be defined as a type IV(a) isotherm with H3 loop, though the offset has increased and the hysteresis has slightly broadened toward lower values of p/p_0. This demonstrates that in addition to the mesopores present in 330-calc, slightly smaller pores are also existing in 600-calc. With regard to the HT-CO_3^{2-}, surface sites or whole pores could have been blocked in 330-calc. HT-CO_3^{2-} is said to be present at interfaces and defect-rich grain boundaries of the calcined oxycarbonate material.[53] Hence, the HT-CO_3^{2-} can block small pores within the material and make them inaccessible for probe molecules. Only after applying higher temperatures, the HT-CO_3^{2-} is decomposed and the surface sites in small pores are exposed and made accessible for the probing gas N_2. As mesopores have a diameter between 2 and 50 nm, this effect would not be visible for smaller mesopores in SEM due to its lower resolution.[67,68]

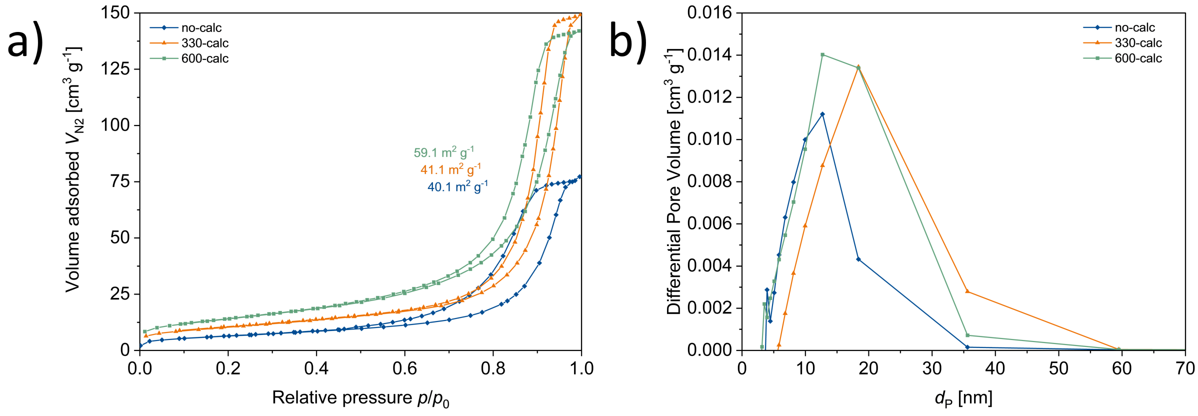

Figure 3.5.: a) N_2 adsorption-desorption isotherms of 125 to 250 µm sieve fractions used to determine the surface areas. b) Pore size distribution determined by the isotherms.

The hystereses of all three materials only close at very high p/p_0 and cannot be described as horizontal in that region. The saturation plateau usually present in that region rather is an inflexion point. This suggests the presence of macropores in the samples. In such a case, the IUPAC emphasized that the total pore volume cannot be evaluated from the isotherms, e.g. by the BJH-method, as it does not cover micro- and macropores.[68] Nonetheless, we can use the BJH-method to analyze the pore size distribution of the mesopores (see Figure 3.5 b) in the SI). The smallest pore size found for no-calc is about 3 nm and the most frequent one 13 nm. The smallest pores in 330-calc are 6 nm wide and the most abundant ones have diameter of 18 nm. This supports the finding of less smaller pores in 330-calc compared to no-calc gained by the isotherms. In comparison to that, 600-calc has a similar pore size distribution as 330-calc for pores larger than 18 nm. Additionally, more pores with a lower diameter are found, as suggested from the isotherms.

Hydrogen temperature programmed reductions were performed up to 800 °C and the profiles are shown in Figure 3.6. The profile of no-calc exhibits one pronounced peak with a maximum at 252 °C, caused by the reduction of Cu^{2+} cations. The peak is almost symmetric, only a very weak shoulder toward lower temperatures is present. This indicates that all Cu species in this sample have a similar environment and are similarly reducible. This result was expected because of the homogeneous metal distribution within the hydrotalcite. The peak position of 330-calc at 248 °C is very close to the one of no-calc. Different to the uncalcined sample, a shoulder on the lower temperature side is visible. As pointed out by Schumann *et al.* and Kühl *et al.*, the shoulder stems from Cu_2O being present as an intermediate in the reduction of CuO to Cu^0. The strong intensity can either be ascribed to the presence of finely dispersed CuO or high-temperature carbonate.[54,56] An indication of HT-CO_3^{2-} being the cause of the shoulder is the absence of such a shoulder in the profile of 600-calc. As shown previously, the carbon content in 600-calc is very low, thus not much HT-CO_3^{2-} is present to affect the reduction of CuO. The reason why such a shoulder was observed in 330-calc is its thermal treatment. In no-calc, the carbonate is only loosely bound in the interlayers, which are still filled with water. Contrarily, the carbonates are directly coordinated to the cationic layers by chemical bonding in 330-calc.[66] More accurately, the sites of removed hydroxyl groups are occupied by O atoms of the carbonates. This chemical bonding is much stronger than the hydrogen interactions and thus has a higher impact on the reduction. The peak maximum of 600-calc at 195 °C is about 50 °C lower compared to no-calc and 330-calc. A lower temperature displays an easier reduction, pointing toward segregated and accessible CuO in this sample.

All three samples exhibit a very broad peak in the range of 350 to 700 °C (see inset in Figure 3.6), though it is weaker in case of 600-calc. This finding suggests that HT-CO_3^{2-} is the cause of this signal. As the TCD only measures a change in the thermal conductivity and is not exclusively sensitive to the hydrogen consumption, the signal could stem from CO_2 formed during the decomposition of HT-CO_3^{2-} in the interlayers. Moreover, the reducing conditions of the TPR could also lead to a hydrogenation of the released CO_2 and thus to an actual hydrogen consumption, as shown by Ota *et al.*[69] In their TPR experiment, the same authors demonstrated the partial reduction of the reducible Zn in a binary ZnAl sample in a broad range of about 400 to 900 °C. Moreover, the partial reduction might have been accompanied by a CuZn alloy formation. For CuZn catalyst systems, the nature of the active site is highly debated.[60,61,70–73] One discussed option is the formation of a CuZn surface alloy of Zn species in close proximity to Cu. Pandit et al. observed such an alloy in a Zn promoted CuO/MgO catalyst.[73] While surface alloy formation was first detected at 200 °C, bulk alloy formation occurred starting from 400 °C. Therefore, the broad signal could be caused by a slow reduction of Zn in proximity to Cu.

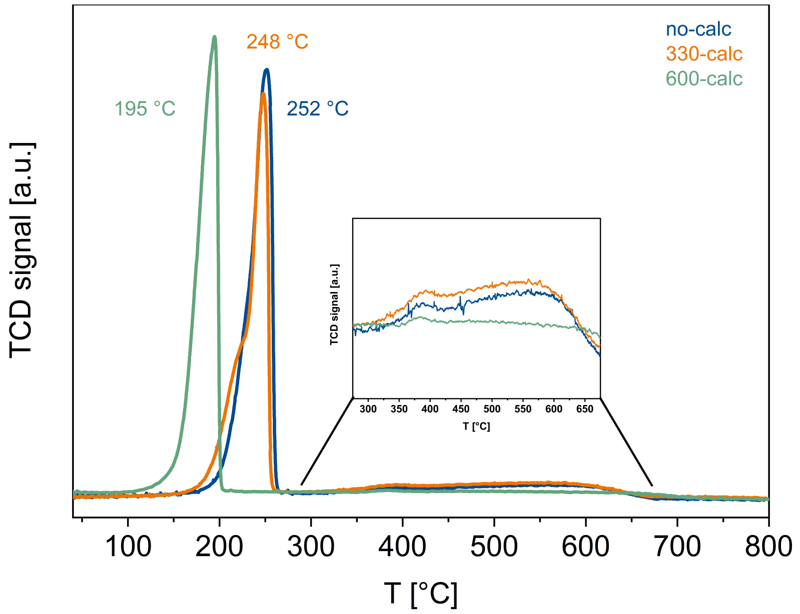

Figure 3.6.: Hydrogen temperature-programmed reduction profiles of 125 - 250 µm sieve fractions in 5 % H_2/Ar at 800 °C (β = 6 °C min^{-1}). The inset shows a zoom of the region from 275 to 675 °C.

X-ray diffraction patterns of the materials reduced at 275 °C are shown in Figure 3.7. All three materials reveal reflections that can be attributed to metallic copper. The signals are quite broad, which is an indication for small Cu^0 crystallites. A very broad feature at 37° 2θ in the pattern of 600-calc illustrates the presence of small amounts of cuprous oxide. As Cu_2O should be reduced quite easily by H_2 at 275 °C, the most likely explanation is a re-oxidation by air that diffused into the capillary before sealing it. Interestingly, none of the materials displays phases that contain Zn or Al. In contrast to that, the XRD pattern of 600-calc previously shown in Figure 3.2 presented some very broad features which fitted the spinel references. In case of $CuZn_2O_4$ being present in 600-calc, the spinel decomposed during reduction of the Cu^{2+} ions and thus can no longer be detected in the reduced sample. Alternatively, structural changes could have happened during reduction, causing the spinel domains to be smaller or less crystalline. A comparison of the diffraction patterns of the precursor, the calcined and the reduced material emphasizes that the phase segregation takes place not until the reduction, as distinct reflections became present only after this step. This is contrary to the conventional malachite-derived catalyst, for which the segregation of CuO and ZnO nanoparticles already happens during calcination.[51]

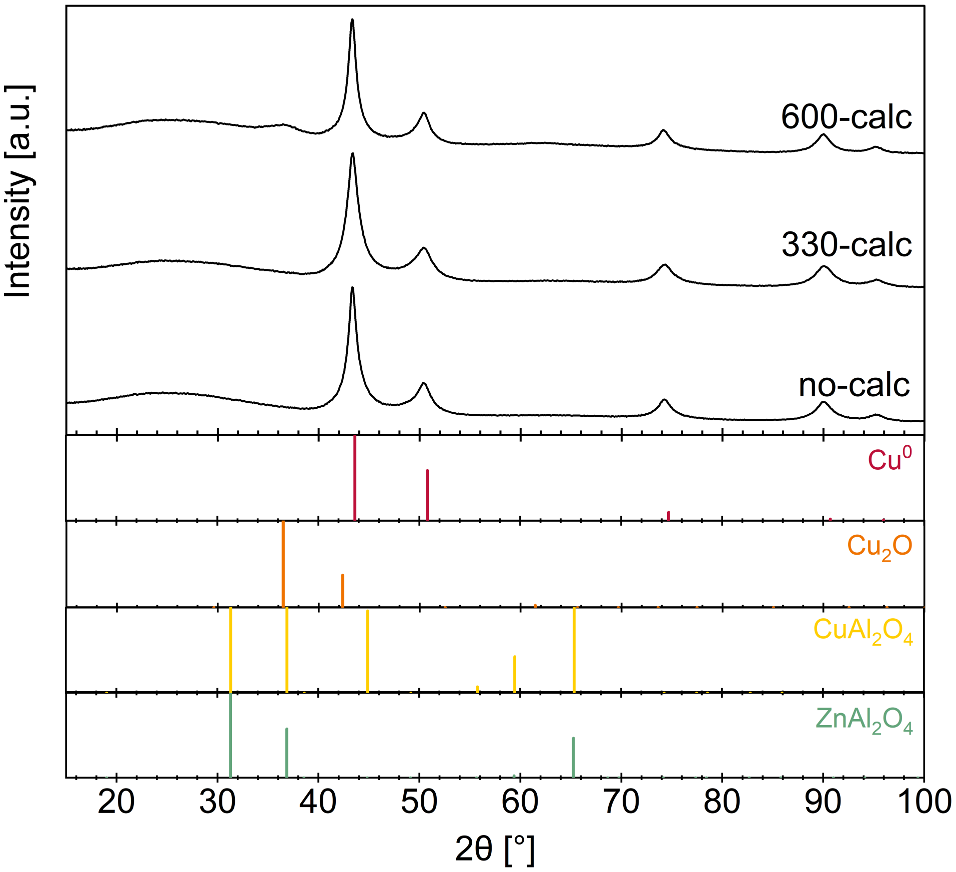

Figure 3.7.: PXRD of reduced samples measured in capillaries after copper surface area measurements and re-reduction at 275 °C. Sieve fractions of 125 - 250 µm were used. References for Cu^0 (red), Cu_2O (orange), $ZnAl_2O_4$ (green) and $CuAl_2O_4$ (yellow) are shown as bars.

The copper surface areas were determined by H_2 transient adsorption (H_2-TA) and N_2O reactive frontal chromatography (N_2O-RFC) experiments performed in a certain sequence (see Figure 3.8). The sequence adapts the measurement protocols of Kuld *et al.* and Fichtl *et al.* on their chemisorption analyses of Cu-based catalysts and takes into consideration their findings and conclusions.[59,70] Starting from the calcined material, the catalyst is activated by a temperature programmed reduction. This results in a material consisting of metallic copper nanoparticles Cu^0, zinc oxide (Zn^{2+}) and a partially reduced zinc species ($Zn^{\delta+}$). In a subsequent H_2-TA at a low temperature of 40 °C, the Cu^0 surface is covered with hydrogen. Fichtl *et al.* showed in an H_2-TPD experiment up to 400 K that for a reduced CZA catalyst, no hydrogen desorbs from the $Zn^{\delta+}$ after prior exposure to it at −196 °C.[59] Thus for our H_2-TA experiment, we can conclude that $Zn^{\delta+}$ does not affect the measured hydrogen uptake. After purging with inert gas at elevated temperatures to clean the surface, N_2O is flowed into the reactor. By that, oxygen is chemisorbed and the surface of the copper nanoparticles is oxidized to Cu^+. Moreover, the $Zn^{\delta+}$ is oxidized to Zn^{2+}. In a second H_2-TA, Cu^+ is reduced back to Cu^0 and subsequently, oxygen leaves the surface as H_2O and hydrogen is adsorbed on the surface. However, due to the less reducible nature of ZnO compared to Cu_2O and the lower temperature compared to the TPR, it remains in its oxidized state. Finally, a second N_2O-RFC is performed. The surface of the copper nanoparticles is again oxidized to Cu^+. But different to the first N_2O-RFC, no reaction with Zn takes place as it already is in an oxidized state. The following reactions occur during this sequence of H_2-TA and N_2O-RFC chemisorption experiments:

$$\text{1}^{\text{st}}\ \mathrm{H_2}\text{-TA :} \quad 4\,\mathrm{Cu}^0 + \mathrm{H}_2 \longrightarrow 2\,\mathrm{Cu}_2^0\mathrm{H} \tag{3.1}$$

$$\mathrm{Zn}^{\delta+} + \mathrm{H}_2 \not\longrightarrow \tag{3.2}$$

$$\text{1}^{\text{st}}\ \mathrm{N_2O}\text{-RFC :} \quad 2\,\mathrm{Cu}^0 + \mathrm{N_2O} \longrightarrow \mathrm{Cu}_2^{\mathrm{I}}\mathrm{O} + \mathrm{N}_2 \tag{3.3}$$

$$\mathrm{Zn}^{\delta+} + \tfrac{2-\delta}{2}\,\mathrm{N_2O} \longrightarrow \mathrm{Zn}^{\mathrm{II}}\mathrm{O} + \tfrac{2-\delta}{2}\,\mathrm{N}_2 \tag{3.4}$$

$$\text{2}^{\text{nd}}\ \mathrm{H_2}\text{-TA :} \quad \mathrm{Cu}_2^{\mathrm{I}}\mathrm{O} + \mathrm{H}_2 \longrightarrow 2\,\mathrm{Cu}^0 + \mathrm{H_2O} \tag{3.5}$$

$$4\,\mathrm{Cu}^0 + \mathrm{H}_2 \longrightarrow 2\,\mathrm{Cu}_2^0\mathrm{H} \tag{3.6}$$

$$\mathrm{Zn}^{\mathrm{II}}\mathrm{O} + \mathrm{H}_2 \not\longrightarrow \tag{3.7}$$

$$\text{2}^{\text{nd}}\ \mathrm{N_2O}\text{-RFC :} \quad 2\,\mathrm{Cu}^0 + \mathrm{N_2O} \longrightarrow \mathrm{Cu}_2^{\mathrm{I}}\mathrm{O} + \mathrm{N}_2 \tag{3.8}$$

$$\mathrm{Zn}^{\mathrm{II}}\mathrm{O} + \mathrm{N_2O} \not\longrightarrow \tag{3.9}$$

Figure 3.8 illustrates this sequence and the corresponding surface reactions:

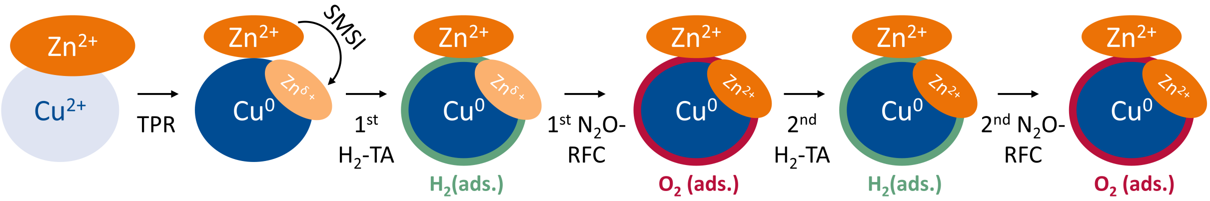

Figure 3.8.: Sequence of surface reactions applied to determine the copper surface areas of the catalysts. Green circles around the Cu^0 particles represent a layer of adsorbed hydrogen on the surface. Red circles represent chemisorbed oxygen forming a monolayer of Cu_2O. Scheme adapted from.[74]

According to Kuld *et al.*, the copper surface area can be calculated by comparing the results of the H_2-TAs subsequent to reduction and to N_2O exposure, respectively.[70] The H_2 uptake after reduction originates from an adsorption of hydrogen on the Cu^0 surface, whereas the uptake after N_2O exposure stems from a reduction of Cu^+ to Cu^0 plus subsequent hydrogen adsorption on Cu^0. Thus, the difference of those experiments gives the H_2 uptake caused by the reduction of the Cu^+ oxidic layer only. This value can then be converted into the exposed copper surface area. Furthermore, both the groups of Kuld and Fichtl point out that for zinc containing catalysts, the copper surface area determined by N_2O-RFC is too high as the N_2O not only oxidizes the Cu^0, but also the $Zn^{\delta+}$. Moreover, when comparing Reaction 3.3 and Reaction 3.4, it becomes obvious by the stochiometry that the N_2O consumption per additionally probed Zn site is even higher than that of a Cu site. We want to show that the overestimation can be avoided by applying our sequential chemisorption method. In the second N_2O-RFC, the starting material is composed of Cu^0 and Zn^{2+} only, without $Zn^{\delta+}$ being present. N_2O consumption will only be caused by Cu^0 oxidation and therefore, it can directly be related to the exposed copper surface area. That is why the second N_2O-RFC can be referred to as a "$Zn^{\delta+}$ corrected N_2O-RFC".[74]

Figure 3.9 shows the determined copper surface areas S_{Cu} of the reduced as-prepared catalysts (plain colored bars) and subsequent to catalytic testing and re-reduction (striped bars). The results of the H_2-TA experiments are shown for completeness. For the further discussion, we only consider the values for S_{Cu} obtained by the first and second N_2O-RFC, as the comparability of values obtained by different chemisorption methods is debatable. E.g., Kuld *et al.* showed that specific copper surfaces areas obtained by H_2-TA and H_2-TPD differed by more than 12 %.[70] Nevertheless, the second H_2-TA was necessary to adjust the oxidation states of Cu and Zn in the sample to 0 and +II as a starting point for the second N_2O-RFC, as depicted in Figure 3.8.

The orange bars in Figure 3.9 ("$Zn^{\delta+}$-affected N_2O-RFC") show the copper surface areas of the reduced sample determined by the first N_2O-RFC in our series. As described above, it is more precisely defined as the combined Cu and $Zn^{\delta+}$ surface area $S_{Cu\&Zn\delta+}$. The green bars ("$Zn^{\delta+}$-corrected N_2O-RFC") show the specific surface areas of the passivated samples obtained by the second N_2O-RFC and they refer to the surface area of Cu only $S_{Cu-only}$, without partially reduced Zn. The difference of the passivated and reduced sample refers to the chemisorption capacity $S_{Zn\delta+}$ caused by the partially reduced Zn.

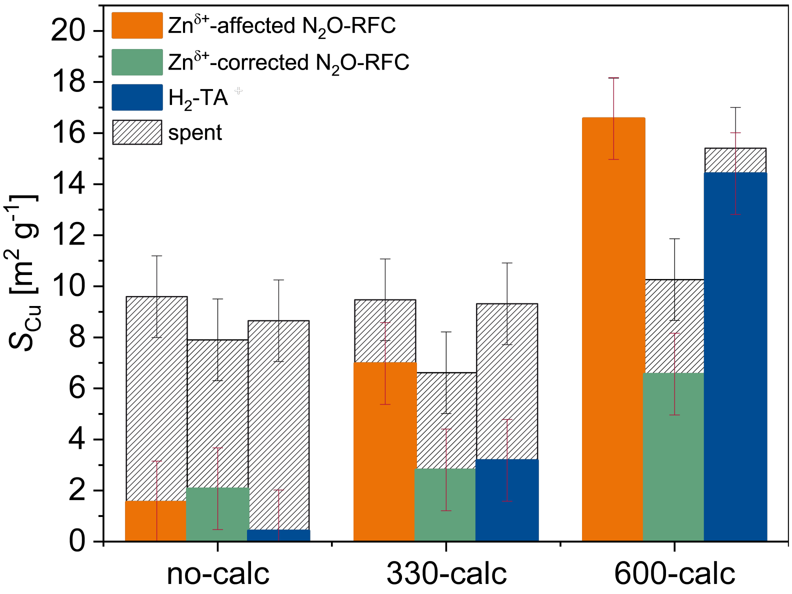

Figure 3.9.: Copper surface areas of no-calc, 330-calc and 600-calc determined by N_2O refractive frontal chromatography of the reduced sample (orange) and of the passivated sample (green) and by H_2 transient adsorption (blue). Areas determined for the as-prepared samples are shown in plain colored bars. Areas of the samples after use in the catalytic experiments are shown in striped bars. The error of the method ($1.6\,m^2\,g^{-1}$) is represented by the error bars in red (as-prepared) and black (spent).

The copper surface area of the as-prepared no-calc was determined to be $1.6\,m^2\,g^{-1}$ by the $Zn^{\delta+}$-affected N_2O-RFC and $2.1\,m^2\,g^{-1}$ by the $Zn^{\delta+}$-corrected N_2O-RFC. In theory, the area obtained for the first N_2O-RFC should always be higher than the one for the second N_2O-RFC. But with regard to the method error of $1.6\,m^2\,g^{-1}$, both areas can be considered equal. Hence, we can infer that no noteworthy amount of $Zn^{\delta+}$ or SMSI is present in this material. For 330-calc, $S_{Cu\&Zn\delta+}$ was found to be $7.0\,m^2\,g^{-1}$ and is in good agreement with $7\,m^2\,g^{-1}$ reported for a LDH material with the same composition by Kühl *et al.*[54] $S_{Cu-only}$ for this material was determined to be $2.8\,m^2\,g^{-1}$. The pronounced difference to $S_{Cu\&Zn\delta+}$ indicates the presence of a SMSI in this catalyst. Compared to no-calc, the value obtained for the $Zn^{\delta+}$-affected N_2O-RFC is considerably higher, while the value for the $Zn^{\delta+}$-corrected N_2O-RFC is the same within the method error. This demonstrates that the calcination of the hydrotalcite precursor led to structural changes which promoted the formation of $Zn^{\delta+}$ during reduction. Such changes could e.g. be a partial rearragement of the metals or the preformation of the spinel structure as described by Behrens *et al.*, both induced by a limited movability of the cations.[53] For 600-calc, both values obtained from the $Zn^{\delta+}$-affected and $Zn^{\delta+}$-corrected N_2O-RFC are significantly higher. In comparison to the other two materials, 600-calc is comprised of crystalline and (partly) segregated phases of CuO and $ZnAl_2O_4$ without HT-CO_3^{2-}. This prior phase segregation shows to have a positive influence on the exposed copper surface area. Moreover, the slightly higher Cu content of 600-calc (see ICP-OES and AAS results in Table 3.1) can also contribute to the higher area detected for this material.

We observed a strong positive influence of the catalytic tests on the exposed copper surface areas, especially for no-calc and 330-calc which still contain HT-CO_3^{2-}. However, we cannot define whether the substantial changes of the catalyst surface were caused by the methanol synthesis or the second reduction at 400 °C (see Table 5.2 in the SI). The areas of no-calc and 330-calc both raised to almost $10\,m^2\,g^{-1}$ for the $Zn^{\delta+}$-affected measurements and the values for the $Zn^{\delta+}$-corrected N_2O-RFC are also in a similar range. Within the scope of the method error, both catalysts assimilated and the spent samples exhibit the same areas of Cu and $Zn^{\delta+}$. The changes can be caused by an ongoing phase separation due to the increased ion movability at the reduction temperatures of 275 °C and 400 °C. Moreover, the decomposition of the present HT-CO_3^{2-} can liberate surface sites or whole pores and make them accessible for the probe molecule N_2O, as discussed previously for the N_2 physisorption experiments. 600-calc clearly exposes more copper sites with $16.5\,m^2\,g^{-1}$ and $10.3\,m^2\,g^{-1}$ for the $Zn^{\delta+}$-affected and $Zn^{\delta+}$-corrected measurements, respectively. The deviation of both values is also the highest for this sample, which implies a higher coverage of Cu by $Zn^{\delta+}$ and hence a more pronounced SMSI. Interestingly, $S_{\mathrm{Cu\&Zn}\delta+}$ stayed constant upon application in the catalytic tests and only the value for $S_{\mathrm{Cu-only}}$ has increased. This shows that although the sum of Cu and $Zn^{\delta+}$ surface sites stayed constant, the quantity of $Zn^{\delta+}$ on the surface has decreased compared to the initial catalyst. Thus, less Cu is covered by $Zn^{\delta+}$ after catalysis. Moreover, no such significant growth as for no-calc and 330-calc can be observed after the catalytic tests. This indicates that different to the other two catalysts, the structural changes were already accomplished prior to catalysis in 600-calc. More precisely, the calcination at 600 °C led to a decomposition of the HT-CO_3^{2-} and to the formation of crystalline CuO and $ZnAl_2O_4$ domains. This is consistent with the XRD patterns of the spent samples, in which the presence of the spinel could be demonstrated for all three catalysts (see Figure 3.12 below), while it was only present for 600-calc in the XRD patterns of the calcined samples (Figure 3.2). Yet the areas of the spent no-calc and 330-calc did not reach the level of 600-calc, even after several days of catalytic testing. The major difference is that while the active 600-calc catalyst resulted from a mixture of CuO and crystalline $ZnAl_2O_4$, 330-calc emerged from CuO in an amorphous Zn,Al-oxide matrix. no-calc behaves similar to 330-calc, as it is first dehydrated and then dehydroxylated to the mixed oxides at a low temperature during the thermal treatment of the reduction. This difference in the initial structures of the (calcined) precursors leads to a difference in the structure of the final activated catalysts and thus also in the exposed Cu surface areas.

H_2-TA experiments (blue bars) should give the same values as the $Zn^{\delta+}$-corrected N_2O-RFC, as both methods probe the surface of copper only. However, the areas determined by H_2-TA are higher for all three catalysts. As explained above, every method gives slightly different values because of the different chemistry, other experiment parameters and further method-specific uncertainties. The overall trend remains the same: While no-calc and 330-calc show similar copper surface areas, 600-calc exposes a considerably higher area. Yet a quantitative discussion is considered only reliable when comparing values obtained by the same method. That is why in the following discussion of the catalytic performance, we will only take into account the areas determined by N_2O-RFC.

3.3.3. Catalytic Performance

The activity of the catalysts was studied in the CO_2 hydrogenation to methanol. Prior to catalysis, the materials were reduced in 5 % H_2 in N_2 at 275 °C for 4 h. Then the temperature was reduced to 235 °C and subsequently, the gas was switched to syngas (H_2:CO_2:N_2 = 9:3:1, 20 bar) and the catalysts were allowed to stabilize for 19 h. N_2 in the syngas mixture served as an internal standard for the gas chromatography (GC) measurements. After this, the catalytic test started. With the same syngas mixture, the temperature of 235 °C was held for another 19 h and the effluent gas stream was analyzed by GC in the beginning, the middle and the end of the time period. The temperature was successively varied to 220, 205 and again 235 °C (second run at this temperature labeled as 235 °C#2) and the performance analyzed in the same manner. A more detailed description of the protocol is given in Table 5.2 in the SI. The conversion and product yields of the three measurements at a given temperature were averaged.

In addition to the presented LDH-derived catalysts, we also used a zinican malachite based catalyst reproduced after Schumann *et al.*[56] It is herein denoted as "CZA". Their catalyst was presented as a reference material and has the composition and phase typical for industrial methanol catalysts (Cu:Zn:Al = 68:29:3). CZA was also exposed to the sequence of surface reactions described earlier in Figure 3.8 to obtain the copper surface area of this material. It was determined to be 29.6 and 14.9 $m^2\,g^{-1}$ for the $Zn^{\delta+}$-affected and -corrected N_2O-RFC, respectively. The conversion and yield for the test at 235 °C (second run) are shown in Figure 3.10 and for the other temperatures in Figure 3.23 in the SI.

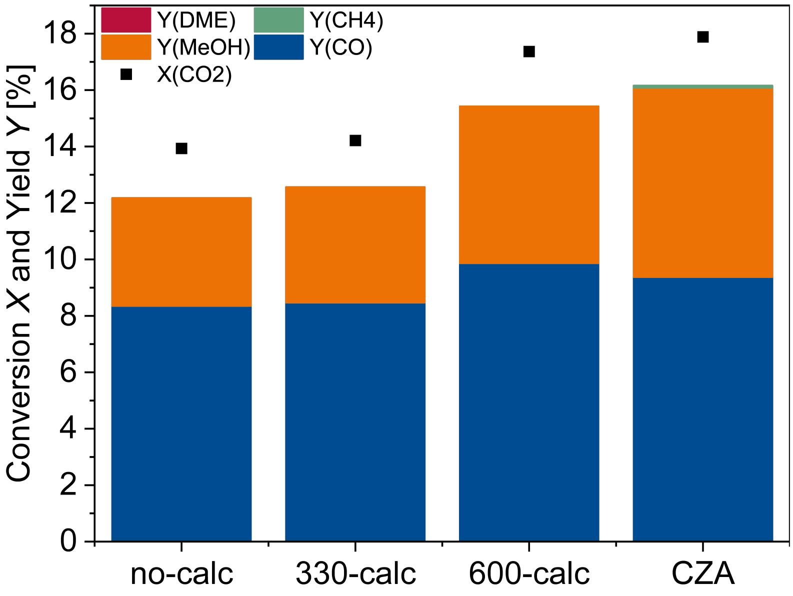

Figure 3.10.: CO_2 conversion X and product yields Y after reduction at 275 °C. The test was performed at 235 °C (second run). Reaction conditions: H_2:CO_2:N_2 = 69:23.2:7.8, $\dot{V}_{\mathrm{norm}}$ = 5.92 ml min^{-1}, p = 20 bar. DME = dimethyl ether, MeOH = methanol.

All catalysts were able to produce methanol under the applied reaction conditions. For the LDH-derived catalysts, 600-calc has the highest methanol yield, while no-calc and 330-calc show a similar performance. This observation is in good agreement with the identified copper surface areas which was the highest for 600-calc and in a similar range for no-calc and 330-calc. The reference CZA showed the highest methanol yield in our test. Although we chose the methanol synthesis as a comparing reaction, high amounts of carbon monoxide were formed during our tests by all catalysts. On the one hand, we used CO-free synthesis gas for our catalytic tests, which promotes the reversed water-gas shift reaction. On the other hand, we were limited to a pressure of 20 bar by the setup, which is comparably low to the industrial applied 50 to 100 bar.

Yet according to thermodynamics, the methanol reaction favors low temperatures and high pressures.[34] Further byproducts were dimethyl ether (DME) and methane with yields below 0.1 % for all temperatures and catalysts. We did not analyze the effluent gas stream for more than the four presented products. Thus, the gap between the CO_2 conversion and sum of product yields can be ascribed to further unknown products.

The methanol formation rate r gives the amount of methanol formed per weight of catalyst (see Figure 3.11 a). For a given temperature, it follows the order r(CZA) > r(600-calc) > r(330-calc) > r(no-calc). Moreover, for the LDH-derived catalysts, it is the highest for the highest reaction temperature. Although the methanol synthesis from CO_2 is an exothermic reaction,[41] the kinetic effect of the rate increase with increasing temperature seems to have a higher impact than the thermodynamics in the examined temperature range. Different to that, CZA has a rate maximum at 220 °C and r is the lowest at 235 °C. By comparing CZA to 600-calc, it becomes evident that 600-calc approaches the rate of CZA with increasing temperature. Hence, it can be suggested that CZA already reached the thermodynamic equilibrium at 220 °C, while the LDH-based catalysts are still in a kinetic regime at this temperature. The reason is the much higher copper surface area of CZA, which allows this catalyst to convert more CO_2 at once per time. Irrespective of the precursor type, the selectivity towards methanol is the highest for the lowest temperature of 205 °C, as expected by the exothermicity of the reaction. 235#2 represents a repetition of the catalytic test at 235 °C. A slight increase of r can be observed for every catalyst in the second run. This indicates that the catalysts had not reached a steady state condition after 19 h of stabilization time. The conversion of CO_2 in the second run also increased a little in case of no-calc and 330-calc (see Figure 3.10 and Figure 3.23a in the SI), which further indicates that the stabilization was not completed. It is likely that the very stable high-temperature carbonate was not fully evaporated after the given stabilization time and it still blocked some of the surface sites or pores within these catalysts.

To further examine the influence of different surface metal species on the catalytic performance, the methanol yields were normalized to the copper surface areas obtained from the $Zn^{\delta+}$-affected and -corrected N_2O-RFCs of the as-prepared samples. The resulting specific activities a_s are shown in Figure 3.11b, c and d for 330-calc, 600-calc and CZA, respectively. Because of the similarity of no-calc and 330-calc, the calculations were only done for the latter one. In case of 330-calc and 600-calc, the specific activity $a_{\mathrm{Cu\&Zn}\delta+}$ normalized to combined Cu and reduced Zn surface sites is the highest for the highest temperature, thus it shows the same trend upon temperature variation as the methanol formation rate r. For each activity $a_{\mathrm{Cu-only}}$ and $a_{\mathrm{Zn}\delta+}$, the methanol yield was ascribed only to a single surface species, thus the values are higher than for the combined species of $a_{\mathrm{Cu\&Zn\delta+}}$. A comparison of $a_{\mathrm{Cu-only}}$ and $a_{\mathrm{Zn\delta+}}$ shows that for both catalysts, each Cu surface site contributes more to the methanol formation than a $\mathrm{Zn}^{\delta+}$ site. Moreover, the ratio of $a_{\mathrm{Cu-only}}$ to $a_{\mathrm{Zn\delta+}}$ is about 3:2 in both cases. This finding is interesting as a much stronger SMSI was found for 600-calc and hence, a higher contribution of the $\mathrm{Zn}^{\delta+}$ sites was expected. In contrast to this, Cu and $\mathrm{Zn}^{\delta+}$ surface sites contribute equally in CZA. Because of the higher methanol yield at 220 °C, the specific activity of CZA is also the highest at this temperature.

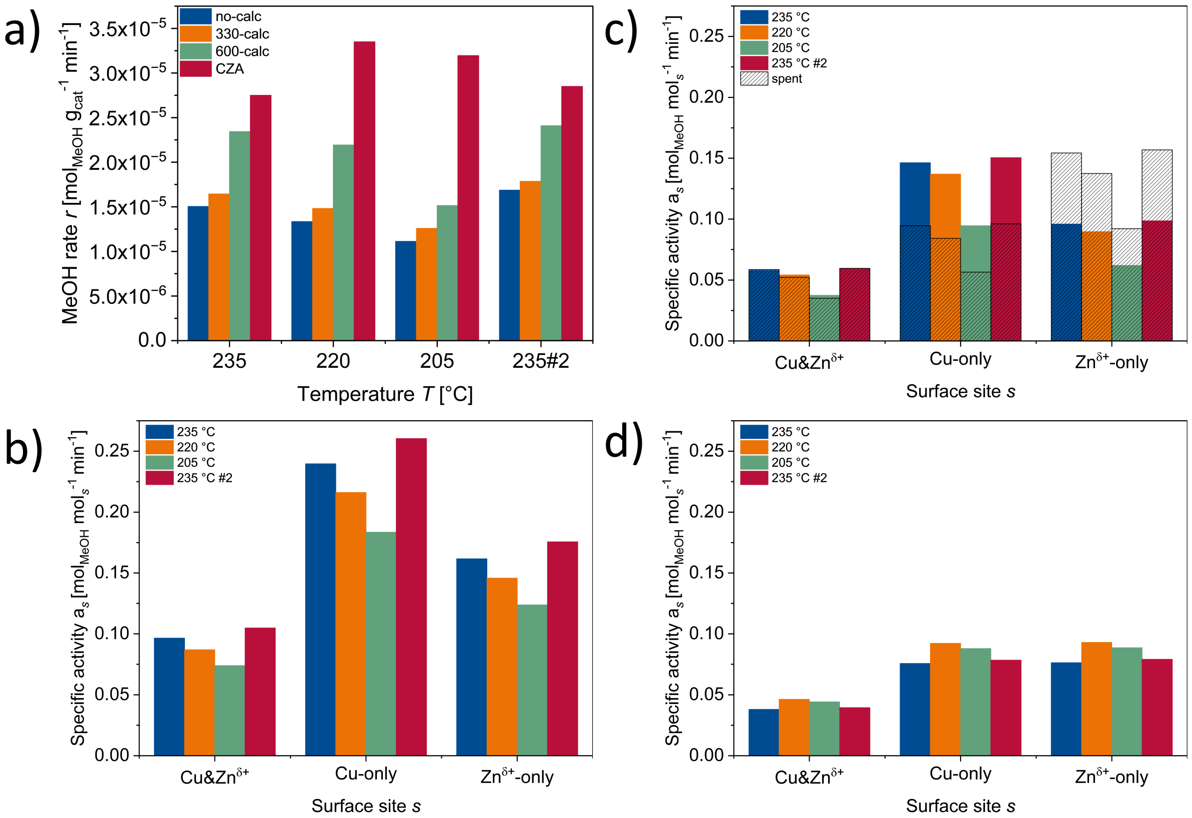

Figure 3.11.: Catalytic performance in the methanol synthesis reaction after reduction at 275 °C. a) Methanol formation rate r normalized by the mass of catalyst. Specific activity a normalized by the amount of combined Cu and $\mathrm{Zn}^{\delta+}$ surface sites, Cu surface sites or $\mathrm{Zn}^{\delta+}$ surface sites of b) 330-calc, c) 600-calc and d) CZA. Surface sites were calculated by the copper surface areas determined by N2O-RFC of the as-prepared samples. Black striped bars represent the specific activity normalized to the surface sites of the spent sample after reduction at 400 °C. Reaction conditions: H_2:CO_2:N_2 = 69:23.2:7.8, $\dot{V}_{\mathrm{norm}} = 5.92\,\mathrm{ml\,min^{-1}}$, $p = 20\,\mathrm{bar}$, T = 205, 220 or 235 °C, respectively. The label #2 marks a second catalytic run at 235 °C.

By the activity $a_{\mathrm{Cu\&Zn\delta+}}$ of each catalyst, their intrinsic activities per surface site can be compared. At 235 °C, the specific activity of 330-calc is more than 2.5 times that of the reference CZA and 600-calc outperforms CZA by more than 50 %. Kühl *et al.* pointed out the less favorable platelet microstructure of LDHs compared to the needle-like shape of a malachite with regard to the copper surface area.[54] By the platelet shape, more copper particles are embedded in the ZnAl matrix and are thus not accessible for reaction gases. However, they stressed the higher intrinsic activity of Cu surface species in their LDH based catalyst compared to a commercial industrial-type one. Those findings are confirmed by the present results. At 220 °C, $a_{\mathrm{Cu\&Zn\delta+}}$ of 330-calc is still twice as high than that of CZA and at 205 °C, it still outperforms CZA by about 70 %. $a_{\mathrm{Cu\&Zn\delta+}}$ of 600-calc is about 17 % higher compared to the reference at 220 °C, but at 205 °C this catalyst is intrinsically less active. Consequently, LDH-derived catalysts are suitable for the use at higher reaction temperatures compared to a malachite-derived one.

Pandit et al. described the formation of a CuZn bulk alloy in a CuMgZn model catalyst by reduction at 400 °C.[73] To examine the impact of the bulk formation on the methanol formation rate, we performed a second catalytic test subsequent to the first one, in which the catalysts were reduced at 400 °C. The results are shown in Figure 3.24 in the SI. Surprisingly, neither the conversion nor the methanol formation rate has changed substantially. The major difference is that r measured at 235 °C in the first run already reached the same level as in the second run and no activation effect is observable. We believe that this is due to the longer stabilization phase. For the test at 400 °C, no fresh catalyst batches were used, but the spent ones were kept and re-reduced at the higher temperature of 400 °C. Thus, for the first run at 235 °C after re-reduction, the catalysts already had time to stabilize for more than four days during the first catalytic test cycle.

For 600-calc, the specific activities were also calculated for the catalytic test after reduction at 400 °C. For the normalization, the Cu surface areas obtained from the spent 600-calc were used (see black striped bars in Figure 3.11c). $a_{\mathrm{Cu\&Zn\delta+}}$ for the as-prepared sample and spent sample normalization are very similar. Both $\mathrm{Zn}^{\delta+}$-affected N_2O-RFCs resulted in the same copper surface area of $16.6\,\mathrm{m}^2\,\mathrm{g}^{-1}$ and additionally, the catalytic performance after reduction at 275 and 400 °C does not deviate considerably. $a_{\mathrm{Cu-only}}$ became smaller because the $\mathrm{Zn}^{\delta+}$-corrected N_2O-RFC of the spent sample yielded a higher $S_{\mathrm{Cu-only}}$ of $10.3\,\mathrm{m}^2\,\mathrm{g}^{-1}$. A higher area stands for more active Cu centers and thus, the methanol yield per center gets smaller for a very similar yield. The number of $\mathrm{Zn}^{\delta+}$ sites decreased in the spent 600-calc. Although there are less $\mathrm{Zn}^{\delta+}$ sites, they intrinsically contribute more to the methanol formation, as can be seen by the increase of $a_{\mathrm{Zn\delta+}}$. It even surmounts $a_{\mathrm{Cu-only}}$, meaning that the $\mathrm{Zn}^{\delta+}$ sites con-

tribute more to the methanol formation than the Cu sites. Hence in the spent sample, the Zn in the support plays a crucial role in the methanol formation and is more than a mere structural promoter.
After removal from the reactor, the spent samples were re-reduced in diluted H_2 at 275 °C and analyzed by XRD. The patterns are shown in Figure 3.12.

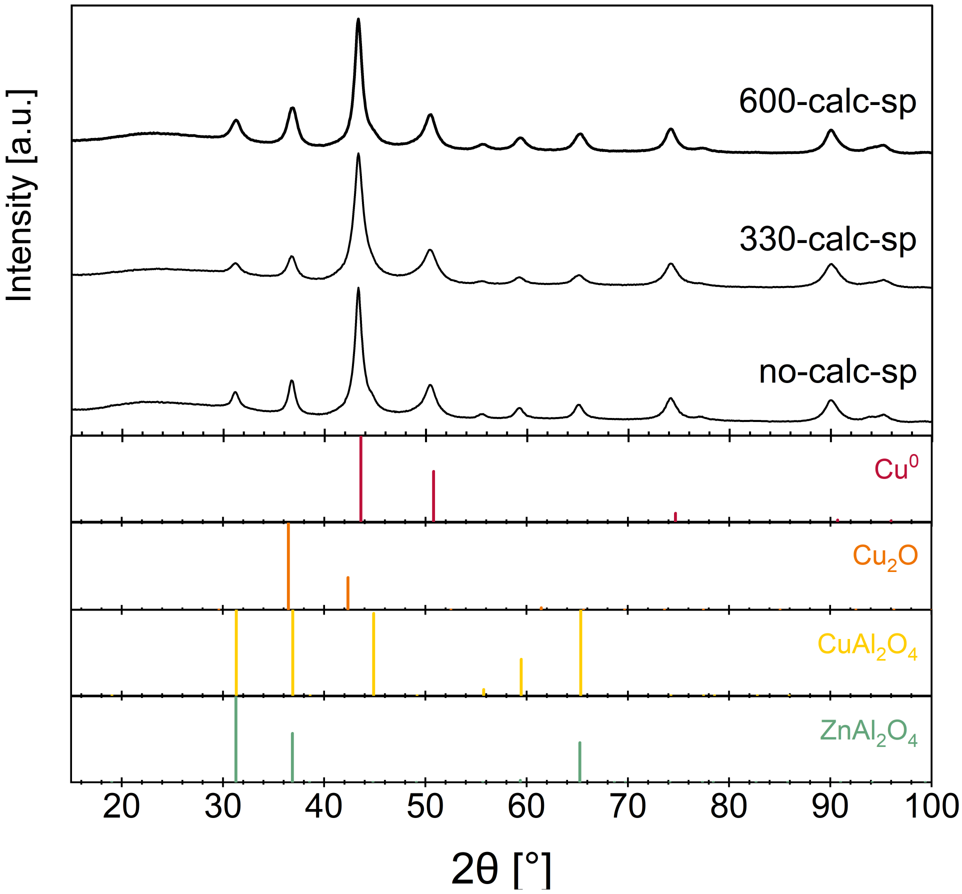

Figure 3.12.: PXRD of spent samples measured in capillaries after copper surface area measurements and re-reduction.

After exposure to synthesis gas at elevated temperatures for several days, the structure of the catalysts has clearly changed compared to the as-prepared material (shown in Figure 3.7). There are still reflections visible which can be attributed to metallic copper that have about the same broadness as for the as-prepared materials. In addition, reflections become present which are caused by a spinel. The spinel acts as a structural promoter or spacer for the copper nanoparticles. Though the presence of a $CuAl_2O_4$ is possible, it is more likely that $ZnAl_2O_4$ is the cause of the reflections. Copper is present as Cu^0 in the reduced samples, while Zn is in the Zn^{2+} state needed for the spinel structure, besides small amounts of partially reduced $Zn^{\delta+}$. As the spinel became detectable by XRD after catalysis, we can conclude that its domain size has increased and that it is in a crystalline state in the spent samples.

It is remarkable that although the size of the spacer domains has increased, it did not harm the Cu nanoparticle dispersion of the catalysts, represented by the exposed copper surface areas. On the contrary, as indicated before, S_{Cu} of the spent samples determined by N_2O-RFC increased substantially for all three materials after catalysis (see Figure 3.9 above). We believe that this is caused by an activation effect during catalysis. The effect is especially pronounced for no-calc and 330-calc which still contain the high-temperature carbonate. As already demonstrated above for the BET surface area, HT-CO_3^{2-} can block small pores within the material and make them inaccessible for gases. By the harsh reaction conditions, the pores are liberated and can be probed in a post-catalysis analysis. As the carbon content in 600-calc is low and most of the HT-CO_3^{2-} has already evaporated during calcination, the activating effect is weaker for this material.

3.4. Summary

LDH-based CuZnAl catalysts with a high intrinsic activity in methanol synthesis were presented. On the one hand, LDH-derived catalysts can evolve from the reduction of Cu^{2+} in an amorphous Zn,Al oxide matrix. This leads to a catalyst with a low Cu surface area in which the HT-CO_3^{2-} is still present. On the other hand, the catalyst can be obtained by reduction of Cu^{2+} embedded in a $ZnAl_2O_4$ spinel. The resulting catalyst has a higher Cu surface area and the HT-CO_3^{2-} is decomposed to a high extent. The latter can be triggered by calcination of the LDH precursor at 600 °C and yields a catalyst which an activity that is comparable to the industrial-type reference. $S_{\mathrm{Cu\&Zn}\delta+}$ of this LDH-derived catalyst is only about half of that of the reference, which demonstrates its high intrinsic activity. The reduction at 400 °C did not considerably change the activity, proving its high stability. In the future, the performance of the LDH-derived catalysts could be further improved by overcoming the less favorable platelet microstructure while keeping the promotional effect of the spinel matrix. In that way, a material with both a high intrinsic activity and good accessibility of the reactive sites could emerge.

3.5. Experimental Section

Catalyst Synthesis

Layered double hydroxides were synthesized by co-precipitation of a 0.8 M metal nitrate solution (molar ratio Cu:Zn:Al = 50:17:33) at 25 °C and pH = 8 in the half-automatized lab reactor OptiMax 1001 from Mettler Toledo. An alkaline solution of 0.6 M NaOH and 0.09 M Na_2CO_3 was used as a precipitation agent. 75 g of the metal solution was dosed into a resevoir of 200 ml deionized water over 30 min. Co-dosing of the precipitation agent was controlled by a computer program to ensure a constant pH value. The precipitate was aged for 1 h in the mother liquor at 25 °C. Afterwards, the precipitate was repeatedly washed with deionized water, dried at 80 °C overnight and thoroughly mortared. The LDH was calcined in a muffle oven in static air for 3 h at 330 °C and 600 °C, respectively (β = 2 °C min^{-1}). For the characterization and catalytic tests, the samples were pressed with a hydraulic press from Perkin-Elmer (Überlingen, Germany) with 5 t for 2 min. The resulting pellets were mortared and sieved to 125 - 250 µm with stainless steel sieves from ATECHNIK (ISO 3310-1, Leinburg, Germany).

X-ray Powder Diffraction Patterns of calcined samples

XRD patterns of the calcined samples were measured at room temperature on an Empyrean diffractometer from Malvern Panalytical equipped with a PIXcel3D detector. Measurements were conducted in Bragg-Brentano geometry with Cu $K_{\alpha 1}$ radiation (λ = 1.54 Å) in the range of 5 to 90°.

X-ray Powder Diffraction Patterns of reduced samples

XRD patterns of the reduced samples were measured in glass capillaries (0.5 mm thickness) on a Stadi-P from STOE equipped with a MYTHEN 1K detector and GE(111) monochromator. Measurements were conducted with Cu $K_{\alpha 1}$ radiation (λ = 1.54 Å) in Debye-Scherrer geometry in the range of 15 to 100°.

Sample Composition Analysis

Mole fractions of metals in the calcined samples were determined by Inductively Coupled Plasma Optical Emission Spectrometry on an ICP-OES Avio 200 from Perkin Elmer. About 10 mg of a sample was dissolved in 0.5 ml HNO_3 (p.a., 65 %) and diluted with distilled water to a total volume of 50 ml. 5 ml of this solution was taken, again diluted to a total volume of 50 ml and used for analysis. Additionally, the molar metal amounts were also identified by atomic absorption spectroscopy on an ICE3500 from

Thermofisher. The carbon and hydrogen content was analyzed by elemental analysis on an EA300 from Eurovector.

Scanning Electron Microscopy and Energy Dispersive X-Ray Mapping

Sample reproductions were used for the images recorded on a Apreo S LoVac from Thermo Fisher Scientific. Prior to measurement, samples were sputtered with Au/Pd (80:20). A back scattering detector was used for imaging. EDX mapping was conducted in the same machine. K edges of Cu, Zn and Al were recorded.

Nitrogen Physisorption

N_2 adsorption-desorption profiles of pressed and sieved samples were measured on a BELSORP MAX from Microtrac Retsch GmbH. Prior to the measurement, the calcined samples were degassed at 100 °C and uncalcined samples at 80 °C for 2 h. The partial pressure p/p_0 was recorded in the range of 0.0 to 0.99 at -196 °C and referenced to an empty cell. The partial pressure range of 0.05 to 0.3 was used to calculate the surface areas by applying the Brunauer-Emmett-Teller (BET) equation to the adsorption branch. The Barrett-Joyner-Halenda (BJH) method was used on the desorption branch to analyze the pore size distribution.

The surface areas of the unsieved samples were measured on a Nova 3200e soprtion station from Quantachrome. p/p_0 in the range of 0.07 to 0.40 was used to determine the surface areas. Prior to the measurements, the samples were degassed at 100 °C (nocalc: 80 °C) for 2 h under vacuum.

Infrared Spectroscopy

IR spectra were recorded on a Bruker ALPHA-P ATR MIR spectrometer in the range of 400 to 4000 cm^{-1}.

Mass Spectrometry-coupled Thermogravimetry

A STA 449C Jupiter from Netsch coupled to an MS was used for TG-MS measurements. About 10 mg of sample was placed in a 85 µl Al_2O_3 pan without a lid. The sample was thermally treated from room temperature to 1000 °C (β = 2 °C min^{-1} in 21 % O_2 in Ar ($\dot{V}$ = 100 ml min^{-1}).

Hydrogen Temperature-Programmed Reduction

Measurements were performed in a Belcat-B catalyst analyzer from BEL JAPAN, Inc.

(Haradanaka Toyonaka, Japan) equipped with a TCD detector. About 70 mg of calcined sample (sieve fraction 125 to 250 µm) were placed onto quarz wool in an U-shaped reactor. Prior to the experiment, the catalyst was dried at 120 °C for 30 min in Ar (80 ml min^{-1}, heating rate β = 5 °C min^{-1}). After cooling to 40 °C, the temperature-programmed reduction was started. The catalyst was reduced in 5 % H_2 in Ar (80 ml min^{-1}) with a heating rate β of 6 °C min^{-1} up to 800 °C. The maximum temperature was held for 30 min. Water was removed by an in-line molecular sieve before the effluent gas reached the TCD.

S_{Cu} Determination by H_2 Transient Adsorption

Measurements were performed in a Belcat-B catalyst analyzer from BEL JAPAN, Inc. (Haradanaka Toyonaka, Japan) subsequent to reduction in 5 % H_2 in Ar at 275 °C ($\dot{V}$ = 35 ml min^{-1}, β = 2 °C min^{-1}, holding time = 4 h) and cooling to 40 °C in He. The gas outlet was connected to an Omnistar GSD 320 mass spectrometer from Pfeiffer Vacuum which was calibrated for H_2, N_2 and N_2O whenever a new catalyst was filled into the analyzer. Prior to the H_2-TA, the lines were purged with He (80 ml min^{-1}) at 40 °C until no more other gases were detected by the MS and then purging was carried on for another 10 min. Afterwards, the gas was switched to 2 % H_2 in He (8 ml min^{-1}) and the downstream hydrogen trace was recorded by the MS for 2 h. We followed the protocol of Kuld *et al.*[70] and compared the hydrogen trace directly after reduction (Cu^0) and after exposure to N_2O (Cu_2O) to determine the copper surface area.

The area under the Cu_2O-signal was subtracted from the one of Cu^0 to obtain the area enclosed from both signals. This area equals the volume of hydrogen V_{H2} consumed for the reduction of Cu_2O to Cu^0. The specific copper surface area S_{Cu} was then calculated by

$$S_{\mathrm{Cu}} = \frac{V_{\mathrm{H2}} \cdot N_A \cdot 2}{V_{\mathrm{norm}} \cdot m_{\mathrm{cat}} \cdot A_{\mathrm{Cu}}} \tag{3.10}$$

N_A is the Avogadro constant and V_{norm} the standard molar volume at 20 °C and 1.013 bar. m_{cat} is the amount of catalyst and A_{Cu} is the number of Cu atoms per surface area as defined by Hinrichsen *et al.* (1.47×10^{19} atoms m^{-2}).[1] The factor 2 originates from the 2:1 stochiometry of Cu to H_2 as shown in Reaction 3.5. Flow-time profiles are shown in Figure 3.20 in the SI. The error of our setup was determined to be 1.6 m^2 g^{-1}.

S_{Cu} Determination by N_2O-Reactive Frontal Chromatography

Measurements were performed subsequent to a H_2-TA on the same setup. The reactor was purged with He (80 ml min^{-1}) until no more other gases were detected by the MS.

Then the catalyst surface was cleaned by heating the reactor to 130 °C ($\beta = 5\,°\mathrm{C\,min^{-1}}$) for 45 min and afterwards cooled down to 60 °C. For the N_2O-RFC, the concept described by Chinchen *et al.*[58] and Hinrichsen *et al.*[1] was followed. A mixture of 1 % N_2O in He (5 ml $\mathrm{min^{-1}}$) was dosed into the reactor for 1 h at 60 °C and the effluent gas was analyzed by the MS.

To determine the Cu surface area, the integral of the N_2 signal from the start to the point of inflection was used, at the intersection of the N_2 and N_2O signal. This integral equals the volume of N_2 (V_{N2}) evolved during oxidation according to Reaction 3.3, Reaction 3.4 and Reaction 3.8. The area obtained from the first N_2O-RFC of the reduced sample refers to the specific area of both Cu and partially reduced Zn $S_{\mathrm{Cu+Zn}}$. The area of the second N_2O-RFC of the passivated sample refers to the specific area of Cu only $S_{\mathrm{Cu-only}}$. The specific surface area of Zn S_{Zn} is defined as the difference between $S_{\mathrm{Cu+Zn}}$ and $S_{\mathrm{Cu-only}}$. The specific surface area S_x (x = Cu+Zn or Cu only) is calculated by

$$S_x = \frac{V_{\mathrm{N2}} \cdot N_A \cdot f_{\mathrm{N2O}}}{V_{\mathrm{norm}} \cdot m_{\mathrm{cat}} \cdot A_{\mathrm{Cu}}} \tag{3.11}$$

N_A is the Avogadro constant and V_{norm} the standard molar volume at 20 °C and 1.013 bar. m_{cat} is the amount of catalyst and A_{Cu} the number of Cu atoms per surface area as defined by Hinrichsen *et al.* (1.47×10^{19} atoms $\mathrm{m^{-2}}$).[1] f_{N2O} is a stochiometric factor of 2.08 found by Chatterjee *et al.* for Cu surface atoms and the N_2O probe molecule during N_2O-RFC.[2] Concentration-time profiles are shown in Figure 3.21 and Figure 3.22 in the SI. The error of our setup was determined to be 1.6 $\mathrm{m^2\,g^{-1}}$.

Catalytic Tests

Tests were performed in a 30-fold tubular parallel reactor. Each tube is 230 mm in length and has a 5 mm outer and 4 mm inner diameter. Heating was enabled by a furnace, equipped with a turbine in the center to ensure an accurate heat exchange. A 31st reactor (6 mm outer diameter) was kept empty and served as a reference. It was preheated to 150 °C outside of the furnace. The gas feed was controlled by digital mass flow controllers from Brooks. 160 mg of 125 to 250 µm particle sizes were applied for each catalyst. Additionally, a pre-bed (1000 mg) and post-bed (172 mg) of SiO_2 with a size of 355 to 500 µm was used. The protocol of the catalytic tests is shown in Table 5.2. The effluent gas stream was analyzed by gas chromatography (on-line Agilent 7890A) successively for each reactor in a series. More information about the setup can be found elsewhere.[75] For each test at a given temperature, the series was repeated two times and the results averaged.

Table 3.2.: Protocol of the catalytic tests applied for methanol synthesis including the holding time t, temperature T, mole fractions x of the gases, heat ramp β, pressure p and total volume flow over all 31 reactors $\dot{V}_{\text{total}}$.

Step	t [h]	T [°C]	x CO_2:H_2:N_2 [%]	β [°C min^{-1}]	p [bar]	$\dot{V}_{\text{total}}$ [ml min^{-1}]
Drying	15	100	0:0:100	5	20	900
Activation	4	275	0:5:95	2	20	300
Cooling	1	235	0:5:95	5	20	300
Stabilization	19	235	23.2:69:7.8	0	20	183.6
Test 1	19	235	23.2:69:7.8	0	20	183.6
Test 2	19	220	23.2:69:7.8	5	20	183.6
Test 3	19	205	23.2:69:7.8	5	20	183.6
Test 4	19	235	23.2:69:7.8	5	20	183.6
Activation	4	400	0:5:95	2	20	300
Cooling	1	235	0:5:95	5	20	300
Test 5	19	235	23.2:69:7.8	0	20	183.6
Test 6	19	220	23.2:69:7.8	5	20	183.6
Test 7	19	205	23.2:69:7.8	5	20	183.6
Test 8	19	235	23.2:69:7.8	5	20	183.6

The methanol production rate r was calculated by

$$r = \frac{S_{\text{MeOH}} \cdot \dot{n}_{\text{CO2,conv}}}{m_{\text{cat}}} \tag{3.12}$$

with S_{MeOH} being the selectivity towards methanol, m_{cat} the amount of catalyst used (160 mg) and $\dot{n}_{\text{CO2,conv}}$ the molar flow of converted CO_2. It is defined as

$$\dot{n}_{\text{CO2,conv}} = \frac{\dot{V}_{\text{reactor}} \cdot x_{\text{CO2}} \cdot X_{\text{CO2}} \cdot \rho_{\text{CO2}}}{M_{\text{CO2}}} \tag{3.13}$$

$\dot{V}_{\text{reactor}}$ is the gas flow per reactor (5.92 ml min^{-1}), x_{CO2} the mole fraction of CO_2 in the syngas (23.2 %), X_{CO2} the conversion of CO_2, ρ_{CO2} the density of CO_2 (1.9767 g L^{-1}) and M_{CO2} the molar mass of CO_2 (44.01 g mol^{-1}).
The specific activity per surface site a_x is defined as

$$a_x = \frac{S_{\text{MeOH}} \cdot \dot{n}_{\text{CO2,conv}}}{N_{\text{surf}}} \tag{3.14}$$

with x being either Cu+$Zn^{\delta+}$, Cu only or $Zn^{\delta+}$ only surface sites. The number of surface sites N_{surf} can be determined from the specific surface areas S_x obtained by N_2O-RFC.

$$N_{\text{surf}} = \frac{S_x \cdot m_{\text{cat}} \cdot A_{\text{Cu}}}{N_A} \tag{3.15}$$

A_{Cu} is the number of Cu atoms per surface area as defined by Hinrichsen *et al.* (1.47×10^{19} atoms m^{-2})[1] and N_A the Avogadro constant.

3.6. Acknowledgment

We thank Andrey Tarasov for TG-MS measurements, Dietrich Tönnes for XRD patterns, Melina Ottenberg for ICP-OES measurements, the IR-department of the Tuczek group (CAU Kiel) for IR spectra, Robin Meya and Beate Römer for elemental analysis and AAS, Kateryna Loza for SEM imaging, Jihao Wang for N_2 physisorption experiments, Benjamin Mockenhaupt for conceptualization of and discussions on H_2-TA and N_2O-RFC chemisorption experiments, Gereon Behrendt for providing CZA reference material and the IMPRS RECHARGE for kind funding and support.

3.7. Authors & Contributions

Jil-Lorean Gieser: Conceptualization, data curation, evaluation, writing, catalyst synthesis, chemisorption experiments
Sebastian Mangelsen: XRD measurements of reduced samples, advising support
Qingxin Yang: Catalytic measurements
Evgenii Kondratenko: Advising support for catalytic measurements
Malte Behrens: Supervision, project administration, proofreading

3.8. Supporting Information

During the co-precipitation, the temperature slightly oscillated around the setpoint of 25 °C as it was controlled by a water-cooled electric heating jacket. The pH also oscillated during the precipitation, but a buffer system developed over time that dampened this behavior. Nonetheless, one outbreak after around 1200 s in which the pH firstly fell and then shortly exceeded 11 was recorded. This was likely caused by an air bubble in the precipitation agent line. When the bubble instead of basic solution was dosed, the pH dropped because of the simultaneous addition of acidic metal solution. The program recognized this drop and then overcompensated it with too much basic precipitant, causing the short outbreak of the pH.

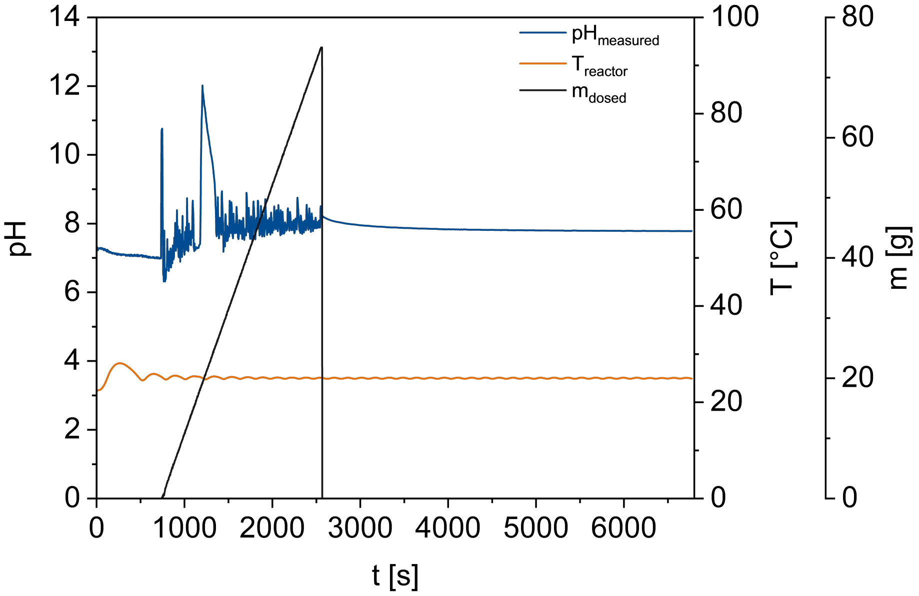

Figure 3.13.: Optimax synthesis protocol of no-calc.

Table 3.3.: Comparison of no-calc and reproductions. Mole fractions x(M) of metals determined by AAS and surface area S_{BET} of unsieved samples determined by N_2 physisorption.

Sample	x(Cu) [mol %]	x(Zn) [mol %]	x(Al) [mol %]	S_{BET} [$\mathrm{m^2\,g^{-1}}$]
no-calc	52.8	15.7	31.5	51.9
reproduction 1	54.5	15.6	30.0	58.7
reproduction 2	53.3	16.6	30.1	87.4

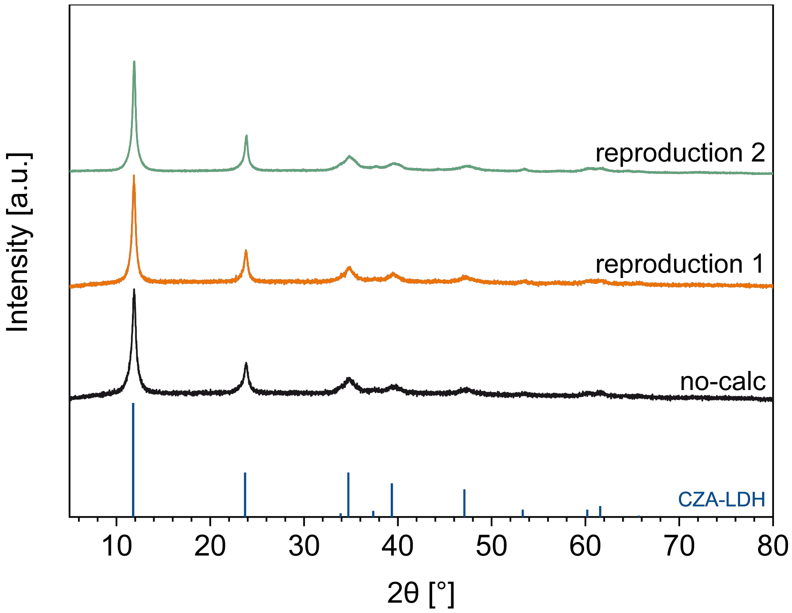

Figure 3.14.: XRD powder patterns of no-calc and its reproductions. Reference for a CuZnAl LDH (blue) is shown as bars.

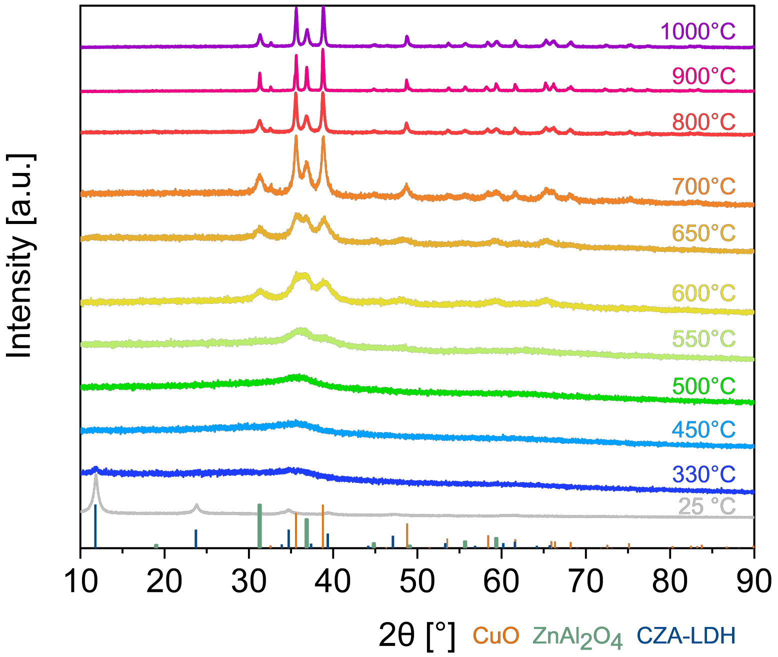

Figure 3.15.: XRD powder patterns of reproductions of uncalcined no-calc calcined material up to 1000 °C. Each calcination was an individual experiment. References for $ZnAl_2O_4$ (green), CuO (orange) and a CuZnAl LDH (blue) are shown as bars.

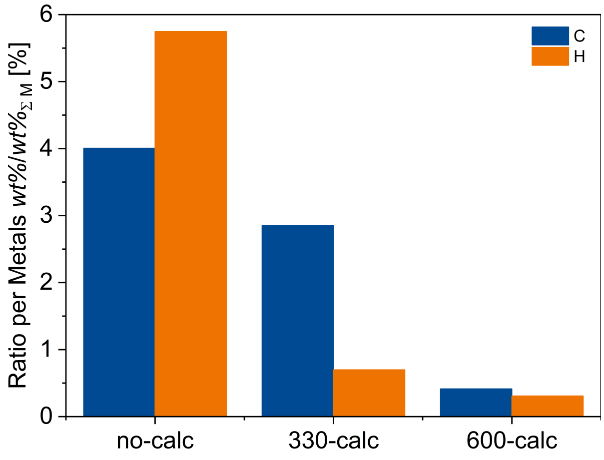

Figure 3.16.: Weight ratios of carbon and hydrogen normalized to the amount of metals Cu, Zn and Al in the as-prepared samples. The ratios were calculated by dividing the mass fractions of carbon and hydrogen determined by elemental analysis by the sum of mass fractions of the metals determined by AAS.

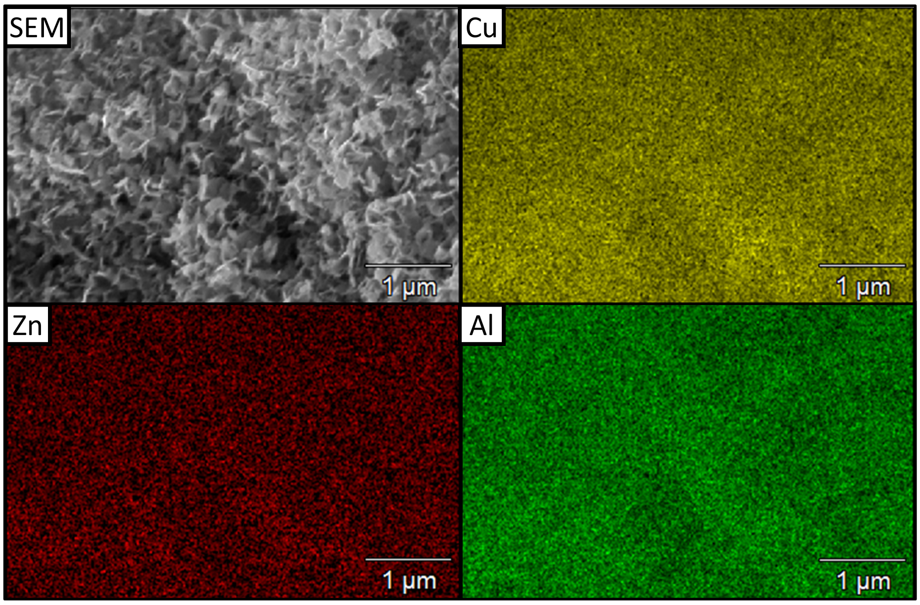

Figure 3.17.: Scanning electron microscopy image of no-calc and corresponding energy dispersive X-ray mapping of Cu, Zn and Al.

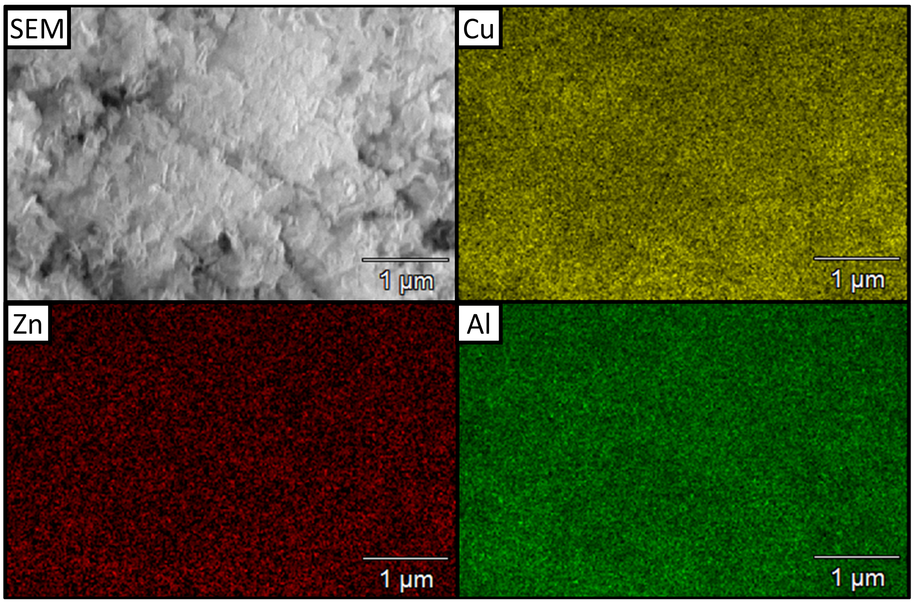

Figure 3.18.: Scanning electron microscopy image of 330-calc and corresponding energy dispersive X-ray mapping of Cu, Zn and Al. Due to strong drifting effects, the SEM image is slightly blurred.

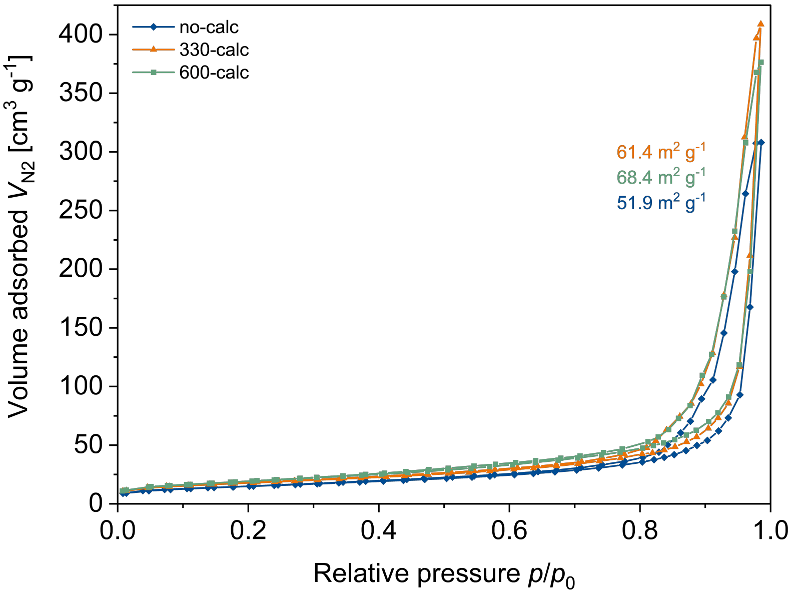

Figure 3.19.: N_2 adsorption-desorption isotherms of unsieved samples used to determine the surface areas.

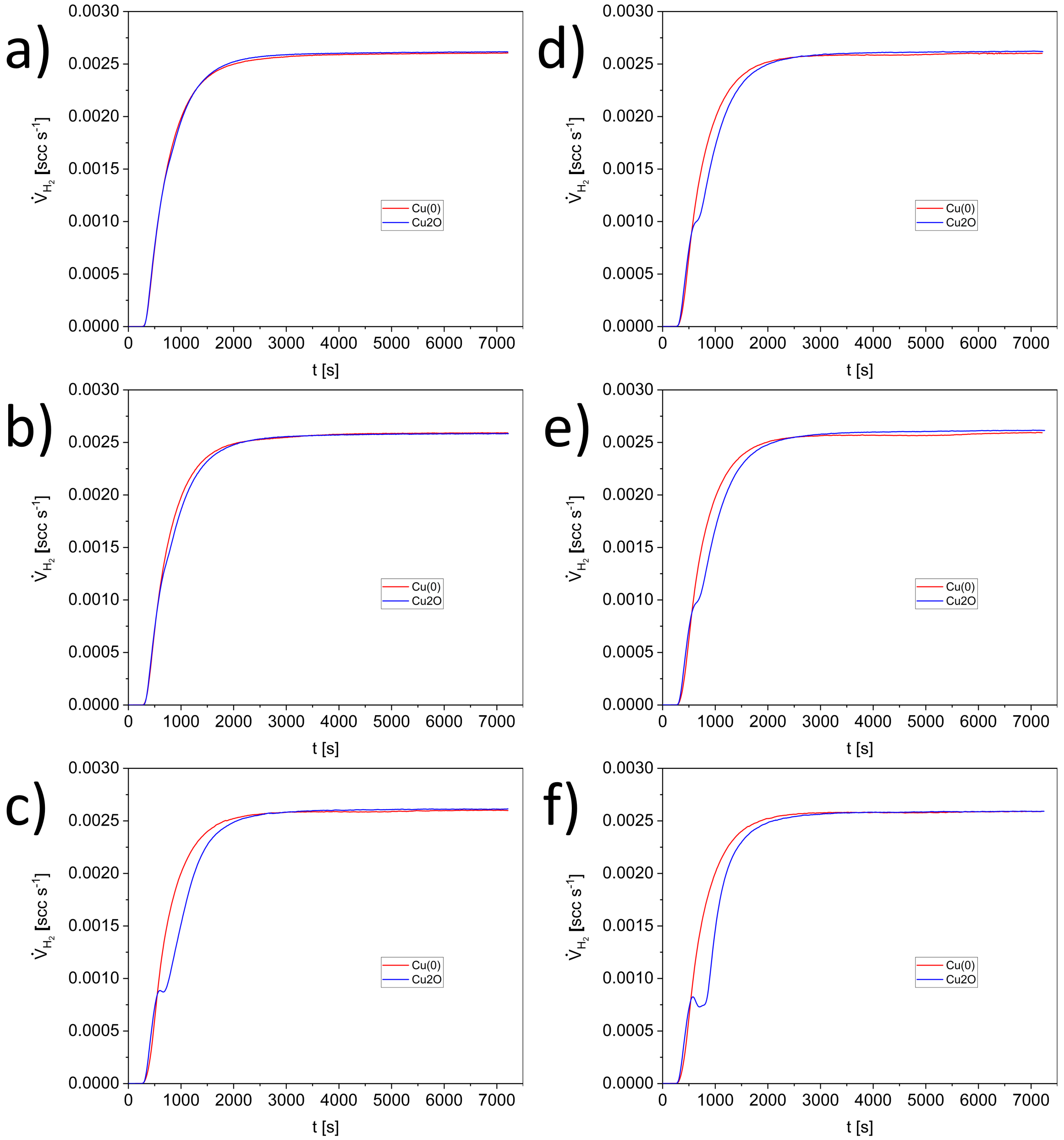

Figure 3.20.: Hydrogen transient adsorption of a-c) as-prepared no-calc, 300-calc and 600-calc and d-f) spent no-calc, 330-calc and 600-calc.

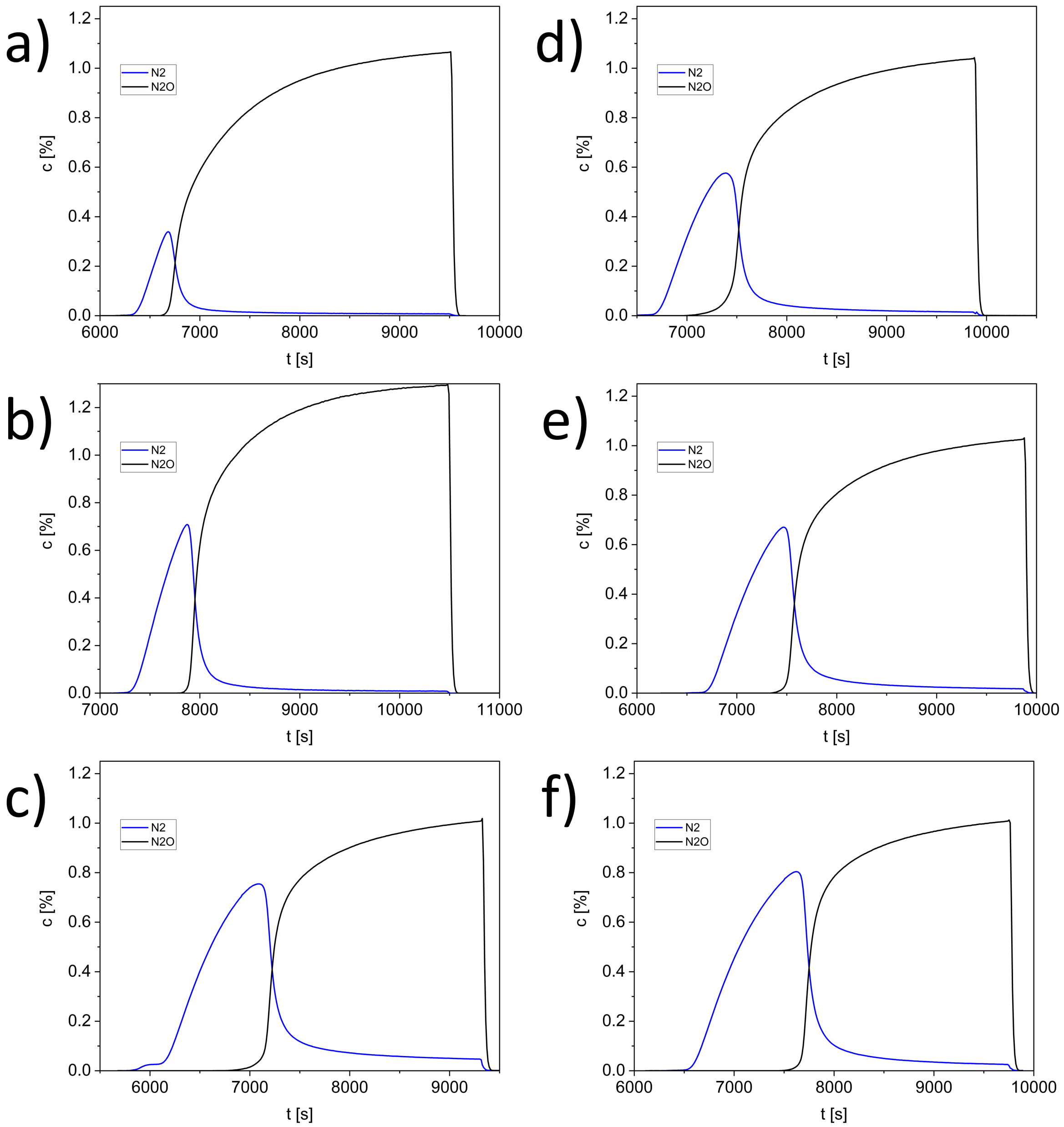

Figure 3.21.: First N_2O reactive frontal chromatography of reduced samples of a-c) as-prepared no-calc, 300-calc and 600-calc and d-f) spent no-calc, 330-calc and 600-calc.

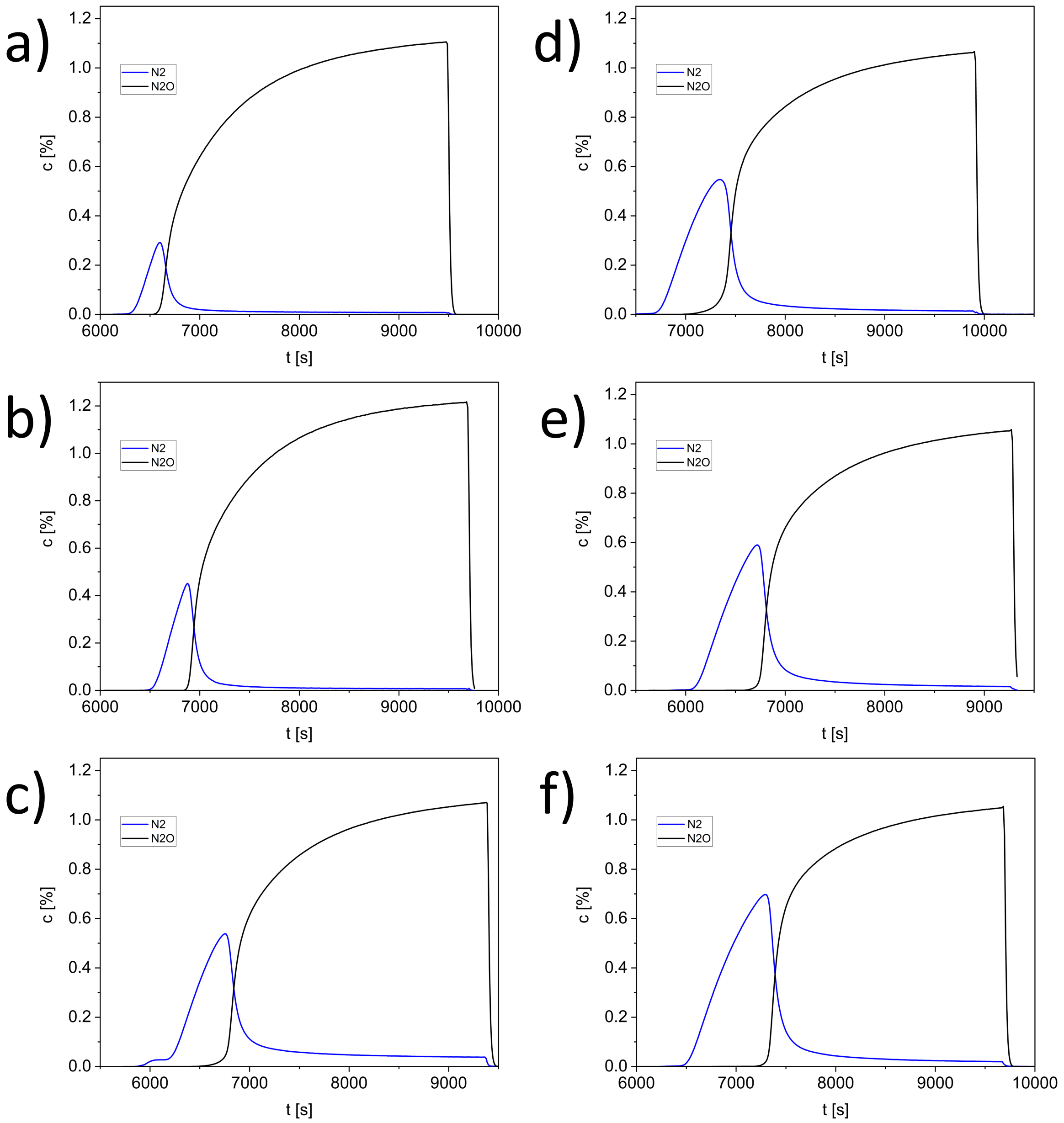

Figure 3.22.: Second N_2O reactive frontal chromatography of passivated samples of a-c) as-prepared no-calc, 300-calc and 600-calc and d-f) spent no-calc, 330-calc and 600-calc.

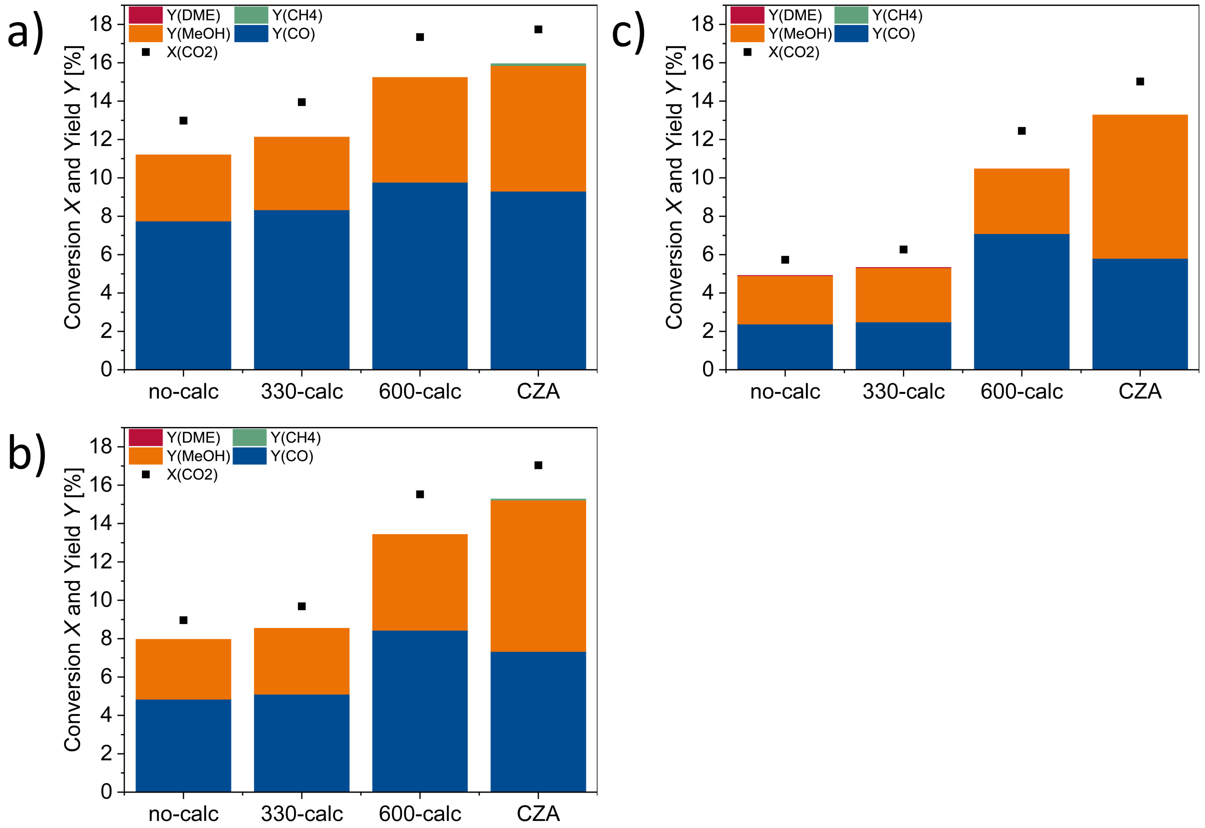

Figure 3.23.: CO_2 conversion X and product yields Y after reduction at 275 °C. Reaction performed at a) 235 °C, b) 220 °C and c) 205 °C. Reaction conditions: H_2:CO_2:N_2 = 69:23.2:7.8, $\dot{V}_{\mathrm{norm}}$ = 5.92 ml min^{-1}, p = 20 bar. DME = dimethyl ether, MeOH = methanol.

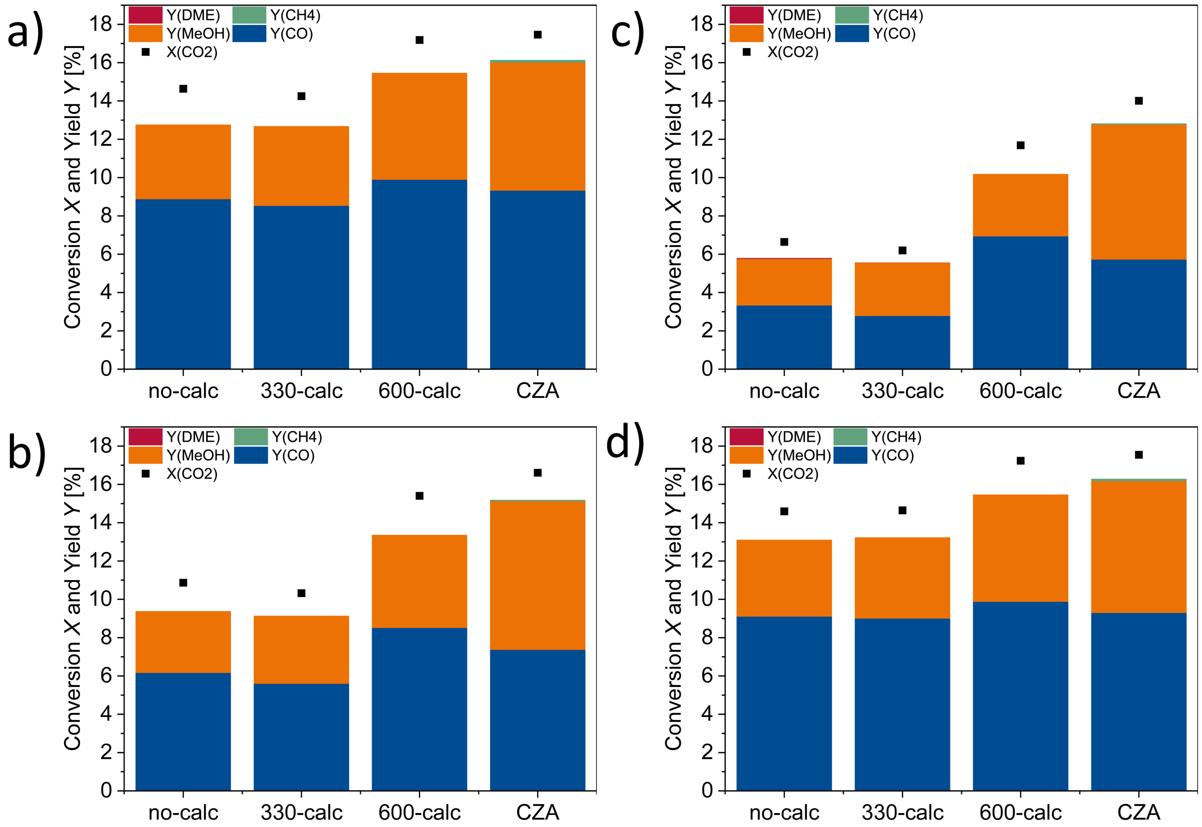

Figure 3.24.: CO_2 conversion X and product yields Y after reduction at 400 °C. Reaction performed at a) 235 °C, b) 220 °C, c) 205 °C and 235 °C (second run). Reaction conditions: H_2:CO_2:N_2 = 69:23.2:7.8, $\dot{V}_{\mathrm{norm}}$ = 5.92 ml min^{-1}, p = 20 bar. DME = dimethyl ether, MeOH = methanol.

4. Liquid-phase Methanol Synthesis over LDH-derived Copper Catalysts in a Batch Reactor

4.1. Abstract

The alcohol-promoted methanol synthesis was studied in ethanol with syngas comprising pure CO_2 in H_2 (CO_2:H_2 = 1:3). As catalysts, binary and ternary materials based on layered double hydroxides (LDHs) with the general composition $(Cu_xZn_yM_z)(OH)_2(CO_3)_{z/2}$ (M = Al or Ga) were used for the first time in this type of reaction. Upon calcination of the LDH precursors, carbonate-modified materials were obtained that had a low crystallinity. The materials can therefore be described as mixed metal oxides or CuO finely dispersed in a preformed ZnM_2O_4 spinel matrix. With increasing Cu content, the spinel-type matrix stayed amorphous, while a growth of crystalline CuO domains could be observed. By ethanol as the alcoholic solvent, the reaction mechanism was altered compared to the industrial gas-phase synthesis. It allowed a reaction at lower temperatures, which is favorable for the conversion due to the exothermicity of the methanol synthesis from syngas. Temperatures as low as 140 °C were sufficient for the reaction to occur due to the facile hydrogenolysis of the intermediate ethyl formate. The influence of Al, Ga and Zn in LDH-derived catalysts as a structural or electronic promoter in this reaction will be investigated regarding the activity and selectivity towards methanol.

4.2. Introduction

Climate neutrality is a common goal of all members of the European Union until 2050.[7] This objective is accompanied by a significant change in economy, such as a rapid decarbonization of our industry and transport sector to reduce greenhouse gas emissions.[76,77] Nowadays, fossil resources (such as crude oil, coal and natural gas) are still primarily used for the energy generation and as a raw material. A shift to renewable resources like wind, solar power and biomass has to be carried out to fulfill the climate goals of the European Union[7,8] and the Paris Agreement of 2015.[9,10]
Green hydrogen became the most important energy carrier of the energy transition as it is a non-fossil and carbon-free material.[22,78] It is usually synthesized by photolysis, electrolysis or thermolysis of water or from biomass fermentation.[79,80] Analogue to grey hydrogen produced from fossil resources, it has a versatile application range and

can be used e.g. for the production of green steel,[25,26] green fertilizers[81,82] or as an alternative fuel.[22,83] Drawbacks of the use of hydrogen in the transportation sector, e.g. in fuel cell electric vehicles (FCEVs), are the low volumetric energy density of H_2 compared to conventional fuels even at elevated pressures and the hazards regarding handling and storage. Due to the required pressure of at least 200 bar and its capability to diffuse through steel, thick-walled tanks have to be used. For a fixed amount of energy, this leads to a tank that is about 10 times as heavy and 20 times as big compared to the required one for conventional gasoline.[27] Moreover, precautions have to be taken because of the high flammability and large explosion range.[21,22]

An alternative is the storage of H_2 in a chemical bound state and synthesis of liquid chemical energy carriers. Advantages are the use of existing infrastructure and experience in terms of distribution and storage of liquid fuels.[34,84] An example of such a liquid fuel is methanol.[85] Already today, methanol is a base chemical with high demand and an increasing annual production rate.[35,36] Next to the direct use as a solvent and production of further base chemicals,[86] it was also found to be suitable as a fuel additive[87] or alternative fuel in spark-ignition engines[88] or methanol fuel cells.[48]

Historically, methanol was produced from CO-rich syngas gas over a ZnO/Cr_2O_3 catalyst at 300 to 400 °C and 100 to 330 bar. Although more active Cu catalysts were already studied in the 1920s, its poisoning by impurities in the syngas was challenging, especially by sulfur.[41,42,89,90] Only when sulfur-free, purified syngas was available, $Cu/ZnO/Al_2O_3$ catalysts were applied industrially in the so-called low-temperature low-pressure process at 220 to 280 °C and 50 to 100 bar.[90,91] Zn was found to be an effective structural promoter. It enabled a high dispersion of Cu and prevented sintering under reaction conditions. Moreover, it also showed to be an electronic promoter. The high activity of those catalysts is attributed to a CuZn synergy, though the debate about its nature is still ongoing. Amongst others, a surface alloy,[92] defective Cu surfaces decorated with partially reduced $Zn^{\delta+}$[60] or Cu particles with a ZnO_x overlayer[61] are discussed. Nonetheless, it is generally accepted that Zn is more than a mere structural promoter and as well beneficial for the activity and selectivity.[93–95] Small amounts of Al_2O_3 were found to be a structural promoter that enhance the catalytic activity and long-term stability by preventing agglomeration of Cu sites. This is facilitated by changing the structural and electronic properties of the ZnO.[42,51,96,97]

Next to this classical ternary catalyst, many other metal oxides were studied as promoters for Cu-based catalysts, such as ZrO_2, SiO_2 and TiO_2.[42,95,98,99] Highly selective catalysts could be obtained by using Ga_2O_3 as a promoter. Lam *et al.* synthesized $CuGa_x$ nanoparticles on SiO_2 and ascribed the improved selectivity and activity to an increased interfacial area between Cu^0 and $Ga^{III}O_x$.[100] Toyir *et al.* concluded from their XPS studies that small particles of Ga_2O_3 influence the oxidation state of Cu from metallic to oxidic, which lead to an enhanced selectivity compared to a catalyst without Ga or with larger Ga particles.[101,102]

The typical syngas mixture comprises CO and H_2 in various ratios, depending on the manufacturing or application process. It is produced e.g. by coal gasification, steam cracking of oil or partial oxidation of oil and natural gas. The most common process today is methane steam reforming.[80,90] For the conventional, gas-phase methanol production, it was found that small amounts of CO_2 in the syngas mixture enhance the reaction rate[93,103,104] and the following reactions occur:[41,51]

$$CO + 2\,H_2 \rightleftharpoons CH_3OH \qquad \Delta H_0 = -91.0\,\mathrm{kJ\,mol^{-1}} \tag{4.1}$$

$$CO_2 + 3\,H_2 \rightleftharpoons CH_3OH + H_2O \qquad \Delta H_0 = -49.8\,\mathrm{kJ\,mol^{-1}} \tag{4.2}$$

$$CO + H_2O \rightleftharpoons CO_2 + H_2 \qquad \Delta H_0 = -41.2\,\mathrm{kJ\,mol^{-1}} \tag{4.3}$$

Methanol is obtained by the hydrogenation of either CO (Reaction 4.1) or CO_2 (Reaction 4.2), though it was shown that over Cu/ZnO catalysts, CO_2 is the favorable carbon source and that Reaction 4.2 proceeds much faster.[49,58,93] The CO_2 hydrogenation results in water being introduced into the reaction mixture as a byproduct. This water can react with CO in the water gas shift (WGS) reaction (Reaction 4.3) to produce further CO_2, explaining the promoting effect of CO in a syngas mixture.

However, in terms of using methanol as sustainable fuel, it has to be made of anthropogenic CO_2 and green hydrogen only, and this CO_2 needs to be used in a circular way.[37,105] Moreover, methanol synthesis from both CO and CO_2 is an exothermic process that thermodynamically favors low temperatures and high pressures. Still the conventional process is conducted at elevated temperatures due to unfavorable kinetics. To overcome this problem, the group of Fujimoto reported a new synthesis route for methanol in 1999 which is not derived from the historical gas-phase process. Instead, they suggested the use of alcohols as a co-catalyst in a three-phase reaction system. The proposed mechanism consists of three reaction steps and is supported by *in situ* studies. When using ethanol as a solvent, those are:[106,107]

$$CO_2 + H_2 \rightleftharpoons HCOOH \tag{4.4}$$

$$HCOOH + EtOH \rightleftharpoons HCOOEt + H_2O \tag{4.5}$$

$$HCOOEt + 2\,H_2 \rightleftharpoons CH_3OH + EtOH \tag{4.6}$$

First, carbon dioxide is hydrogenated to formic acid (Reaction 4.4). The acid then reacts with the alcoholic solvent to an ester (Reaction 4.5). Lastly, the ester undergoes a hydrogenolysis (Reaction 4.6). Therein, methanol is formed and the solvent is gained back. In total, Reaction 4.2 is realized by this mechanism. It was designed to use pure CO_2 as a carbon source and the reaction can already take place at temperatures as low as 150 °C. Later, the same group showed that this reaction can also be operated with a conventional, CO-rich syngas mixture as the WGS reaction occurs simultaneously to procduce CO_2.[108] In addition, a linear increase of conversion with increasing pressure was found[109,110] and the formation of the ester (Reaction 4.5) was identified to be rate-determining.[108,111–113] The group of Jung examined the required catalyst properties for this reaction in detail. They pointed out that unlike the conventional gas-phase synthesis, not only Cu metal sites need to be considered, but also acidic sites which are needed for the esterification. A correlation between the number of strong acid sites and methanol yield was found.[113,114] Nieminen *et al.* could significantly increase the methanol yield by removing the byproduct water with a molecular sieve.[110] Contrarily, no effect of water addition to the reaction system was found by the Tsubaki group.[108,111,115] Yet the group of Nieminen used pure CO_2 as a carbon source instead of a mixture of CO and CO_2 in case of the Tsubaki group. This certainly shows that although the alcohol-assisted synthesis both works with conventional syngas and pure CO_2, the reaction conditions need to be chosen carefully. Furthermore, in a syngas composition variation, an increasing methanol and ester yield was found with increasing CO_2 content, with pure CO_2 giving the best results. This emphasizes that this mechanism is especially suited for syngas consisting of pure CO_2.[109]

As the product methanol is an alcohol itself, it should be capable of promoting its synthesis in an autocatalytic way. Indeed, the use of methanol as a solvent was already suggested and conducted by the groups of Fujimoto and Tsubaki.[106,108,111,112] Thrane *et al.* were the first to propose that this autocatalytic effect also occurs in the industrial, gas-phase methanol synthesis and is responsible for the majority of turnovers.[116] To elucidate the mechanism, Schwiederowski *et al.* conducted high-pressure gas-phase pulse experiments in which defined amounts of methanol were dosed to a reaction mixture at industrially relevant steady-state conditions. They observed a surplus of methanol after methanol pulses and the amount increased exponentially with the amount of dosed methanol, proving its autocatalytic effect. Moreover, pulses of the assumed intermediate methyl formate also led to an increased methanol formation.[117]

Although the effect of the syngas composition[109,115] and type of alcohol[111,112,118] was addressed in previous publications, only little is known about the influence of the catalyst phases. Many groups used commercial catalyst that consist of mixed metal phases and cannot be studied in detail due to confidentiality reasons. In case of presented self-synthesized catalysts, they were either not made from single-phase precursors or not characterized in detail. In this study, we will apply non-commercial catalysts derived from layered double hydroxide (LDH) precursors in the alcohol-assisted CO_2 hydrogenation to methanol.

The structure of LDHs, also known as hydrotalcites, is derived from the mineral brucite $Mg(OH)_2$ and consists of cationic layers that are octahedrally coordinated by hydroxyl groups. By exchanging some of the bivalent cations by trivalent ones, the layers are positively charged. This excess charge is compensated by anions that are found next to water in the interlayers. The general formula is $[M^{2+}_{1-x}M^{3+}_{x}]^{x+}[A_{x/n}]^{n-} \cdot m\mathrm{H_2O}$ with M being a cation, A an anion, n the charge of the anion and x a variable in the range of 0.2 to 0.33.[52,119] LDHs are promising catalyst precursors as they showed to have a high intrinsic activity in the gas-phase methanol synthesis.[54,55] Moreover, their composition can be varied in a broad range, both regarding the metal ratios and the number of respective metals. This allows for the synthesis of materials with a complex metal mixture within a single phase. To our knowledge, this type of material has not been applied yet in the alcohol-assisted methanol synthesis. In the following, the performance of catalysts made of this specific phase will be investigated and the effect of temperature, Cu content and the promoters Zn, Al and Ga will be studied.

4.3. Results & Discussion

4.3.1. Hydrotalcite Precursor

Ternary LDH materials with varying amounts of Cu, Zn, Al and Ga were synthesized *via* co-precipitation. The Cu amount was varied from 50 to 70 % and the ratio of Zn to Al was kept constant at 1:2. The notation was chosen in such a way that it gives the type of metals and the amount of Cu. For example, the material named CZA-55 has a molar ratio Cu:Zn:Al of 55:15:30. In addition, Al was substituted by Ga in CZG-50. Moreover, two binary materials were prepared without Zn. They are denoted CA-67 and CG-67 and have a composition of 67:33 Cu:Al or Cu:Ga, respectively.

The powder XRD patterns of all synthesized materials are shown in Figure 4.1. Phase-pure CZA hydrotalcites could be obtained for a Cu content up to 65 %. In CZA-67 and CZA-70, small reflections are present indicating the presence of a malachite byphase.

The Ga-substituted CZG-50 and CG-67 formed larger crystallites, hence they show slightly sharper signals than their Al containing analogues. No reference for a CZG-LDH could be found in open databases. However, the obtained pattern fits the one reported in other publications for CZG-LDHs with different metal ratios.[55,120,121] Due to the larger radius of Ga^{3+} compared to Al^{3+}, the reflections of CZG-50 are shifted to lower angles compared to CZA-50.

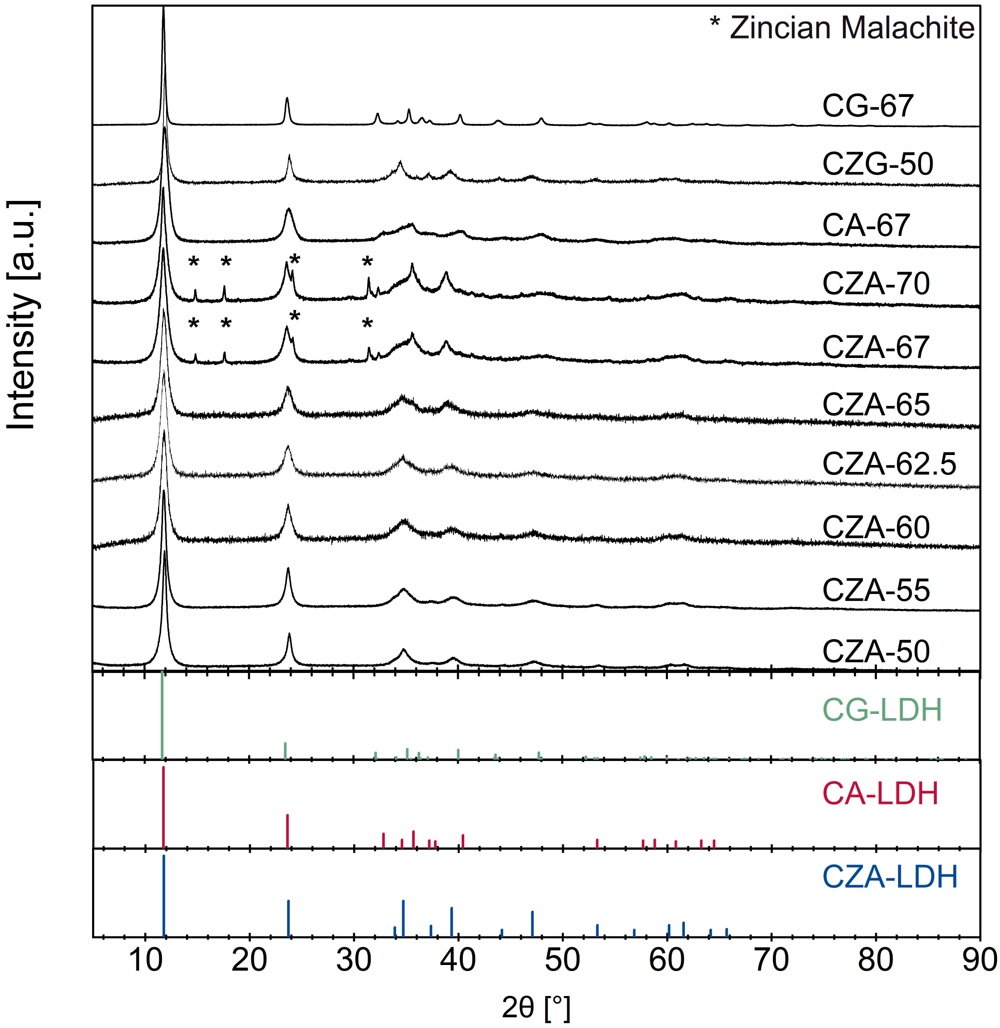

Figure 4.1.: XRD powder patterns of hydrotalcite precursors. References for a binary CG (green), binary CA-LDH (red) and ternary CuZnAl-LDH (blue) are shown as bars. Reflections of a zincian malachite byphase are marked with asterisks.

The interaction of the metal layers with the interlayer molecules was analyzed by infrared spectroscopy (see Figure 4.2). The bending mode at 1639 cm^{-1} can be attributed to water in the interlayers. A broad signal at about 3400 cm^{-1} is caused by OH stretching both from the interlayer water and the hydroxyl groups in the cationic layer. The band at 1357 cm^{-1} is caused by the ν_3 antisymmetric strechting mode of interlayer carbonate.[62–64] The band position of carbonate is shifted compared to the free anion at 1415 cm^{-1}, indicating a strong hydrogen bonding with the layer hydroxy groups and interlayer water.[65] A further band at 849 cm^{-1} can be attributed to the ν_2 out-of-plane stretching of carbonate. Metal-OH deformations cause the band at 577 cm^{-1}.[63,122] For Ga-containing samples, this position is shifted to 526 cm^{-1} as the Ga-OH bond is slightly weaker than the Al-OH bond. The zincian malachite byphase in CZA-67 and CZA-70 found in the XRD patterns is also observable in the IR spectra.[46,122] The positions are marked with asterisks. While in CZA-67 only the strongest band at 1048 cm^{-1} is visible, CZA-70 has additional bands at 820 cm^{-1} and 1501 cm^{-1}. This indicates that the amount of byphase is higher in the latter material.

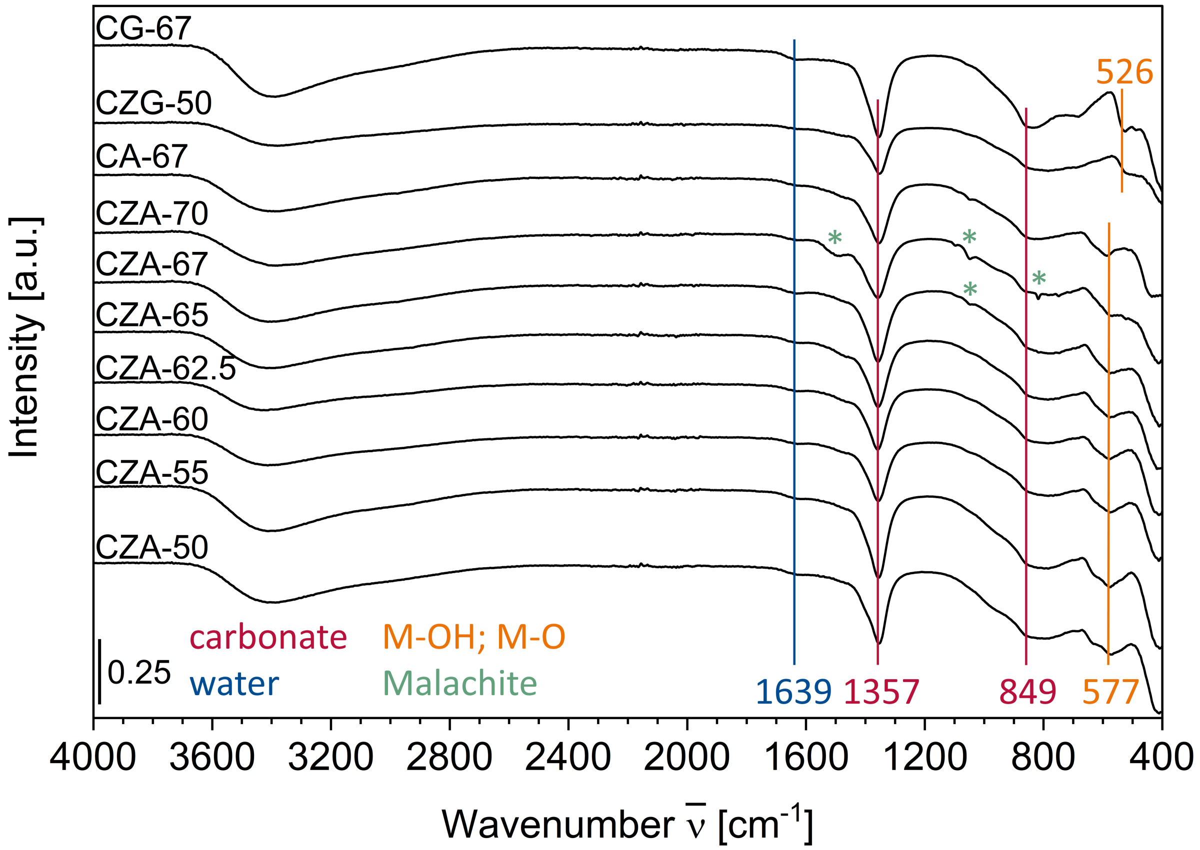

Figure 4.2.: Infrared spectra of hydrotalcite precursors measured in transmission mode.

The molar composition of the hydrotalcite precursors were determined by ICP-OES (see Table 4.1). Apart from CG-67, the identified amounts of Cu exceed the target values by about 3 mol %). The Zn to Al ratio in the ternary CZA materials approximately fit the targeted 1:2 ratio. Deviations from the target composition must have occurred during co-precipitation and aging, possibly caused by a preferential precipitation of Cu compared to Zn and Al at the given conditions. A systematic error of the ICP device is less likely as the composition was cross-checked by atomic absorption spectrometry (AAS). Also with this method, the determined Cu amounts were higher than adjusted in the metal salt solution used during co-precipitation. According to the AAS results, CG-67 also follows the trend of too much Cu incorporation.

All ternary catalysts have a surface area in the range of (61 ± 5) $m^2\,g^{-1}$ with CZA-62.5 having the highest area of 65.1 $m^2\,g^{-1}$. The two binary catalysts CA-67 and CG-67 have a somewhat lower area of 43.1 and 42.4 $m^2\,g^{-1}$, respectively. A high surface area is desirable as it offers more catalytically active surface sites. The results point out the importance of Zn as a structural promoter. The adsorption-desorption isotherms used to determine the areas are found in Figure 4.14 and the resulting pore size distributions in Figure 4.15 in the SI. All LDHs show type IV(a) isotherms with type H3 hystereses, caused by mesopores resulting from the aggregation of the LDH platelets. The saturation plateau at high relative pressures can rather be described as an inflexion point at $p/p_0 = 1$, which is typical for these plate-like particles.[67,68] The majority of the pores in all materials have a diameter of 20 to 60 nm. Only in CZA-62.5 and CG-67, the most abundant pores are below 20 nm.

Table 4.1.: Mole fractions of metals x(M) determined by ICP-OES and surface area S_{BET} of hydrotalcite precursors.

sample	x(Cu) [mol %]	x(Zn) [mol %]	x(Al or Ga) [mol %]	S_{BET} [$m^2\,g^{-1}$]
CZA-50	52.9	16.4	30.3	58.7
CZA-55	57.7	14.4	27.4	63.1
CZA-60	62.7	12.6	24.1	60.5
CZA-62.5	64.9	11.9	22.7	65.1
CZA-65	67.3	11.3	20.8	56.4
CZA-67	69.2	10.0	20.4	61.8
CZA-70	72.6	8.7	18.4	57.1
CA-67	69.6	0.0	30.0	43.1
CZG-50	53.5	17.4	28.4	62.1
CG-67	65.7	0.0	33.8	42.4

4.3.2. Calcined Material

All hydrotalcite precursors were calcined at 330 °C in static air. Additionally, CZA-50 was also calcined at 600 °C and this material was denoted CZA-50-600. PXRD analysis reveals the formation of poorly crystalline materials by thermal treatment at a low temperature of 330 °C. For CZA-50, only one broad reflection at about 36.0° 2θ is visible, indicating the presence of CuO.

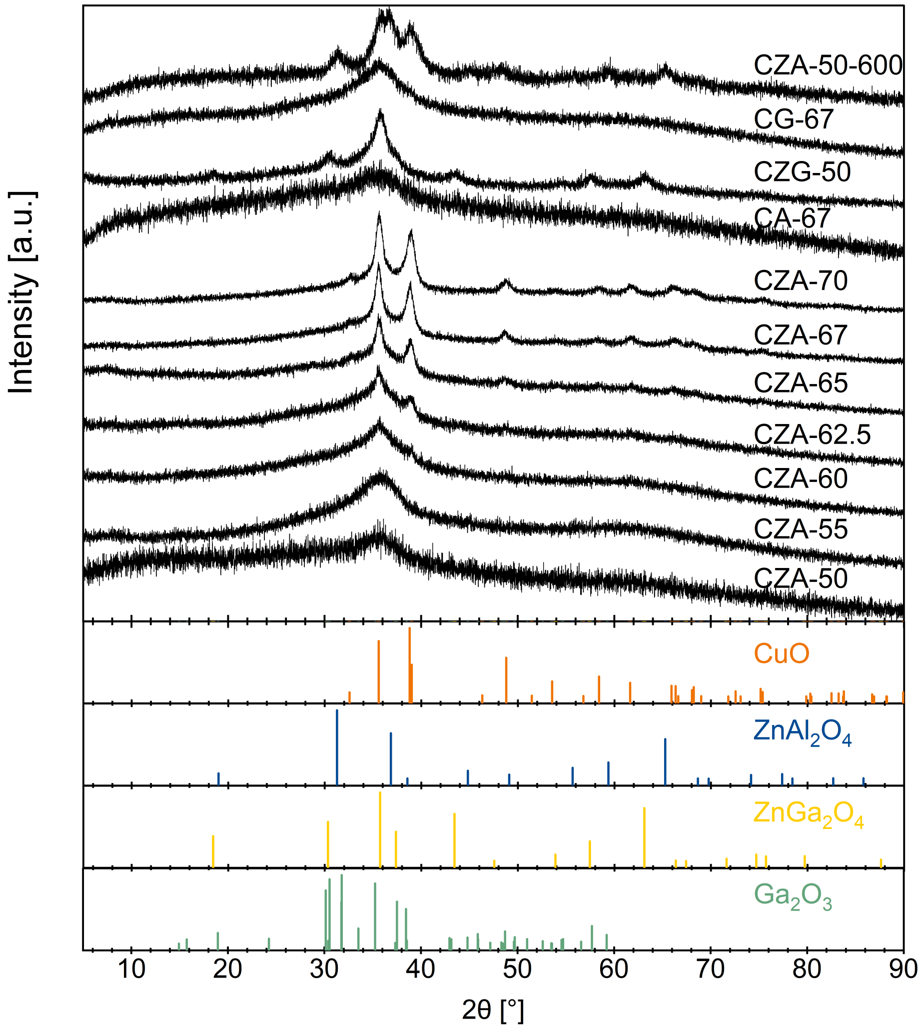

Figure 4.3.: XRD powder patterns of calcined precursors. References for CuO (orange), $ZnAl_2O_4$ (blue), $ZnGa_2O_4$ (yellow) and Ga_2O_3 (green) are shown as bars.

With increasing Cu content, a shoulder at 38.7° 2θ and an additional reflection at 48.8° 2θ arises, which can be ascribed to CuO. No indication for the presence of Zn or Al containing phases can be found because they form an amorphous matrix. Behrens *et al.* ascribed this to the preformation of a spinel phase by a beginning mobility and solid state diffusion of Al^{3+} ions.[53] According to them, the energy input by heating is not high enough for crystallization, but only for local rearrangements. With Cu being a Jahn-Teller ion, its corresponding oxide has a low symmetry and is not miscible with the spinel. Thus, it segregates from the oxidic ZnAl matrix and forms CuO particles. With increasing Cu content, more Cu is available to form more and bigger crystallites and the reflections for CuO become more intense. Interestingly, CA-67 is less crystalline than CZA-67 despite having the same Cu content. Hence, without Zn acting as a structural promoter, the segregation of CuO from Al_2O_3 is more difficult compared to the segregation from $ZnAl_2O_4$. After calcination at 600 °C, the presence of the ZnAl spinel becomes clearly visible by the reflections located at 31.3, 59.4 and 65.3° 2θ in CZA-50-600. Substitution of Al by Ga leads to a more pronounced segregation of CuO and the spinel phase. Compared to CZA-50, distinct reflections are visible in CZG-50 that display the presence of both CuO and $ZnGa_2O_4$. This shows that the mobility of Ga^{3+} ions is higher compared to Al^{3+} ions at the given calcination temperature of 330 °C. In the binary catalyst CG-67, the segregation is less facile in absence of Zn, similar to CA-67. However, the signal at 36° 2θ referring to CuO is more intense and the presence of Ga_2O_3 is indicated by a shoulder toward lower angles, which further shows the higher mobility of Ga ions compared to Al ions.

The presence of Ga_2O_3 in CG-67 is further implied by IR spectroscopy (see Figure 4.4 b). The corresponding bands are marked with asterisks at 459 and 660 cm^{-1}. Interestingly, CZG-50 also has a band at 660 cm^{-1} and an additional one at 447 cm^{-1}. A Ga_2O_3 byphase in this catalyst was not traceable in the XRD pattern as the positions of the reflections are in close vicinity to the ones for the ZnGa spinel. A small band at 2338 cm^{-1} is attributed to adsorbed CO or CO_2 from the atmosphere.[123,124] M-O vibrations of Al containing samples are located at a slightly higher wavenumber of 475 cm^{-1}. Despite the thermal treatment, signals caused by carbonate are still detectable and their positions are similar for all calcined materials. The band at 827 cm^{-1} is caused by the ν_2 out-of-plane deformation mode. A splitting of the ν_3 band into two peaks at 1486 and 1380 cm^{-1} is observable. Splitting occurs when the symmetry (D_{3h}) of the carbonate ion is lowered, e.g. by a mono- or bidentate coordination to the remaining layer hydroxyl groups. The splitting can also be caused by an incorporation of the carbonates into the cationic layer. Additionally, the lowered symmetry is displayed by a weak band of the ν_1 vibration mode located at about 1050 cm^{-1}, which is usually IR inactive.[62–64] In CZA-50-600, the intensity of the split ν_3 band is drastically decreased and the other bands referring to carbonate are not present. This shows that the amount of carbonate in this material is much lower than in the materials calcined at 330 °C. In general, the presence of carbonate in the samples after calcination is ascribed to the so-called high-temperature carbonate (HT-CO_3^{2-}). The decarbonization can be analyzed e.g. by the CO_2 trace in TG-MS measurements. The CO_2 peak maximum refers to the stability of the HT-CO_3^{2-} and is dependent on the precursor phase like malachite (350 °C), rosasite (400 °C) and aurichalcite (480 °C).[46] For calcined LDH materials, a peak maximum ranging from 427 °C to 618 °C can be found, depending on the metal type and ratio.[53,54,62,64] During the calcination of CZA-50-600 at 600 °C, the temperature was high enough to evaporate the HT-CO_3^{2-} and thus, most of the carbonate was removed from this sample. A TGMS measurement of the CZA-50 precursor was shown previously in Figure 3.1 of Section 3.

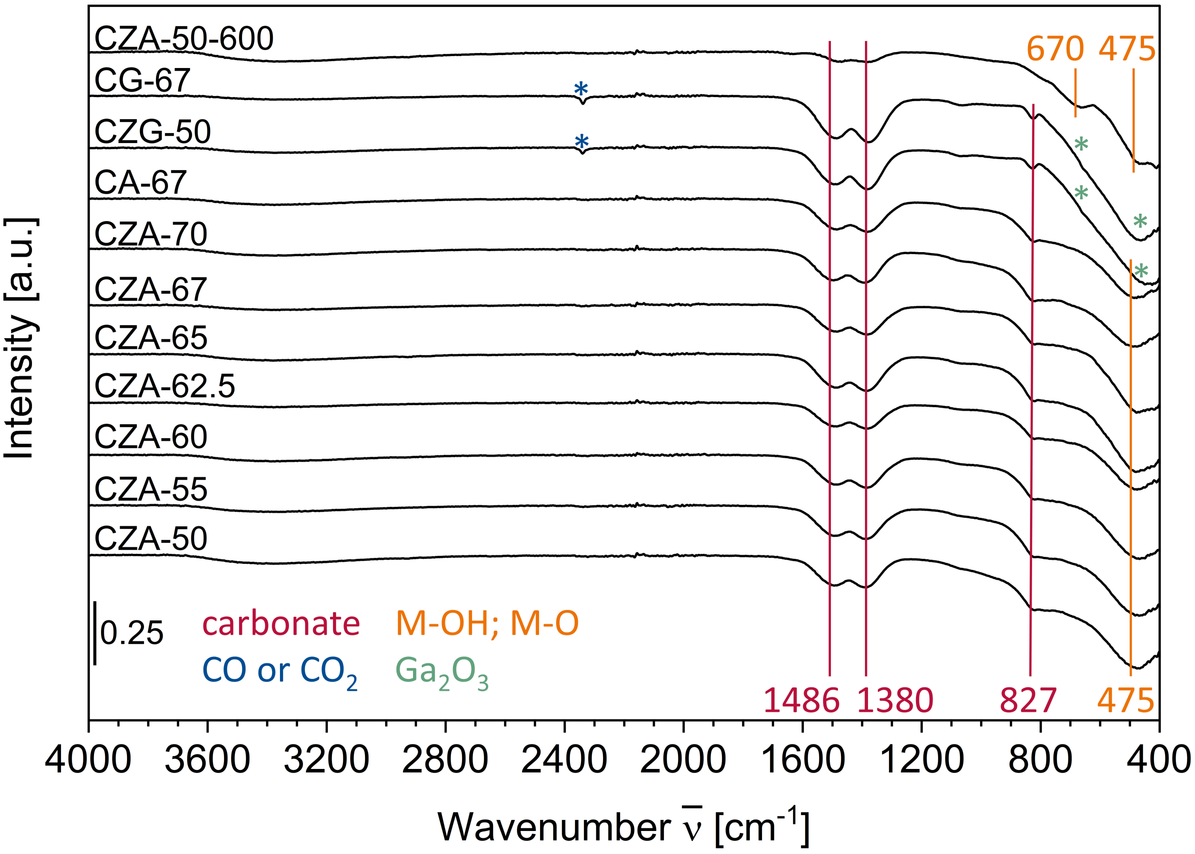

Figure 4.4.: Infrared spectra of hydrotalcite precursors measured in transmission mode.

A slight increase of the Cu content up to 1 mol % is observable after calcination in most materials (see Table 4.2). Only CZA-50-600 differs from this trend as the fraction of Cu increased by 3.7 mol % at the expense of the Al fraction from the precursor to the calcined material. The reason for the depletion is not clear. It is likely that by the higher ion mobility during the calcination at 600 °C, the Al^{3+} ions formed an amorphous Al_2O_3 byphase, which is indicated by a slight halo in the XRD pattern (see Figure 4.4). Part of this Al_2O_3 might have deposited on the combustion dish walls.

Table 4.2.: Mole fractions of metals x(M) determined by ICP-OES and surface area S_{BET} of calcined materials.

sample	x(Cu) [mol %]	x(Zn) [mol %]	x(Al or Ga) [mol %]	S_{BET} [$m^2 g^{-1}$]
CZA-50	53.5	16.1	29.2	61.4
CZA-55	58.7	13.9	26.2	57.5
CZA-60	63.2	12.4	23.3	51.1
CZA-62.5	65.4	11.6	21.7	60.3
CZA-65	68.2	10.0	20.6	68.3
CZA-67	70.0	9.4	19.3	58.1
CZA-70	72.7	8.6	18.5	49.0
CA-67	70.1	0.2	29.4	39.9
CZG-50	53.5	17.3	28.3	45.6
CG-67	65.4	0.0	34.1	39.6
CZA-50-600	56.6	16.3	26.3	68.3

No clear trend is observed regarding the influence of the calcination of the surface area. For the series with increasing Cu amount, the areas slightly decreased on average and the scattering increased to $(59 \pm 10)\,m^2\,g^{-1}$. By comparing the surface areas of CZA-50 and CZA-50-600, the high-temperature calcination at 600 °C shows to cause a higher surface area. The major difference between both materials is the presence of large amounts of high-temperature carbonate in CZA-50. It is proposed that the HT-CO_3^{2-} is located in the interlayers, at defect sites or at phase boundaries.[45,53,54] Thus, it can block adsorption sites or whole pores, making them inaccessible for the probe molecule N_2. It is debatable whether the surface area of CZA-50 is indeed smaller or cannot be accessed by the N_2 physisorption method. The areas of the binary catalysts CA-67 and CG-67 stayed almost constant with a loss of about $3\,m^2\,g^{-1}$. The area of CZG-50 decreased most during calcination by $16.5\,m^2\,g^{-1}$, showing that $ZnGa_2O_4$ is a weaker structural promoter for the CuO particles than $ZnAl_2O_4$. The shape of the isotherms has not changed during the calcination and can still be defined as type IV(a) isotherms with H3 hystereses (see Figure 4.16 in the SI). The pore size distributions of the calcined materials are shown in Figure 4.17 in the SI. Only minor changes are found compared to the hydrotalcites. The most abundant pore size is still in the range of 20 to $60\,m^2\,g^{-1}$ and the calcined CZA-62.5 is now in line with the other materials.

On average, CZA-50-600 has slightly more pores below 20 $m^2\,g^{-1}$ than CZA-50, which supports the idea of pore blocking by HT-CO_3^{2-} in the latter material.
The reducibility of the materials was tested by temperature-programmed reductions in diluted hydrogen (TPR, see Figure 4.5). Three peak regions can be found for the materials: a first one with maxima in the range of 240 to 265 °C (A), a second one at 200 to 225 °C (B) and a third one at about 175 °C (C). In the CZA series with varying Cu content, the high-temperature peaks A are ascribed to highly dispersed Cu oxide in the spinel matrix. By the mild calcination, the homogeneous mixture of cations in the LDH was mainly preserved. This type of Cu is difficult to reduce as the reducible Cu^{2+} is strongly bonded to the irreducible Zn^{2+} and Al^{3+} by O^{2-} or CO_3^{2-} bridges. These bonds need to be cleaved before Cu can segregate from the matrix to form Cu^0 particles and hence, a high reduction temperature is required.[53,54]

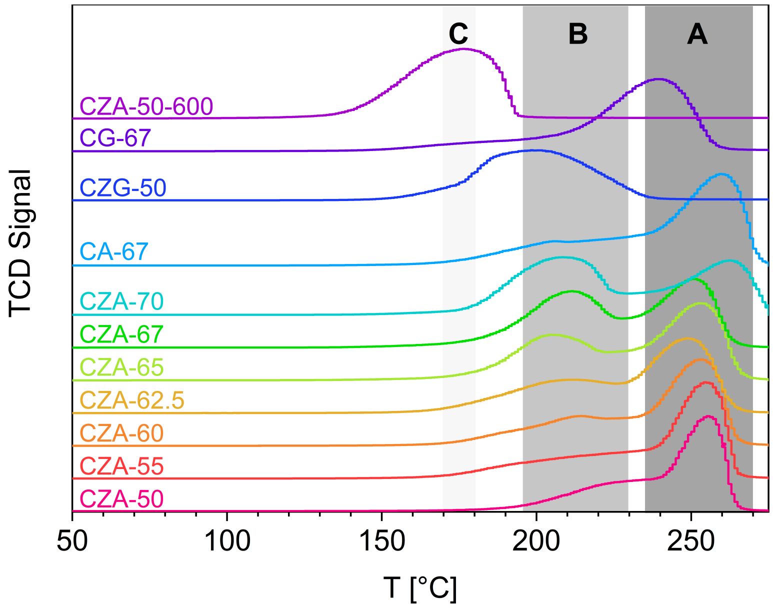

Figure 4.5.: H_2-TPR profiles of various LDH-derived catalysts in 5 % H_2 in Ar. The range of peak types A, B and C are marked in grey. T_{max} = 275 °C, β = 2 °C min^{-1}.

The type B peak at around 225 °C in CZA-50 can rather be described as a shoulder of the high-temperature peak A. The onset is positioned at 170 °C, which is a typical temperature for the reduction of CuO in Cu/ZnO catalysts. The reduction of Cu^{2+} in Cu/ZnO catalysts was found to occur in a two-step process with Cu_2O as an intermediate.[125] The shoulder is therefore assigned to the formation of Cu_2O. With increasing Cu content, the shoulder develops to an individual peak. In CZA-70, it has about the same size as peak A. Additionally, the maximum shifts to lower temperatures. The crystallite size of CuO increases with increasing Cu content, as found by the sharpening of reflections in the XRD patterns (Figure 4.3). Larger and more crystalline CuO is easier to reduce, hence the required temperature is lower. Moreover, the larger crystallites are less embedded in the Zn,Al matrix than smaller ones, making the accessible CuO surface area larger. This leads to peak B being more intense as more Cu_2O is formed at once during a TPR. However, in CZA-67 and CZA-70, peak B is especially intense and the trend of the decreasing peak maximum temperature reverses, both for peak A and B. It is unlikely that the malachite byphase is the cause. Firstly, the amount of byphase is low according to the intensity in XRD. Secondly, an industrial-type catalyst based on zincian malachite as a precursor was found to have a peak maximum that is about 70 °C lower compared to LDH-based Cu catalysts.[54,56] Instead, mass transfer limitations of H_2 from the surface to the bulk or of O^{2-} from the bulk to the surface need to be considered for those larger Cu crystallites. Gentry *et al.* showed for ion-exchanged Cu zeolites that by an increasing amount of sample, the peak maximum shifts to higher temperatures.[126] They ascribed this both to H_2 concentration gradients and a temperature difference between the sample and the temperature sensor due to the increased catalyst bed height. Transferred to the present case, a temperature difference is unlikely as the same amount of sample (100 mg) was used for each TPR. Instead, a constant sample weight combined with a higher Cu content will also increase the amount of reducible Cu and cause a temperature shift. Hence, at about 65 % of Cu in the samples, the increasing effect of sheer Cu mass overcomes the decreasing effect of larger crystallites.

In the profile of CZA-50-600, only one peak of type C is detectable at 177 °C. This peak is assigned to pure, granular CuO. The Cu in this material is easy to reduce at low temperatures as the separation of Cu and the spinel already took place during the calcination at an elevated temperature of 600 °C, hence it is easily accessible. The Zn-free, binary CA-67 has a pronounced type A peak with a weak shoulder to the lower temperature side. In the XRD profiles, it was found by the poorly resolved reflections that the calcined CA-67 is less crystalline than CZA-67 with the same Cu content. This is also represented in the TPR profiles of these two materials. While large fractions of the Cu in CZA-67 can be reduced already at 212 °C (peak B), the major H_2 consumption is only found at 260 °C for CA-67 (peak A) as the Cu is less segregated and therefore less accessible. The Ga-containing binary analogue CG-67 has a similar signal shape with only one peak and a weak shoulder. However, the peak maximum is shifted by about 20 °C to a lower temperature, indicating that the Cu particles are either less dispersed or less embedded in the Ga oxide matrix compared to a Al oxide matrix. Finally, the higher crystallinity and thus higher segregation of the Cu particles in CZG-50 compared to CZA-50 leads to a reduction at already low temperatures. Only one, broad reduction peak can be found for this material with an onset at 170 °C. This demonstrates that as soon as Cu_2O is formed, it is further reduced to Cu^0 easily, causing the peaks of the consecutive reductions steps to overlap into one broad signal. The Cu surface areas of the materials were determined by a sequence of chemisorption experiments described earlier by our group[74] and in Section 3 in this work. A N_2O reactive frontal chromatography (N_2O-RFC) of a freshly reduced catalyst gives the combined area of Cu^0 and $Zn^{\delta+}$ surface sites $S_{Cu\&Zn\delta+}$ as both Cu and partially reduced Zn will be oxidized by N_2O to Cu_2O and ZnO, respectively. By a treatment with diluted H_2 at a low temperature of 40 °C, the Cu_2O can be reduced back to Cu^0, while ZnO stays unaffected. After this, a second N_2O-RFC will give the surface area of metallic Cu S_{Cu} only, as the Zn is already in an oxidized state. The two N_2O-RFCs are referred to as a "$Zn^{\delta+}$-affected" and "$Zn^{\delta+}$-corrected" N_2O-RFC, respectively. A more detailed explanation can be found in Section 3 and the results are shown in Figure 4.6.

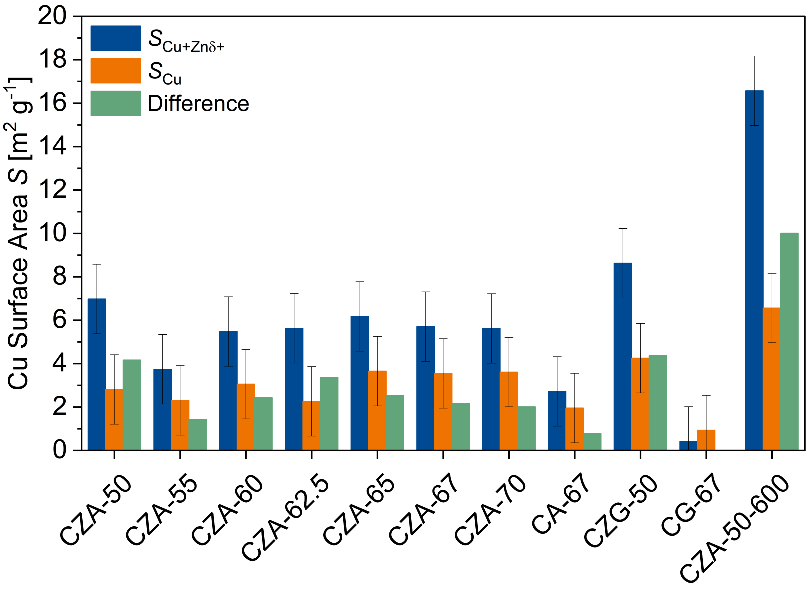

Figure 4.6.: Copper surface areas determined by N_2O reactive frontal chromatography. $S_{Cu\&Zn\delta+}$ refers to the area determined right after reduction in a H_2-TPR. S_{Cu} was determined in a second N_2O-RFC after exposure to diluted hydrogen at 40 °C. The error bars give the method error of $1.6\,m^2\,g^{-1}$.

The Cu content variation in CZA shows that similar areas of pure Cu sites S_{Cu} (orange bars) were formed in all materials with regard to the measurement error. Nonetheless, a volcano shape is obtained and the highest area is found in CZA-65 ($3.6\,m^2\,g^{-1}$). On the one hand, high amounts of Cu generate more Cu surface sites, on the other hand enough promoter is needed to avoid sintering and agglomeration of Cu. The diametrical demands of both factors lead to an optimum Cu content of 65 %.

By the difference of $S_{\mathrm{Cu\&Zn\delta+}}$ to S_{Cu}, the amount of the partially reduced Zn ($Zn^{\delta+}$) can be estimated, which is a measure for the strength of the metal-support interaction (SMSI) in the catalyst. Again, the determined areas are in the same range, though a local maximum can be found in CZA-65. Interestingly, $S_{\mathrm{Cu\&Zn\delta+}}$ found for CZA-50 represents another maximum. Although the amount of pure Cu sites is similar in CZA-65 and CZA-50, the latter one hence contains a higher amount of $Zn^{\delta+}$. Next to that, CZA-62.5 has the second most amount of $Zn^{\delta+}$. As no Zn is present in both binary catalysts CA-67 and CG-67, the determined values for $S_{\mathrm{Cu\&Zn\delta+}}$ and S_{Cu} should be equal. Within the method error, this hypothesis can be confirmed. Both materials expose lower Cu surface areas than the ternary ones, showing that Zn is an important structural promoter for the dispersion of Cu. CZG-50 has slightly more Cu surface sites than the Al-containing analogue CZA-50, while the amount of $Zn^{\delta+}$ is about the same. Lastly, significantly higher numbers of both Cu and $Zn^{\delta+}$ sites can be found in CZA-50-600. This material was calcined at elevated temperatures of 600 °C, causing a segregation of crystalline CuO and $ZnAl_2O_4$ phases and a decomposition of most HT-CO_3^{2-}. This crystalline starting point for the reductive activation seems to have a positive influence on the microstructure of the evolving catalyst regarding its surface area.

4.3.3. Catalytic Performance

The activity of the catalysts was tested in the liquid-phase methanol synthesis. In a 300 ml batch reactor, the pre-reduced catalyst was suspended in ethanol and the mixture heated to the desired temperature. Then 50 bar of syngas (H_2:CO_2 = 3:1) was added and a slurry phase was generated by extensive mixing. This moment was defined as the beginning of the reaction $t = 0\,\mathrm{h}$. Ethanol was used as an alcoholic solvent to enable the alcohol-assisted methanol synthesis mechanism. To track the course of reaction, samples were taken over time and analyzed by gas chromatography. All reactions were performed for 6 h and after cooling down to room temperature, an additional sample was taken. In the following diagrams, this sample is shown at $t = 6.5\,\mathrm{h}$, although the exact time for cooling down usually varied, depending e.g. on the previously applied reaction temperature. A resulting time-resolved reaction profile is exemplary shown in Figure 4.7 for the performance of CZA-62.5 at 160 °C. Methanol (MeOH) is formed as a main product and the amount rises linearly up to about 3 h. Afterwards, the slope is decreasing. Ethyl formate (EF) is an intermediate product in the reaction to MeOH and its concentration also rises linearly within the first 3 h. After that, it stays approximately constant. Typically, the concentration of an intermediate in a batch reaction has a maximum and falls to zero at the end of the reaction. That is either the case when all substrate is consumed or when the reaction mixture reached the thermodynamic equilibrium. Hence, reaching a plateau indicates the beginning of a thermodynamically controlled reaction after 3 h. At the start of the reaction t = 0 h, the presence of acetaldehyde (AcAld) could be detected, although pure ethanol was used as a solvent. During the heating phase, no hydrogen is present in the reaction mixture and hence, the environment is not reducible. At the applied temperature, Cu catalysts showed to be efficient in the dehydrogenation of ethanol to AcAld already at atmospheric pressure,[127–130] and also other alcohols could be dehydrogenated over Cu-based catalysts.[131] Furthermore, other groups also observed the presence of dehydrogenation products of their solvents in the alcohol-assisted methanol synthesis.[110,113,114,118] In our reactions, H_2 is introduced to the reaction mixture at t = 0 h and by that, the reversed reaction back to ethanol is enabled.

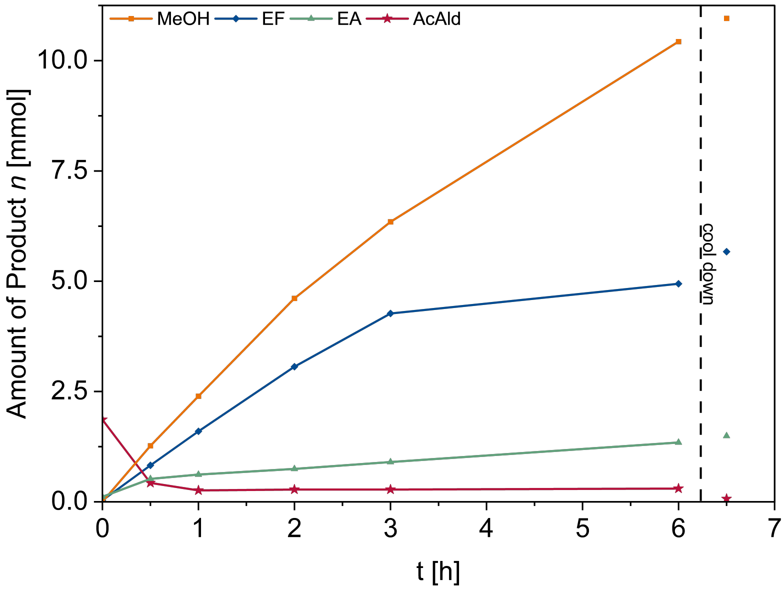

Figure 4.7.: Product-time profile for a reaction performed at 160 °C over CZA-62.5. The data shown at 6.5 h represent the product mixture taken after cooling down. MeOH = methanol, EF = ethyl formate, EA = ethyl acetate, AcAld = acetaldehyde. Reaction conditions: p = 50 bar, H_2:CO_2 = 3:1, rpm = 1000 min^{-1}, m_{cat} = 0.50 g.

Ethyl acetate (EA) is a side product and is formed in a low, but increasing amount. EA could be formed in different ways that are depicted in Figure 4.8. For all possible routes, AcAld needs to be produced from EtOH first (a). A standard approach of forming an ester is the esterification of an acid and an alcohol, in our case acetic acid (AA) and ethanol (b).[132,133] However, a mineral acid would be needed to catalyze this reaction and in addition, no AA was detected in all the conducted experiments. A further option is the formation of a hemiacetal with subsequent dehydrogenation (c). This can either be catalyzed by acids or bases.[132,134] Finally, an industrially applied process for the production of EA is the Tishchenko reaction.[90] In this reaction, two molecules of aldehyde react to the corresponding ester. Although homogeneous catalysts in the form of metal alkoxides are most common, e.g. from Na or Al, the use of heterogeneous alkaline catalysts such as alumina was also examined.[135] As Al sites are present in most of the present catalysts, either in the form of Al_2O_3 or $ZnAl_2O_4$ and as alumina is known to be amphoteric, this reaction could also have occured during the tests.

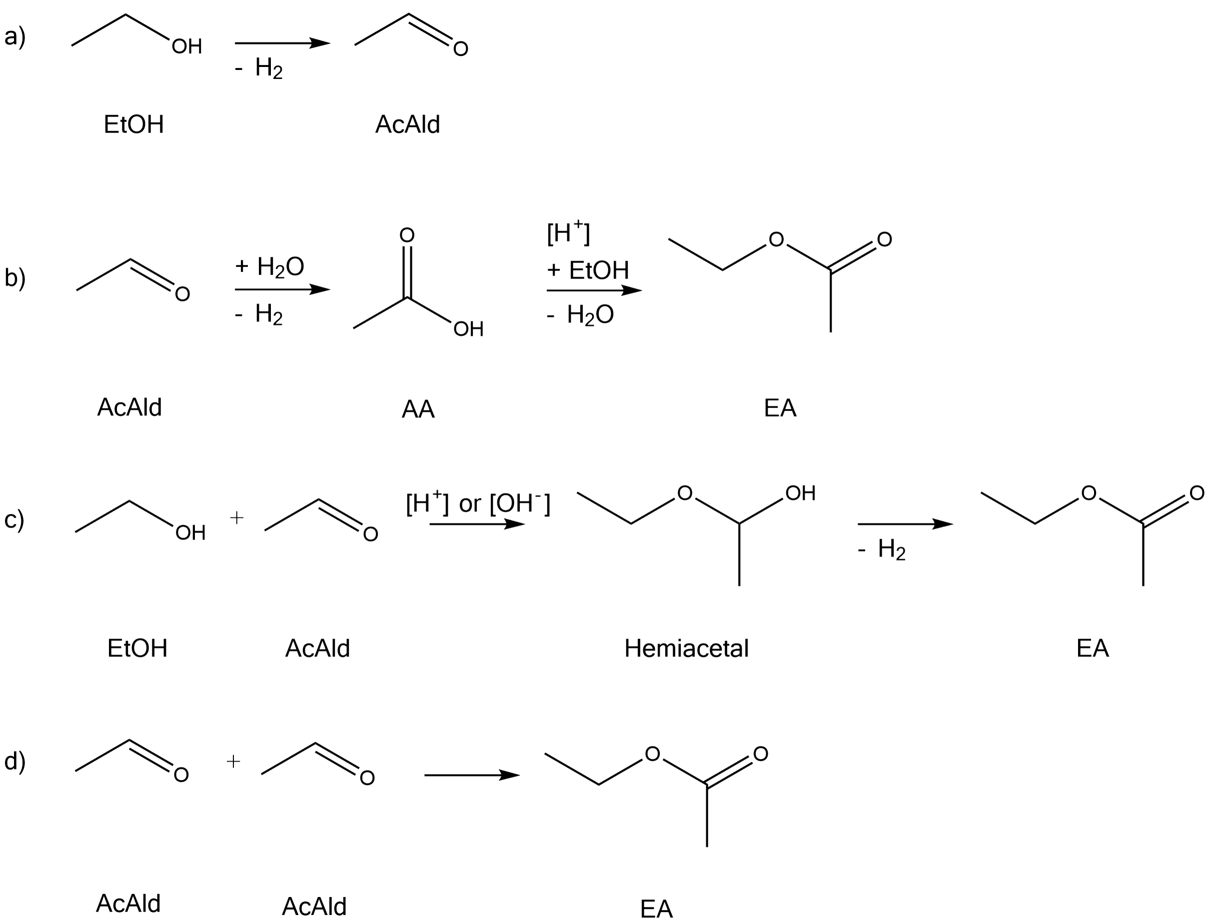

Figure 4.8.: Ethyl acetate (EA) formation routes. a) Formation of the intermediate acetaldehyde (AcAld). b) Formation of EA by esterification, c) a hemiacetal intermediate and d) Tishchenko reaction.

It should be noted that while the inventors of the alcohol-assisted synthesis did not report the formation of EA,[106,108] other groups recorded the formation of dehydrogenation products.[110,113,114,118] This is quite surprising as the presence of hydrogen at elevated pressures should suppress the dehydrogenation occuring in route (a), (c) and (d). Contrarily, the group of Santacesaria found that over industrial CuO/ZnO/Al_2O_3 and CuO/$CuCr_2O_4$ catalysts, the dehydrogenation occurred even for EtOH vapor in a pure H_2 stream.[136] While at lower pressures of 1 bar AcAld was the main product, the selectivity could be shifted to EA by increasing the H_2 pressure to 20 bar. In the present case, this explains why small amounts of AcAld could still be detected after introducing syngas to the reaction mixture.

No statement can be made whether route c or d or a mixture of both leads to EA in the present reaction. On the one hand, no hemiacetal intermediate could be detected, but this could also be due to a short lifetime of this substance. On the other hand, in the heterogeneously catalyzed Tishchenko reaction only surface species are formed as intermediates, making a sampling difficult. Nonetheless, AcAld can be defined as an intermediate in the formation of EA. Besides, we could not detect formic acid in any of our catalytic tests, demonstrating that it is readily converted to ethyl formate as soon as it is produced. Alternatively, the group of Tsubaki proposed that formic acid is only present in the form of surface-bound formate and reacts to the ester as an adsorbed species. Hence, no free formic acid can be detected in the reaction medium.[107,108]

By the course of the profiles of MeOH and EF in Figure 4.7 it can be inferred that within the first two hours, the reaction is kinetically controlled as the amounts increase linearly. After this, the thermodynamic equilibrium has to be considered. Because a proper comparison of catalysts is only possible without the influence of an equilibrium limitation, only the initial rates will be looked at. This is carried out by regarding the product mixtures after 2 h of reaction time.

To analyze the effect of temperature on the catalyst activity and selectivity, reactions were performed at temperatures between 140 and 220 °C with CZA-50 and CZA-50-600. Figure 4.9 shows the product yields over these catalysts after 2 h of reaction time. Next to MeOH (orange columns) as the main product, the yields of the intermediate EF (blue columns) and the side products EA (green colummns) and AcAld (red columns) are shown. Additionally, the black columns (“other”) summarize the yields of further side products, which start to form at elevated temperatures of 200 °C and were mostly 1-butanol and 2-butanol in this study. At 140 °C, MeOH and EF are formed next to trace amounts of EA over CZA-50. Hence, the catalyst already works as such low temperatures in combination with the alcohol-assisted mechanism, although the overall yields are small due to the kinetics. A maximum MeOH yield can be found at 160 °C. At higher temperatures, the MeOH yield decreases and instead, more EA is formed and AcAld is present. The production of EA and AcAld rise exponentially with the temperature and more other side products are detectable. 2-butanol starts to form at 200 °C and 1-butanol at 220 °C. In addition, a pressure increase could be observed over time for those two temperatures, likely due to the formation of H_2 by the increased EA formation. On the other hand, no more MeOH or EF is observable at the highest reaction temperature of 220 °C. There are two major reasons for this behavior. Firstly, the methanol formation is an exothermic reaction for which a temperature increase is unfavorable. Secondly, the overall pressure in all experiments was kept constant at 50 bar, meaning that the ratio of partial pressures of the syngas and the solvent vapor varied with the temperature. At the highest reaction temperature, the concentration of syngas was the lowest, meaning that less reactant was available. The suppression of MeOH formation at elevated temperatures also shows that the EA and MeOH formation share the same active sites. In detail, the Cu sites catalyze the formation of formate (Reaction 4.4) and the hydrogenolysis of EF (Reaction 4.6), but they can also catalyze the dehydrogenation of ethanol to AcAld. Alumina is known to be amphoteric and ZnO has acidic properties. For the formation of EF (Reaction 4.5), lewis acid sites are needed. Contrarily, the Tishechenko reaction is catalyzed by lewis bases. The hemiacetal formation is either acid or base catalyzed. At elevated temperatures, the EA formation becomes predominant as it favors high temperatures,[136] while MeOH formation favors low temperatures due to its exothermicity.[41,51]

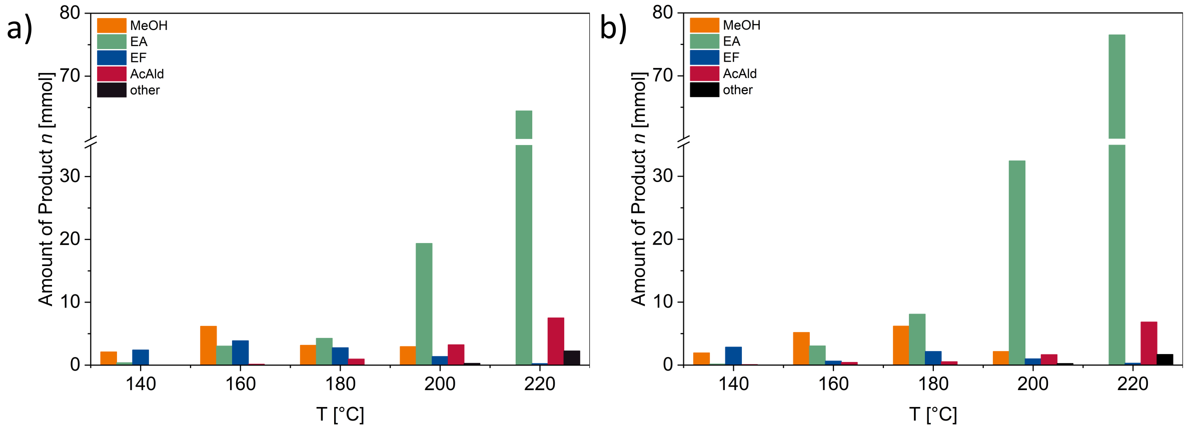

Figure 4.9.: Amount of products after 2 h of reaction time over a) CZA-50 and b) CZA-50-600. The temperature was varied in five independent experiments. MeOH = methanol, EF = ethyl formate, EA = ethyl acetate. Reaction conditions: p = 50 bar, H_2:CO_2 = 3:1, rpm = 1000 min^{-1}, m_{cat} = 1.00 g.

CZA-50-600 performs similar to CZA-50. The major difference is the position of the MeOH maximum. It has shifted from 160 to 180 °C. In addition, more EA is formed at a given temperature. The results are unexpected as CZA-50-600 showed both a higher BET surface area and specific Cu surface area compared to CZA-50. Yet the MeOH formation is not improved. This indicates that the additional Cu surface sites gained by the high-temperature calcination do not act as active sites for the MeOH synthesis. The reason might be that in an effective MeOH synthesis catalyst, Cu and Zn need to be in close proximity to enable a synergistic effect.[51,61] Contrarily, the sharpened reflections in the XRD pattern of CZA-50-600 indicate that the Cu crystallites are enlarged compared to CZA-50 (see Figure 4.3). This is disadvantageous for the formation of interfaces between Cu and Zn. Instead, the larger crystallites can act as dehydrogenation sites to from AcAld. Besides, a segregation of the spinel phase from the Cu phase was found in the XRD pattern. Those larger spinel domains compared to CZA-50 could also add to the increased tendency to form EA.

The MeOH production of both CZA-50 and CZA-50-600 was compared to a commercial methanol synthesis catalyst (see Figure 4.10). The commercial catalyst produces more MeOH at a given temperature in the examined temperature range. Nevertheless, also with this catalyst a volcano-shape can be observed with a maximum MeOH yield at 180 °C. At lower temperatures, the performance of the commercial and the presented LDH-based catalysts is comparable, as both the MeOH yield and the side product formation is in the same range (compare Figure 4.22 in the SI and Figure 4.9). Yet at higher reaction temperatures of 200 and 220 °C, a stronger tendency of the commercial catalyst toward the formation of 1-butanol is found.

As the reaction performed at 160 °C showed a high yield of MeOH and at the same time low yield of byproducts, this temperature was used to compare the performance of the synthesized catalysts in the alcohol-assisted methanol synthesis. The results are shown in Figure 4.11. In the CZA catalyst series with varying Cu amount, a clear maximum for both MeOH and EF can be found for CZA-62.5. This ratio of metallic Cu to spinel seems to represent an optimum for the needs of this mechanism. That is the number of lewis acids sites and hydrogenating sites needed for the individual steps of the mechanism, but the degree of interfacial sites can also be tuned by this ratio. Furthermore, this catalyst exhibited the lowest reduction temperature within the CZA peak series, indicating a comparably good accessibility of Cu for gaseous reactants. The amount of EA and further side products is about the same for all catalysts in this series.

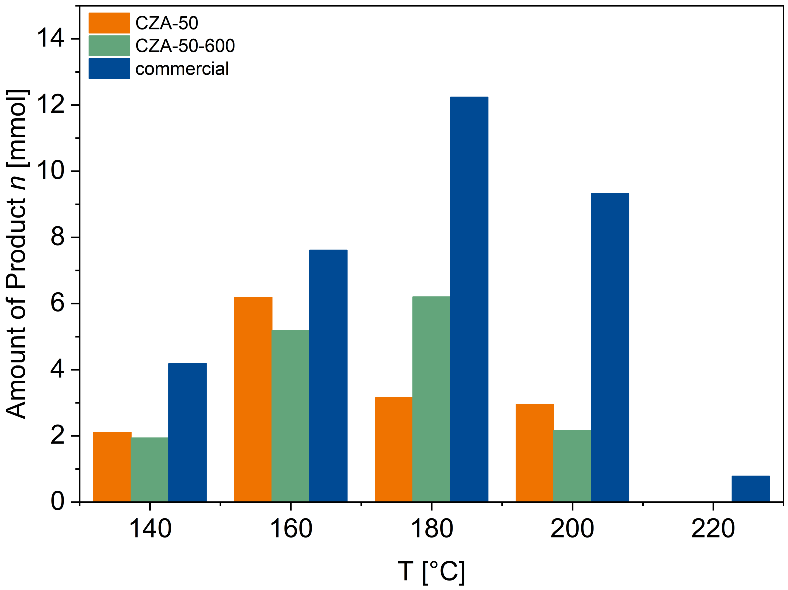

Figure 4.10.: Amount of methanol formed after 2 h of reaction time over CZA-50, CZA-50-600 and a commercial methanol synthesis catalyst at various temperatures. MeOH = methanol, EF = ethyl formate, EA = ethyl acetate. Reaction conditions: p = 50 bar, H_2:CO_2 = 3:1, rpm = 1000 min^{-1}, m_{cat} = 1.00 g.

As already found for the temperature variation, the performance of CZA-50-600 has not improved compared to CZA-50, although a considerably higher Cu surface area was determined for this material (see Figure 4.6). Instead, the quantity of the side product EA has increased. This shows that for the alcohol-assisted mechanism, the number of Cu surface sites alone is not a measure for the activity of a catalyst. Instead, the microstructure in terms of surrounding surface sites and interfaces also plays an important role. The Cu surface area of CZA-50-600 might be larger than the one of CZA-50, but due to the bigger crystallites, the number of interfaces between Cu and the spinel has not increased. Yet those neighboring sites seem to be especially important for the methanol formation.

The binary CA-67 produced the largest amounts of EF, but only few MeOH, showing that the first two steps of this mechanism (Reaction 4.4 and Reaction 4.5) can be effectively catalyzed. However, CA-67 cannot catalyze the hydrogenation of the ester (Reaction 4.6) as effectively as CZA-67 with the same Cu content. This clearly demonstrates the importance of Zn not only as a structural, but also electronic promoter. The results are in line with the findings of Tsubaki *et al.* who obtained high amounts of EF over a Cu/Al_2O_3 catalyst. Only when a Cu/ZnO catalyst was added, methanol production was observed.[108] In the reaction mixture of the Ga promoted CZG-50, slightly higher amounts of EF were found. However, the total amount of produced EF rather is the sum of EF and MeOH found in the mixture, as EF reacts further to MeOH in a 1:1 stochiometry. Hence, less EF was formed over this catalyst compared to CZA-50 within the 2 h of reaction time. Moreover, there is more EF than MeOH found in the mixture, which is another difference to CZA-50. The binary CG-67 produces the same amount of EF as CZG-50. However, it is less active than its Al containing equivalent CA-67 and produces no MeOH at all. As there was no formic acid found in the reaction mixtures, it can be inferred that the EF formation (Reaction 4.5) also occurs swiftly over Ga containing catalyst. The hydrogenating steps (Reaction 4.4 and Reaction 4.6) on the Cu sites are less efficiently catalyzed. Hence, the results show that Ga is a less effective structural promoter than Al, both in the binary and ternary catalysts. This is also indicated by the larger Cu domains in the calcined samples found by XRD for the Ga containing materials compared to the Al equivalents.

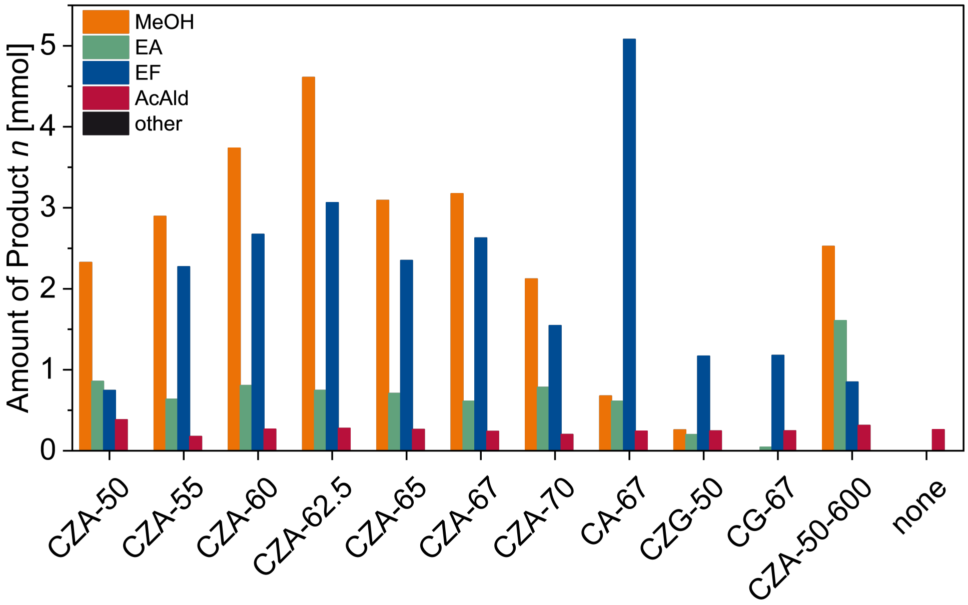

Figure 4.11.: Amount of products after 2 h of reaction time over various LDH-derived catalysts at 160 °C. MeOH = methanol, EF = ethyl formate, EA = ethyl acetate. Reaction conditions: p = 50 bar, H_2:CO_2 = 3:1, rpm = 1000 min^{-1}, m_{cat} = 0.50 g. Yield of other products are too small to be seen by eye.

The results also show that Zn is important electronic promoter. Without Zn, EF can still be formed by the Cu sites, proving the ability to hydrogenate CO_2 to formic acid (step 1). However, the final step, meaning the hydrogenation and cleavage of the ester to ethanol and methanol (step 3), is retarded, leading to low yields of the desired MeOH. Interestingly, AcAld is also formed in a blank test without any catalyst. The used reactor is made of corrosion resistant stainless steel (Hastelloy) and is cleaned with diluted nitric acid and ethanol after each experiment. That is why remnants of a catalyst from previous reactions can be excluded as a source of the EtOH dehydrogenation.

4.3.4. Catalyst Stability

After reaction and cooling down to room temperature, the catalysts were filtered off and dried at 80 °C overnight in air to analyze them by XRD once more (see Figure 4.12). Despite the air contact, reflections of metallic Cu can be found in all samples at 43.3 and 50.5° 2θ, likely due to the formation of a passivating oxidic layer. In the CZA series, the reflections are sharper the higher the Cu content. This is in line to the CuO signals of the calcined samples (Figure 4.3). Another similarity to the calcined samples is the absence of any indications for Zn or Al containing phases. Instead, intense reflections of Cu_2O can be found at 36.5° 2θ. Additionally, a weak shoulder at about 38.8° 2θ hints at the presence of CuO. Moreover, an increasing halo at angles below 10° 2θ with decreasing Cu content indicates the presence of amorphous byphases.

CZA-50-600 shows the most crystalline diffractogram. Next to Cu^0, Cu_2O and CuO, reflections of the $ZnAl_2O_4$ spinel can be found at 31.2, 59.3 and 65.3° 2θ. In the binary CA-67 and CG-67, a mixture of Cu^0 and Cu_2O can be found. By the intensities of the main reflections at 36.5 and 43.3° 2θ, it can be stated that CA-67 contains more Cu_2O, while in CG-67 the fraction of Cu^0 is larger. The presence of Al_2O_3 or Ga_2O_3 is not visible in the XRD patterns. In CZG-50, clear indications for the $ZnGa_2O_4$ spinel are found at 18.4, 30.3, 57.4 and 63.1° 2θ next to Cu^0 and Cu_2O. This shows that compared to CZA-50 with the same molar ratio of Cu and spinel, $ZnGa_2O_4$ has a higher tendency to form larger crystallites than $ZnAl_2O_4$, likely due to a segregation of the spinel from the Cu phases. The absence of spinel reflections and broadness of Cu^0 and Cu_2O reflections in the CZA samples (calcined at low temperatures) confirm the stabilizing effect of $ZnAl_2O_4$, while the stabilizing effect of the promoter $ZnGa_2O_4$ is weaker.

The stability of the catalysts during the reaction was exemplarily tested on CZA-50 and CZA-50-600. After a first reaction over 6 h, the catalyst was filtered off and dried. Next to re-reducing the remaining material, the remnants were weight and again used for methanol synthesis at identical conditions. In total, three reactions were performed in a row with one batch of catalyst. Not all of the material could be retrieved. The obtained product yields were normalized to the mass of reduced catalyst to enable a quantitative comparison (see Figure 4.13).

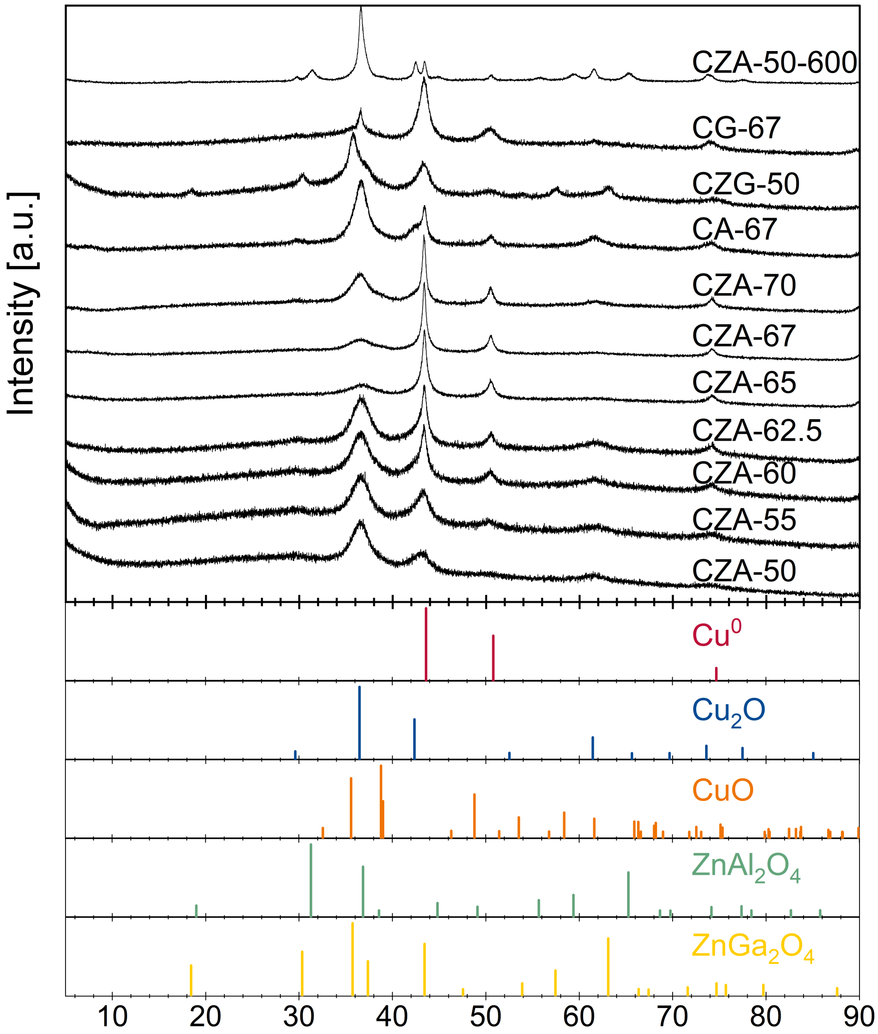

Figure 4.12.: XRD powder patterns of spent samples after air contact. References for Cu^0 (red), Cu_2O (blue), CuO (orange), $ZnAl_2O_4$ (green) and $ZnGa_2O_4$ (yellow) are shown as bars.

The yields obtained over CZA-50 drop by about one third from the first to the second cycle, both for the desired MeOH and the side product EA. In the third cycle, the yield of EA again decreased drastically, while only a small drop is found for MeOH. On the other hand, the yield of AcAld slightly increases with every cycle. The trends can be described as exponential decreases (MeOH + EA) or increases (AcAld), respectively. From the trends of those three cycles, a stabilization of the catalytic performance similar to the results of the third cycle is expected. In case of CZA-50-600, the loss in MeOH yield is less pronounced. Instead, in increase of AcAld and EA formation can be observed. As EA formation is known to occur on promoted alumina,[135] the increased EA yields can be attributed to the larger $ZnAl_2O_4$ spinel domains that have formed during catalysis which were found in the XRD patterns of the spent sample (see Figure 4.12). The less distinctive changes between the cycles show that CZA-50-600 is less affected by aging. It is likely that this material was pre-aged by the higher calcination temperature, while aging of CZA-50 takes more time due to the lower applied temperatures.

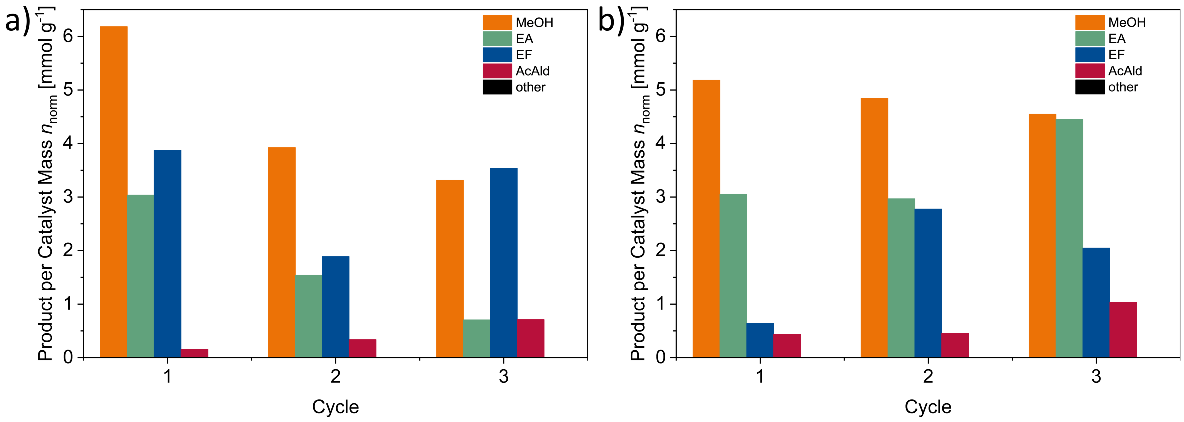

Figure 4.13.: Recycling study showing the amount of products per catalyst mass after 2 h of reaction time over a) CZA-50 and b) CZA-50-600 at 160 °C. The catalyst was re-reduced and weighed prior to the next catalytic cycle. MeOH = methanol, EF = ethyl formate, EA = ethyl acetate. Reaction conditions: $p = 50\,\text{bar}$, H_2:CO_2 = 3:1, rpm = 1000 min^{-1}. Yield of other products are too small to be seen by eye.

4.4. Summary

The application of Cu-based catalysts derived from a LDH structure in the liquid-phase, alcohol-assisted methanol synthesis was reported for the first time. MeOH could already be produced at temperatures as low as 140 °C and a maximum yield was found at 160 to 180 °C. By the well-defined precursor and intermediate, structure-activity relationships could be defined. (1) The importance of Zn as a electronic promoter was identified by a variation of promoting metals. Zn-less catalysts produced almost no MeOH but only the intermediated EF. Only in the presence of Zn, noteworthy amounts of MeOH were detected. (2) The MeOH yield over Al containing catalysts was higher than over their Ga containing equivalents. This is attributed to the stronger structural promotion of Al compared to Ga, leading to smaller CuO domains in the calcined materials. (3) A molar ratio of 62.5:12.5:25 Cu:Zn:Al in the precursor showed to be the optimum mixture for the production of methanol. At this ratio, the number of acid sites on the spinel needed for the formation of EF are in good balance with the number of hydrogenation sites on the Cu needed for the FA formation and hydrogenolysis of EF. (4) By a reaction temperature variation, it was shown that the formation of MeOH and side products (AcAld and EA) occur over the same active sites. A high-temperature calcination of a CZA catalyst revealed that EA formation is favored over larger spinel phase domains, while MeOH formation requires the presence of a high amount of interfaces of Cu^0 and spinel. From this it follows that neither the BET surface area nor the specific Cu surface area alone are a measure for the catalytic performance. Instead, catalysts have to be analyzed holistically and the microstructure in terms of domain sizes and phase boundaries need to be taken into account.

To prevent EA side product formation in future experiments, we will employ catalysts with lower amounts of spinel or alumina, respectively. Due to the limitation of the M^{2+} to M^{3+} ratio in the LDH structure, another type of precursor has to be used. For example, industrial-type catalysts with only 3 mol % Al based on a zinician malachite precursor were presented.[56] They showed to be active in the conventional gas-phase process and are promising candidates for the alcohol-assisted synthesis.

Overall, it was shown that LDH-based catalysts are active in the alcohol-assisted methanol synthesis and that their catalytic performance can be improved by carefully choosing the promoters, metal ratios and synthesis conditions.

4.5. Experimental

Catalyst Synthesis

LDHs were synthesized by co-precipitation of a 0.8 M metal nitrate solution with the desired molar ratio of Cu, Zn, Al and Ga at 25 °C and pH = 8 in the half-automatized lab reactor OptiMax 1001 from Mettler Toledo. An alkaline solution of 0.6 M NaOH and 0.09 M Na_2CO_3 was used as a precipitation agent. 75 g of the metal solution was dosed into a resevoir of 200 ml deionized water over 30 min. Co-dosing of the precipitation agent was controlled by a computer program to ensure a constant pH value. The precipitate was aged for 1 h in the mother liquor at 25 °C. Afterwards, the precipitate was repeatedly washed with deionized water, dried at 80 °C overnight and thoroughly mortared. The LDHs were calcined in a muffle oven in static air for 3 h at 330 °C and 600 °C, respectively (β = 2 °C min^{-1}). Due to the required catalyst masses e.g. for the temperature variation, some materials had to be synthesized in more than one precipitation batch. A comparison of different batches of CZA-50 is shown in the supporting information of Section 3 (therein called no-calc). A commercial methanol synthesis catalyst from Alfa Aesar was used as a reference material. Pellets were ground and a sieve fraction of 250 to 355 µm was used.

X-ray Powder Diffraction Patterns

XRD patterns were measured at room temperature on an Empyrean diffractometer from Malvern Panalytical equipped with a PIXcel3D detector. Measurements were conducted in Bragg-Brentano geometry with Cu $K_{\alpha 1}$ radiation (λ = 1.54 Å) in the range of 5 to 90°. The reference for the CG LDH was computed by adjusting the cell parameters of a binary Cu,Ga system to the space group $C2/m$ known for LDHs.[137]

Sample Composition Analysis

Mole fractions of metals in the calcined samples were determined by Inductively Coupled Plasma Optical Emission Spectrometry on an ICP-OES Avio 200 from Perkin Elmer. About 10 mg of a sample was dissolved in 0.5 ml HNO_3 (p.a., 65 %) and diluted with distilled water to a total volume of 50 ml. 5 ml of this solution was taken,again diluted to a total volume of 50 ml and used for analysis. Additionally, the molar metal amounts of the LDH precursors were also identified by atomic absorption spectroscopy on an ICE3500 from Thermofisher. The carbon and hydrogen content was analyzed by elemental analysis on an EA300 from Eurovector.

Nitrogen Physisorption

N_2 adsorption-desorption profiles were measured on a Nova 3200e sorption station from Quantachrome. Prior to measuring, the samples were degassed under vacuum at 80 °C (LDHs) or 100 °C (calcined materials) for 2 h. The partial pressures p/p_0 were measured at −196 °C and normalized to a reference cell. The Brunauer-Emmett-Teller (BET) equation was applied in the range of p/p_0 = 0.07 - 0.40 to calculate the surface areas. The pore size distributions were determined by the desorption branches of the isotherms.

Infrared Spectroscopy

IR spectra were recorded on a Bruker ALPHA-P ATR MIR spectrometer in the range of 400 to 4000 cm^{-1}.

Hydrogen Temperature-Programmed Reduction

Measurements were performed in a Belcat-B catalyst analyzer from BEL JAPAN, Inc. equipped with a thermal conductivity detector (TCD). About 100 mg of calcined sample (sieve fraction 125 to 250 µm) were placed onto quarz wool in an U-shaped reactor. Prior to the experiment, the catalyst was dried at 100 °C for 60 min in He (80 $ml\,min^{-1}$, heating rate β = 5 $°C\,min^{-1}$). After cooling to 40 °C, the temperature-programmed reduction was started. The catalyst was reduced in 5 % H_2 in Ar (35 $ml\,min^{-1}$) with a heating rate β of 2 $°C\,min^{-1}$ up to 275 °C. The maximum temperature was held for 4 h. Water was removed by an in-line molecular sieve before the effluent gas reached the TCD.

S_{Cu} Determination by N_2O-Reactive Frontal Chromatography

Measurements were performed subsequent to a H_2-TPR on the same setup. The gas outlet was connected to an Omnistar GSD 320 mass spectrometer from Pfeiffer Vacuum which was calibrated for N_2 and N_2O whenever a new catalyst was filled into the analyzer. The reactor was purged with He (80 $ml\,min^{-1}$) at 40 °C until no more other gases were detected by the MS. Then the catalyst surface was cleaned by heating the reactor to 130 °C (β = 5 $°C\,min^{-1}$) for 45 min and afterwards cooled down to 60 °C. For the N_2O-RFC, the concept described by Chinchen *et al.*[58] and Hinrichsen *et al.*[1] was followed. A mixture of 1 % N_2O in He (5 $ml\,min^{-1}$) was dosed into the reactor for 1 h at 60 °C and the effluent gas was analyzed by the MS. Concentration-time profiles are shown in Figure 4.18 to Figure 4.21 in the SI.

To determine the Cu surface area, the integral of the N_2 signal from the start to the point of inflection was used, at the intersection of the N_2 and N_2O signal. This integral equals the volume of N_2 (V_{N2}) evolved during oxidation of the catalyst surface:

$$1^{st}\ N_2O\text{-RFC}: \qquad 2\,Cu^0 + N_2O \longrightarrow Cu^I_2O + N_2 \tag{4.7}$$

$$Zn^{\delta+} + \tfrac{2-\delta}{2}\,N_2O \longrightarrow Zn^{II}O + \tfrac{2-\delta}{2}\,N_2 \tag{4.8}$$

$$\text{reduction}: \qquad Cu^I_2O + H_2 \longrightarrow 2\,Cu^0 + H_2O \tag{4.9}$$

$$Zn^{II}O + H_2 \nrightarrow \tag{4.10}$$

$$2^{nd}\ N_2O\text{-RFC}: \qquad 2\,Cu^0 + N_2O \longrightarrow Cu^I_2O + N_2 \tag{4.11}$$

$$Zn^{II}O + N_2O \nrightarrow \tag{4.12}$$

The area obtained from the first N_2O-RFC of the reduced sample refers to the specific area of both Cu and partially reduced Zn $S_{\text{Cu+Zn}}$. The area of the second N_2O-RFC of the passivated sample refers to the specific area of Cu only $S_{\text{Cu−only}}$. The difference between $S_{\text{Cu+Zn}}$ and $S_{\text{Cu−only}}$ is a measure for the amount of partially reduced Zn. The specific surface area S_x (x = Cu+Zn or Cu only) is calculated by

$$S_x = \frac{V_{N2} \cdot N_A \cdot f_{N2O}}{V_{\text{norm}} \cdot m_{\text{cat}} \cdot A_{\text{Cu}}} \tag{4.13}$$

N_A is the Avogadro constant and V_{norm} the standard molar volume at 20 °C and 1.013 bar. m_{cat} is the amount of catalyst and A_{Cu} the number of Cu atoms per surface area as defined by Hinrichsen *et al.* (1.47×10^{19} atoms m^{-2}).[1] f_{N2O} is a stochiometric factor of 2.08 found by Chatterjee *et al.* for Cu surface atoms and the N_2O probe molecule during N_2O-RFC.[2] The error of the setup was determined to be 1.6 $m^2\,g^{-1}$.

Catalytic Tests in the Liquid Phase

The alcohol-assisted methanol synthesis was conducted in a fixed head 4560 mini reactor with a 4848 controller from Parr Instrument Company. The inside of the 300 ml reactor was equipped with a thermocouple, a cooling loop operated by a magnetic valve, a dip tube with a 10 µm frit for sampling and a gas entrainment impeller. Prior to reaction, the catalyst was reduced in a separate setup. A tube furnace of about 15 cm length was used and the catalyst was reduced in 20 % H_2 in Ar at 300 °C for 2 h (β =

2 °C min^{-1}). After cooling down, the reactor was transferred to a glovebox and depending on the reaction, 0.50 or 1.00 g of catalyst was weighed into a catalyst dosing unit (XCAD). The XCAD is an autoclave accessory that allows an inert transfer of the catalyst. After mounting the XCAD to the autoclave head, 150 ml of ethanol were filled into the reactor. Then the reaction chamber was purged with Ar several times under vigorous stirring. Afterwards, the catalyst was dosed by 5 bar of Ar into the autoclave and the heating to the desired reaction temperature was conducted by a band heater. When the temperature was reached, syngas (H_2:CO_2 = 3:1) was introduced to the autoclave and a total pressure of 50 bar was applied. This time of syngas addition was assigned as the beginning of the reaction t = 0 h. Liquid samples were taken before adding the catalyst, after 0.5, 1, 2, 3 and 6 h and after cooling down to room temperature. Aside from the cool down sample, sampling was conducted by the dip tube. A sample was only collected after discarding the first 1 - 2 ml to purge the tube. Each sampling led to a pressure drop of about 1 bar.
The samples were analyzed by a GC 2010 Plus equipped with a mass spectrometer MS-QP 2020 from Shimadzu. A CP-Wax 52 CB (60 m length, 0.25 mm inner diameter, 0.25 µm film thickness) from Agilent was installed. The measurement program started with a temperature of 50 °C and was held for 5 min. Then the temperature was increased to 120 °C with 25 °C min^{-1} and held for another 10 min. 0.3 µl of sample were injected at 250 °C (split ratio 1:50) with He as a carrier gas (linear velocity = 40 cm s^{-1}, total flow = 127 mL min^{-1}). The detector temperature was 220 °C and masses from 10 to 200 m/z were recorded. A five point calibration for every compound was prepared beforehand. The error of the GC-MS instrument in case of methanol was determined to be 2.6 % and the combined GC-MS and autoclave process error 5.1 %.

4.6. Acknowledgment

We thank Sebastian Mangelsen for computing the CG reference, Dietrich Tönnes for XRD measurements, Melina Ottenberg for ICP-OES measurements, the IR-department of the Tuczek group (CAU Kiel) for IR spectra, Robin Meya and Beate Römer for elemental analysis, Benjamin Mockenhaupt for conceptualization of and discussions on H_2-TA and N_2O-RFC chemisorption experiments and the IMPRS RECHARGE for kind funding and support.

4.7. Authors & Contributions

Jil-Lorean Gieser: Evaluation, writing, catalyst synthesis, physisorption and chemisorption experiments, catalytic tests, GC-MS measurements and evaluation
Alina Jakubowski: GC-MS method development and measurements
Malte Behrens: Supervision, project administration, proofreading

4.8. Supporting Information

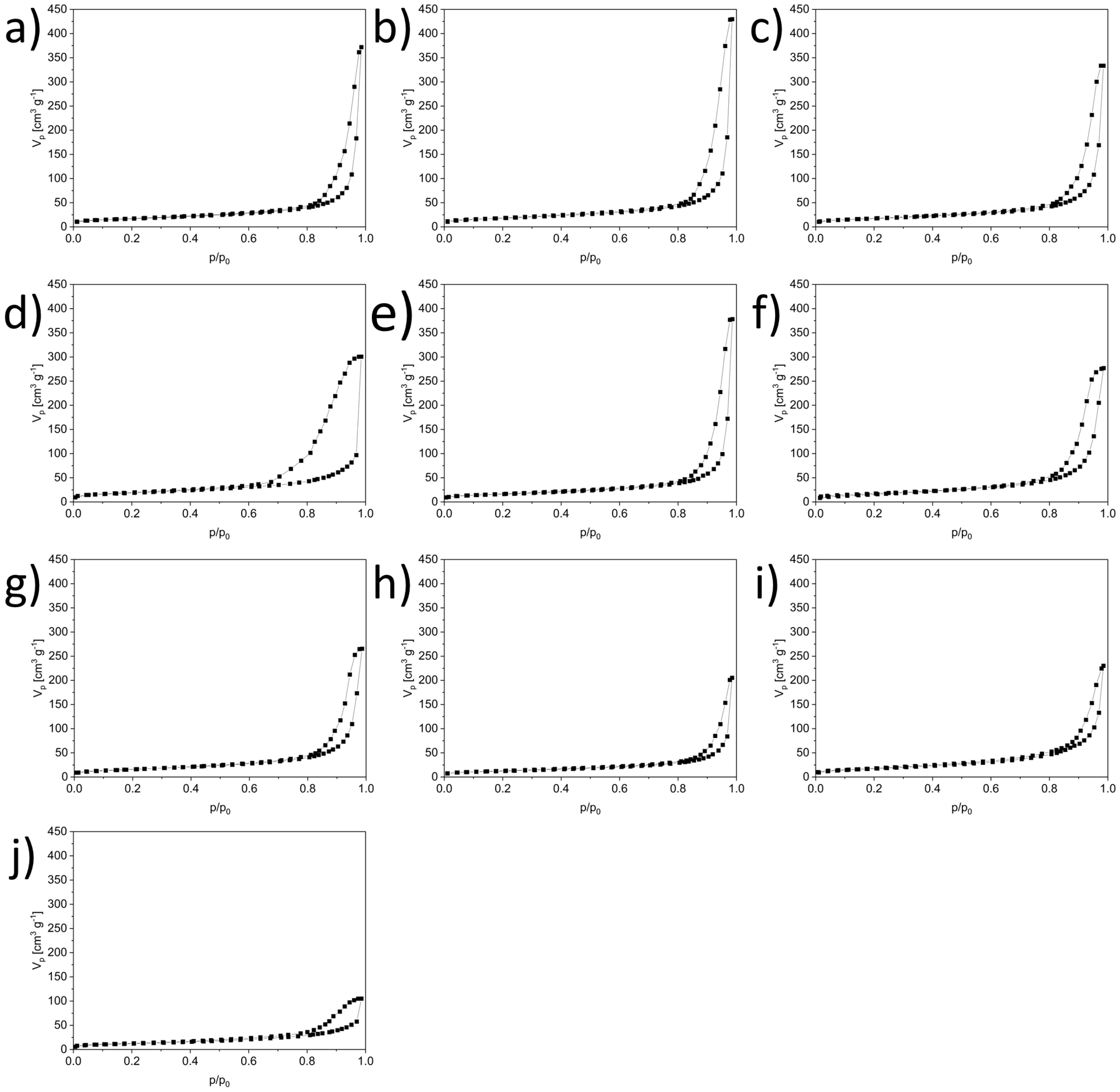

Figure 4.14.: N_2 adsorption-desorption isotherms used to determine the surface areas of hydrotalcite precursors. a) CZA-50 b) CZA-55 c) CZA-60 d) CZA-62.5 e) CZA-65 f) CZA-67 g) CZA-70 h) CA-67 i) CZG-50 j) CG-67.

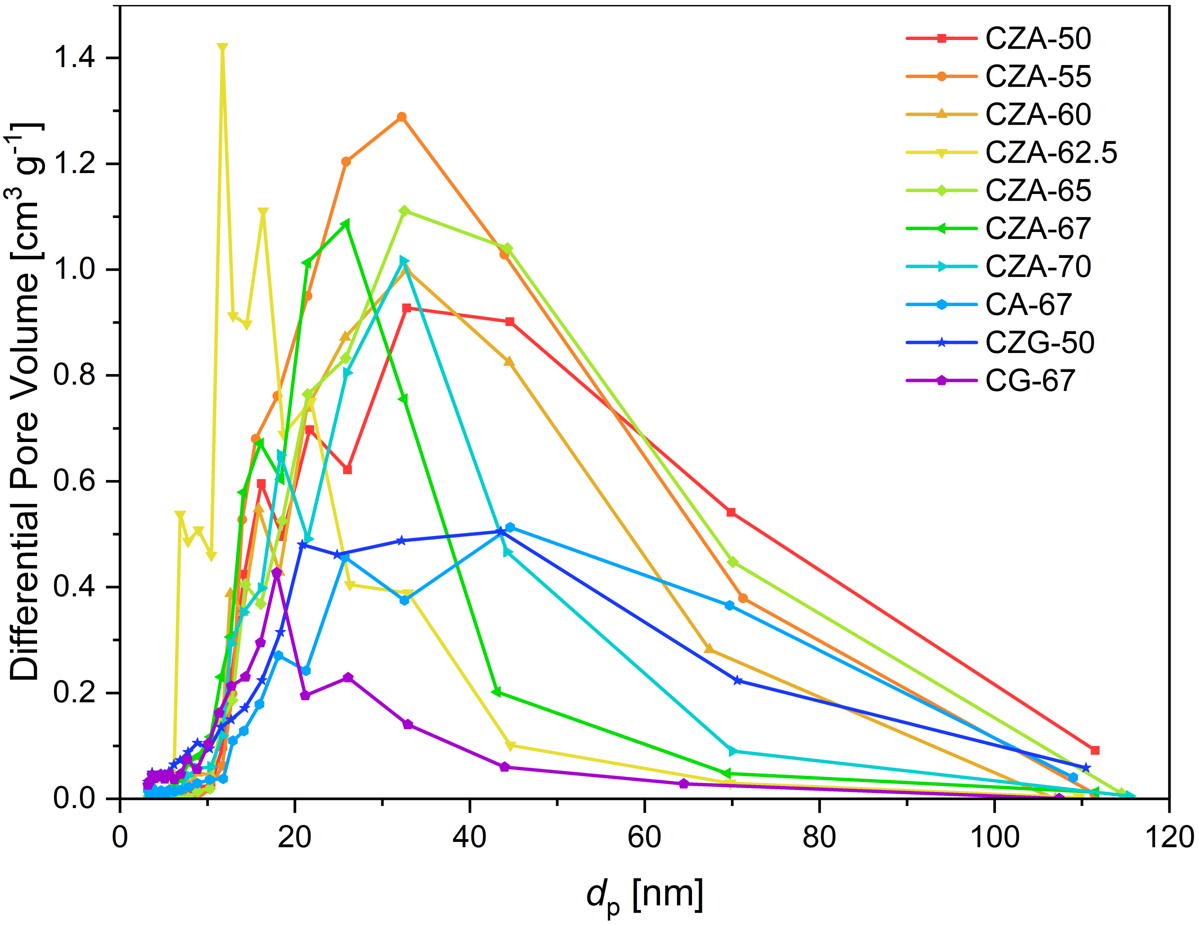

Figure 4.15.: Pore size distribution of LDH precursors determined from the desorption branch.

Table 4.3.: Mole fractions of metals $x(\mathrm{M})$ in the LDH precursors determined by atomic absorption spectrometry.

sample	$x(\mathrm{Cu})$ [mol %]	$x(\mathrm{Zn})$ [mol %]	$x(\mathrm{Al\ or\ Ga})$ [mol %]
CZA-50	53.3	16.6	30.1
CZA-55	59.2	14.2	26.5
CZA-60	64.9	12.7	22.4
CZA-62.5	65.9	11.6	22.4
CZA-65	69.3	11.1	19.6
CZA-67	71.6	10.3	18.2
CZA-70	75.9	7.9	16.2
CA-67	75.6	0.0	24.4
CZG-50	53.7	16.6	29.7
CG-67	72.2	0.0	27.8

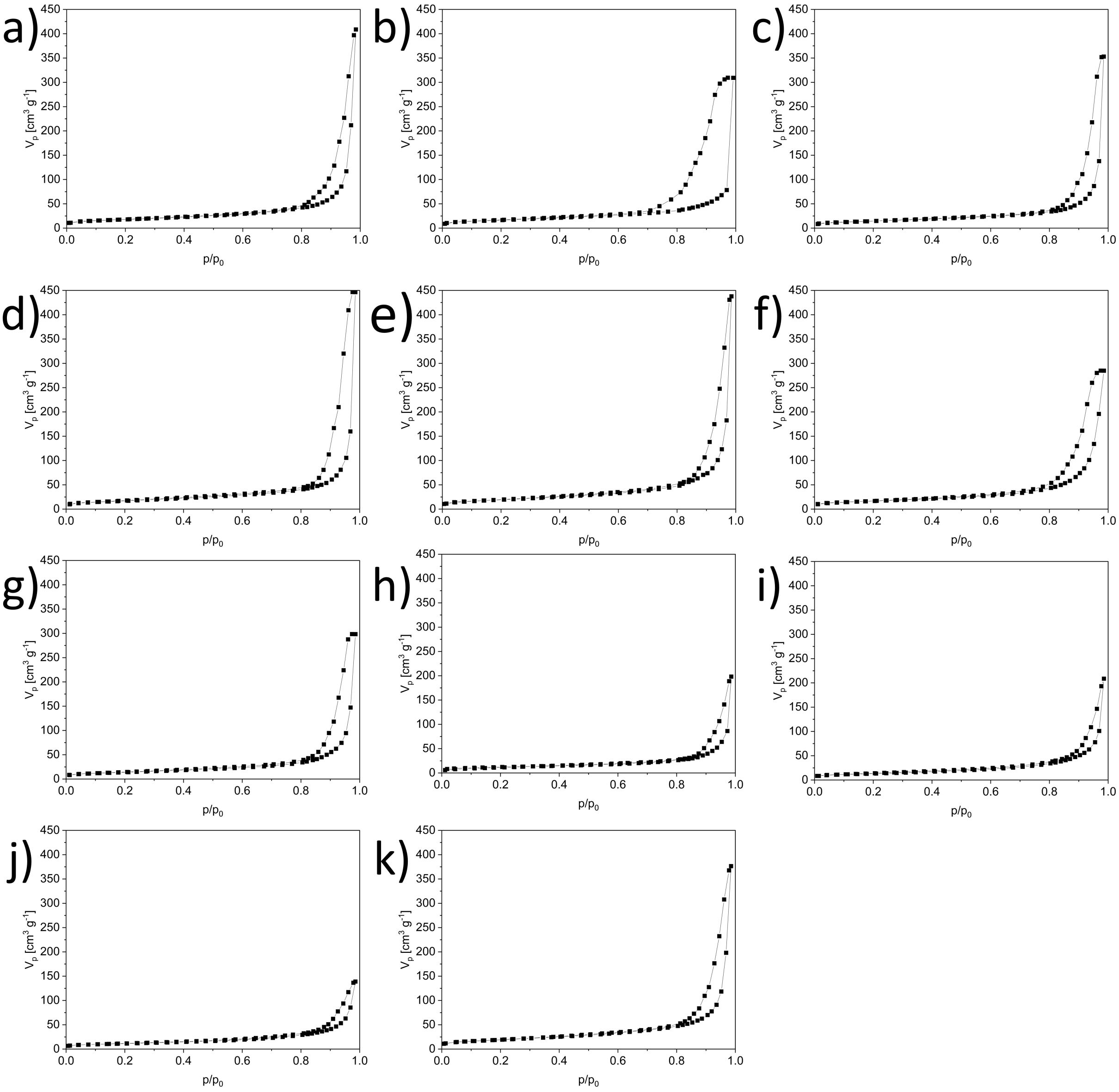

Figure 4.16.: N_2 adsorption-desorption isotherms used to determine the surface areas of calcined precursors. a) CZA-50 b) CZA-55 c) CZA-60 d) CZA-62.5 e) CZA-65 f) CZA-67 g) CZA-70 h) CA-67 i) CZG-50 j) CG-67 k)CZA-50-600.

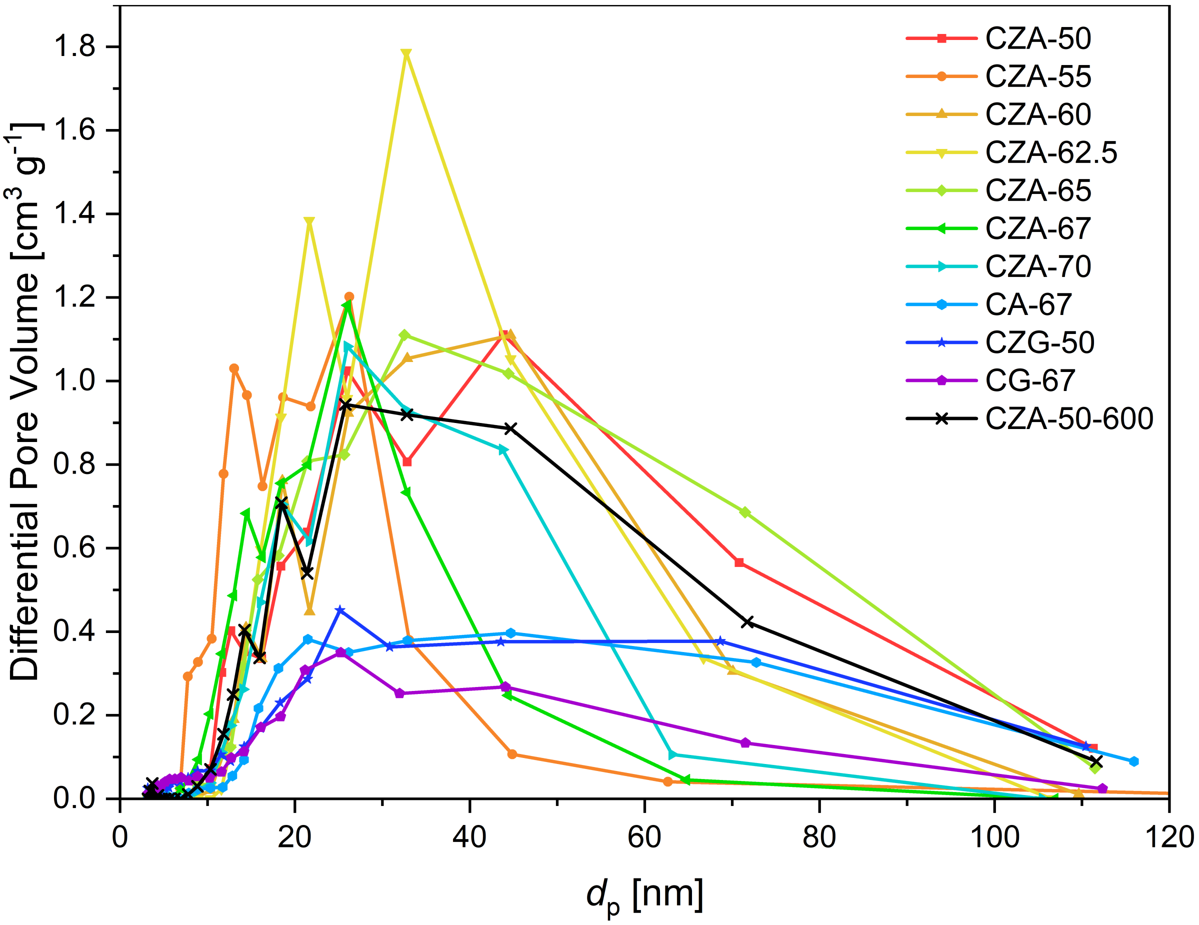

Figure 4.17.: Pore size distribution of calcined precursors determined from the desorption branch.

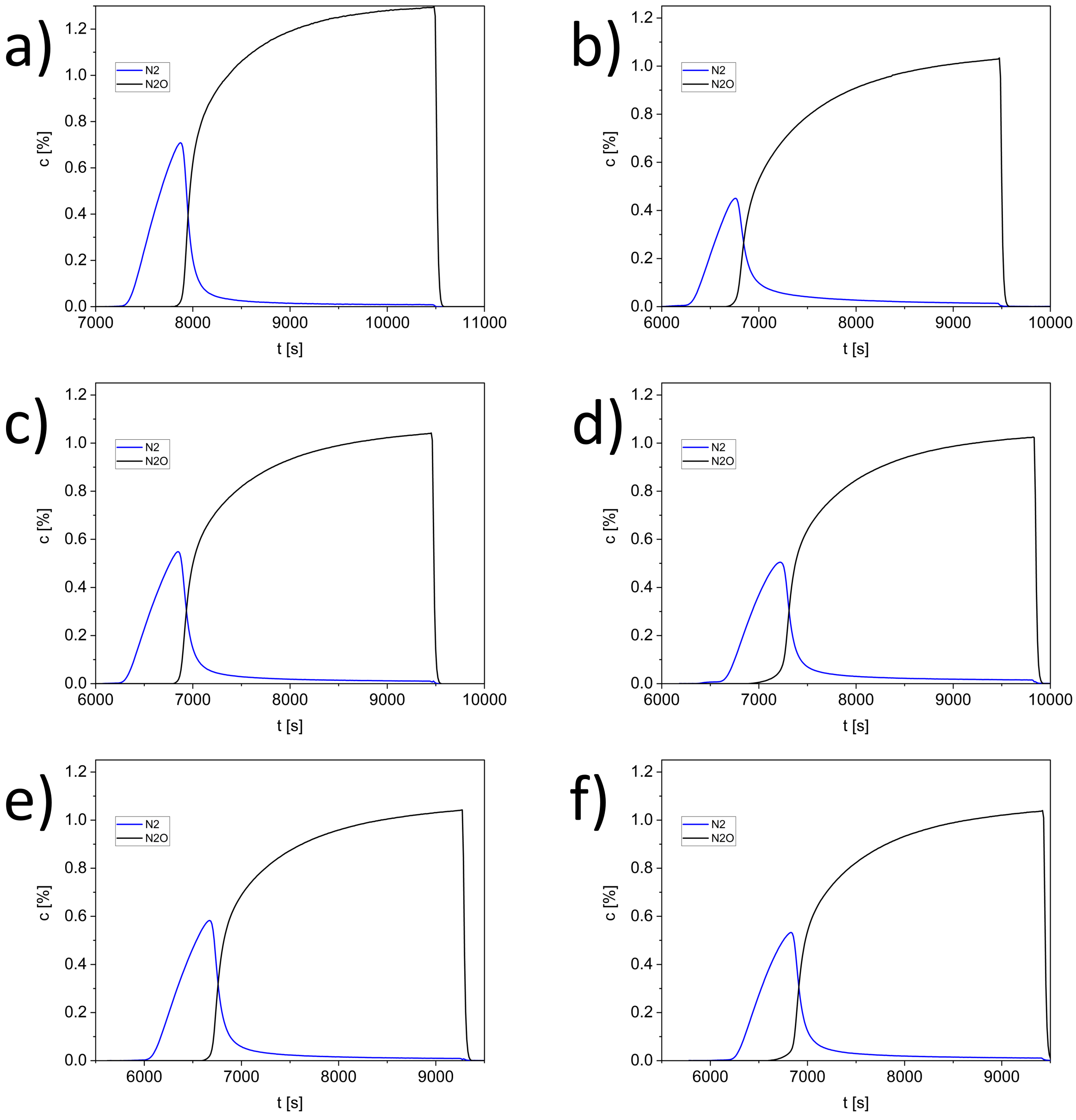

Figure 4.18.: First N_2O reactive frontal chromatography of reduced samples of a) CZA-50 b) CZA-55 c) CZA-60 d) CZA-62.5 e) CZA-65 f) CZA-67 g) CZA-70 h) CA-67 i) CZG-50 j) CG-67 k) CZA-50-600.

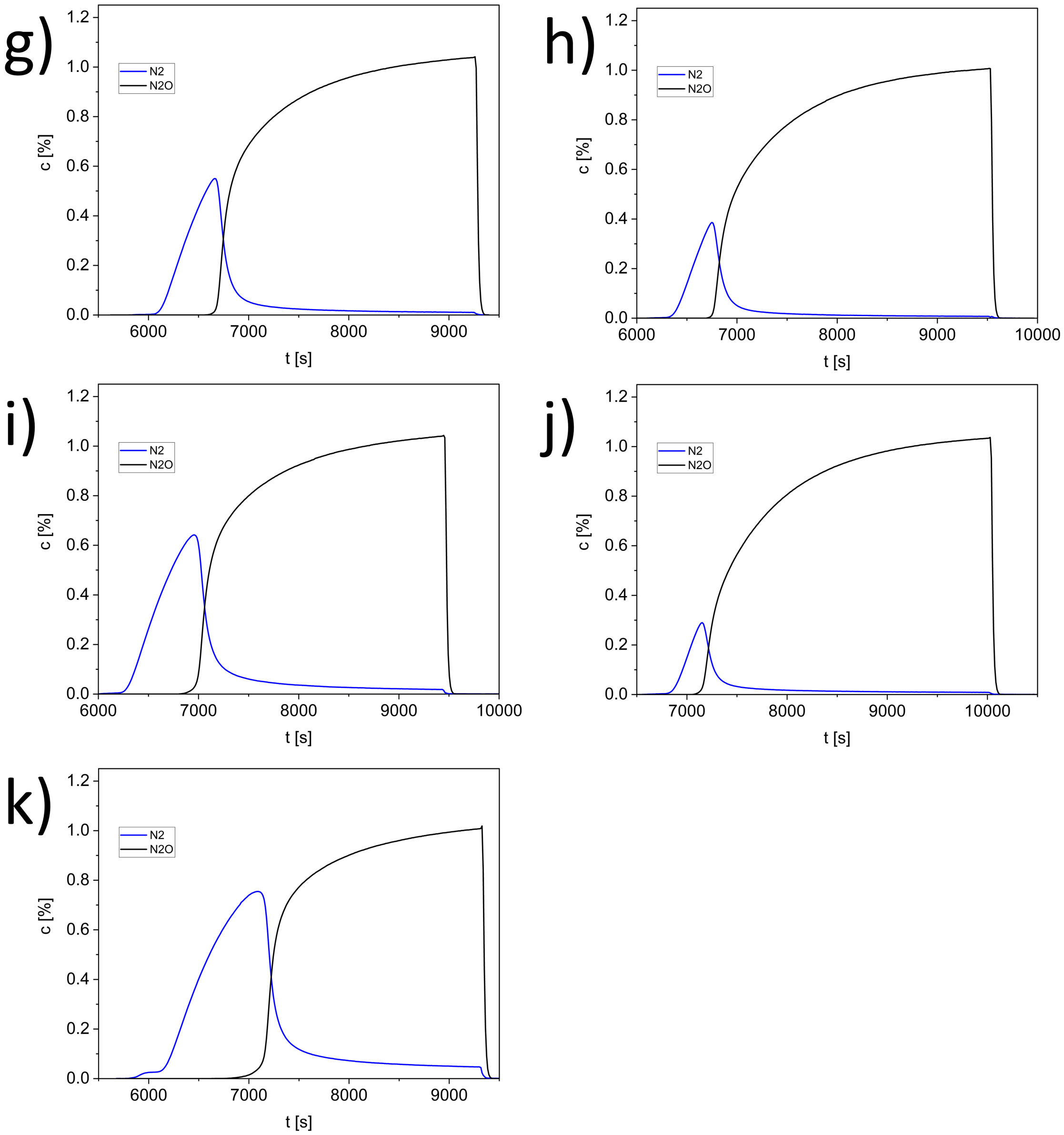

Figure 4.19.: (Continuation) First N_2O reactive frontal chromatography of reduced samples of g) CZA-70 h) CA-67 i) CZG-50 j) CG-67 k) CZA-50-600.

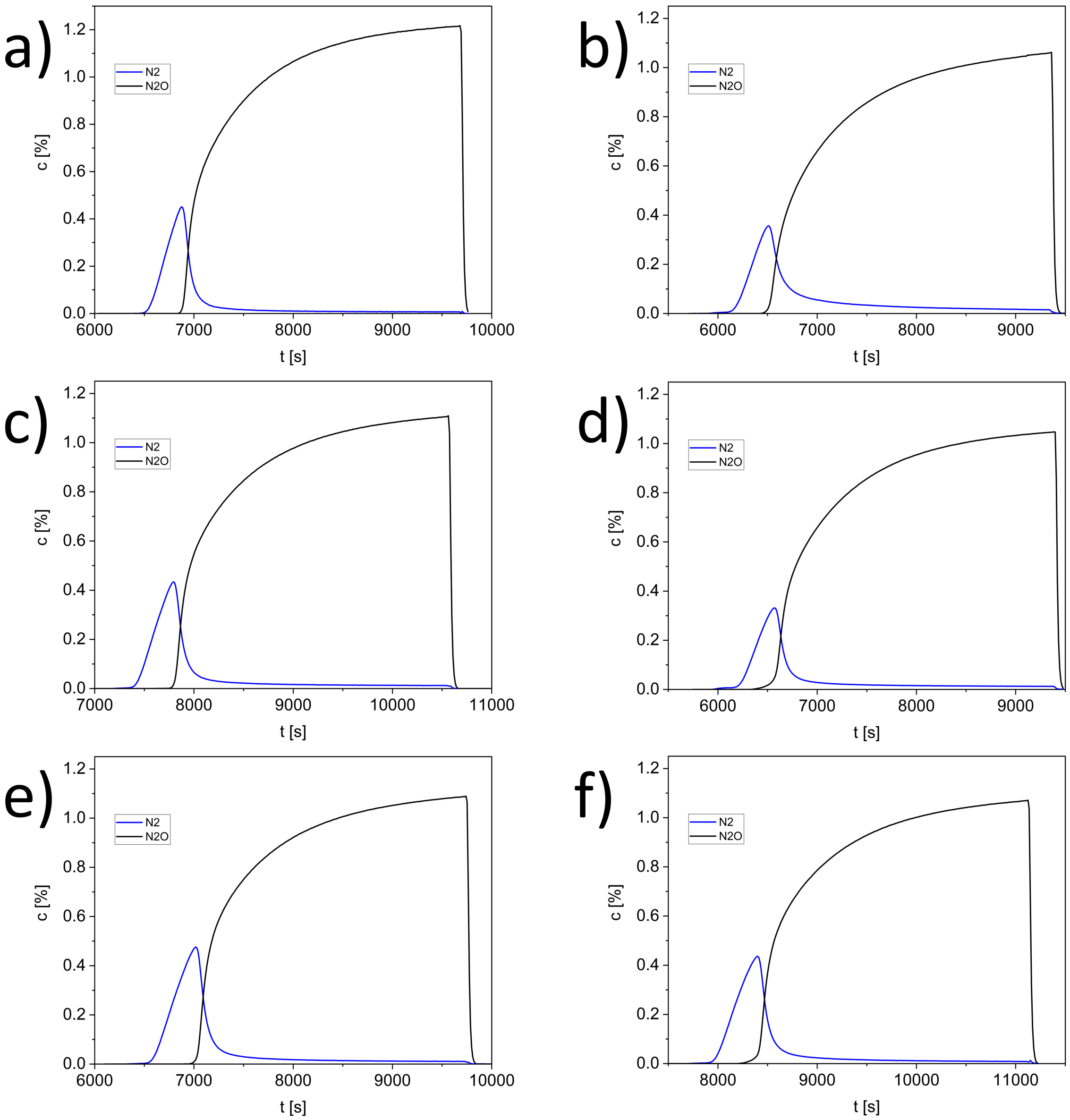

Figure 4.20.: Second N_2O reactive frontal chromatography of reduced samples of a) CZA-50 b) CZA-55 c) CZA-60 d) CZA-62.5 e) CZA-65 f) CZA-67.

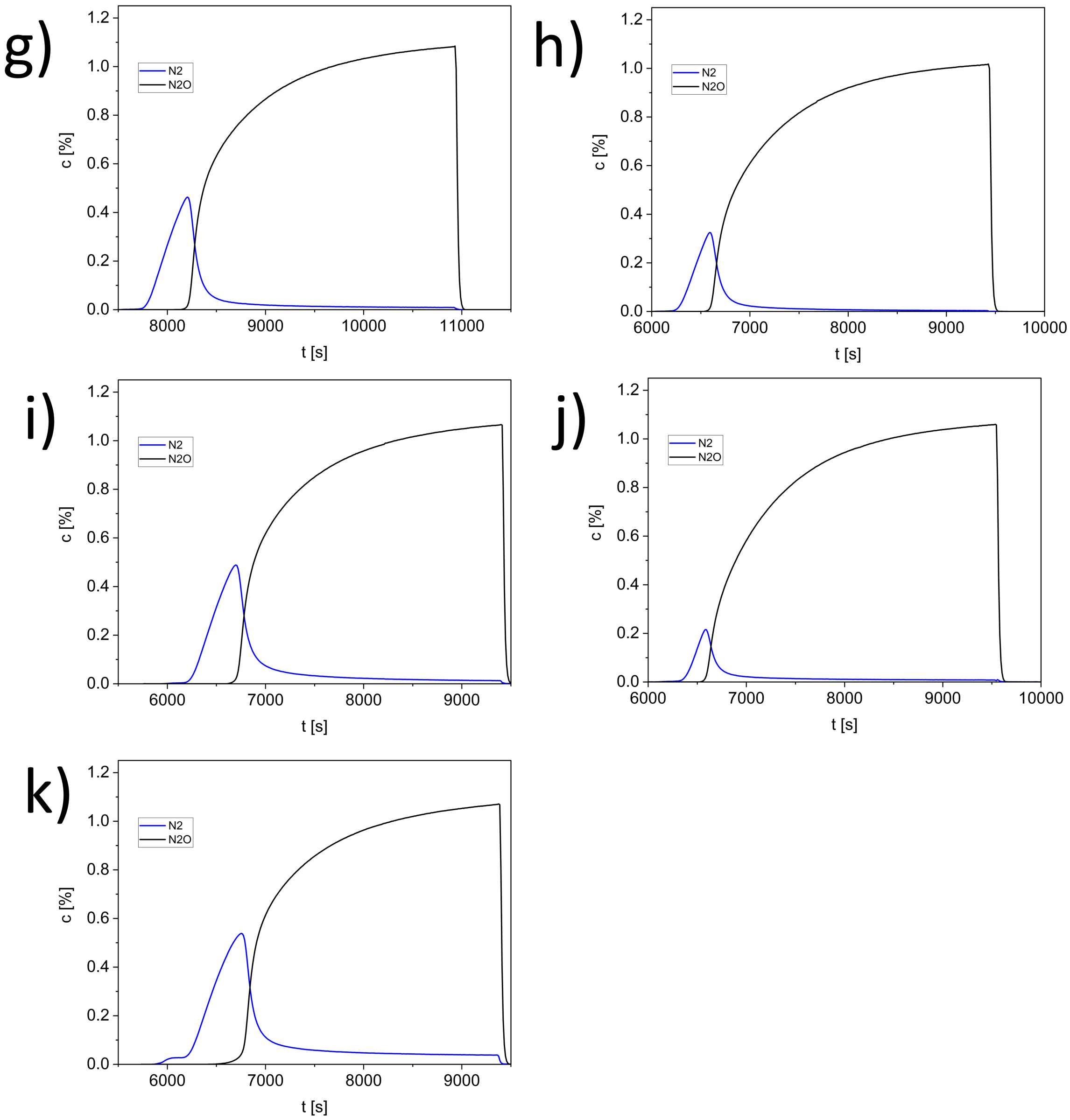

Figure 4.21.: (Continuation) Second N_2O reactive frontal chromatography of reduced samples of g) CZA-70 h) CA-67 i) CZG-50 j) CG-67 k) CZA-50-600.

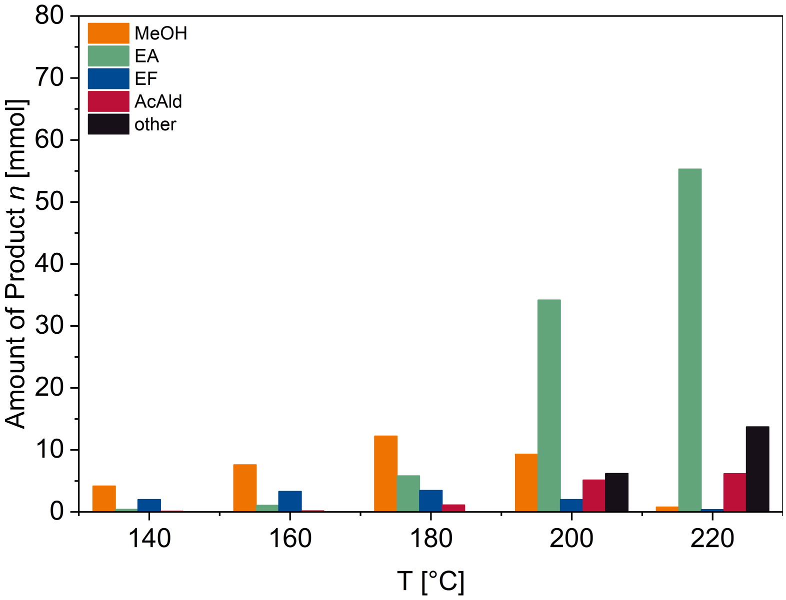

Figure 4.22.: Amount of products after 2 h of reaction time over a commercial methanol synthesis catalyst. The temperature was varied in five independent experiments. MeOH = methanol, EF = ethyl formate, EA = ethyl acetate. Reaction conditions: p = 50 bar, H_2:CO_2 = 3:1, rpm = 1000 min^{-1}, m_{cat} = 1.00 g.

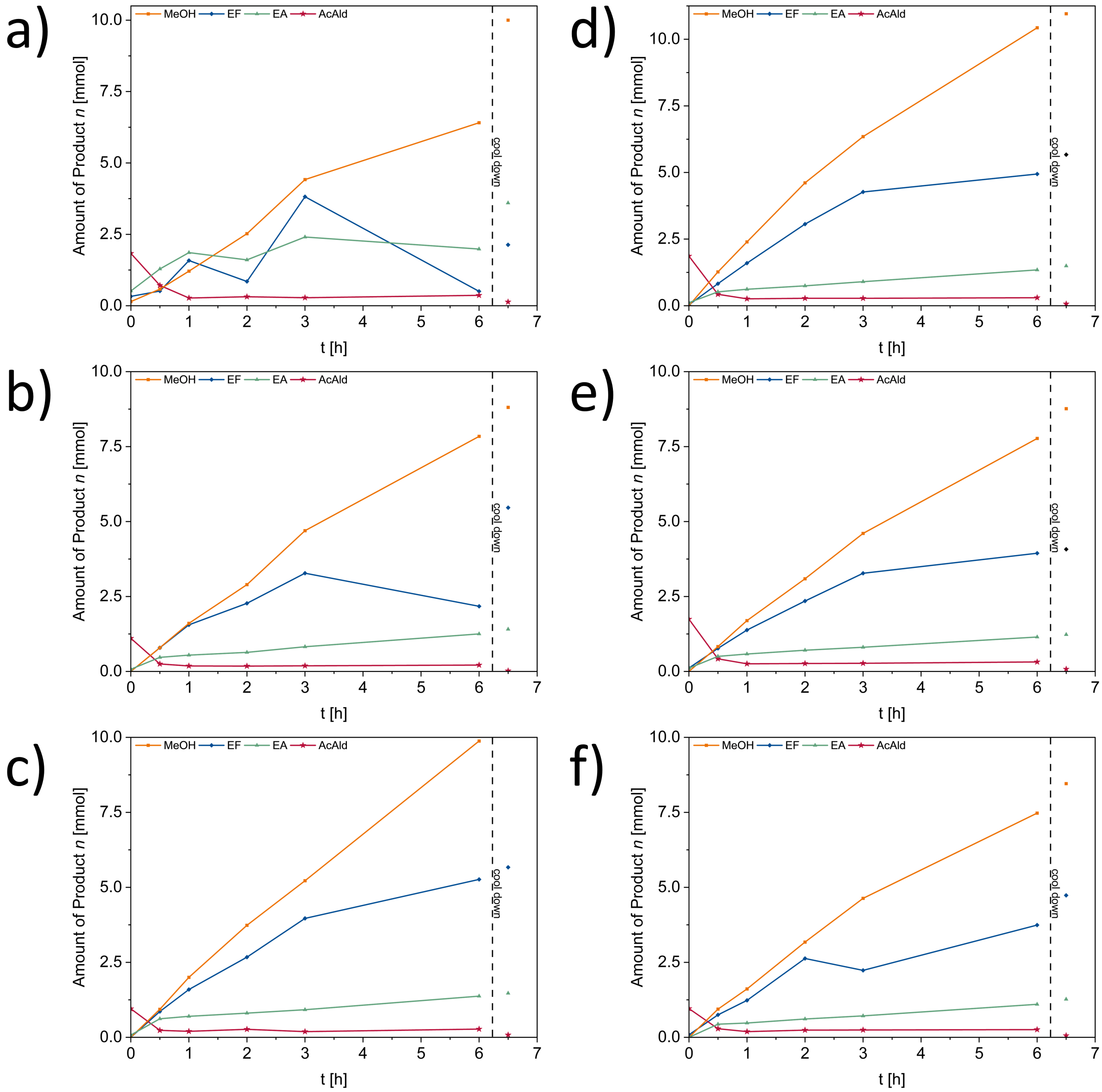

Figure 4.23.: Product-time profiles of reactions performed at 160 °C over various catalysts. a) CZA-50 b) CZA-55 c) CZA-60 d) CZA-62.5 e) CZA-65 f) CZA-67. The data shown at 6.5 h represent the product mixture taken after cooling down. MeOH = methanol, EF = ethyl formate, EA = ethyl acetate, AcAld = acetaldehyde. Reaction conditions: p = 50 bar, H_2:CO_2 = 3:1, rpm = 1000 min^{-1}, m_{cat} = 0.5 g.

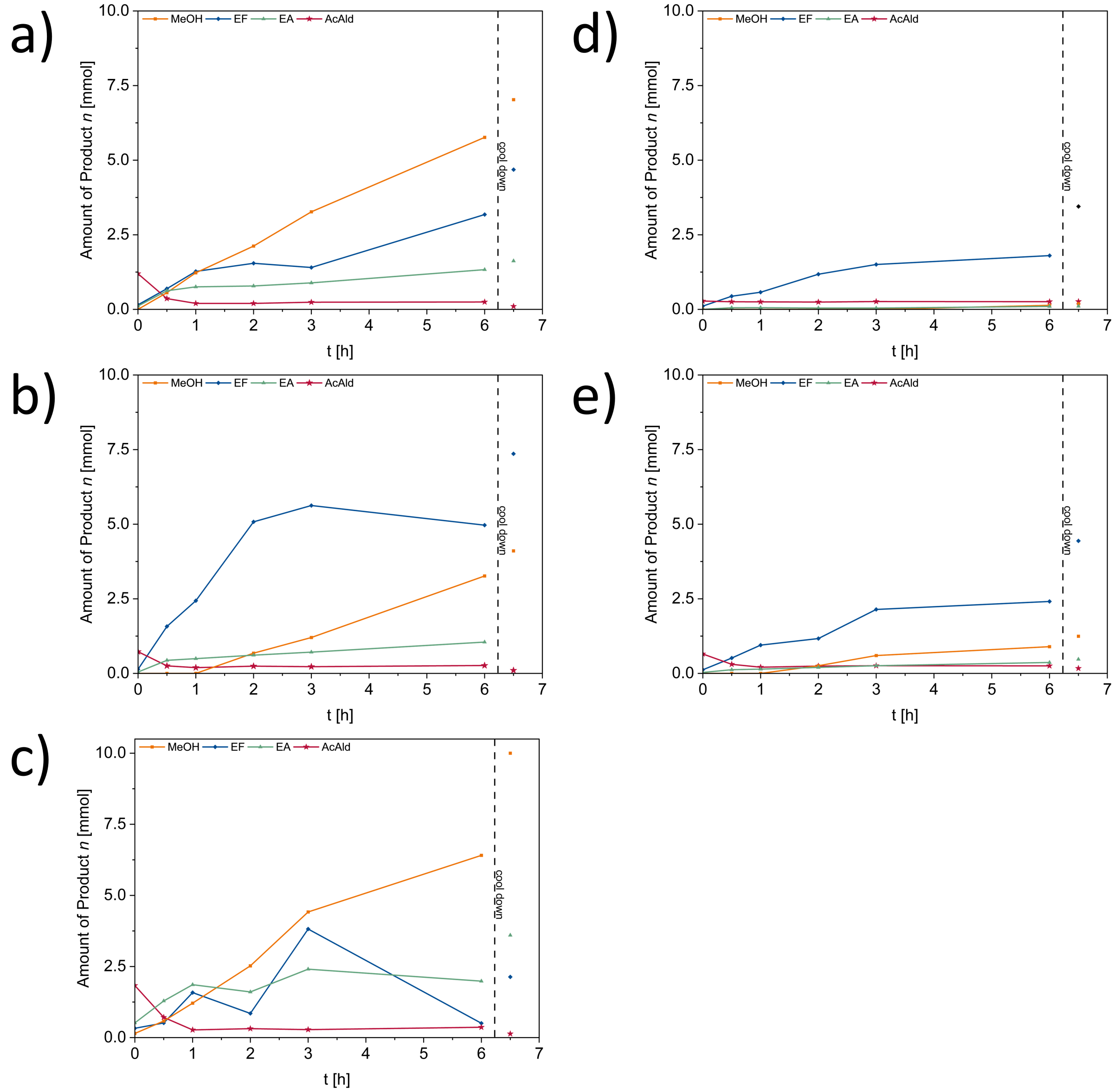

Figure 4.24.: Product-time profiles of reactions performed at 160 °C over various catalysts. a) CZA-70 b) CA-67 c) CZG-50 d) CG-67 e) CZA-50-600. The data shown at 6.5 h represent the product mixture taken after cooling down. MeOH = methanol, EF = ethyl formate, EA = ethyl acetate, AcAld = acetaldehyde. Reaction conditions: p = 50 bar, H_2:CO_2 = 3:1, rpm = 1000 min^{-1}, m_{cat} = 0.5 g.

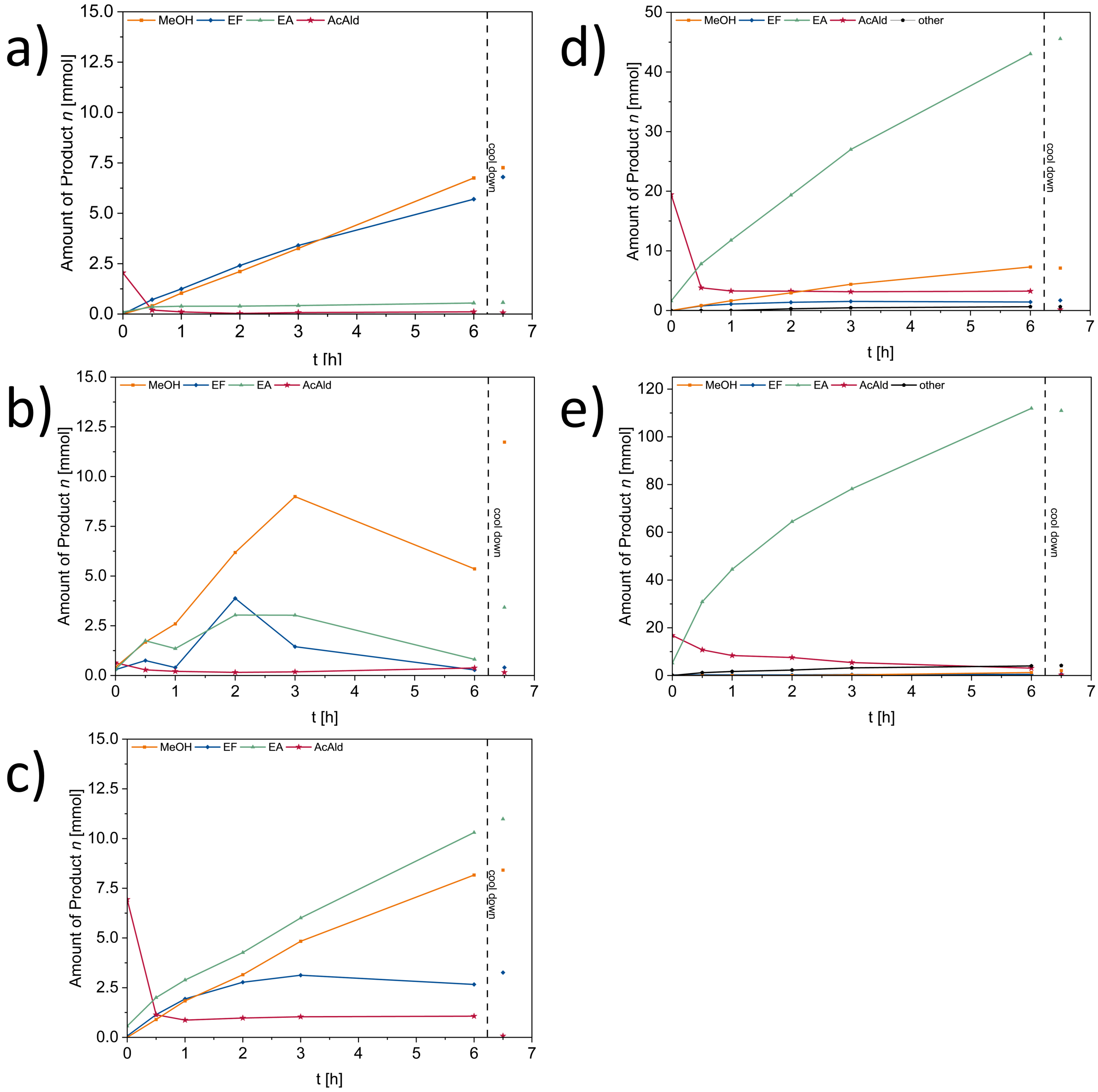

Figure 4.25.: Product-time profiles over CZA-50 at a) 140 °C b) 160 °C c) 180 °C d) 200 °C e) 220 °C. The data shown at 6.5 h represent the product mixture taken after cooling down. MeOH = methanol, EF = ethyl formate, EA = ethyl acetate, AcAld = acetaldehyde. Reaction conditions: p = 50 bar, H_2:CO_2 = 3:1, rpm = 1000 min^{-1}, m_{cat} = 1.00 g.

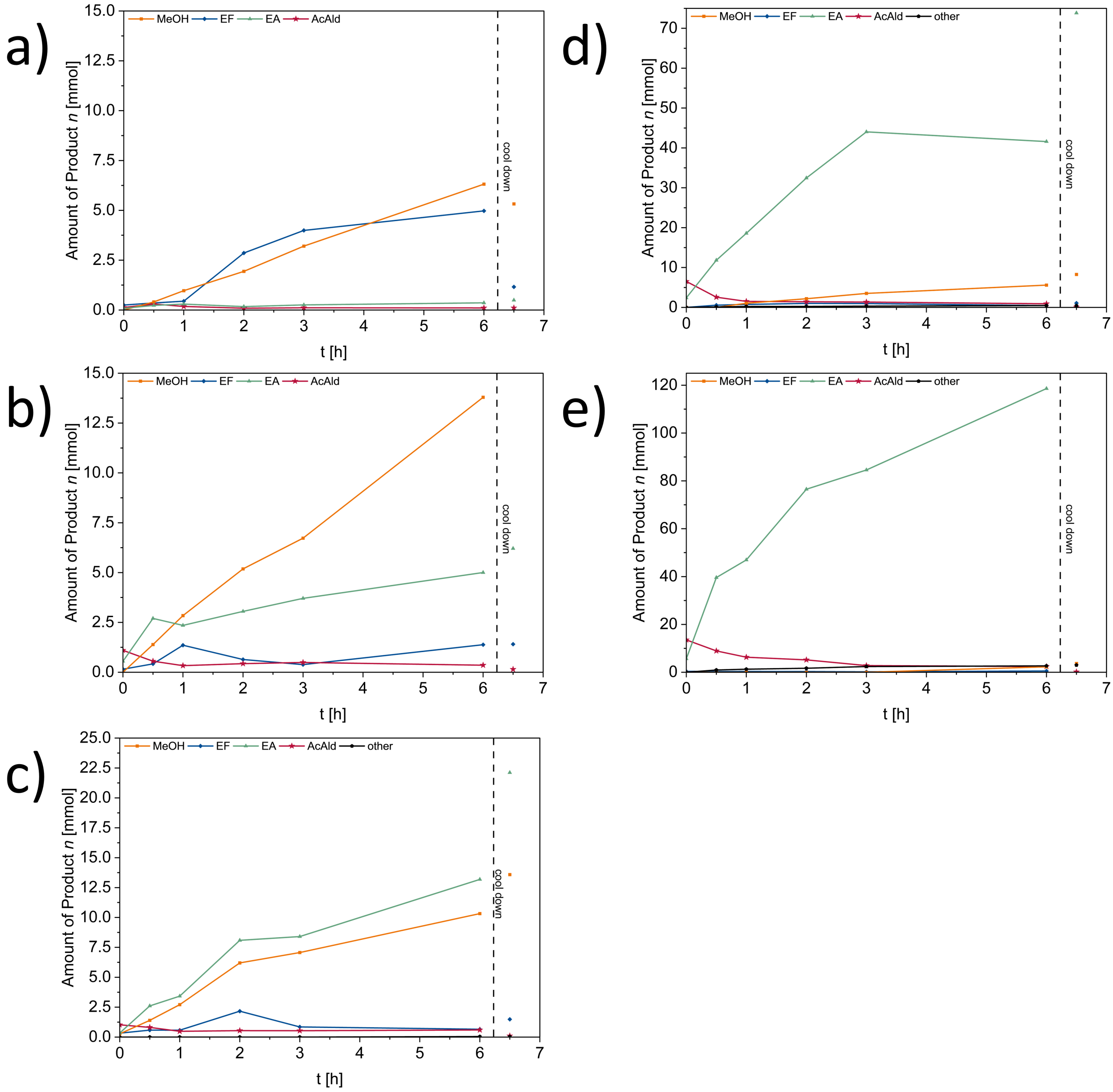

Figure 4.26.: Product-time profiles over CZA-50-600 at a) 140 °C b) 160 °C c) 180 °C d) 200 °C e) 220 °C. The data shown at 6.5 h represent the product mixture taken after cooling down. MeOH = methanol, EF = ethyl formate, EA = ethyl acetate, AcAld = acetaldehyde. Reaction conditions: p = 50 bar, H_2:CO_2 = 3:1, rpm = 1000 min^{-1}, m_{cat} = 1.00 g.

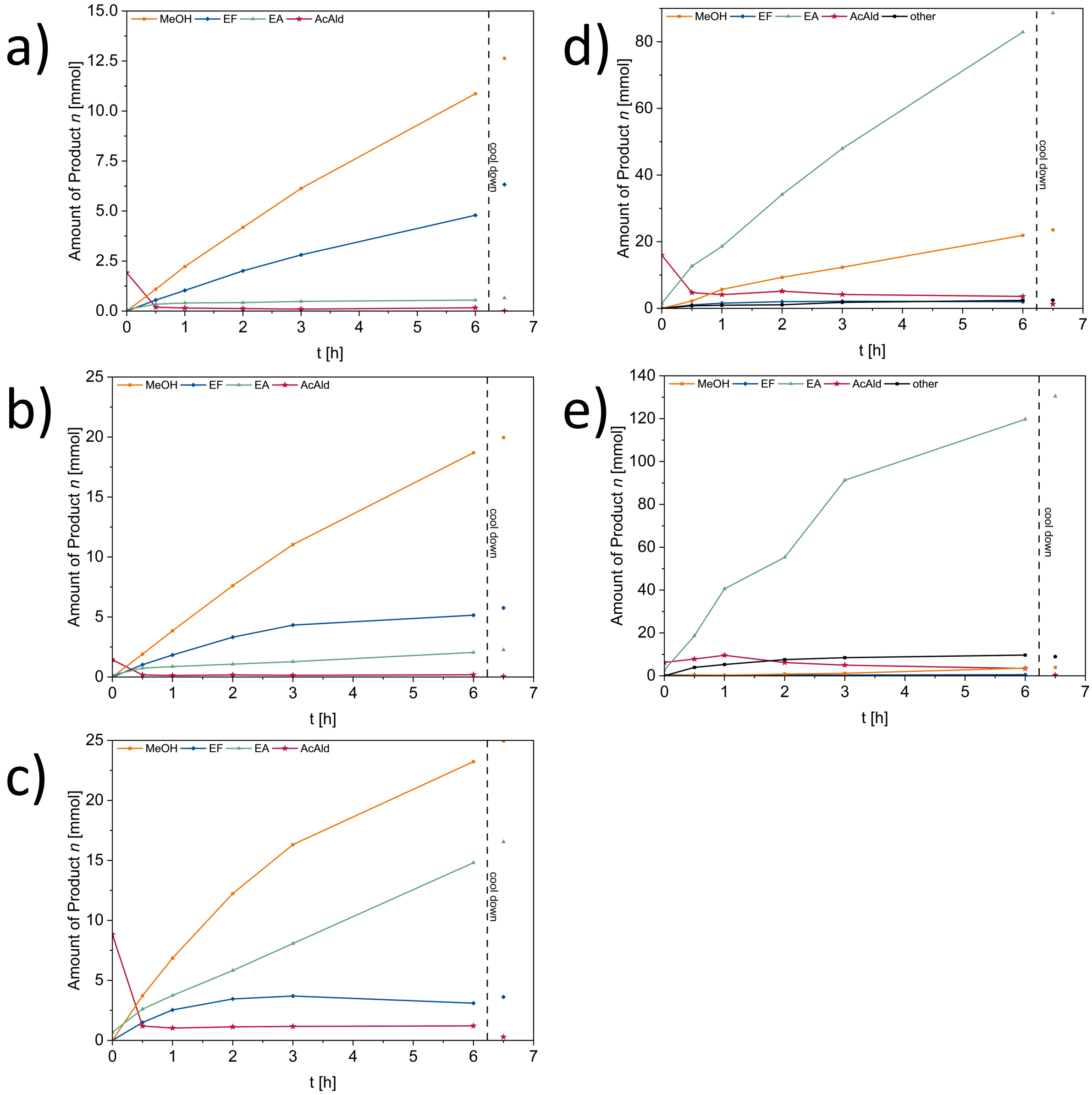

Figure 4.27.: Product-time profiles over a commercial methanol synthesis catalyst at a) 140 °C b) 160 °C c) 180 °C d) 200 °C e) 220 °C. The data shown at 6.5 h represent the product mixture taken after cooling down. MeOH = methanol, EF = ethyl formate, EA = ethyl acetate, AcAld = acetaldehyde. Reaction conditions: p = 50 bar, H_2:CO_2 = 3:1, rpm = 1000 min^{-1}, m_{cat} = 1.00 g.

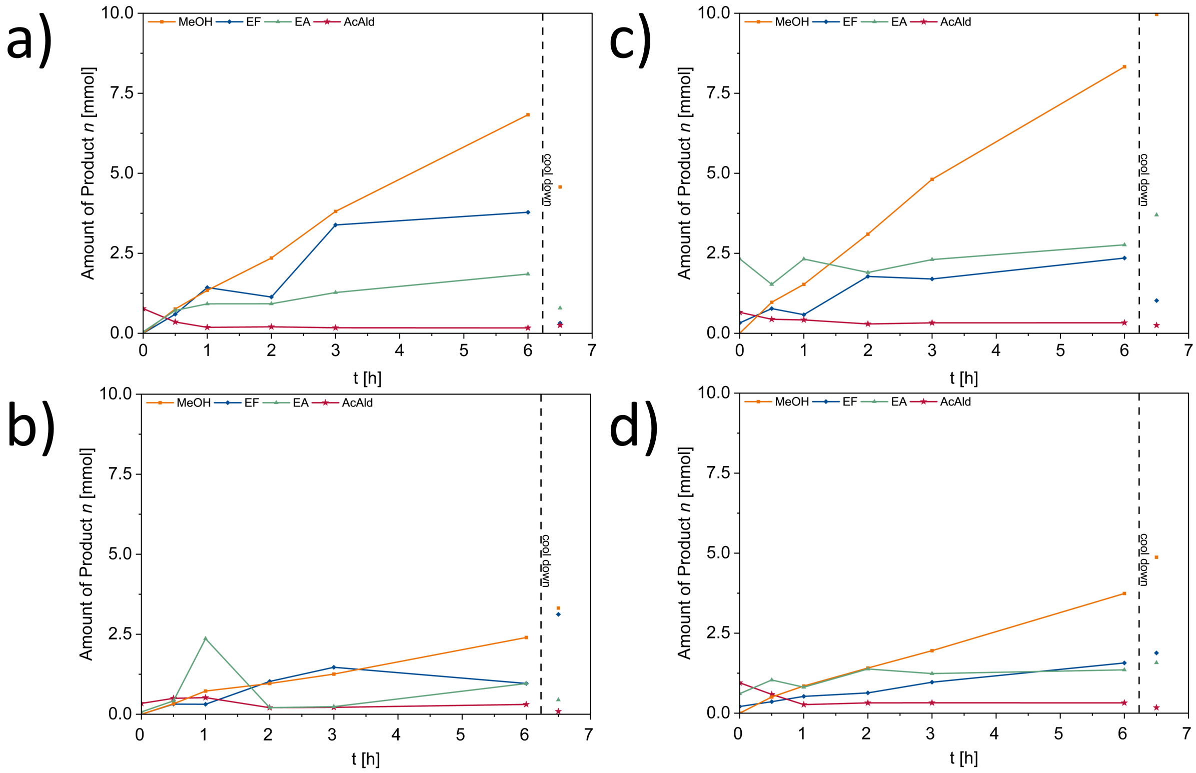

Figure 4.28.: Product-time profiles of the catalyst recycling study at 160 °C. a) Second cycle of CZA-50 b) third cycle of CZA-50 c) second cycle of CZA-50-600 d) third cycle of CZA-50-600. The data shown at 6.5 h represent the product mixture taken after cooling down. MeOH = methanol, EF = ethyl formate, EA = ethyl acetate, AcAld = acetaldehyde. Reaction conditions: p = 50 bar, H_2:CO_2 = 3:1, rpm = 1000 min^{-1}.

5. Comparison of the Methanol Synthesis Activity in the Gas and Liquid Phase

5.1. Abstract

The CO_2 hydrogenation to methanol is conducted both in the gas- and liquid-phase process. The industrially known gas-phase process is performed continuously in a tubular reactor. Liquid-phase reactions are alcohol-assisted and performed batchwise with ethanol as a co-catalyst, leading to an altered reaction mechanism. Two sets of catalysts are applied in both processes. One set is based on the layered double hydroxide (LDH) structure, while the second one is derived from zinican malachite. Crucial differences of the two sets are the precursor phases, Cu crystallite sizes and amount of ternary cationic promoters. Resulting product distributions and methanol formation rates are compared. This allows for a specification of possible differences in the requirements for the catalyst regarding its microstructure and metal ratio. Furthermore, it is evaluated whether the novel alcohol-assisted liquid-phase process is able to compete with the industrially applied gas-phase methanol synthesis.

5.2. Introduction

Methanol (MeOH) is a base chemical with an increasing annual production rate. It has been used for decades directly as a solvent or to produce derivatives such as acetic acid, methyl-*tert*-butyl ether and formaldehyde. Those are utilized to fabricate resins, plastics, paints, pesticides and pharmaceuticals.[35,41,138] It also gained attention as a fuel additive. Next to that, the use as a sole fuel in combustion engines or the development of MeOH fuel cells is being researched.[35,48,88] When producing MeOH from CO_2 and green hydrogen, it can be used in a circular way. It can then act as an e-fuel and help to minimize the carbon footprint of the transportation sector.[36–38]
The large-scale industrial process we know today is employed since the 1960s. In this low-pressure gas-phase reaction, MeOH is produced from syngas at 220 to 280 °C and 50 to 100 bar.[90,91] The typical catalyst comprises Cu as the main component. Zn serves as an electronic promoter and Al was found to be a structural promoter to increase the exposed Cu surface area and to stabilize the catalyst. Usually, a Cu:Zn molar ratio of about 2:1 and a total amount of 5 to 10 mol % Al are used.[42,93–97] The catalyst is prepared by precursors of mixed metal hydroxycarbonates, calcination to the corre-

sponding oxides and subsequent reduction of the Cu oxide to the metallic state. Representative precursor phases of the industrial catalyst are rosasite $(Cu,Zn)_2(CO_3)(OH)_2$, the closely related zincian malachite $(Cu,Zn)_2(CO_3)(OH)_2$ and aurichalcite $(Cu,Zn)_5(OH)_6(CO_3)_2$.[46,139] Next to that, the phase of layered double hydroxides $(Cu,Zn)_6Al_2CO_3(OH)_{16}$ (LDHs) could be found as well. However, this structure usually needs at least 20 mol % of trivalent metal to be formed. Thus, it is found as a minor phase, as the Al content in the typical MeOH synthesis catalyst is lower.[44,52,119]
The following reaction occur during the gas-phase MeOH synthesis:[41,51]

$$CO + 2\,H_2 \rightleftharpoons CH_3OH \qquad \Delta H_0 = -91.0\,\mathrm{kJ\,mol^{-1}} \tag{5.1}$$

$$CO_2 + 3\,H_2 \rightleftharpoons CH_3OH + H_2O \qquad \Delta H_0 = -49.8\,\mathrm{kJ\,mol^{-1}} \tag{5.2}$$

$$CO + H_2O \rightleftharpoons CO_2 + H_2 \qquad \Delta H_0 = -41.2\,\mathrm{kJ\,mol^{-1}} \tag{5.3}$$

Both CO and CO_2 can be used as a starting material (Reaction 5.1 and Reaction 5.2, respectively). In the CO hydrogenation mechanism, carbon- and oxygen-bound species occur. Contrarily, the pathway of CO_2 hydrogenation only proceeds *via* oxygen-bound intermediates and transition states.[49,93] In the presence of Zn, species that are bound by oxygen atoms become stabilized and hence, CO_2 hydrogenation is promoted.[93,140] Moreover, it was found that small amounts of CO_2 in the syngas increase the MeOH yield. CO and CO_2 are interconvertible by the watergas shift reaction (Reaction 5.3) and the extent is dependent on the ratio of substrates to products and the temperature.[103,104,141] When using CO_2 as a carbon source, one equivalent of water is produced as a co-product. Water is mostly reported to have an inhibiting effect, because it sticks on the catalyst's surface and thus blocks active sites. Nonetheless, a positive influence in terms of a shortened induction period was also reported.[49,116,142,143] Irrespective of the carbon source, the MeOH synthesis is an exothermic process. This results in a limited single-pass yield at the commonly applied reaction conditions. A lower reaction temperature could increase the thermodynamically achievable yield. Yet due to the kinetic nature of this gas-phase reaction, it proceeds slowly at a decreased temperature, making it less economic.[34,42]
To circumvent the issue of slow kinetics, Fan *et al.* proposed a novel reaction mechanism with an alcohol as an active solvent or co-catalyst, respectively. In this three-step mechanism, the reaction pathway is altered and CO_2 is the sole carbon source. The

following reactions occur with ethanol (EtOH) as a solvent:

$$CO_2 + H_2 \rightleftharpoons HCOOH \tag{5.4}$$

$$HCOOH + EtOH \rightleftharpoons HCOOEt + H_2O \tag{5.5}$$

$$HCOOEt + 2\,H_2 \rightleftharpoons CH_3OH + EtOH \tag{5.6}$$

First, CO_2 is hydrogenated to formic acid (Reaction 5.4). Next, the acid is esterificated by the solvent and co-catalyst EtOH to ethyl formate (Reaction 5.5). This reaction requires an acid site, which can e.g. be found on ZnO. Additionally, one equivalent of water is formed. Finally, the ester is hydrogenated to MeOH and the solvent is retrieved (Reaction 5.6). The present mechanism already proceeds at temperatures as low as 150 °C and the liquid phase facilitates heat removal. This generates less costs for heating and causes fewer catalyst sintering compared to the gas-phase reaction.[109,114,144] Moreover, it was shown that it can also be performed with conventional, CO-rich synthesis gas. In that case, CO is transformed to CO_2 beforehand in the watergas shift reaction (Reaction 5.3).[108,113] Disadvantages of this process are a more complicated product separation. MeOH needs to be removed from the solvent/catalyst suspension. In addition, it can form azeotropes with some of the potential side products.[145]

Until now, catalysts were optimized with the knowledge of the industrial gas-phase MeOH synthesis. Usually, those were also applied in the alcohol-assisted liquid-phase process. However, it is known that the esterification demands acid sites and that molecules with longer carbon chains $>C_1$ need to interact with the catalyst's surface. This brings up the question whether the requirements for the catalyst in the gas- and liquid-phase reaction could be different. In this study, two sets of catalysts derived from the malachite and LDH structure will be applied in both processes. By a comparison of product distribution and MeOH yields, conclusions will be drawn about the impact of metal ratios, precursor phases and microstructures of the applied catalysts. Furthermore, it will be evaluated whether the novel liquid-phase process can compete with the industrial gas-phase MeOH synthesis. This would allow for a novel synthesis route at lower temperatures and higher conversion.

5.3. Results & Discussion

5.3.1. Co-Precipitation and Calcination

Two sets of materials were synthesized in a semi-automatic lab reactor that enabled a constant temperature, pH value, stirring and dosing speed of metal salt solutions and precipitation agents. The first set is derived from the zincian malachite structure and was calcined at 350 °C. The materials are denoted Mal-CZ, Mal-CZAG and Mal-CZA, in which the presence of copper, zinc, aluminum and gallium is indicated by the corresponding initial letter of the element. The second set of materials originates from the LDH structure. Starting from the same CZA precursor, one part was calcined at 600 °C, another one at 330 °C and a third part was left uncalcined. They are denoted LDH-600-calc, LDH-330-calc and LDH-no-calc, respectively. The LDH-derived catalysts were already presented in Section 3 and Section 4 but for the sake of completeness, some characterization data is shown again.

5.3.2. Catalyst Characterization

All materials were analyzed by powder X-ray diffraction (see Figure 5.1). CuO is present in the malachite-type materials, as evidenced by the reflections at 35, 39 and 48° 2θ. In the binary Mal-CZ, the presence of ZnO is indicated at 32 and 56° 2θ. This sample shows sharper reflections and hence is more crystalline than the other malachite-derived materials. Contrarily, the reflections of Mal-CZAG and Mal-CZA are broader and remnants of the malachite precursor are visible at 17 and 33° 2θ. It is known that even small amounts of a ternary promoter such as Al or Ga tune the electronic and structural properties of ZnO by incorporation or doping, respectively. Thereby the dispersion of Cu in the malachite structure is promoted, leading to the broader reflections.[72,96,97] LDH-no-calc is a phase-pure hydrotalcite and fits the reference with the composition $Cu_3Zn_3Al_2(OH)_{16}CO_3 \cdot 4H_2O$. When calcined at 330 °C, a poorly crystalline material emerges with only one broad reflection at about 35.0° 2θ, indicating small CuO crystallites. No indications for a Zn or Al containing phase are found, suggesting an amorphous oxide matrix of those two elements. By the thermal treatment at 600 °C, a $ZnAl_2O_4$ spinel phase becomes detectable at 31, 37, 59 and 65° 2θ next to CuO. Behrens *et al.* proposed the preformation of an amorphous spinel matrix at lower temperatures. However, an entire demixing of CuO and spinel phase is necessary for crystallization and this solid state diffusion will only occur at elevated temperatures of about 600 °C.[53]

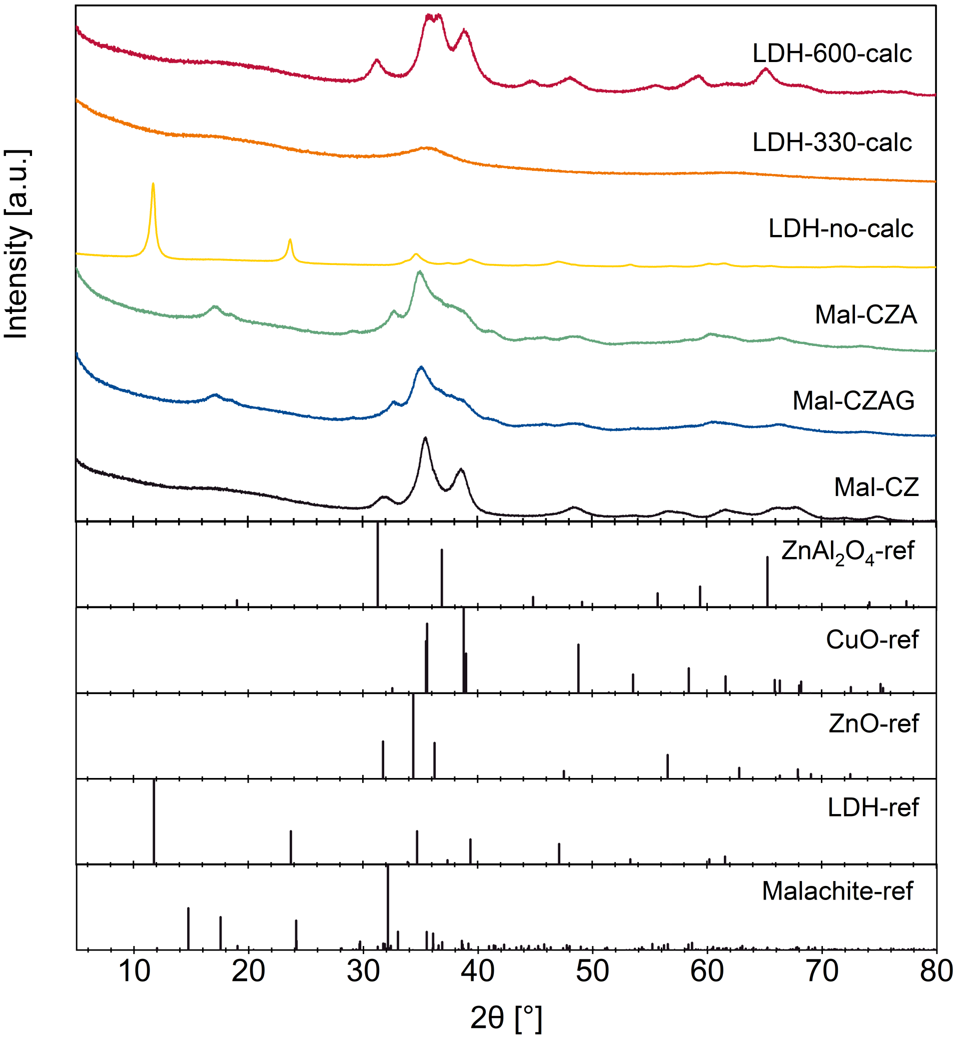

Figure 5.1.: XRD powder patterns of LDH- and malachite-derived catalysts. References are shown below as bars and marked with the suffix "-ref": $ZnAl_2O_4$ (ICSD 75091), CuO (ICSD 16025), ZnO (ICSD 67848), LDH (ICDD 37-0629) and Malachite (ICSD 260813).

The molar composition of the catalysts was determined by ICP-OES (see Table 5.1). The results are in good agreement with the targeted values. Merely in LDH-600-calc, the Cu content is too high at the expense of the Al content. This is unexpected as all LDH-derived materials are prepared from the same LDH batch and the metal ratio should not change during the calcination. The reason for this Al depletion is not clear. A possible explanation is the deposition of an amorphous Al oxide phase on the combustion dish walls during the calcination step. Alternatively, this Al oxide phase was not completely dissolved during the sample preparation in nitric acid, but the remnants were to small to be seen by eye. Depending on the type of phase, Al_2O_3 is either only soluble in strong bases or acids or not soluble at all.[146] The incomplete dissolution then could have led to an altered metal ratio in the liquid solution compared to the solid sample.

Table 5.1.: Mole fractions x(M) of Cu, Zn, Al and Ga determined by ICP-OES and targeted values [mol %].

	ICP-OES results				Target values			
sample	x(Cu)	x(Zn)	x(Al)	x(Ga)	x(Cu)	x(Zn)	x(Al)	x(Ga)
Mal-CZ	70.4	29.3	0.0	0.0	70.0	30.0	0.0	0.0
Mal-CZAG	68.2	29.0	1.3	1.3	68.0	29.0	1.5	1.5
Mal-CZA	68.4	28.9	2.6	0.0	68.0	29.0	3.0	0.0
LDH-no-calc	52.8	16.9	29.5	0.0	50.0	16.7	33.3	0.0
LDH-330-calc	52.4	16.8	30.0	0.0	50.0	16.7	33.3	0.0
LDH-600-calc	56.6	16.3	26.3	0.0	50.0	16.7	33.3	0.0

Nitrogen physisorption identifies the surface areas S_{BET} and pore size distributions of the catalysts (see Figure 5.2). S_{BET} of the binary Mal-CZ is $58.7\,\mathrm{m^2\,g^{-1}}$. The area of Mal-CZAG is twice as high. Also Mal-CZA has an increased surface area compared to the binary Mal-CZ. This again shows that already small amounts of trivalent promoter, which are 3 mol % in the present case, can greatly influence the structural properties of a catalyst. The isotherms are of type IV(a) with a mixed H1 and H3 hysteresis. The steep and narrow H1 hysteresis is usually found for materials with a narrow mesopore size. The hysteresis only closes near $p/p_0 = 1$, which is defined as a H3 hysteresis. Moreover, the isotherm cannot be described as nearly horizontal at high relative pressures. Both indicates the presence of macropores.[67,68] Malachite has a needle-like microstructure.[51] The macropores thus can be present in the form of cavities shaped by the needles.

Next to that, the LDH-derived materials have a somewhat lower surface area. Merely S_{BET} of LDH-600-calc is comparable to Mal-CZ with $59.1\,\mathrm{m^2\,g^{-1}}$. The isotherms can be characterized as type IV(a) with H3 hystereses. Those are also typical for platelet-like materials and non-rigid aggregates.[67,68] It was shown by SEM imaging that LDH materials with a similar composition form platelets.[54] Here, the mesopores originate from the aggregation of the platelets. The calcination of the LDH at elevated temperatures showed to be beneficial for the surface area. The so-called high-temperature carbonate HT-CO_3^{2-} is believed to be located in the interlayers, phase boundaries or defect sites.[45,53,54] For similar LDH materials, a decomposition temperature of 616 °C was found for HT-CO_3^{2-},[54] though it is dependent on the type and amount of metals.[55] The HT-CO_3^{2-} could block adsorption sites or whole pores in LDH-no-calc and LDH-330-calc. In this way, they become inaccessible for the probe molecule N_2. Only after decomposition at increased temperatures, the sites are liberated and can add to the determined surface area in LDH-600-calc.

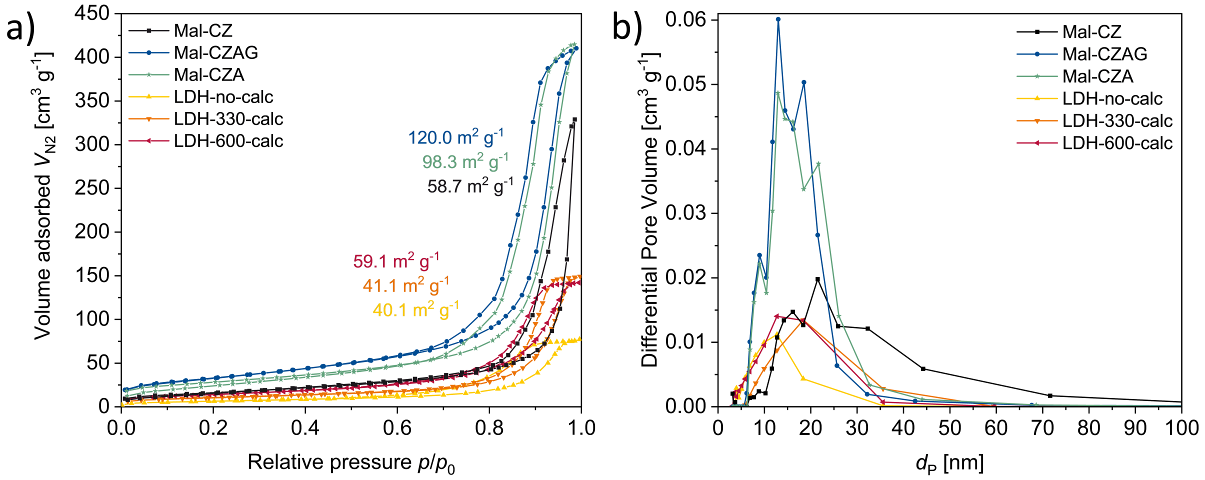

Figure 5.2.: a) Nitrogen adsorption-desorption isotherms used to calculate the surface areas and b) pore size distribution determined from the desorption branches.

The most abundant pores in all materials are in the range of 10 to 25 nm. However, the hystereses of the malachite-derived catalysts are larger than the ones of the LDH-derived materials. This is caused by a higher number of mesopores in the former ones. The pore size distribution of Mal-CZ is slightly shifted to higher pore diameters d_P. As the pore size distribution was determined by the BJH method, only mesopores can be evaluated, no micro- or macropores. However, the shape of the isotherms is indicative of macropores. That is why conclusions from the pore size to the catalytic activity need to be drawn with caution.

The final catalysts are obtained by reduction of Cu^{II} to metallic Cu in diluted hydrogen and elevated temperatures. To analyze their reducibility, temperature-programmed reductions were performed (H_2-TPR, see Figure 5.3). The profile of Mal-CZA consists of one peak with a slight shoulder to the lower temperature side. The peak maximum at 201 °C is in good agreement to 211 °C reported for a benchmark catalyst with the same metal ratio.[56] The maximum of Mal-CZAG is slightly lower, but the peak shape is similar. Mal-CZ differs from the other two malachite-derived materials. At least three peaks can be identified and the largest one is positioned at 175 °C. But also here, a shoulder to the lower temperature side is recognizable. CuO is reduced in a two-step process with Cu_2O as an intermediate. The shoulder is ascribed to the formation of amorphous Cu_2O that is kinetically stabilized and thus, the reduction is retarded.[56] The presence of numerous peaks in Mal-CZ indicates Cu species with different chemical environments. However, no hints for additional Cu containing phases were found by XRD. Hence, X-ray amorphous phases need to be considered. Moreover, an inhomogeneous Cu domain size distribution could also lead to multiple peaks. The lower maximum peak temperature of Mal-CZ indicates larger Cu domains as already found by XRD. Larger domains are more easily accessible and have less interaction to neighboring domains, e.g. *via* oxygen bridges. By that, they are easier to reduce and the overall reduction temperature is lower.

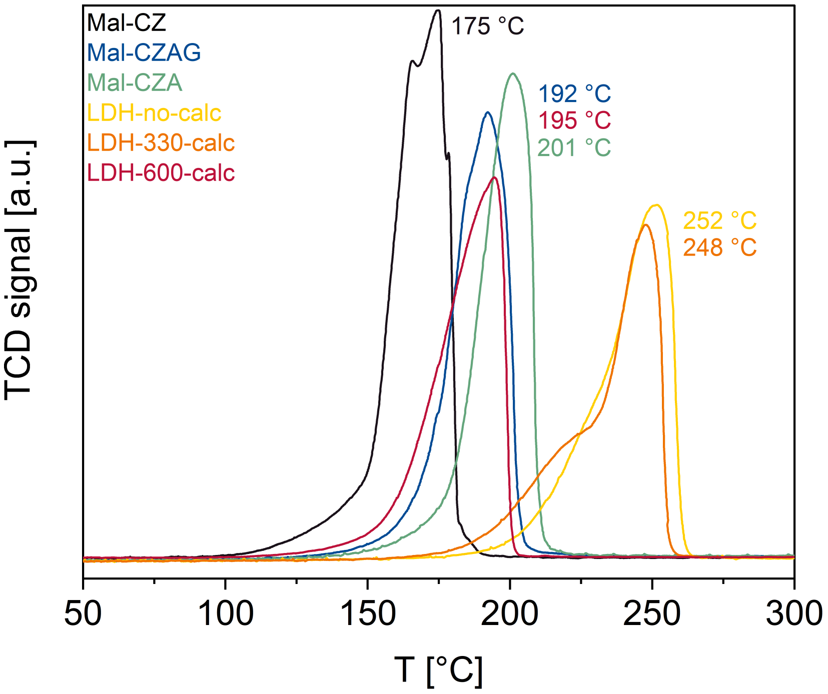

Figure 5.3.: H_2-TPR profiles in 5 % H_2 in Ar. $\beta = 6\,°C\,min^{-1}$.

The peak maxima of LDH-no-calc and LDH-330-calc are found at significantly higher temperatures of about 250 °C. Compared to Mal-CZA, the LDH materials have a multiple times higher Al content (2.6 % compared to about 30 % according to ICP-OES). Moreover, it was shown by SEM imaging and EDX mapping that the cations are homogeneously distributed in the LDH and after calcination at 330 °C (see SI of Section 3). The Cu needs to segregate from the irreducible Zn,Al matrix before it can form metallic Cu nanoparticles. The barrier for this solid state diffusion is higher for the Cu in the LDH derived materials because it is well-dispersed, while CuO and ZnO have already separated during the calcination step in Mal-CZA.[50,51] The homogeneous distribution also causes the more pronounced shoulder in the profiles of LDH-no-calc and

LDH-330-calc. It leads to a restricted accessibility of the Cu cations and they are bound to the Zn,Al matrix through O^{2-} or CO_3^{2-} bridges. Both lead to a retarded reduction to Cu_2O and subsequently to Cu^0. The reduction peak maximum of LDH-600-calc is about 50 °C lower and the shoulder is smaller. Similar to the malachite-derived materials, the segregation of CuO from the oxide matrix already took place during the calcination. This enhances the accessibility and facilitates the reduction. Moreover, a TG-MS of the LDH precursor showed that the HT-CO_3^{2-} decomposes at the applied calcination temperature of 600 °C (see Figure 3.1 in Section 3). Thereby, no bridging carbonate is present in this sample anymore that could retard the reduction.

5.3.3. Catalytic Performance

The activity of the catalysts was studied in the gas-phase and liquid-phase CO_2 hydrogenation to methanol (MeOH). For the LDH-derived materials, the catalytic results were already presented in the previous sections. They are shown again for a better comparability to the malachite-derived materials and to contrast the gas-phase and the liquid-phase process.

The gas-phase hydrogenation was conducted in a 30-fold parallel tubular reactor at 220 °C. Malachite-derived catalysts produced more MeOH than the LDH-derived ones and the use of Mal-CZAG and Mal-CZA gave the highest yield of MeOH. For the latter one, small amounts of methane were found, while CO and MeOH were the only products detected over Mal-CZAG. Mal-CZ produced similar amounts of CO, but less MeOH. This shows that a trivalent metal in the malachite structure not only influences the structural properties, but also promotes the activity towards MeOH. Furthermore, Ga as an additional promoter is more advantageous than Al alone. The yield is only minorly improved, but it suppresses a side reaction to methane. For the set of LDH-derived catalysts, LDH-no-calc and LDH-330-calc performed similar. Both the CO and MeOH yield could be increased by the calcination at 600 °C. The major differences of this sample are the larger Cu crystallites and the crystalline spinel matrix. Those seem to be advantages for the activity under the applied reaction conditions.

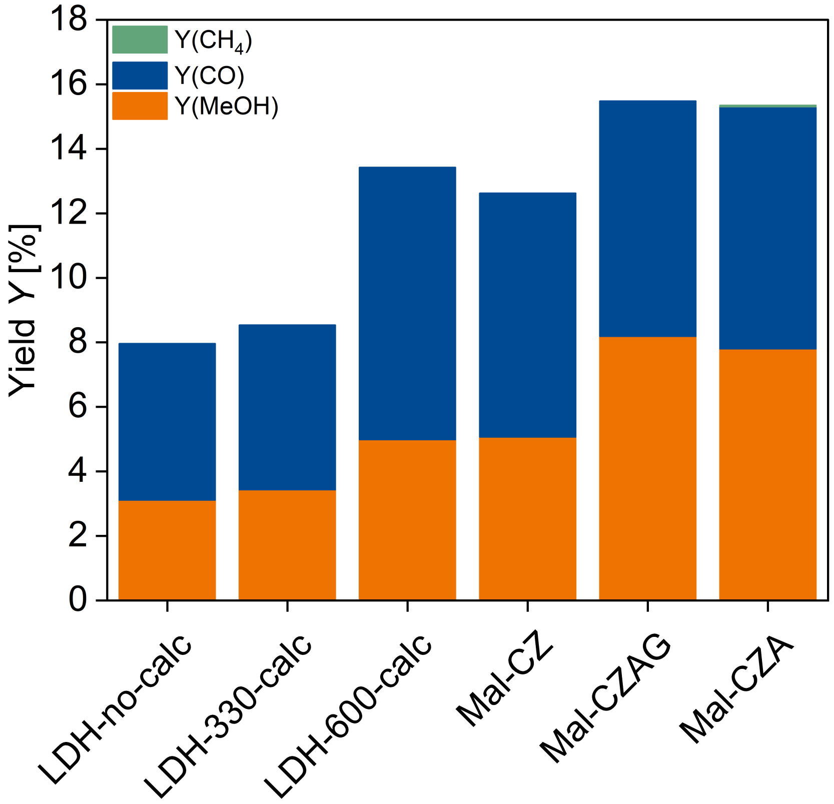

Figure 5.4.: Product yields Y in the gas-phase CO_2 hydrogenation after reduction at 275 °C. Reaction conditions: H_2:CO_2:N_2 = 69:23.2:7.8, $\dot{V}_{\mathrm{norm}}$ = 5.92 ml min^{-1}, p = 20 bar, T = 220 °C.

The liquid-phase CO_2 hydrogenation was conducted in a 300 ml batch reactor at 160 °C with ethanol (EtOH) as a solvent and co-catalyst. Although the reactions were conducted for 6 h, the catalytic performance is compared after 2 h of reaction time (see Figure 5.6). Within this first 2 h, a linear increase of the products could be observed (see Figure 5.8 in the SI). Therefore, a kinetically controlled reaction is presumed. Afterwards, a thermodynamic equilibrium or limitation has to be considered, as the reaction is performed batchwise.

The product distribution after 2 h of reaction is a mixture of MeOH, the intermediate ethyl formate (EF) and the side products acetaldehyde (AcAld) and ethyl acetate (EA). Acetaldehyde (AcAld) is a side product formed by a dehydrogenation of the solvent EtOH over Cu-based catalysts. According to the equilibrium of Le Chatelier, the addition of syngas comprising hydrogen in large parts should suppress the dehydrogenation. However, Santacesaria *et al.* showed that this reaction can even occur in a hydrogen atmosphere at an elevated pressure.[136] AcAld further reacts to ethyl aceate (EA). This can either proceed with one equivalent of EtOH with a hemiacetal as an intermediate,[132,134] or with another equivalent of AcAld in the Tishchenko reaction.[90,135] The pathyways toward EA formation are summarized in Figure 5.5.

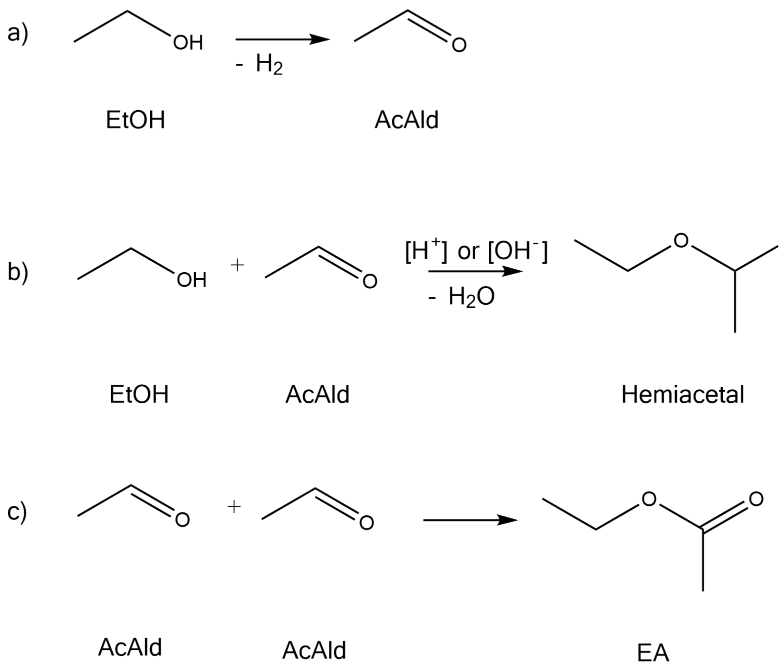

Figure 5.5.: Pathyways of EA formation in the alcohol-assisted reaction. a) Dehydrogenation of EtOH b) EA formation over a hemiacetal intermediate and c) by the Tishchenko reaction.

The product yields differ significantly between the individual catalysts and the set of malachite-derived materials do not outperform the LDH-based samples as clearly as in the gas-phase reaction. The malachite-type sample with the highest MeOH production is Mal-CZAG. The small amount of ethyl formate (EF) found in the sample shows that this compound is effectively hydrogenated to MeOH and EtOH as soon as it is produced (Reaction 5.6). Mal-CZA produced less MeOH and more EF, revealing that the hydrogenation of EF is somewhat less efficient over this catalyst. Significantly less MeOH was produced by Mal-CZ. Overall, the order of catalytic performance of this set of samples matches the one found for the gas-phase reactions, both in terms of activity and MeOH selectivity.

Most MeOH and EF was produced by LDH-600-calc. In general, hydrogenating (Cu) sites are needed to produce MeOH, while the ester EF is formed over acidic sites. The number of both types of sites need to be balanced to yield a high amount of MeOH. Although the metal ratio is the same, LDH-no-calc and LDH-330-calc produced fewer MeOH. Hence, the high-temperature calcination of LDH-600-calc led to the formation of active sites that are more suitable for this alcohol-assisted process. Those could be positioned on the crystalline spinel domains and serve as efficient acidic sites. In the other two LDH-derived catalysts, the cations are still thoroughly mixed and the spinel is either not formed at all or only prearranged in an amorphous state. Moreover, the amount of spinel (about 50 %) in LDH-600-calc is higher than the amount of (doped) ZnO in the malachite-derived catalysts (about 30 %). This higher number of promoter seems to be favorable for the MeOH formation. However, the catalysts with the highest MeOH production LDH-600-calc and Mal-CZAG also produced most EA. A reaction temperature variation shown in Section 4 revealed that the higher the temperature, the higher the EA yield. By lowering the temperature to 140 °C, EA formation could almost be completely suppressed, but the EF and MeOH yield also decreased. This indicates that both MeOH and EA formation share the same active sites.

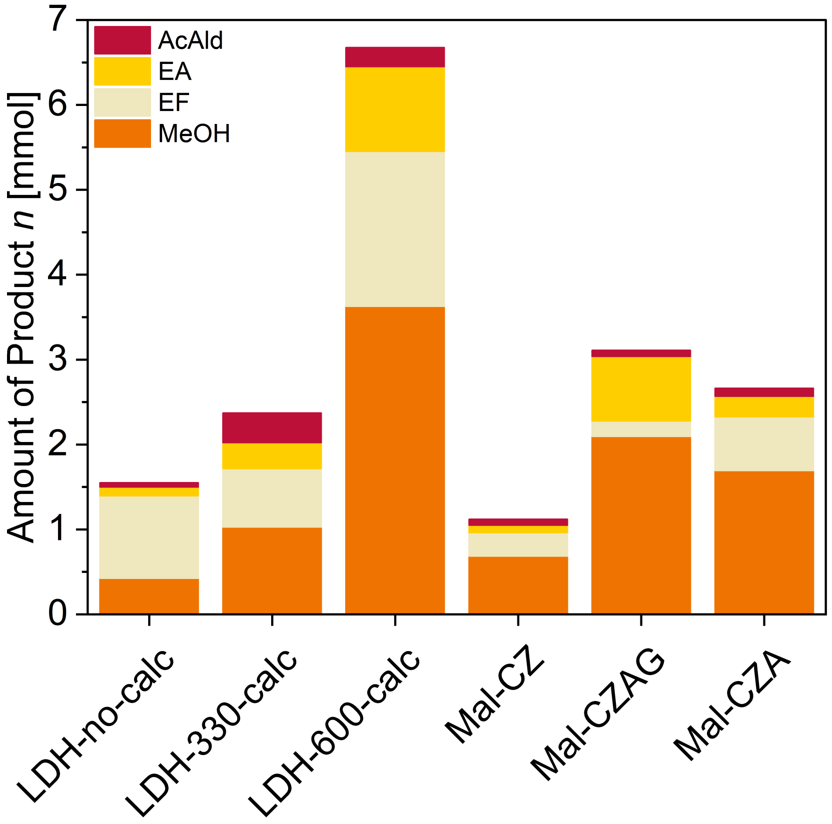

Figure 5.6.: Amount of products in the alcohol-assisted reaction after 2 h of reaction time at 160 °C. MeOH = methanol, EF = ethyl formate, EA = ethyl acetate. Reaction conditions: p = 50 bar, H_2:CO_2 = 3:1, rpm = 1000 min^{-1}, m_{cat} = 0.50 g.

Formic acid (FA) was found in neither of the reaction mixtures, although it is an intermediate formed in the first step of the mechanism (Reaction 5.4). The group of Tsubaki explained this by a surface-bound formate species instead of the free acid.[108] Another explanation is the FA formation being rate-determining. As soon as FA is produced, it reacts further to EF. This second explanation contradicts the publications of the Tsubaki group who claimed that the EF formation is rate-determining. However, in preliminary tests that were conducted for the present batch reactions, a rapid EF formation was observed (see Section 6). A mixture of 10 % FA in EtOH was used as a solvent at 160 °C and the FA concentration decreased quickly to produce EF, even in the absence of a catalyst.

As a linear increase of reaction products was found in the liquid-phase reactions within the first 2 h, a constant reaction rate is presumed. Hence, the MeOH formation rate r_{liquid} can be calculated from the amounts of product n found after this time. It allows for a comparison of r_{gas} obtained from the gas-phase reactions (see Figure 5.7). Within the same set of catalysts, the order of r is the same in the gas and liquid phase. However, changes in this order become visible when comparing all of the six presented catalysts. While Mal-CZAG showed the best performance in the gas-phase reaction, it was surpassed by LDH-600-calc in the liquid-phase reaction. Moreover, LDH-330-calc produced more MeOH than Mal-CZ in the liquid phase. The results show that there is not one optimum catalyst for MeOH synthesis, but that is has to be adjusted to the process. For the alcohol-assisted process, the higher number of acidic sites in the LDH-derived materials compared to the malachite-derived ones, given by the higher amount of Al and Zn, showed to be advantageous for the MeOH production.

It is striking that r obtained for both processes is in the same order of magnitude, ranging from 0.007 to 0.060 $\text{mmol g}^{-1}\text{ min}^{-1}$. This demonstrates that the quite novel alcohol-assisted process can - at least regarding the space-time-yield of the catalyst - compete with the industrially applied gas-phase process. A techno-economic study is not part of this report, but can be found elsewhere.[145] Major disadvantages mentioned for the alcohol-assisted process are the number and type of byproducts that need to be separated from the product. Some of them, including EA, form an azeotrope with MeOH. However, it was already proposed and shown that MeOH itself could be used as a solvent instead of EtOH in an autocatalytic way.[106,111,112] The C_1 analogue to AcAld formed by dehydrogenation of the solvent would be formaldehyde. Accordingly, this would react to methyl formate (MF) as an analogue to EA. Interestingly, MF would also be the intermediate ester formed in the second step of the mechanism when using MeOH as a solvent (compare to Reaction 5.5). Thus, the formation of disturbing side products could be avoided by a deliberate tuning of the process conditions. In the present study, EtOH was chosen as a solvent for an easier product analysis. If MeOH was used, it could not be distinguished from the MeOH formed as a product. That is, unless expensive isotope-labeled substrates were used. When catalyst screening tests are completed, this is indeed a perspective to prove the competitiveness of the alcohol-assisted process to the industrial gas-phase one.

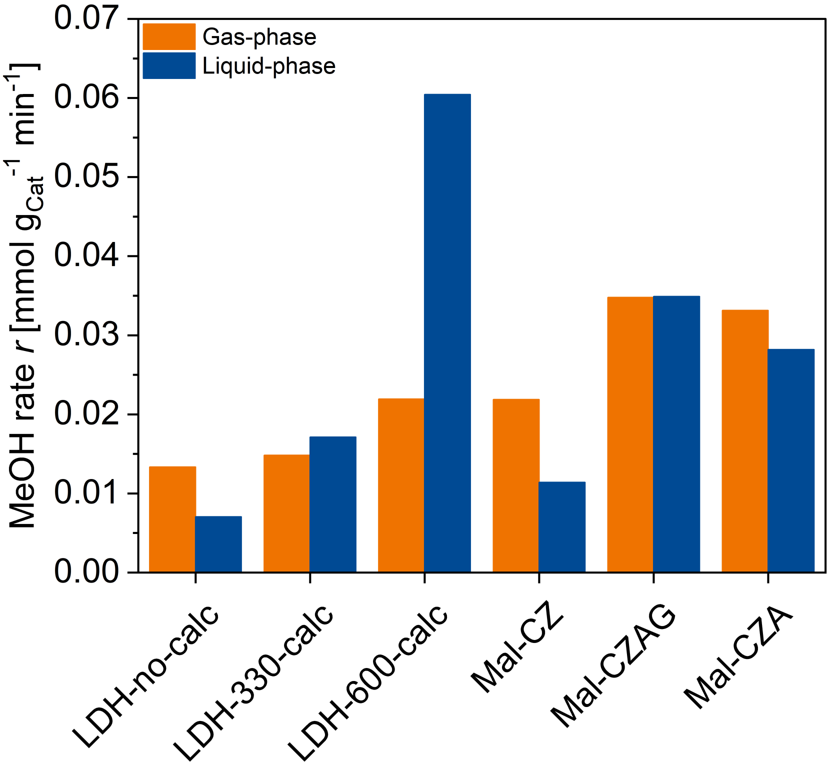

Figure 5.7.: Comparison of MeOH production rates r of the gas-phase process (orange columns) and liquid-phase, alcohol-assisted process (blue columns).

5.4. Summary

LDH- and malachite-derived catalysts were applied both in the gas- and liquid-phase CO_2 hydrogenation. The promotion of ternary cations (Al and Ga) in malachite-derived materials caused smaller Cu domains and higher surface areas. In the CO_2 hydrogenation, this led to a higher activity and MeOH selectivity both in the gas and liquid phase. For LDH-derived catalysts, the calcination at 330 °C showed to have a low impact compared to an uncalcined material regarding Cu domain size and catalytic performance. Contrarily, the calcination at 600 °C increased the Cu domain size and resulted in the formation of a Zn,Al spinel. This showed to be advantageous for the MeOH formation, especially in the liquid phase.

A comparison of both processes revealed different demands on the catalyst to maximize the MeOH yield. While malachite-derived catalysts were more suitable for the gas-phase process, catalyst based on the LDH structure could overcome their activity when calcined at 600 °C. Larger Cu and spinel domains in the latter material were found to be a significant difference, next to an increased amount of ternary promoter. This proved to be advantageous for the EF formation in the liquid-phase process, which requires acidic sites. In the gas-phase reaction, too much acidic sites rather led to an increased CO formation.

The results show that there is no general best MeOH synthesis catalyst, but that it rather has to be adapted to the type and conditions of the process. Moreover, by the MeOH formation rates normalized to the mass of catalyst it was demonstrated that the novel alcohol-assisted liquid-phase process has the potential to compete with the industrially applied gas-phase process. More research has to be conducted to lower the side-product formation. This could either be done by developing a more selective catalyst, or by tuning the process conditions, e.g. with MeOH as a co-catalyst and solvent. In this way, this novel low-temperature process has the potential to overcome the current state of the art gas-phase process.

5.5. Experimental Section

Catalyst Synthesis

Layered double hydroxides were synthesized by co-precipitation of a 0.8 M metal nitrate solution (molar ratio Cu:Zn:Al = 50:17:33) at 25 °C and pH = 8 in the half-automatized lab reactor OptiMax 1001 from Mettler Toledo. An alkaline solution of 0.6 M NaOH and 0.09 M Na_2CO_3 was used as a precipitation agent. 75 g of the metal solution was dosed into a resevoir of 200 ml deionized water over 30 min. Co-dosing of the precipitation agent was controlled by the computer program iControl to ensure a constant pH value. The precipitate was aged for 1 h in the mother liquor at 25 °C. Afterwards, the precipitate was repeatedly washed with deionized water, dried at 80 °C overnight and thoroughly mortared. The LDH was calcined in a muffle oven in static air for 3 h at 330 °C and 600 °C, respectively (β = 2 °C min^{-1}).

Malachite-derived materials were synthesized in the same manner. A 1 M metal nitrate solution with the corresponding ratio of metals and a 1.6 M Na_2CO_3 solution was used to precipitate the precursor at 65 °C and pH = 6.5. After dosing, the precipitate was aged until a pH drop occurred plus another 30 min. The dried precursor was calcined in a muffle oven in static air for 3 h at 350 °C (β = 2 °C min^{-1}).

All samples were pressed with a hydraulic press from Perkin-Elmer (Überlingen, Germany) with 5 t for 2 min. The resulting pellets were mortared and sieved with stainless steel sieves from ATECHNIK (ISO 3310-1, Leinburg, Germany). Unless otherwise noted, a sieve fraction of 125 - 250 µm was used for the presented study.

X-ray Powder Diffraction Patterns of calcined samples

XRD patterns were measured in transmission mode on a Stadi-P from STOE equipped with a MYTHEN 1K detector and GE(111) monochromator. Measurements were conducted with Cu $K_{\alpha 1}$ radiation (λ = 1.540 60 Å) in the range of 5 to 80° 2θ.

Inductively Coupled Plasma Optical Emission Spectrometry

Mole fractions of metals in the calcined samples were determined on an ICP-OES Avio 200 from Perkin Elmer. About 10 mg of a sample was dissolved in 0.5 ml HNO_3 (p.a., 65 %) and diluted with distilled water to a total volume of 50 ml. 5 ml of this solution was taken, again diluted to a total volume of 50 ml and used for analysis.

Nitrogen Physisorption

N_2 adsorption-desorption profiles of LDH-derived catalysts were measured on a BELSORP MAX from Microtrac Retsch GmbH. Prior to the measurement, the calcined samples were degassed at 100 °C and uncalcined samples at 80 °C for 2 h. The partial pressure p/p_0 was recorded in the range of 0.0 to 0.99 at −196 °C and referenced to an empty cell. The partial pressure range of 0.05 to 0.3 was used to calculate the surface areas by applying the Brunauer-Emmett-Teller (BET) equation to the adsorption branch.
The isotherms of the malachite-derived samples were measured on a Nova 3200e soprtion station from Quantachrome. p/p_0 in the range of 0.07 to 0.40 was used to determine the surface areas. Prior to the measurements, the samples were degassed at 100 °C for 2 h under vacuum. The Barrett-Joyner-Halenda (BJH) method was used on the desorption branch to analyze the pore size distribution for both sets of catalysts.

Hydrogen Temperature-Programmed Reduction

Measurements were performed in a Belcat-B catalyst analyzer from BEL JAPAN, Inc. (Haradanaka Toyonaka, Japan) equipped with a TCD detector. About 70 mg of calcined sample were placed onto quarz wool in an U-shaped reactor. Prior to the experiment, the catalyst was dried at 120 °C for 30 min in Ar (80 ml min^{-1}, heating rate β = 5 °C min^{-1}). After cooling to 40 °C, the temperature-programmed reduction was started. The catalyst was reduced in 5 % H_2 in Ar (80 ml min^{-1}) with a heating rate β

of 6 °C min^{-1}. Water was removed by an in-line molecular sieve before the effluent gas reached the TCD.

Gas-phase CO_2 Hydrogenation

Tests were performed in a 30-fold tubular parallel reactor. Each tube was 230 mm in length and had a 5 mm outer and 4 mm inner diameter. Heating was enabled by a furnace, equipped with a turbine in the center to ensure an accurate heat exchange. A 31st reactor (6 mm outer diameter) was kept empty and served as a reference. It was preheated to 150 °C outside of the furnace. The gas feed was controlled by digital mass flow controllers from Brooks. 160 mg of 125 to 250 µm particle sizes were applied for each catalyst. Additionally, a pre-bed (1000 mg) and post-bed (172 mg) of SiO_2 with a size of 355 to 500 µm was used. The effluent gas stream was analyzed by gas chromatography (on-line Agilent 7890A) successively for each reactor in a series. The series was measured three times and the results were averaged. More information about the setup can be found elsewhere.[75] The catalytic results that are shown were obtained at a reaction temperature of 220 °C. They are part of a larger catalytic test. Its protocol is shown in Table 5.2 and the present data was recorded in "Test 2".

The methanol production rate r_{gas} was calculated by

$$r_{\text{gas}} = \frac{S_{\text{MeOH}} \cdot \dot{n}_{\text{CO2,conv}}}{m_{\text{cat}}} \tag{5.7}$$

with S_{MeOH} being the selectivity towards methanol, m_{cat} the amount of catalyst used and $\dot{n}_{\text{CO2,conv}}$ the molar flow of converted CO_2. It is defined as

$$\dot{n}_{\text{CO2,conv}} = \frac{\dot{V}_{\text{reactor}} \cdot x_{\text{CO2}} \cdot X_{\text{CO2}} \cdot \rho_{\text{CO2}}}{M_{\text{CO2}}} \tag{5.8}$$

$\dot{V}_{\text{reactor}}$ is the gas flow per reactor (5.92 ml min^{-1}), x_{CO2} the mole fraction of CO_2 in the syngas (23.2 %), X_{CO2} the conversion of CO_2, ρ_{CO2} the density of CO_2 (1.9767 g L^{-1}) and M_{CO2} the molar mass of CO_2 (44.01 g mol^{-1}).

Table 5.2.: Protocol of the catalytic tests applied for methanol synthesis including the holding time t, temperature T, mole fractions x of the gases, heat ramp β, pressure p and total volume flow over all 31 reactors $\dot{V}_{\mathrm{total}}$.

Step	t [h]	T [°C]	x CO_2:H_2:N_2 [%]	β [$°C\,min^{-1}$]	p [bar]	$\dot{V}_{\mathrm{total}}$ [$ml\,min^{-1}$]
Drying	15	100	0:0:100	5	20	900
Activation	4	275	0:5:95	2	20	300
Cooling	1	235	0:5:95	5	20	300
Stabilization	19	235	23.2:69:7.8	0	20	183.6
Test 1	19	235	23.2:69:7.8	0	20	183.6
Test 2	19	220	23.2:69:7.8	5	20	183.6
Test 3	19	205	23.2:69:7.8	5	20	183.6
Test 4	19	235	23.2:69:7.8	5	20	183.6
Activation	4	400	0:5:95	2	20	300
Cooling	1	235	0:5:95	5	20	300
Test 5	19	235	23.2:69:7.8	0	20	183.6
Test 6	19	220	23.2:69:7.8	5	20	183.6
Test 7	19	205	23.2:69:7.8	5	20	183.6
Test 8	19	235	23.2:69:7.8	5	20	183.6

Liquid-phase CO_2 Hydrogenation

The tests were performed in a alcohol-assisted manner first described by Fan *et al.*[106] They were conducted in a fixed head 4560 mini reactor with a 4848 controller from Parr Instrument Company. The inside of the 300 ml reactor was equipped with a thermocouple, a cooling loop operated by a magnetic valve, a dip tube with a 10 µm frit for sampling and a gas entrainment impeller. Prior to reaction, the catalyst was reduced in a separate setup. For the malachite-derived materials, a size of 125 - 250 µm was used and for the LDH-derived materials a size of 250 - 355 µm. A tube furnace of about 15 cm length was applied and the catalyst was reduced in 20 % H_2 in Ar at 300 °C for 2 h (β = 2 $°C\,min^{-1}$). After cooling down, the reactor was transferred to a glovebox and 0.50 g of catalyst was weighed into a catalyst dosing unit (XCAD). The XCAD is an autoclave accessory that allows an inert transfer of the catalyst. After mounting the XCAD to the autoclave head, 150 ml of ethanol were filled into the reactor as a solvent and co-catalyst. Then the reaction chamber was purged with Ar several times under vigorous stirring. Afterwards, the catalyst was dosed by 5 bar of Ar into the autoclave and the heating to 160 °C was conducted by a band heater. When the temperature was reached, syngas (H_2:CO_2 = 3:1) was introduced to the autoclave and a total pressure of 50 bar was applied. This time of syngas addition was assigned as the beginning of the reaction t = 0 h. Liquid samples were taken before adding the catalyst, after 0.5, 1, 2, 3 and 6 h and after cooling down to room temperature. Aside from the cool down sample, sampling was conducted by the dip tube. A sample was only collected after discarding the first 1 - 2 ml to purge the tube. Each sampling led to a pressure drop of about 1 bar.

The samples were analyzed by a GC 2010 Plus equipped with a mass spectrometer MS-QP 2020 from Shimadzu. A CP-Wax 52 CB (60 m length, 0.25 mm inner diameter, 0.25 µm film thickness) from Agilent was installed. The measurement program started with a temperature of 50 °C and was held for 5 min. Then the temperature was increased to 120 °C with 25 °C min^{-1} and held for another 10 min. 0.3 µl of sample were injected at 250 °C (split ratio 1:50) with He as a carrier gas (linear velocity = 40 $\mathrm{cm\,s}^{-1}$, total flow = 127 $\mathrm{mL\,min}^{-1}$). The detector temperature was 220 °C and masses from 10 to 200 m/z were recorded. A five point calibration for every compound was prepared beforehand. The error of the GC-MS instrument in case of methanol was determined to be 2.6 % and the combined GC-MS and autoclave process error 5.1 %.

To calculate the methanol production rate r_{liquid}, a constant reaction rate in the first 2 h was presumed.

$$r_{\mathrm{liquid}} = \frac{n_{\mathrm{2h,MeOH}}}{120\,\mathrm{min} \cdot m_{\mathrm{cat}}} \tag{5.9}$$

$n_{\mathrm{2h,MeOH}}$ is the amount of MeOH formed after 2 h of reaction time and m_{cat} the mass of reduced catalyst.

5.6. Authors & Contributions

Jil-Lorean Gieser: Conceptualization, data curation and evaluation, writing, LDH catalyst synthesis and characterization, alcohol-assisted reactions, GC-MS measurements and evaluation
Sebastian Mangelsen: XRD measurements
Gereon Behrendt: Malachite catalyst synthesis and characterization
Alina Jakubowski: GC-MS method development and measurements
Qingxin Yang: Gas-phase reactions
Evgenii Kondratenko: Advising support for gas-phase reactions
Malte Behrens: Supervision, project administration, proofreading

5.7. Acknowledgment

We thank Melina Ottenberg for ICP-OES measurements, Jihao Wang for N_2 physisorption experiments and the IMPRS RECHARGE for kind funding and support.

5.8. Supporting Information

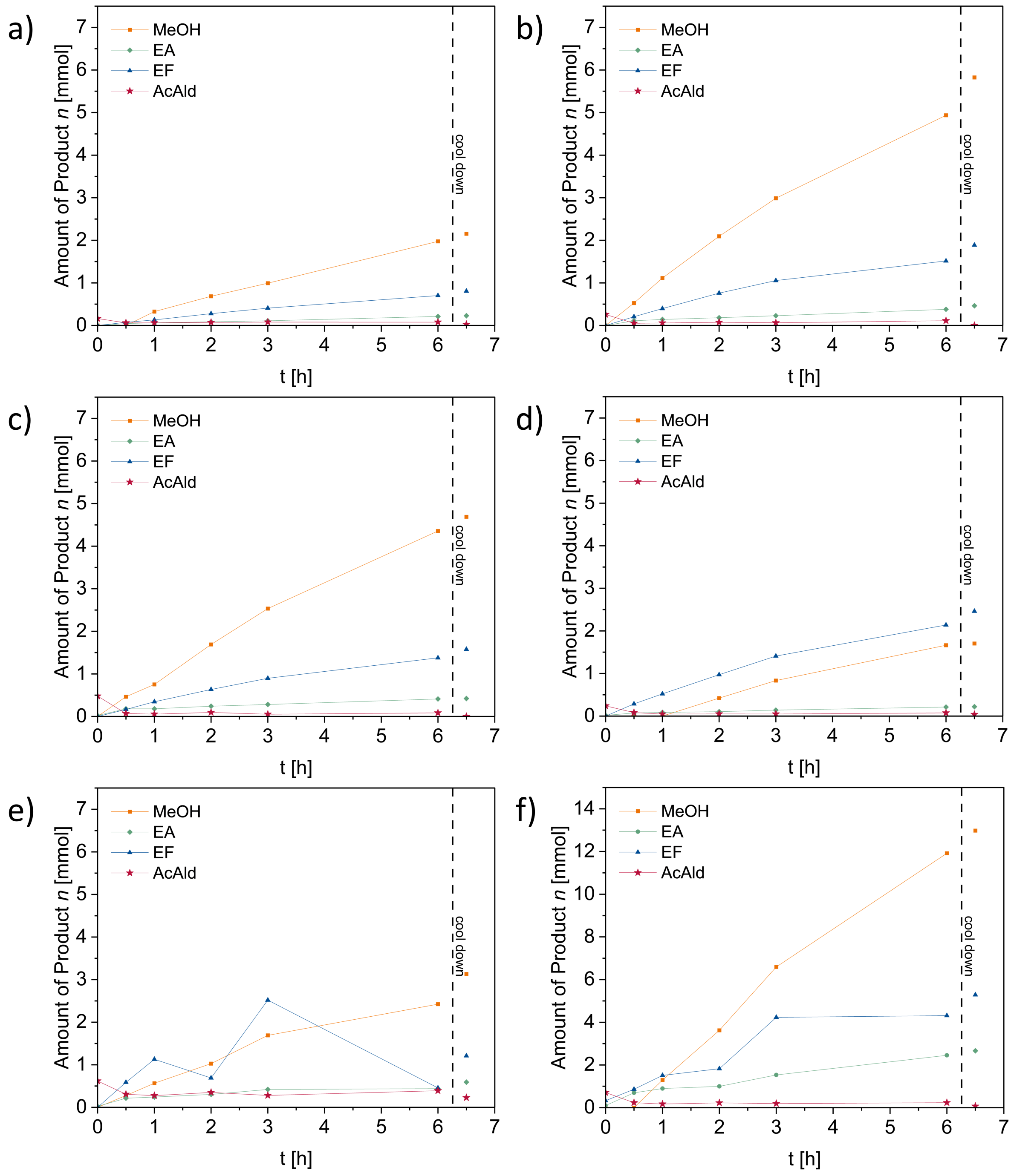

Figure 5.8.: Product-time profiles of reactions performed at 160 °C. a) Mal-CZ b) Mal-CZAG c) Mal-CZA d) LDH-no-calc e) LDH-330-calc and f) LDH-600-calc. The data shown at 6.5 h represent the product mixture taken after cooling down. MeOH = methanol, EF = ethyl formate, EA = ethyl acetate, AcAld = acetaldehyde. Reaction conditions: $p = 50\,\text{bar}$, H_2:CO_2 = 3:1, rpm = $1000\,\text{min}^{-1}$, $m_{\text{cat}} = 0.50\,\text{g}$.

6. Additional Research

6.1. Vacuum-assisted Calcination

6.1.1. Introduction

This section is an extension of Section 3 by the use of two additional catalysts. The materials were synthesized from the same precursor no-calc as the aforementioned catalysts (no-calc, 330-calc and 600-calc) and subjected to the same analyses. They were calcined in a dynamic vacuum of 1×10^{-3} mbar at 330 °C and 600 °C and are denoted 330+V-calc and 600+V-calc, respectively. The process of the calcination in a vacuum is denoted by us as a "vacuum-assisted calcination". For the sake of an easy comparison, the data of no-calc, 330-calc and 600-calc were replotted along with the data for these two additional catalysts. Thus, some information in this section may double with the one given in Section 3. The data of 330+V-calc and 600+V-calc were not included in the previous study because their calcination conditions turned out to be not precisely defined. We found this by an *in situ* PXRD study of no-calc conducted in vacuum up to 600 °C (see below). The spent sample contained a large fraction of Cu_2O and had a yellow color. It should mirror the properties of 600+V-calc due to the same temperature and similar pressure applied during calcination. But different than expected, 600+V-calc had a black color and did not show such clear indications for the presence of Cu_2O. Because of this and further differences in the characterization we must assume that the calcination of 330+V-calc and 600+V-calc did not proceed as planned. More details are given below.

6.1.2. Results & Discussion

Definition of the Target Materials

Thermogravimetric measurements of the hydrotalcite precursor no-calc were conducted at pressures of 1013 mbar, 3 mbar and 1×10^{-3} mbar and the results are shown in Figure 6.1. The measurement at ambient pressure was already shown in Section 3 and has two main mass loss steps. The first one up to 300 °C is ascribed to the loss of water and loosely bound carbonates in the interlayer. The second one is caused by the evaporation of the high-temperature carbonate HT-CO_3^{2-}. The curve recorded at 3 mbar is similar to the one recorded at ambient pressure. The mass loss up to 200 °C is more rapid which indicates an evaporation of interlayer molecules at lower temperatures. A major difference is the presence of an additional third distinct step at around 850 °C. The step was accompanied by an oxygen evolution measured by mass spectrometry of the effluent gas (not shown for clarity), indicating the reduction of Cu (as the most reducible metal in this LDH) to Cu_2O or Cu^0. The TG curve measured at 1×10^{-3} mbar shows a clearly different course. The mass loss up to 300 °C is more rapid and only one distinct plateau is observable. The plateau occurs from 300 to 550 °C and is positioned at a mass loss of about 32 %. This value was only reached after 600 °C for the other two pressures when the HT-CO_3^{2-} had evaporated. Hence, we can infer that at a pressure of 1×10^{-3} mbar, the HT-CO_3^{2-} already evaporates at temperatures as low as 300 °C. Starting from 550 °C, the mass loss is permanently increasing and no more distinct plateau is traceable. We assume that from there on, a series of reduction processes is occurring. But as the measurement at this pressure had to be conducted on another thermobalance, we could not analyze the effluent gas stream for traces of O_2.

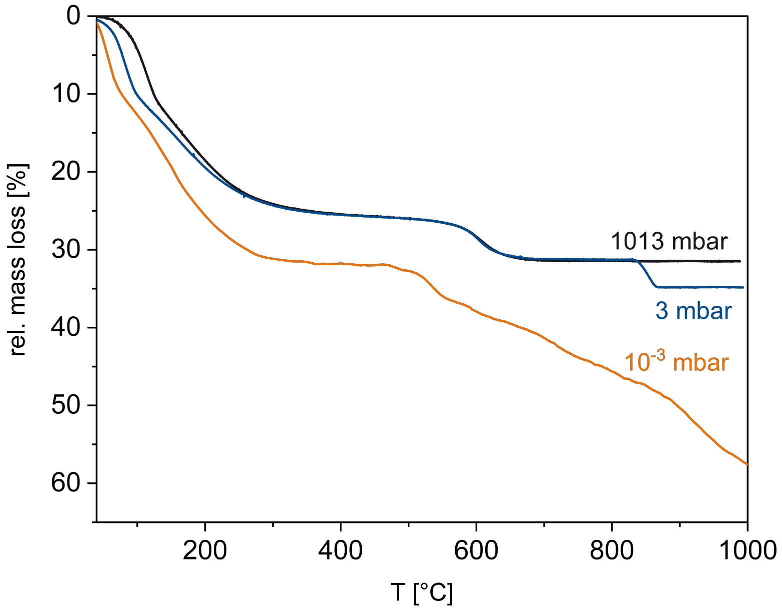

Figure 6.1.: Thermogravimetric anaylsis of no-calc up to 1000 °C (β = 2 °C min^{-1}). Pressures of 1013 mbar, 3 mbar and 1×10^{-3} mbar were applied.

To analyze the effect of the vacuum-assisted calcination, we conducted an *in situ* PXRD measurement in vacuum in which the temperature was raised stepwise and diffraction patterns were recorded after every step (see Figure 6.2 a). The 003 reflection of the LDH at 11.8° 2θ shifts toward higher angles already at 50 °C. It is a measure for the cationic layer distance and indicates a shrinkage of the interlayers a due to the loss of interlayer water and carbonate. An amorphous region was found in a broad range of 100 to 500 °C. A very broad signal at about 35° 2θ in that region can either be ascribed to a residual LDH structure or to CuO evolving. Above 500 °C, the evolving reflections can be attributed tu Cu_2O and a $ZnAl_2O_4$ spinel. A rietveld refinement of the diffraction pattern obtained at 600 °C is shown in Figure 6.2 b) and the calculated phase composition in Table 6.1. From the metal ratio of the solution used during precipitation of the LDH, a 1:1 ratio of a Cu phase and the spinel was expected. This is in good agreement with the 49.3 $wt\%$ calculated for the spinel phase. Moreover, about 80 % of the Cu is reduced to Cu_2O, explaining the yellow color of the spent sample in this experiment. A picture of the spent sample is shown in Figure 6.12 in the SI. It should be noted that although we aimed at a pressure of 1×10^{-3} mbar, we could only reach 2×10^{-2} mbar during the study. Compared to the TG measurements, this means that the observed phase changes might occur at slightly lower temperatures than detected in this experiment.

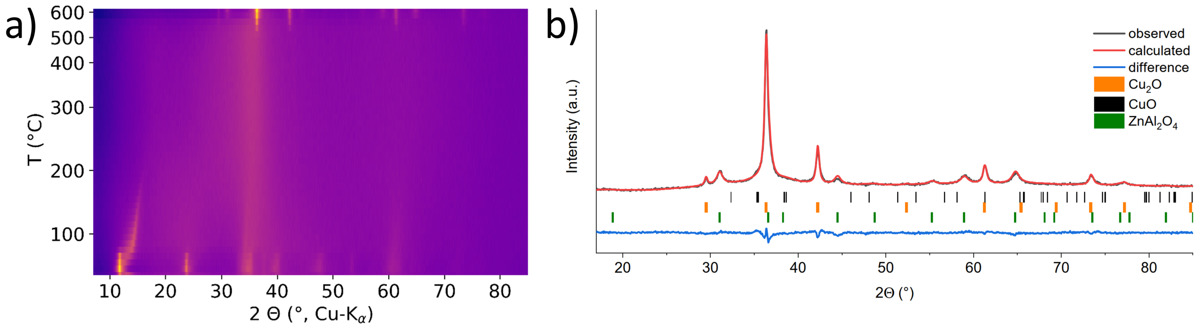

Figure 6.2.: a) Heatmap of the temperature-resolved PXRD study of a CuZnAl LDH precursor at 2×10^{-2} mbar. A diffractogram was recorded every 10 °C in the range of 30 to 350 °C and every 25 °C up to 600 °C. Light colors indicate high intensities. b) Rietveld refinement of the diffractogram obtained at 600 °C.

Table 6.1.: Composition of the LDH-derived sample calcined at 600 °C and 2×10^{-2} mbar determined by Rietveld refinement.

Phase [$wt\%$]			Elemental [mol %]		
$\omega(CuO)$	$\omega(Cu_2O)$	$\omega(ZnAl_2O_4)$	$x(Cu)$	$x(Zn)$	$x(Al)$
11.1	40.7	49.3	47.3	17.6	35.1

Based on the TG measurement at 1×10^{-3} mbar, we chose the calcination conditions of 330 °C and 1×10^{-3} mbar to obtain a material that does not contain any more HT-CO_3^{2-} but was only treated at low temperatures to avoid possible sintering effects. This material is denoted 330+V-calc. 600+V-calc is calcined at 600 °C and 1×10^{-3} mbar and serves as a reference material exposed to higher temperatures in a vacuum.

Synthesis & Characterization

The calcination was conducted in a tube furnace that was connected to a vacuum pump. The pump was switched on throughout the whole experiment, including heating and cooling phase. Although we reached a pressure of 1×10^{-3} mbar in the beginning of the experiment, a deviation from the aimed pressure was observed soon after the heating process was started. This was due to the interlayer water, carbonates and hydroxyls that evaporated into the gas phase.

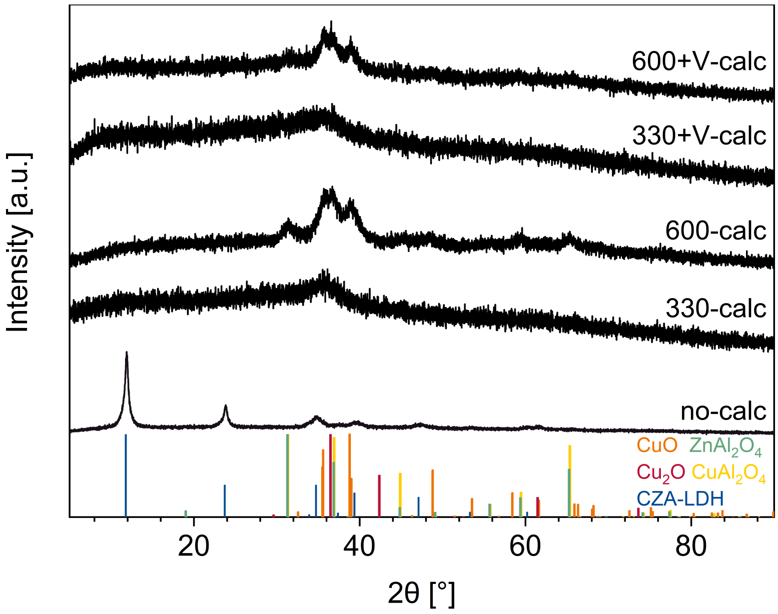

Figure 6.3.: XRD powder patterns of the as-prepared and calcined material. References for CuO (orange), Cu_2O (red), a CuZnAl LDH (blue), $ZnAl_2O_4$ (green) and $CuAl_2O_4$ (yellow) are shown as bars.

Diffractograms of the calcined materials, including the ones from the previous study, are shown in Figure 6.3. The calcination of 330+V-calc resulted in a poorly crystalline material with one very broad reflection at about 35°, as was expected from the temperature-resolved PXRD study. On the other hand, 600+V-calc also has a low crystallinity and shows few broad reflections. A weak signal at about 31° 2θ indicates the presence of a spinel. As the rietfeld refinement including $ZnAl_2O_4$ fitted well, the presence of either this spinel or a mixture of $CuAl_2O_4$ and $ZnAl_2O_4$ is most likely. Both spinels are difficult to distinguish by XRD as their reflections overlap to a great extent. The reflections at about 35° 2θ and 39° 2θ could imply the presence of CuO, though the former one could also be caused by Cu_2O. The diffraction pattern resembles the one of 600+calc calcined at ambient pressure, although we expected a much more defined and crystalline pattern from the temperature-resolved PXRD study. The discrepancy could either be caused by an incomplete calcination or simply by the use of another diffractometer for the patterns in this figure. Moreover, this prepared material has a black color, different to the yellow color found for the spent sample of the PXRD study. In Section 3 we showed that the properties of the materials are highly dependent on the presence of the high-temperature carbonate. Hence we scanned the catalysts for the presence of carbonates by infrared spectroscopy and elemental analysis.

IR spectroscopy clearly reveals the presence of carbonate in both vacuum-assisted calcined samples. As for their counterparts calcined at atmospheric pressure, the ν_3 antisymmetric stretching band is split into two bands at 1484 and 1372 $\mathrm{cm^{-1}}$. Moreover, the ν_2 out-of-plane stretching at 829 $\mathrm{cm^{-1}}$ is detectable, too. The signal intensity of the carbonate bands in 330+V-calc is high, similar to 330-calc. The intensity for 600+V-calc is a bit lower than for 330+V-calc, but clearly visible. Further signals at 460 and 470 $\mathrm{cm^{-1}}$ can be attributed to CuO and a very weak band at about 3400 $\mathrm{cm^{-1}}$ to re-adsorbed water, as discussed previously. Elemental analysis confirms the presence of carbonate in the samples (see Figure 6.13 in the SI). The C weight ratio of 330+V-calc is in the same range as the one of 330-calc, hence the HT-$\mathrm{CO_3^{2-}}$ was not decomposed by the vacuum-assisted calcination. The C weight ratio of 600+V-calc is lower, but still considerably higher than in 600-calc. The H weight ratio is in the same range for all calcined catalysts, though it is lower for the samples treated at 600 °C. As described previously, this can be attributed to the decomposition of the LDH structure and hence, the absence of interlayers that could be rehydrated.

Multiple reasons can account for the insufficnet removal of HT-$\mathrm{CO_3^{2-}}$ in the vacuum-calcined samples. As noted earlier, the pressure of 1×10^{-3} mbar was only reached at the beginning of the calcination. Because of the evolved gases during heating, the pressure increased during calcination, though it never was above the 2×10^{-2} mbar applied for the temperature-resolved PXRD study. Moreover, the temperature was only measured by the sensor of the tube furnace. The furnace might not have been well calibrated or could not control the temperature accurately because of its age. In addition, the temperature measured by the furnace does not necessarily have to match the temperature of the sample inside the glass tube. Furthermore, the duration of the calcination might not have been long enough to fully remove the carbonate. Finally, there could also be a discrepancy of the temperatures measured by the furnace, the thermobalance and the cell used for the PXRD study.

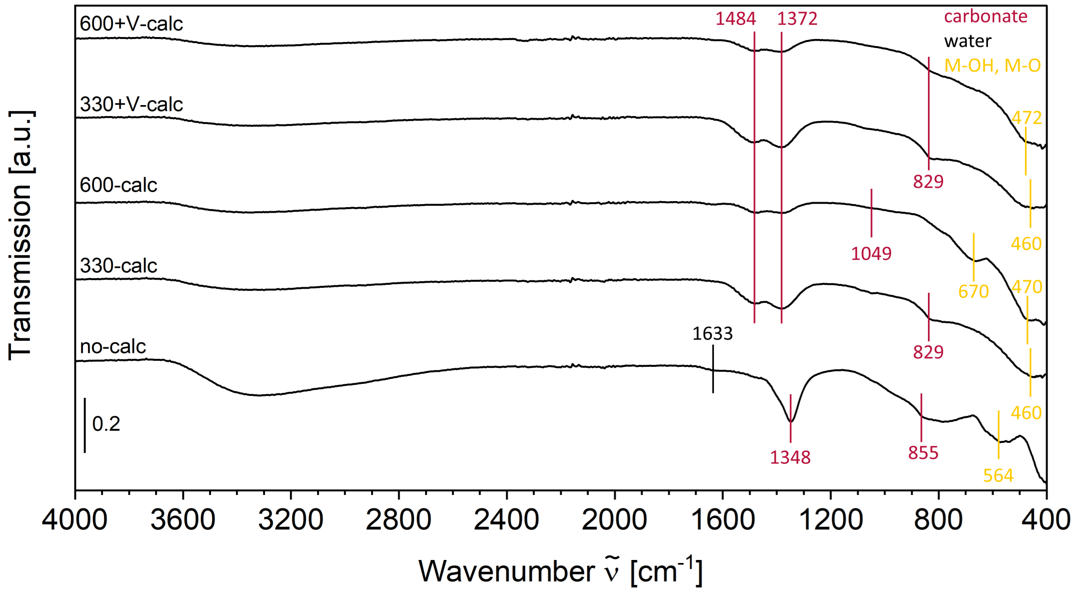

Figure 6.4.: Infrared spectra of the catalysts measured in transmission mode.

The metal composition and surface area of all catalysts are shown in Table 6.2. The mole fractions of Cu, Zn and Al of 330+V-calc are in good agreement with the precursor no-calc. 600+V-calc shows as a slightly higher Cu content at the expense of the Al content, though it is not as pronounced as in 600-calc. None of the vacuum-assisted calcined samples shows a pore liberation effect by the BET surface areas as found for 600-calc. The surface area of 330+V-calc is slightly lower and the one of 600+V-calc similar to the one of 330-calc. This can be ascribed to the HT-CO_3^{2-} still being present in these samples and blocking the pores for probe molecules like N_2.

Table 6.2.: Mole fractions of metals x(M) determined by ICP-OES and surface area S_{BET} of 125 - 250 µm sieve fractions.

sample	x(Cu) [mol %]	x(Zn) [mol %]	x(Al) [mol %]	S_{BET} [$m^2\,g^{-1}$]
no-calc	52.8	16.9	29.5	40.1
330-calc	52.4	16.8	30.0	41.1
600-calc	56.6	16.3	26.3	59.1
330+V-calc	52.9	16.5	29.9	35.8
600+V-calc	54.6	16.1	28.7	40.7
Target	50.0	16.7	33.3	-

The N_2-adsorption-desorption isotherms and pore size distributions can be found in Figure 6.5. The isotherm of 330+V-calc is a type IV(a) isotherm with a H3 hysteresis loop, similar to the one of 330-calc. A few more broader pores and less smaller ones are present in the vacuum-calcined sample. The isotherm of 600+V-calc is positioned between the ones of 330-calc and 600-calc. In the area of small p/p_0 refering to smaller mesopores, the isotherm resembles the one of 330-calc. This is a further indication of pore blocking by HT-CO_3^{2-} as less pores below 6 nm are probed than in 600-calc. For higher p/p_0, the isotherm lies above the one of 330-calc and the most abundant pores have a diameter of 18 nm. The measurements show that regarding the porosity, 600+V-calc is in a state between 330-calc and 600-calc, analogous to the carbon content.

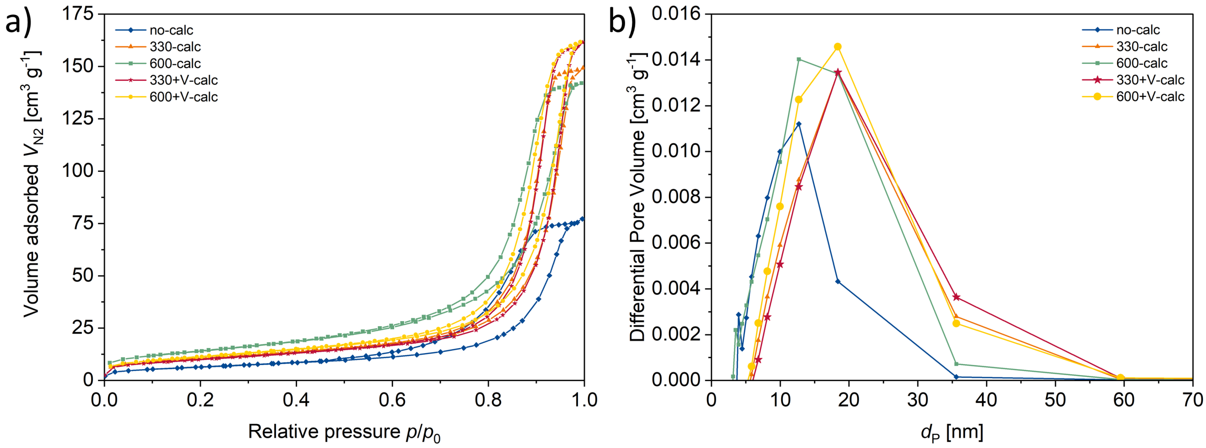

Figure 6.5.: a) N_2 adsorption-desorption isotherms of 125 to 250 µm sieve fractions used to determine the surface areas. b) Pore size distributions determined by the isotherms.

SEM images of reproductions of the two additional samples are shown in Figure 6.6. 330+V-calc consists of defined platelets as found for the hydrotalcite precursor. Contrarily, the platelets of 600+V-calc form agglomerates, similar to 600-calc. The analogue optical impression of both materials to their counterparts calcined at ambient pressure suggests that the hydrotalcite structure was preserved in 330+V-calc, while no more interlayers are present in 600+V-calc.

PXRDs of all samples were recorded in the reduced state before and after catalysis (see Figure 6.7). Before the catalytic tests, reflections for metallic Cu are present in all samples. 600+V-calc is the only catalyst that already displays the presence of the spinel in the as-prepared sample. On the other hand, 330+V-calc is the one catalyst that does not indicate the presence of the spinel in the spent sample. We could state that the calcination conditions for 600+V-calc were harsh enough to foster the mobility of the ions, so that spinel domains were formed that were big enough to be detected by XRD. On the other hand, we cannot explain the missing spinel phase in the spent sample of 330+V-calc. Moreover, we should be able to see the spinel in the as-prepared 600-calc sample as well, as it was calcined at the same temperature as 600+V-calc and the ion movability should be similar. Thus, we must consider a mix-up of the capillaries of as-prepared 600+V-calc and spent 330+V-calc either during the preparation or measurement.

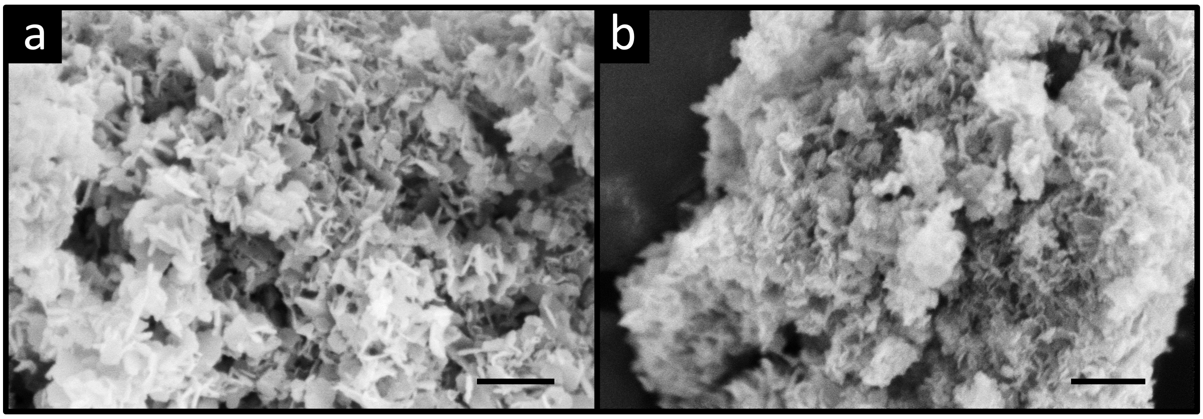

Figure 6.6.: Scanning electron microscopy images of a) 330+V-calc and b) 600+V-calc. Black bars indicate 500 nm.

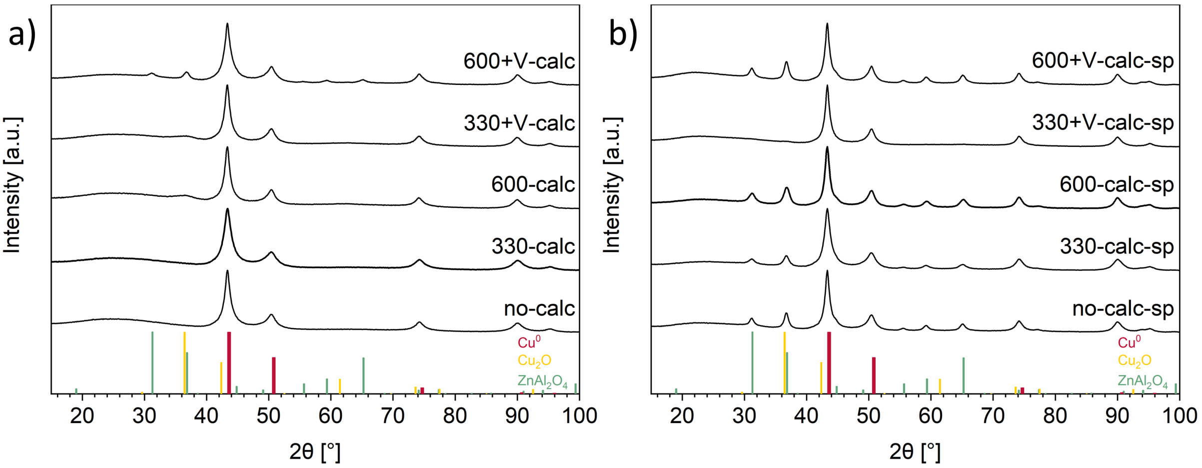

Figure 6.7.: PXRD of a) as-prepared and b) spent samples measured in capillaries after copper surface area measurements and re-reduction at 275 °C. Sieve fractions of 125 - 250 µm were used. References for $ZnAl_2O_4$ (green), Cu_2O (yellow) and Cu^0 (red) are shown as bars.

The reducibility of the samples of the vacuum-assisted calcination was tested in a H_2-TPR (see Figure 6.8). 330+V-calc has a peak maximum at 258 °C and a pronounced shoulder toward the lower temperature side. The peak shape and position resembles the one of 330-calc. As described previously, reduction of CuO occurs in a two-step process from Cu_2O to Cu^0. Because of the present HT-CO_3^{2-}, the reduction of Cu_2O is delayed and causes the shoulder in the signal. 600+V-calc has a peak maximum at 222 °C and a very weak shoulder toward lower temperatures. The maximum is 27 °C higher than that of 600-calc, but also about 30 °C lower than the maxima of the samples calcined at 330 °C. The calcination temperature of 600 °C was high enough to foster the mobility of the ions and to let small copper particles form from initially homogeneously mixed cations. Cu particles are easier to reduce than single Cu ions embedded in a ZnAl matrix, hence the peak maximum temperature is lower than for 330-calc. On the other hand, the HT-CO_3^{2-} is still included in the sample and it retards the reduction of Cu_2O, which is why the peak maximum is higher than for 600-calc. The inlet in Figure 6.8 shows a closeup of the signal in the temperature range of 275 to 675 °C. The signal shape and height of 330+V-calc resembles the one of 330-calc, though the position is shifted to higher temperatures, analogous to the main redcution peak. The signal of 600+V-calc has a lower intensity, but is still higher than that of 600-calc. The results suggest that the signal is caused by the HT-CO_3^{2-} as its intensity correlates with the C weight ratio in the samples. It is either generated directly by evolving CO_2, or by a real hydrogen consumption due to the hydrogenation of CO_2.[69]

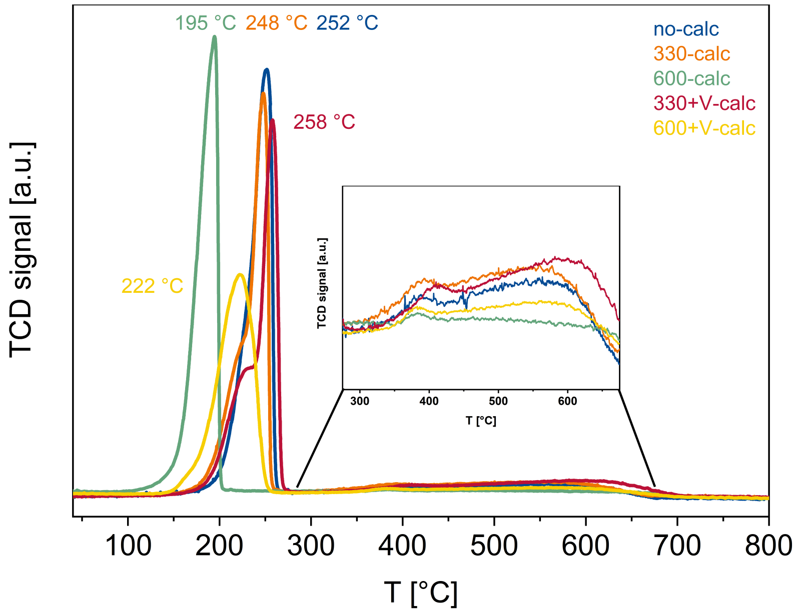

Figure 6.8.: Hydrogen temperature-programmed reduction profiles of 125 - 250 µm sieve fractions in 5 % H_2/Ar at 800 °C (β = 6 °C min^{-1}). The inset shows a zoom of the region from 275 to 675 °C.

The copper surface areas were determined by a sequence of different chemisorption techniques as described in Section 3. The as-prepared 330+V-calc exposes a Cu surface area of 4.4 m^2 g^{-1} in the Zn$^{\delta+}$-affected N$_2$*O*-RFC and 4.0 m^2 g^{-1} for the Zn$^{\delta+}$-corrected one. The difference of both gives a very small area for the Zn$^{\delta+}$ surface sites $S_{\mathrm{Zn}\delta+}$. Especially with regard to the method error of 1.6 m^2 g^{-1}, it can be argued that no Zn$^{\delta+}$ sites and thus no SMSI is present in this catalyst, similar to no-calc. 600+V-calc exposes a somewhat higher area of 8.1 and 5.8 m^2 g^{-1} for the Zn$^{\delta+}$-affected and -corrected N$_2$O-RFC, respectively. The value for the pure Cu sites $S_{\mathrm{Cu-only}}$ is similar to 600-calc, while the value for the combined Cu and Zn$^{\delta+}$ sites $S_{\mathrm{Cu\&Zn}\delta+}$ is lower. This shows that although the same amount of Cu sites could be generated in 600+V-calc, less Zn$^{\delta+}$ was formed. From the TG measurements in vacuum, we expected a similar area for both catalysts calcined at 600 °C. But as we already found that 600+V-calc still contains high-temperature carbonate, the insufficient calcination can be specified as the reason for the poor SMSI in this material.

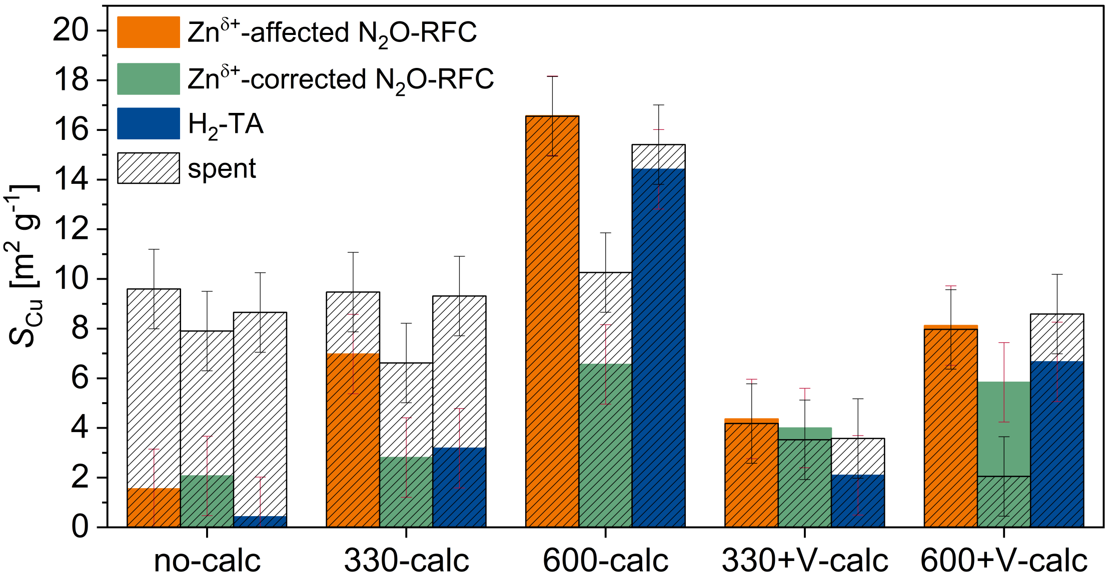

Figure 6.9.: Copper surface areas determined by N$_2$O refractive frontal chromatography of the reduced sample (orange) and of the passivated sample (green) and by H$_2$ transient adsorption (blue). Areas determined for the as-prepared samples are shown in plain colored bars. Areas of the samples after use in the catalytic experiments are shown in striped bars. The error of the method (1.6 m^2 g^{-1}) is represented by the error bars in red (as-prepared) and black (spent).

After catalysis, the spent samples approximately have the same Cu surface areas as the as-prepared ones, only $S_{\mathrm{Cu-only}}$ of 600+V-calc decreased significantly. Hence, no activation effect of the process conditions such as for no-calc and 330-calc can be found.

This is unexpected as previously, we ascribed the increase to a pore liberation effect due to the decomposition of HT-CO_3^{2-} during the catalytic tests. As both samples still contained HT-CO_3^{2-}, the copper surface areas should have increased. Further investigations need to be done to explain this circumstance, e.g. examining the microstructure of the materials in more detail to find differences caused by the calcnation in vacuum or at ambient pressure. The concentration-time profiles for the H_2-TAs and N_2O-RFC experiments are shown in Figure 6.14, Figure 6.15 and Figure 6.16 in the SI.

Catalytic Tests

All catalysts were tested in the CO_2 hydrogenation to methanol. 330+V-calc performs similar to its counterpart 330-calc calcined at ambient pressure at all applied process temperatures (see Figure 6.10). This was to be expected due to the characterization results that showed only little structural and compositional differences between those materials.

Contrarily, major differences were found between 600-calc and 600+V-calc. Nonetheless, the vacuum-calcined sample shows only slightly lower CO_2 conversions and methanol yields. This result is quite surprising as $S_{\mathrm{Cu\&Zn}\delta+}$ of this catalyst is much lower and no such pronounced SMSI is present. However, if only taking into account the areas obtained by the $Zn^{\delta+}$-corrected N_2O-RFC for all LDH-derived catalysts, the conversions correlate well with $S_{\mathrm{Cu-only}}$. This points out the importance of a full surface characterization for comparing and ranking catalysts (as enabled by our chemisorption sequence) rather than only comparing the Cu surface areas obtained from a single N_2O-RFC or even only considering BET surface areas. Analogous to the materials presented before, the vacuum-calcined catalysts were also reduced at 400 °C to foster the formation of a CuZn alloy. However, no substantial changes in conversion or yield were found (see Figure 6.17 in the SI).

The methanol production rate r represents the amount of methanol formed per mass of catalyst and is shown in Figure 6.11 a). 330-calc and 330+V-calc have similar rates in the whole investigated temperature range. However, while the overall rate is decreasing with decreasing temperature for both catalysts, the rate of 330+V-calc surpasses the rate of 330-calc at lower temperatures. The same trend can be found for 600-calc and 600+V-calc. Consequently, the vacuum-calcined samples have a slightly higher selectivity towards methanol at 205 °C than the catalysts prepared at ambient pressure.

The specific activities a_s give the amount of methanol formed per product site s, with s being either Cu and $Zn^{\delta+}$, Cu only or $Zn^{\delta+}$ only. Both vacuum-calcined samples have specific activities that are multiple times higher than that of the reference CZA.

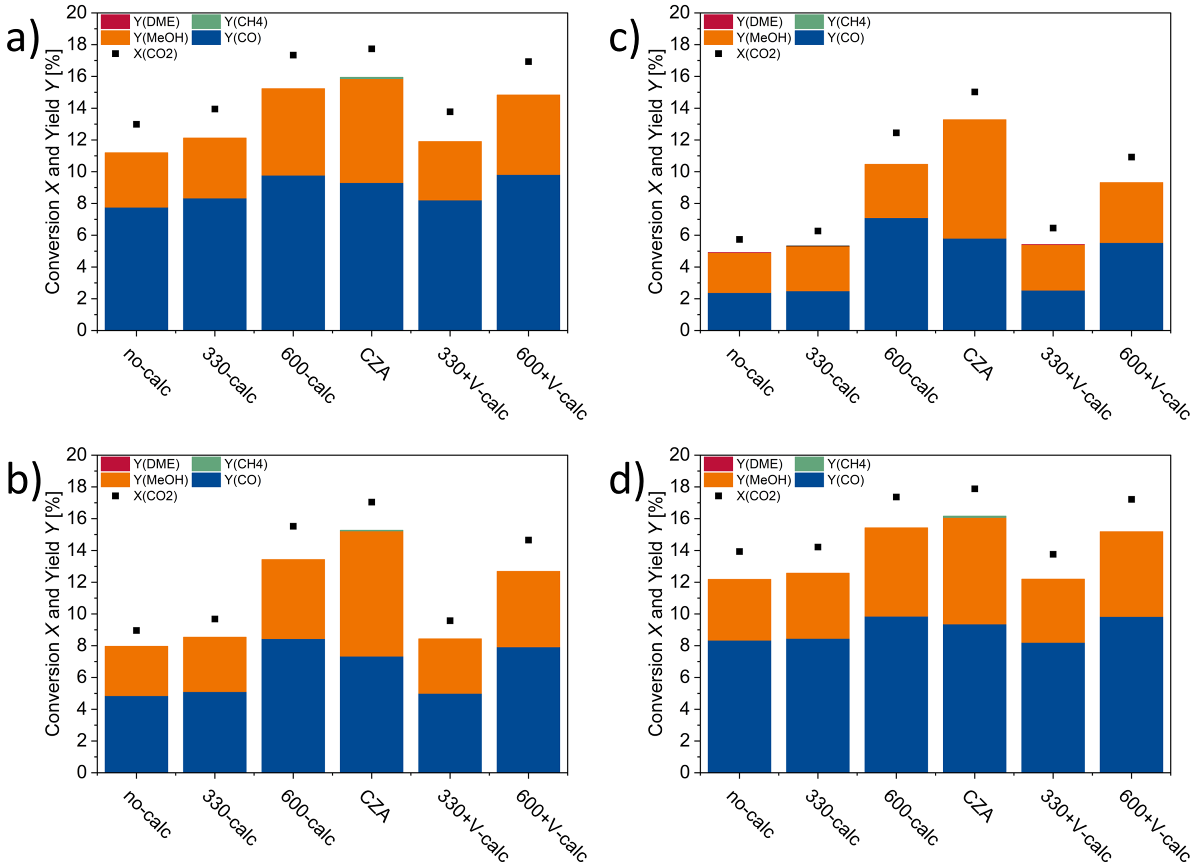

Figure 6.10.: CO_2 conversion X and product yields Y after reduction at 275 °C. Reaction performed at a) 235 °C, b) 220 °C, c) 205 °C and 235 °C (second run). Reaction conditions: H_2:CO_2:N_2 = 69:23.2:7.8, $\dot{V}_{\mathrm{norm}} = 5.92\,\mathrm{ml\,min^{-1}}$, $p = 20\,\mathrm{bar}$. DME = dimethyl ether, MeOH = methanol.

Because of the CuZn synergy, it is not possible to resolve the contributions of single Cu and $Zn^{\delta+}$ sites to the overall methanol production. Nonetheless, qualitative trends can be seen by comparing different catalysts. Hence, although the amount of $Zn^{\delta+}$ is low in both catalysts, these few sites seem to contribute a lot to the overall methanol production compared to the ones in CZA. Because of the low absolute value obtained for S_{Zn} in 330+V-calc, the error of a_{Zn} of this material is high and the results need to be interpreted with caution.

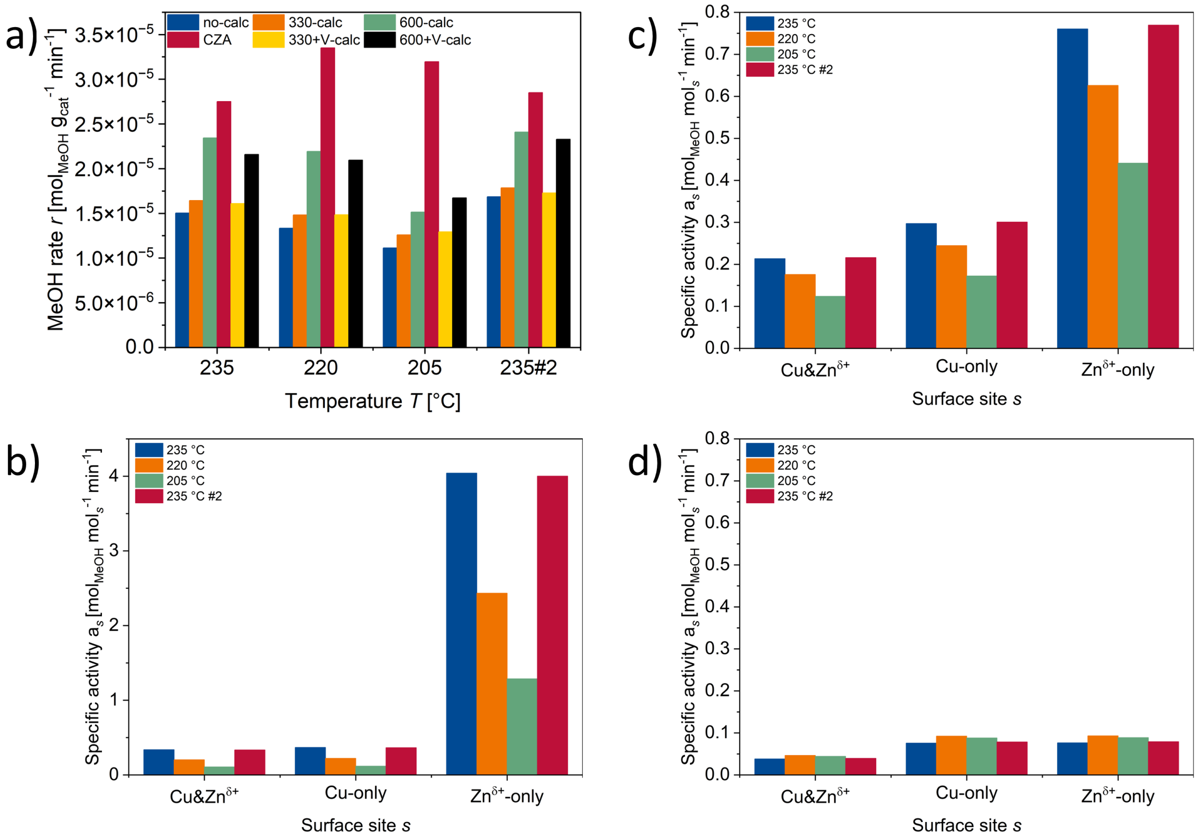

Figure 6.11.: Catalytic performance in the methanol synthesis reaction after reduction at 275 °C. a) Methanol formation rate r normalized by the mass of catalyst. Specific activity a normalized by the amount of combined Cu and $Zn^{\delta+}$ surface sites, Cu surface sites or $Zn^{\delta+}$ surface sites of b) 330+V-calc, c) 600+V-calc and d) CZA. Surface sites were calculated by the copper surface areas determined by N2O-RFC of the as-prepared samples. Reaction conditions: H_2:CO_2:N_2 = 69:23.2:7.8, $\dot{V}_{\mathrm{norm}} = 5.92\,\mathrm{ml\,min^{-1}}$, p = 20 bar, T = 205, 220 or 235 °C, respectively. The label #2 marks a second catalytic run at 275 °C.

6.1.3. Summary

In this work, we presented a synthesis route for a LDH-derived copper catalyst by a vacuum-assisted calcination. The aim was to synthesize a material that does not contain any high-temperature carbonate, but at the same time do not suffer from sintering effects due to high calcination temperatures. By thermogravimetric measurements and a temperature-resolved PXRD study in vacuum, we found a simple way to remove the HT-CO_3^{2-} from the hydrotalcite precursor. It decomposes at mild temperatures when applying a vacuum during calcination. However, reproducing these results in larger quantities in a tube furnace turned out to be challenging, as those samples still contained the HT-CO_3^{2-} and were not as crystalline as suggested by the PXRD study. Accordingly, we must state that the calcination conditions of the two vacuum-calcined samples are not clearly defined. That makes it hard to interpret the presented catalytic results.

The vacuum-calcined samples showed methanol formation rates similar to their counterparts calcined at ambient pressure, despite their different copper surface areas and carbon contents. These results again show that the copper surface area alone is not a sufficient measure for the activity of a catalyst and that various aspects have to be taken into consideration, such as the calcination conditions and phase composition.

6.1.4. Experimental

Unless stated otherwise, measurements were conducted analogously to Section 3.

Vacuum-assisted Calcination

The calcination in vacuum was conducted in a tube furnace equipped with a glass tube of 30 mm diameter. About 1.5 g of LDH precursor was placed in a combustion boat and put into the glass tube. One end of the tube was plugged and the other one was connected to a vacuum pump. The calcination was started after the vacuum of 1×10^{-3} mbar was held for 15 min. The temperature was risen with 5 °C min^{-1} and held for 2 h. The vacuum pump was constantly connected until the end of the cool down to room temperature.

Thermogravimetric Measurements at reduced Pressure

The measurement at 1×10^{-3} mbar was conducted on a Netzsch TG 209 F1 Libra. The measurement at 3 mbar were recorded on a Netsch STA 449 C Jupiter as described previously for the data recorded at ambient pressure.

Temperature-resolved X-ray powder diffraction

The temperature-resolved PXRD was measured in Bragg-Brentano geometry on a Panalytical Empyrean diffractometer equipped with Ni-filtered Cu-K_α radiation, a fixed divergence slit (0.5°), a PIXcel 1D detector and an Anton Paar XRK 900 heating chamber. The sample was measured in dynamic vacuum at a pressure of 2×10^{-2} mbar and the temperature was varied from 30 to 350 °C in increments of 10 °C, and further to 600 °C in steps of 25 °C. The collection time for each pattern was about 12 min.

6.1.5. Acknowledgment

We thank Sebastian Mangelsen for the temperature-resolved PXRD study and XRD measurements of reduced samples, Andrey Tarasov for TG-MS measurements at different pressures and Tobias Bochmann for SEM images.

6.1.6. Supporting Information

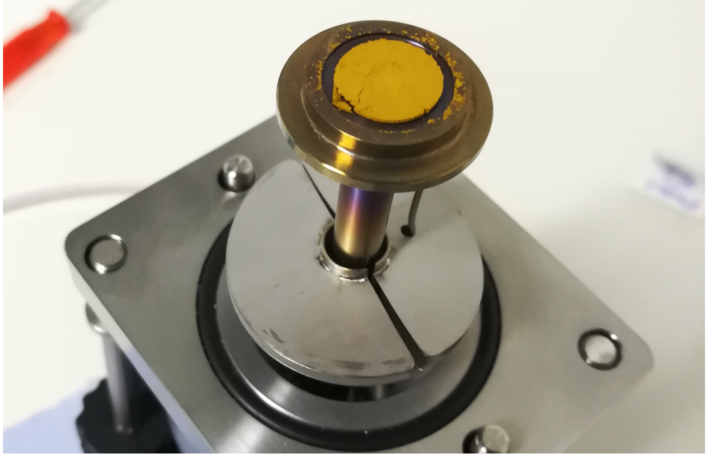

Figure 6.12.: Picture of the spent sample in the temperature-resolved PXRD study.

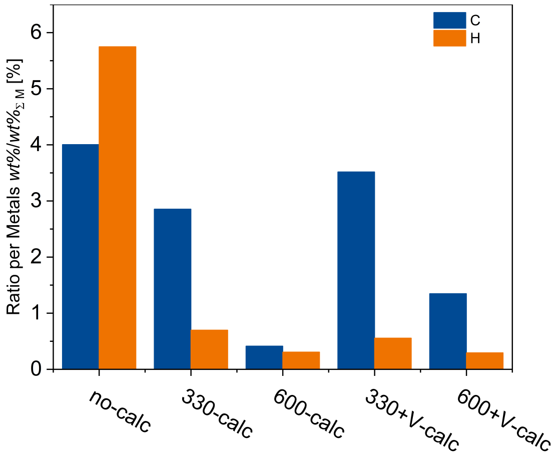

Figure 6.13.: Weight ratios of carbon and hydrogen normalized to the amount of metals Cu, Zn and Al in the as-prepared samples. The ratios were calculated by dividing the mass fractions of carbon and hydrogen determined by elemental analysis by the sum of mass fractions of the metals determined by AAS.

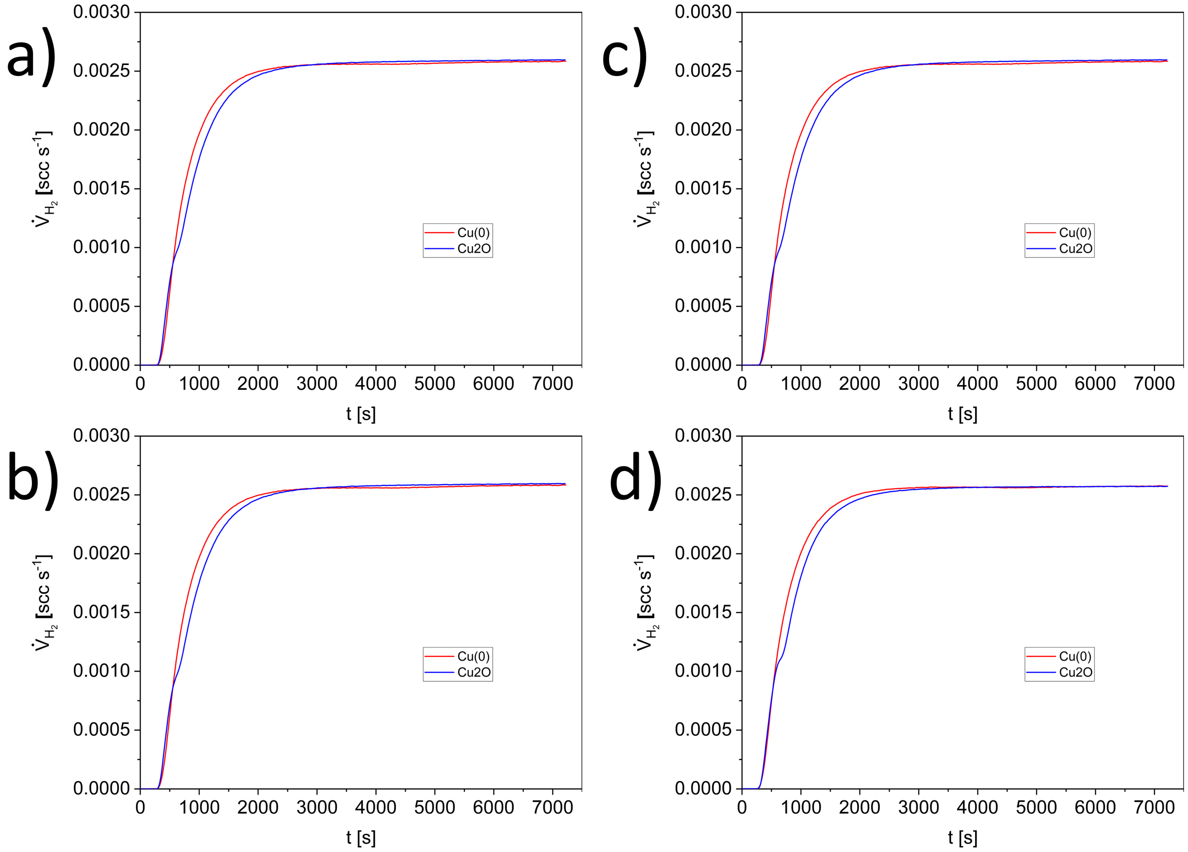

Figure 6.14.: Hydrogen transient adsorption of a-b) as-prepared and c-d) spent 330+V-calc and 600+V-calc.

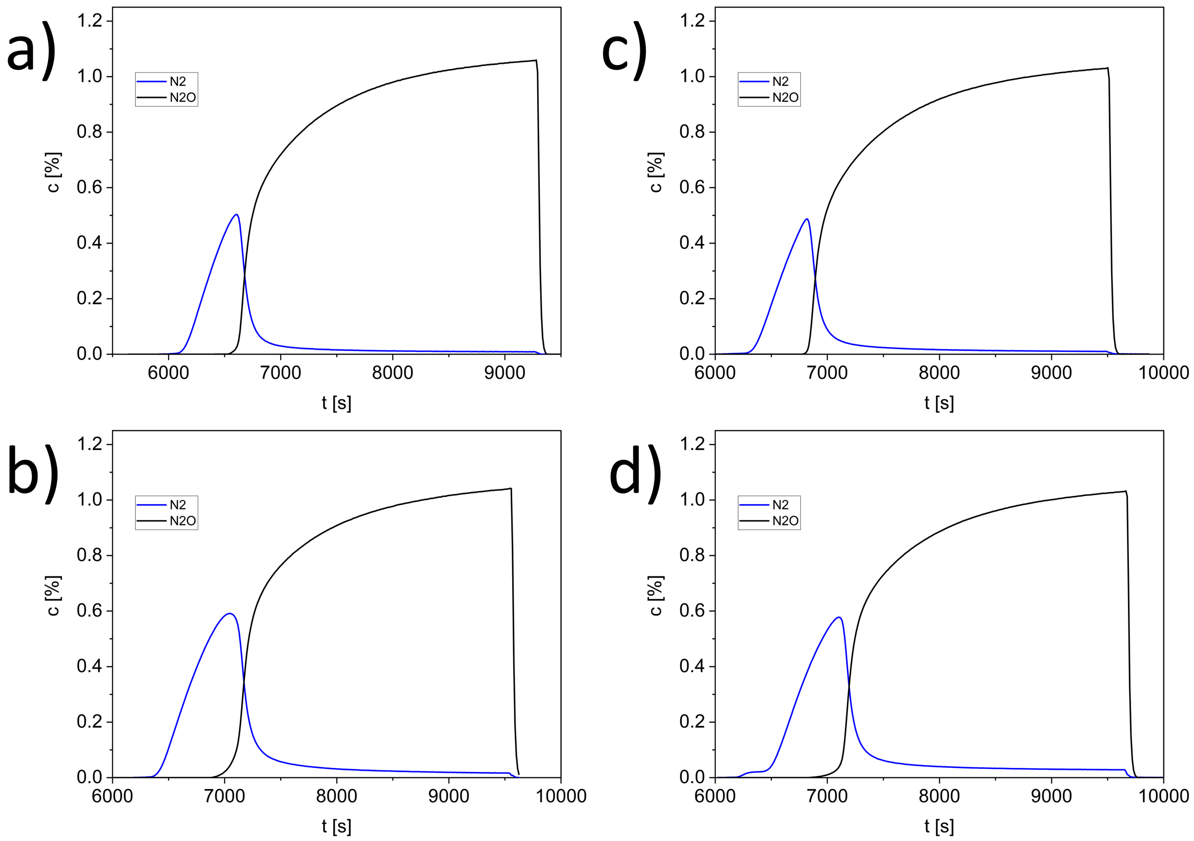

Figure 6.15.: First N_2O reactive frontal chromatography of reduced samples of a-b) as-prepared and c-d) spent 330+V-calc and 600+V-calc.

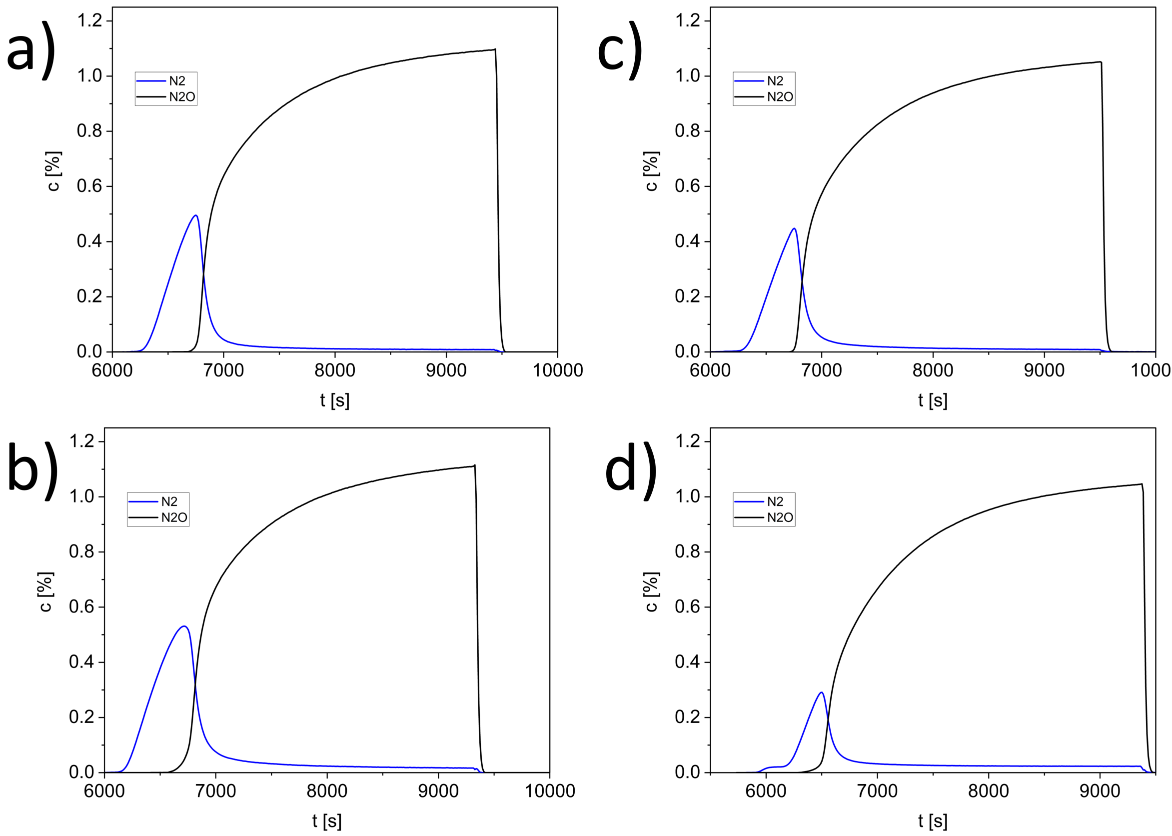

Figure 6.16.: Second N_2O reactive frontal chromatography of passivated samples of a-b) as-prepared and c-d) spent 330+V-calc and 600+V-calc.

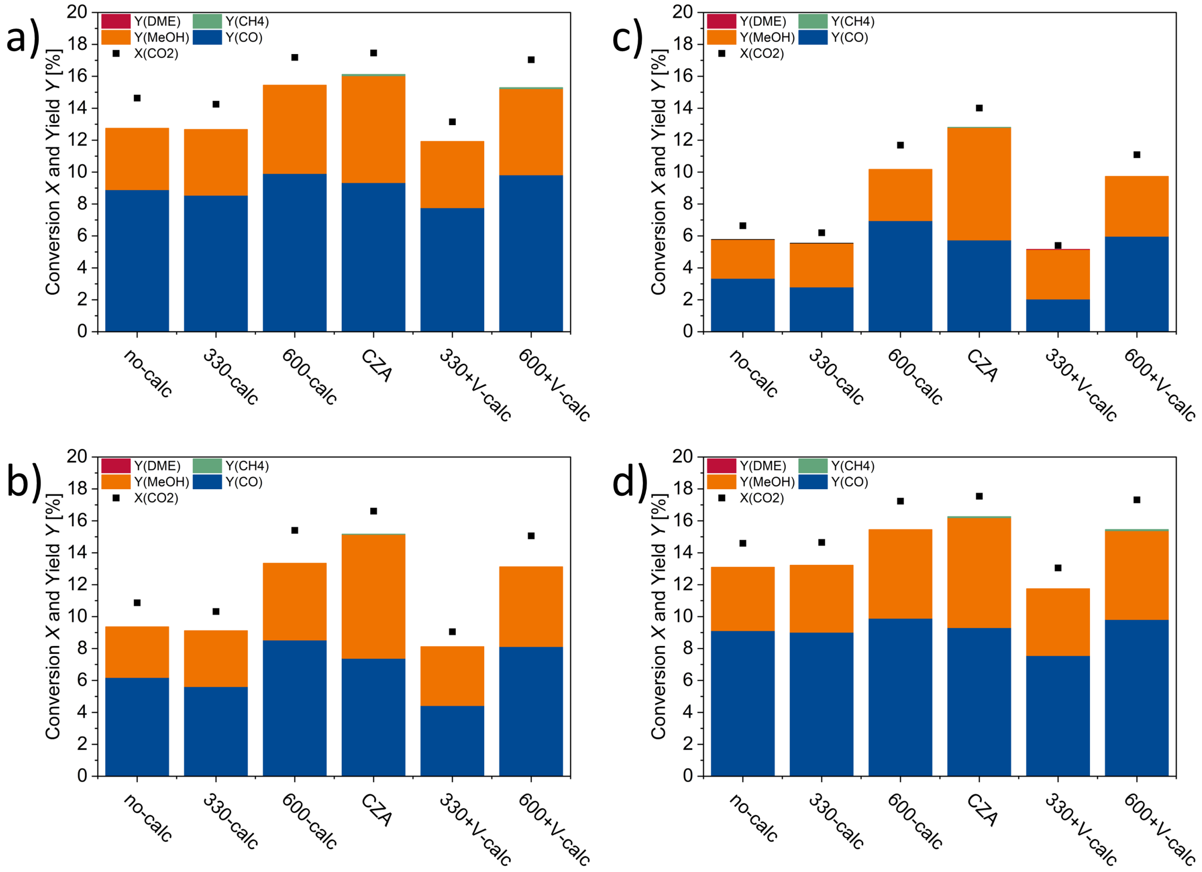

Figure 6.17.: CO_2 conversion X and product yields Y after reduction at 400 °C. Reaction performed at a) 235 °C, b) 220 °C, c) 205 °C and 235 °C (second run). Reaction conditions: H_2:CO_2:N_2 = 69:23.2:7.8, $\dot{V}_{\mathrm{norm}} = 5.92\,\mathrm{ml\,min^{-1}}$, $p = 20\,\mathrm{bar}$. DME = dimethyl ether, MeOH = methanol.

6.2. Preliminary Tests for the Liquid Phase Methanol Synthesis

In Section 4, the results of the alcohol-assisted methanol synthesis in the liquid phase over LDH-based catalysts were presented. In advance to those reactions, preliminary tests were conducted to become familiar with both the reaction itself and with the applied autoclave setup. A detailed description of the setup is given in Section 2. The prelimiary tests are collected in this extra section as some of them can only be discussed on a qualitative basis and for others, the results are not clearly interpretable. E.g., 10 % of the solvent EtOH was substituted by intermediates in some experiments. This can lead to an altered solubility of the syngas and products in the slurry mixture. The resulting product yields were located in the upper limit of the calibration and need to be interpreted with caution. Moreover, the GC calibration for product quantification was conducted in EtOH and therefore, it is only valid for this solvent. Nonetheless, few experiments were conducted in other solvents to investigate the influence of the solvent on the reaction.

In the following discussion, it will be referred to mechanistic steps 1 - 3 previously reported in literature:[106]

$$\mathrm{CO_2 + H_2 \rightleftharpoons HCOOH} \tag{6.1}$$

$$\mathrm{HCOOH + EtOH \rightleftharpoons HCOOEt + H_2O} \tag{6.2}$$

$$\mathrm{HCOOEt + 2\,H_2 \rightleftharpoons CH_3OH + EtOH} \tag{6.3}$$

6.2.1. Materials & Methods

Most preliminary tests were performed over a commercial methanol synthesis catalyst from Alfa Aesar (sieve fraction 250 - 355 µm). In some experiments, the influence of catalyst pretreatment was tested on a LDH-based material. This is the sample CZA-50 with a atomic ratio of Cu:Zn:Al = 50:17:33 presented earlier in Section 4. Due to the high required amount of catalyst for the different tests, multiple batches of this material were used. A comparison of different LDH batches with this composition was shown in the supporting information of Section 3 (therein called no-calc).

Unless stated otherwise, measurements were conducted analogously to Section 4. Two major differences need to be stressed. Firstly, no samples were taken at 0, 0.5 and 1 h in some experiments. Secondly, in most preliminary experiments, the catalyst was only dosed after heating up the reactor, together with the syngas. In later experiments, this was changed as considerable amounts of catalyst sticked on the upper reactor walls when dosing it in the hot reactor state. This was due to the solvent vapor that condensed on the walls or the vapor wetting the catalyst powder before it could enter the liquid phase.

6.2.2. Solvent Variation

We chose a series of primary and secondary alcohols to conduct the alcohol-assisted methanol synthesis at 220 °C (see Table 6.3). Interestingly, most methanol was produced in ethanol and with primary alcohols, more methanol was found than for secondary ones. This is a contradiction to the results of the Tsubaki group who showed that secondary alcohols are favorable over primary ones due to the balance of electronical and sterical effects.[112,115] Yet it fits the results of Likhittaphon *et al.* who found an increasing methanol yield with decreasing C-number of the alcohol. There is no simple explanation for the differing results, though the water within the used solvent might play a role. Depending on the authors and the type of syngas used (CO and CO_2 or CO_2 only), contradicting results are reported, ranging from an promoting effect[143] over no effect[111,115] to an inhibiting effect.[110] Moreover, the applied temperature of 220 °C is higher than for the experiments reported in literature.

Table 6.3.: Qualitative analysis of the solvent variation. Reactions were performed for 2 h at 220 °C and 50 bar of syngas (H_2:CO_2 = 3:1). No samples were taken during the reactions (except for ethanol). A commercial catalyst (1.00 g) was used and added together with the syngas after heating up (except for ethanol: addition before heating).

solvent	MeOH	FA ester	aldehyde or ketone	solvent ester or ether
ethanol	7.8 mmol	ethyl formate	acet aldehyde	ethyl acetate, ethyl ether
1-propanol	1.3 mmol	-	propanal	propyl propionate
2-propanol	0.3 mmol	-	-	-
1-butanol	2.1 mmol	butyl formate	-	butanoic acid butyl ester
2-butanol	0 mmol	-	2-butanone	di-sec-butyl ether

The table also lists further compounds found in the liquid samples. The formic acid (FA) ester is an intermediate formed in the second step of the alcohol-assisted mechanism. Its presence supports the correctness of the proposed three-step mechanism. The FA ester is only found for ethanol and 1-butanol. However, it has to be noted that the library of the GC-MS was not complete and therefore, the presence of not every respective compound could be validated. The presence of aldehydes or ketones reveals

the dehydrogenation of the alcoholic solvents as a side reaction and it occurred irrespectively of the carbon number. These products can then further react with a second molecule of solvent to the corresponding di-solvent ester. Moreover, a dehydration to the corresponding di-ether can also occur, as shown in the column of the table.
In further experiments, a lower temperature of 160 °C was found to be advantageous in terms of methanol yield and side product avoidance (see Figure 4.9 in Section 4). Both polar and unpolar non-alcoholic solvents were also applied in the reaction at this lowered temperature (see Figure 6.18).

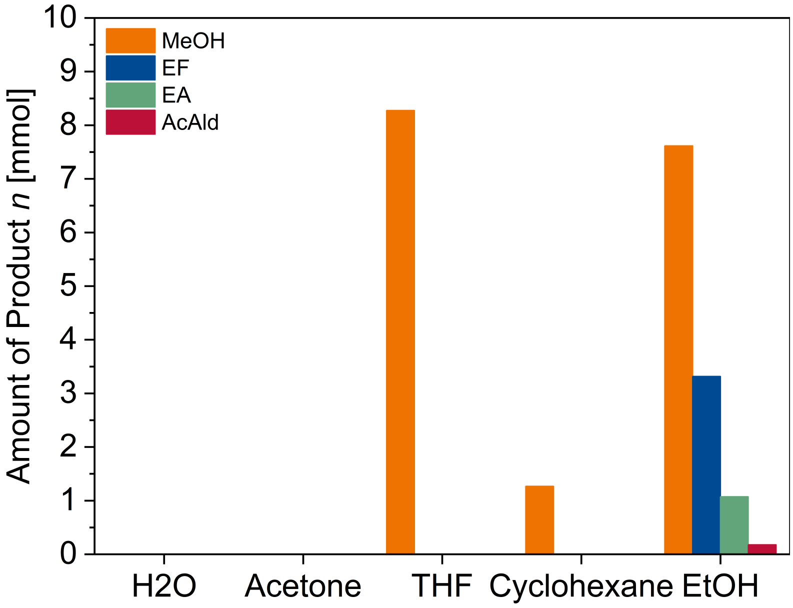

Figure 6.18.: Solvent variation in the methanol synthesis reaction. All reactions were performed for 2 h at 160 °C and 50 bar of syngas (H_2:CO_2 = 3:1) in 150 ml of solvent. Samples were also taken after 0, 0.5 and 1 h. A commercial catalyst (1.00 g) was used and added together with the syngas after heating up (except for ethanol: addition before heating).

In the strongly polar solvents water and acetone, no liquid products could be found. However, considerable amounts of methanol were produced in THF and cyclohexane. These results are unexpected as the promoting effect by an ester formation as an intermediate should only be possible by an alcohol. Yet is has to be noted that in all these solvent variation reactions, remnants of ethanol were found in the samples, although the reactor was previously washed with the corresponding solvent. Hence, it is likely that those remnants were catalytically active. Although this mixing of solvents was not intended, it might show a way to improve the process. Neither in THF nor in cyclohexane byproducts of the ethanol dehydrogenation (AcAld or EA) were found. Moreover, the methanol yield in THF even surpasses the one in ethanol. As the alcohol only serves as a co-catalyst, it does not need to constitute the whole liquid phase and can be adjusted to the amount of solid catalyst or active sites, respectively. The results in THF and cyclohexane indicate that by reducing the overall amount, side reactions of the alcohol can be avoided or diminished. Moreover, by fine-tuning the ratio of alcohol to non-alcoholic solvent, even higher methanol yields could be reached. Additionally, a product separation could be facilitated in case of unpolar solvents like cyclohexane, as methanol is not soluble in it.

6.2.3. Mechanistic Investigations

To further promote the proposed three-step reaction mechanism, 15 ml of ethanol were substituted by formic acid, giving a solution of 10 % FA in ethanol. The 10 % were chosen instead of a full solvent substitution in order to not change the reaction system too drastically, e.g. due to a varying solubility of the syngas in the liquid. As FA is the intermediate formed in the first mechanism step, increased yields of EF and methanol should be obtained. In Figure 6.19, the results of three reactions with additional FA are shown. The first one was conducted with syngas and with a commercial catalyst, the second one without syngas but with catalyst, and the third one with syngas but without catalyst. In the first reaction, large amounts of EF were formed, supporting that it is indeed formed from FA and ethanol according to the second mechanistic step. However, it has to be noted that the level of EF was already formed at $t = 0\,h$ and did not change throughout the reaction. Firstly, this shows that the second step of the mechanism proceeds easily and is not rate-determining. Secondly, the catalyst was only added at $t = 0\,h$, meaning that EF even formed without a solid catalyst being present. This is further validated by the third reaction, in which no catalyst was used but still large quantities of EF were found. The esterification is an acid-catalyst reaction and hence, the abundant FA catalyzed its own reaction with ethanol.

The results are in contradiction with the conclusions made by the Tsubaki group as they claimed the ester formation (from different alcoholic solvents) to be rate-determining.[108,111] The group justified this by the low concentration of ester detected in the reactions. The absence of FA was explained by surface formate species being formed instead of the free acid. However, the present results show that FA is easily converted to EF. Hence, it can be concluded that the EF concentration is low due to a small amount of FA being present and that the FA formation is rate-determining rather than the EF formation. The difference between the first and third reaction, meaning a reaction with or without a catalyst, is that methanol was only formed in the presence of a solid catalyst. This shows that for the final step, the Cu catalyst has to be present to enable the hydrogenolysis of EF.

Interestingly, methanol was also formed in the second reaction in which no syngas was added. However, hydrogen is required for the third mechanistic step to form methanol from EF. In a further reaction with pure FA as a solvent and without any catalyst, we could observe a rapid pressure increase of 10 bar within 15 min. Moreover, it is known that FA is quite unstable and decomposes by one of the following reactions:[147,148]

$$HCOOH \rightleftharpoons CO_2 + H_2 \tag{6.4}$$

$$HCOOH \rightleftharpoons CO + H_2O \tag{6.5}$$

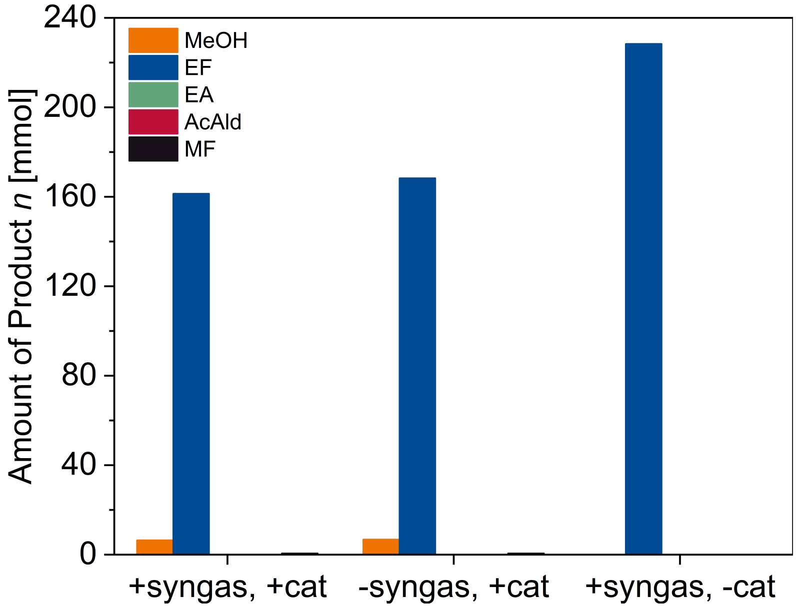

Figure 6.19.: Catalytic results of reactions performed in 10 % formic acid (FA) in ethanol. The standard reaction was performed for 2 h at 160 °C and 50 bar of syngas (H_2:CO_2 = 3:1) in 150 ml of solvent. Samples were also taken after 0, 0.5 and 1 h. A commercial catalyst (1.00 g) was used and added together with the syngas after heating up. Residual amounts of FA are not shown. The reaction without syngas was conducted in 5 bar Ar.

Hence, the observed pressure increase is caused by a gas formation from the FA decomposition and the required H_2 is formed by it. Minor amounts of methyl formate (MF) were also detected and they stem from a transesterification of EF with the formed methanol. It is striking that no AcAld or EA was formed in this reaction, different to the reaction in pure ethanol (see "EtOH" in Figure 6.18). AcAld formation occurs on (de-)hydrogenating Cu sites of the solid catalyst and can react further to EA by different routes. Although no catalyst is needed by FA to react to EF, the presence of FA somehow seems to influence the catalyst and inhibits the side product formation. The formic acid adsorbs on the Cu surface in a dissociated form as formate $HCOO_{ads}$ and hydrogen H_{ads} to form EF. Due to the high amount of FA in this reactions, it is possible that the Cu sites were blocked by formate and hence no ethanol could adsorb on the Cu sites.

In a further set of reactions, 15 ml of ethanol were substituted by EF and the results are shown in Figure 6.20. The amount of produced methanol is almost ten times as high compared to a reaction conducted in pure ethanol (see "EtOH" in Figure 6.18). This clearly supports the idea of methanol being formed by a hydrogenolysis of EF according to the third reaction step.

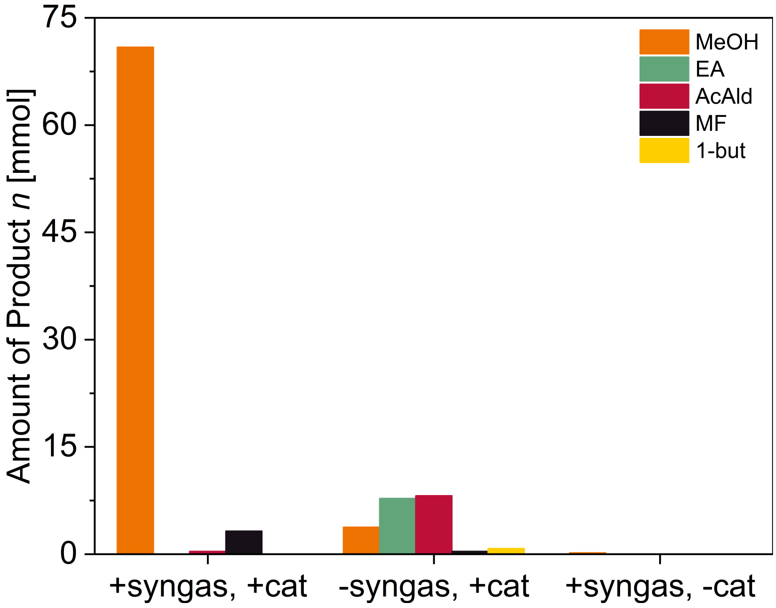

Figure 6.20.: Catalytic results of reactions performed in 10 % ethyl formate (EF) in ethanol. The standard reaction was performed for 2 h at 160 °C and 50 bar of syngas (H_2:CO_2 = 3:1) in 150 ml of solvent. Samples were also taken after 0, 0.5 and 1 h. A commercial catalyst (1.00 g) was used and added together with the syngas after heating up. Residual amounts of EF are not shown. The reaction without syngas was conducted in 5 bar Ar.

Due to the high amount of methanol and EF in the reaction mixture, a transesterification becomes more likely and hence, considerable amounts of MF were formed. Again, no EA and only minor amounts of AcAld were formed, different to the reaction in pure ethanol. As the EF hydrogenolysis and ethanol dehydrogenation share the same Cu sites, the latter one seems to be restrained by the former one. Compared to that, the yield of dehydrogenation products is high in the reaction without syngas. As no hydrogen was added in this reaction, EF cannot easily react further to methanol and ethanol dehydrogenation becomes dominant. Yet there was a small amount of methanol formed. Similar to the reactions with additional FA, the backward reactions must have occured from EF over FA to CO_2 and H_2. Finally, basically no reaction occurred without a catalyst being present. This is in line to the reactions with additional FA, as the Cu sites are needed to conduct the hydrogenolysis of EF in the last reaction step.

The three reactions with or without syngas and catalyst were also performed in pure EF (see Figure 6.21). In the reaction with both syngas and catalyst, about 20 mmol of methanol were formed, which is less than the 71 mmol formed in the experiment with 10 % EF in ethanol. However, MF was the main product, originating from the acid-catalyzed transesterification with methanol. Because of that, the MF yield has to be added to the methanol yield as each molecule of MF was produced from one molecule of methanol formed beforehand. This gives a methanol yield that is about twice as high as in the experiment with diluted EF.

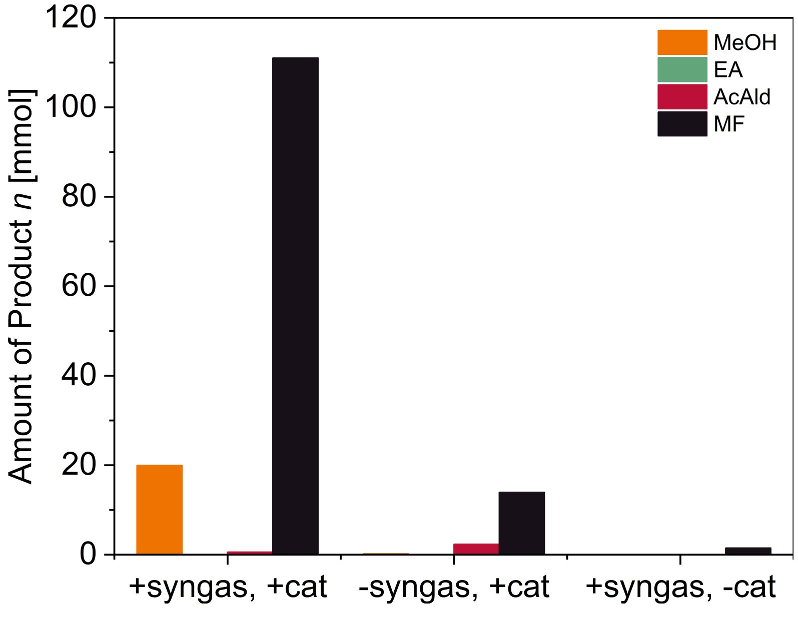

Figure 6.21.: Catalytic results of reactions performed in pure ethyl formate (EF). The standard reaction was performed for 2 h at 160 °C and 50 bar of syngas (H_2:CO_2 = 3:1) in 150 ml of solvent. Samples were also taken after 0, 0.5 and 1 h. A commercial catalyst (1.00 g) was used and added together with the syngas after heating up. Residual amounts of EF are not shown. The reaction without syngas was conducted in 5 bar Ar.

Although the yield has doubled, a somewhat higher yield was expected in the presence of 150 ml substrate. The solubility of hydrogen in EF is higher than in ethanol, making a substrate limitation unlikely as a reason.[149] Another explanation is a limitation of this reaction by the kinetics at the applied temperature. In the reaction without syngas, basically no free methanol could be found but only some MF. Again, without hydrogen being present, no methanol should have formed at all. Hence, the backward reaction to FA and further to H_2 and CO_2 also took place in this test. Finally, without a catalyst being present, essentially no reaction occurred. The trace amounts of MF are rather seen as an artifact or contamination than a reaction product.

6.2.4. Further Investigations

As described above, contradicting results regarding the role of water were reported in literature. Hence, we applied two different kinds of water scavengers to test its influence on the catalytic performance. The first one was the chemical water scavenger tetraethyl orthosilicate ($Si(OEt)_4$, TEOS). In the presence of water, it reacts to SiO_2 and four molecules of ethanol. Thus, the water is trapped in a chemically bound state. In the test, 15 ml of ethanol were substituted by TEOS. The results are shown in Figure 6.22 and compared to a reaction without a scavenger ("none (comm.)"). TEOS showed to be disadvantageous for the reaction as the methanol yield dropped to less than one fourth of the reaction without a scavenger.

As it cannot be concluded whether this is caused by the water withdrawal or by an unwanted interaction of TEOS with the commercial catalyst, a physical water scavenger was applied in a second reaction. Herein, a molecular sieve with a pore size of 3 Å and particle size of 250 to 355 mm was dried in static for 3 h at 330 °C and transferred into a glovebox. 1.00 g of it was added to 1.00 g of LDH-based catalyst (CZA-50) and simultaneously dosed into the reactor. The evolving water was supposed to adsorb on the surface and inside the pores of the molecular sieve and hence, it is withdrawn from the reaction mixture by physically binding it. But also in this reaction, the addition of a water scavenger turned out to be disadvantageous. Nieminen *et al.* could improve the methanol yield by adding a molecular sieve to the reaction mixture.[110] Different to the present case, they used a molecular sieve with 4 Å pore size and 150 - 500 Å particle size. However, these differences should not turn the scavenger addition from advantageous to disadvantageous. The reasons for the differing results remain unclear.

In a further set of experiments, the influence of the catalyst pretreatment was examined (see Figure 6.23). As the commercial catalyst is only available in a calcined form, the LDH-based CZA-50 presented in the previous sections was used instead. In the standard procedure, the LDH precursor is first calcined in static air and then reduced in diluted hydrogen before transferring it to the reactor inertly. The calcination was varied by either conducting it in flowing Ar or omitting it completely. Additionally, an uncalcined and unreduced material was also applied for the reaction.

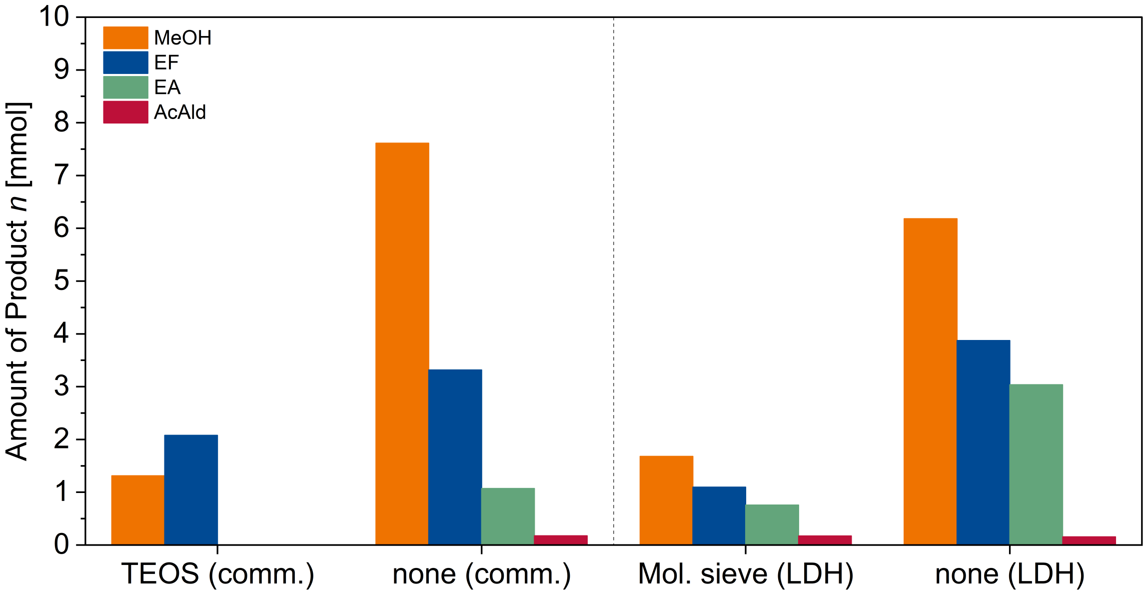

Figure 6.22.: Catalytic results of reactions performed in ethanol. The standard reaction was performed for 2 h at 160 °C and 50 bar of syngas (H_2:CO_2 = 3:1) in 150 ml of solvent. In case of the reaction with TEOS, 15 ml of ethanol were substituted by TEOS. In case of the molecular sieve, 1.00 g of dried sieve (sieve fraction 250 - 355 bar) was added to the catalyst. Samples were also taken after 0, 0.5 and 1 h. 1.00 g of catalyst was used and added before heating up, except for the reaction with TEOS. (comm.) = commercial catalyst and (LDH) = LDH-based catalyst.

Both by omitting the calcination step and by conducting it in Ar, the EA side product formation could be lowered. EA is assumed to form over alumina by the Tishchenko reaction or by an hemiacetal intermediate after a previous AcAld formation. During the calcination in air, the LDH precursor is in contact with oxygen at an elevated temperature. By the Ar atmosphere, the oxygen is absent and by omitting the calcination, no reaction with oxygen will occur either. The materials were not further examined, though it can be assumed that by this circumstance, the Al-O bond on the surface is not as strong as in the air-calcined material, e.g. because of OH^- groups being present instead of O^{2-}. However, the methanol yield over those two catalysts is also lower compared to the air-calcined material, making them less active in general. This shows that the calcination not only has an effect on the alumina, but on the whole catalyst. Small amounts of methanol were also formed by an uncalcined and unreducing catalyst, meaning an as-prepared LDH precursor. Especially the third step of the mechanism, which is the EF hydrogenolysis to methanol and ethanol, was revealed by the above results to only occur in the presence of a reduced Cu catalyst. In H_2-TPR experiments, the onset temperature for Cu reduction in most of the presented LDH-based materials was found to be 170 °C (see Figure 4.5 in Section 4). Nonetheless, few Cu sites seemed to have been reduced by the syngas at a lower temperature of 160 °C within this experiment, allowing for the formation of MeOH. The results show that although methanol synthesis is generally also possible by employing the as-prepared LDH, the catalytic performance can be clearly improved by a calcination and reduction step.

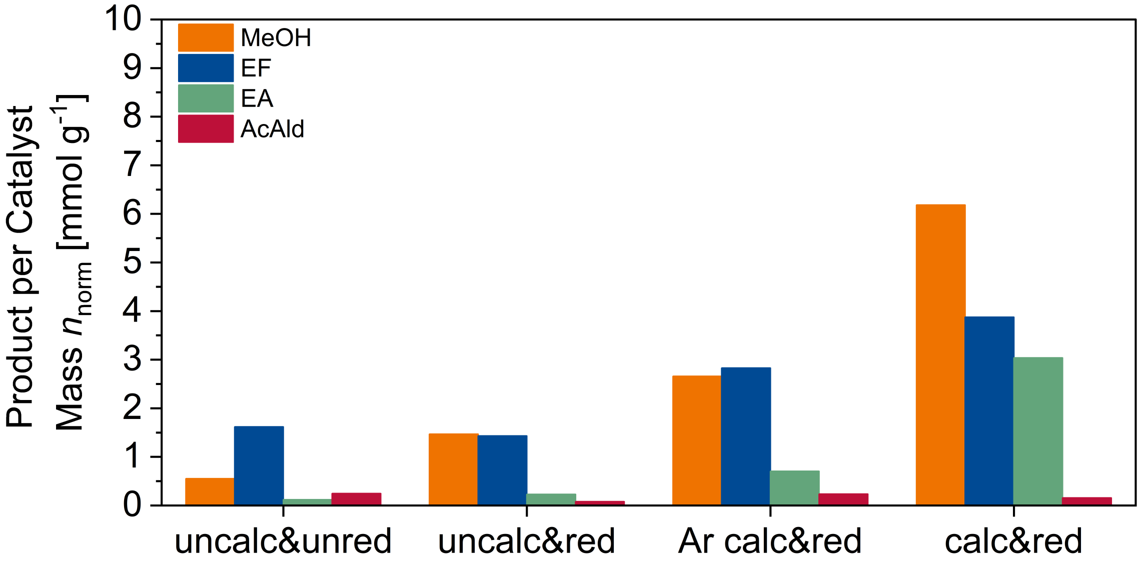

Figure 6.23.: Catalytic results of reactions performed in ethanol. All reactions were performed for 2 h at 160 °C and 50 bar of syngas (H_2:CO_2 = 3:1) in 150 ml of solvent. Samples were also taken after 0, 0.5 and 1 h. The LDH-based catalyst was added before heating up. (un-)calc = (not) calcined, (un-)red = (not) reduced, Ar calc = calcined in flowing Ar.

6.2.5. Summary

By the preliminary tests for the alcohol-assisted methanol synthesis, many indications were found that support the three-step reaction mechanism. By varying the alcohol chain length from C2 to C4, the formic acid ester intermediate could be detected and the highest methanol yield was found in ethanol. But also side products that originate from a dehydrogenation of the alcoholic solvent were detectable. The use of only small amounts of alcohol as a co-catalyst diluted in a less polar or unpolar solvent turned out to be a possible solution to avoid those side products. When adding the intermediate FA to the reaction mixture, a rapid EF formation could be observed, even in the absence of a solid catalyst. In contrast to that, EF could only be further converted to methanol in the presence of a catalyst. By increased concentrations of EF and methanol, a transesterification to methyl formate was facilitated. Overall, the present results suggest that the first mechanistic step, meaning the formation of FA from syngas, is rate-determining. The esterification can be easily conducted and the final hydrogenolysis requires the presence of a catalyst.

6.3. Comparison of Sieved and Unsieved Catalysts

The catalysts presented in Section 4 were used unsieved, while the ones used in Section 3 and Section 5 were pressed and sieved beforehand. For that, a pellet of 1 µm diameter was formed by applying a force of 5 t for 2 min. Subsequently, the pellet was mortared and sieved to the desired grain size (125 to 250 µm or 250 to 355 cm, respectively). To study the influence of pressing and sieving, the experiments shown in Figure 4.11 in Section 4 were repeated with pressed and sieved catalysts with a grain size of 250 to 355 cm. The results are compared in Figure 6.24 a (unsieved) and b (pressed and sieved). The yields of MeOH and EF are lower for most pressed and sieved catalysts. Merely the EF yields of CA-67, CZG-50 and CZA-50-600 as well as the MeOH yield of CG-67 and CZA-50-600 increased compared to the unsieved form. The catalysts used in this study are all derived from the LDH structure. Their pore volume is mainly formed by the space between the agglomerated layers. The results indicate that the layers were pressed together. Thereby, the interlayer space and accessible surface area has decreased. An evidence for this is the comparison of the surface areas of the three catalysts presented in Section 3 before and after pressing and sieving (see Table 6.4). The surface areas of all materials decreased by pressing. The effect is least severe for 600-calc, which is the same material as LDH-600-calc, synthesized in a different batch. It has to be noted though that measurements were conducted on different machines for the set of sieved and unsieved materials. However, the reason for the positive catalytic effect of pressing and sieving in LDH-50-600 is not clear. In the previous sections is was found that this material consists of large Cu^0 and spinel domains and contains only few HT-CO_3^{2-}. The pressing could have led to even larger domains that are no longer separated by the interlayer space. In Section 5 it was concluded that at least for the alcohol-assisted liquid-phase reaction, larger domains are advantageous for the MeOH yield.

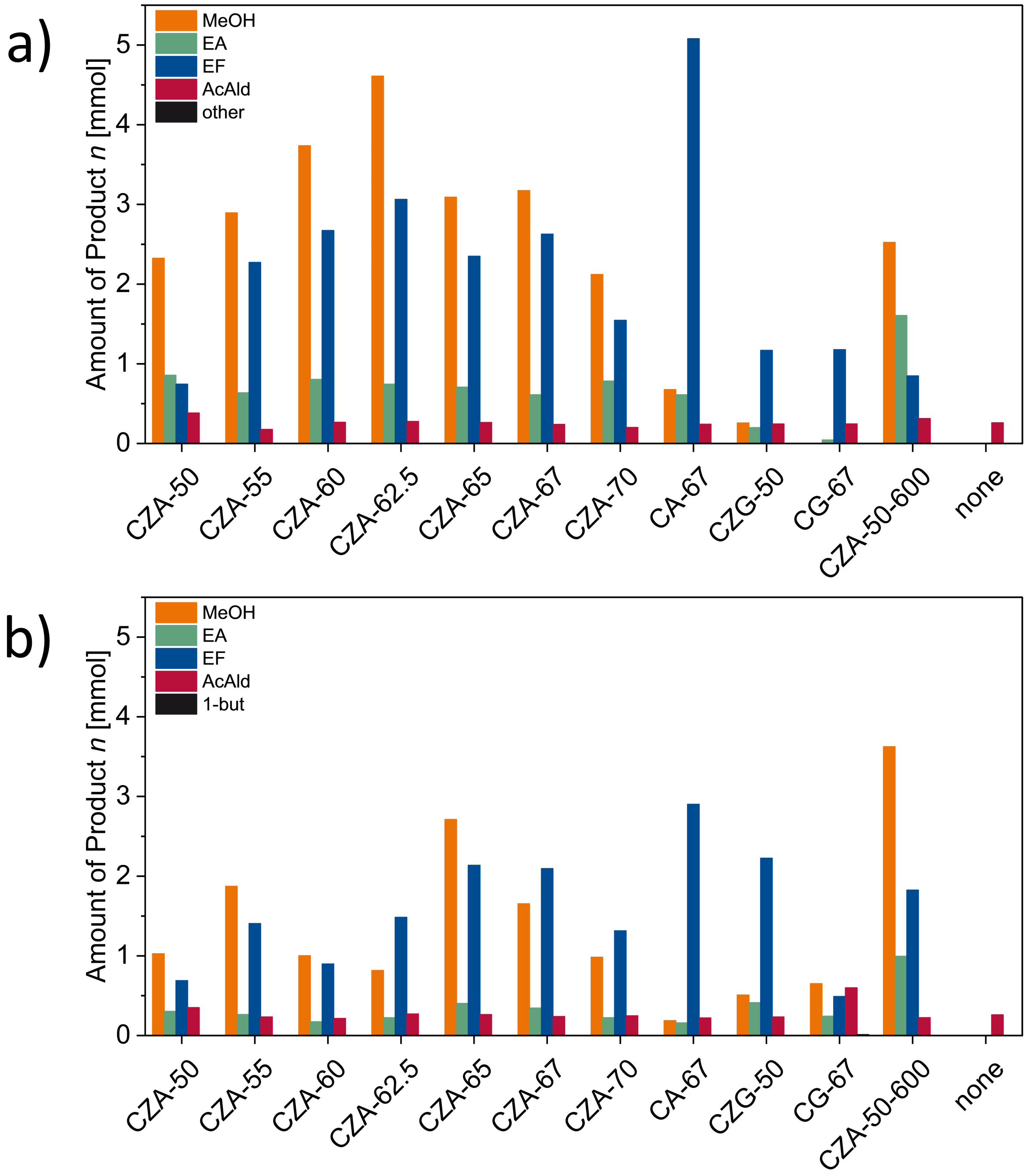

Figure 6.24.: Amount of products after 2 h of reaction time over various LDH-derived catalysts at 160 °C. a) Unsieved catalysts and b) pressed and sieved catalysts with 250 to 355 microm particle size. MeOH = methanol, EF = ethyl formate, EA = ethyl acetate, 1-but = 1-butanol. Reaction conditions: p = 50 bar, H_2:CO_2 = 3:1, rpm = 1000 min^{-1}, m_{cat} = 0.50 g. Yield of other products are too small to be seen by eye.

Table 6.4.: Surface area S_{BET} of materials before and after pressing and sieving.

sample	S_{BET} pressed and sieved [$\mathrm{m^2\,g^{-1}}$]	S_{BET} unsieved [$\mathrm{m^2\,g^{-1}}$]
no-calc	40.1	51.9
330-calc	41.1	61.4
600-calc	59.1	68.4

Regarding the side products, there is a clear trend of an decreased yield of EA upon pressing and sieving. Contrarily, the yield of AcAld remained almost unchanged. As suspected earlier, small amounts of AcAld seem to form without the contribution of a catalyst. It was also formed in the blank test without a catalyst in a comparable amount. Either, there is a catalytically active species present in the autoclave in the form of catalyst residues from previous experiments or the autoclave vessel itself is somehow active. Or the AcAld formation can proceed without a catalyst, just by thermal activation. To answer this question, a vessel of another material would be needed or an inert teflon inlet.

In summary, it was shown that pressing and sieving has a great impact on the catalytic activity. Although the MeOH yield for few catalysts could be increased, a general negative trend was found. This is reasoned by the decreased surface area that results from diminishing the interlayer space of the LDH-based materials.

7. Conclusion and Outlook

In this thesis, the MeOH synthesis from CO_2 over Cu-based catalysts was studied in the gas- and liquid-phase process with an emphasis on LDH-derived materials. The three main sections 3, 4 and 5 had their individual summary and in Section 6, additional research to the previous sections was described. The following conclusion will connect the key findings to form an overall picture.

In Section 3, the catalyst class of LDHs was introduced and applied in the gas-phase MeOH synthesis. The LDH structure allowed for a distribution of the metals on the atomic scale. Upon reduction, the Cu cations needed to break O^{2-} and CO_3^{2-} bridges to the Zn,Al matrix to be mobile and form Cu^0 domains by solid diffusion. As bond breaking and diffusion requires a certain amount of energy, the peak maximum temperature found by H_2-TPR was higher compared to a malachite-derived benchmark catalyst. Calcining the material at 330 °C only had a minor effect and the homogeneous distribution of metals was maintained. At 600 °C however, domains of CuO and a $ZnAl_2O_4$ spinel were detected by XRD and the reduction temperature decreased by 50 °C. The calcination greatly diminished the amount of HT-CO_3^{2-}. Together with the higher thermal energy input, this enabled a preformation of CuO domains that were more easily reducible than atomically distributed Cu^{2+}. In the CO_2 hydrogenation, this material showed a higher conversion and MeOH yield than the low-temperature or uncalcined sample. In comparison to the malachite-derived benchmark catalyst, LDH-derived materials were somewhat less active. Contrarily, their intrinsic activity normalized to the number of Cu surface sites was significantly higher. This was ascribed to the favorable microstructure of metallic copper in a Zn,Al matrix.

The dedicated application of LDH-derived materials in the alcohol-assisted liquid-phase reaction was studied in Section 4. By the use of an alcohol as a solvent and co-catalyst, the reaction mechanism was altered compared to the gas-phase process. This facilitated a reaction at lower temperatures. Starting from the molar composition of 50:17:33 = Cu:Zn:Al employed in the previous section, the amount of Cu was gradually increased while maintaining a Zn:Al ratio of 1:2. Moreover, Al was substituted by Ga and additionally, two binary, Zn-free materials were synthesized. Phase-pure ternary CZA materials could be obtained up to 65 mol % of Cu. At higher amounts, a malachite byphase was formed. The BET surface areas of ternary LDHs was in the range of $(61 \pm 5)\,m^2\,g^{-1}$. For binary CA and CG, it was about $20\,m^2\,g^{-1}$ lower, indicating the importance of Zn not only as an electronic, but also structural promoter. Ga showed to be a weaker structural promoter than Al. Firstly, the XRD reflections of calcined Ga-substituted materials were sharper than the ones of their Al-containing analogues, suggesting larger domain sizes. Secondly, their maximum peak temperatures in TPR experiments were lower, which is an indication of a weaker binding of Cu to the surrounding matrix or of larger domain sizes. The type of trivalent promoter only had a minor influence on the exposed Cu surface area. Instead, the presence or absence of Zn showed to be crucial. The areas of binary catalysts were significantly lower. This led to a lower MeOH production. Especially the last mechanistic step, which is the hydrogenolysis of the ester to form MeOH, hardly occurred in the absence of Zn. Furthermore, fewer MeOH was produced over Ga-substituted samples compared to their Al-containing analogues. A maximum in MeOH production was found for a Cu content of 62.5 mol %. This ratio displayed an optimum for the number of reducing to acidic sites, required by the individual mechanistic steps. Regarding the temperature, an optimum of 160 °C was found. At lower temperatures, the MeOH yield was too low due to the slow kinetics. At higher temperatures, the formation of the side product EA dominated the catalytic tests, which arised from the dehydrogenation of the solvent EtOH. The complete suppression of MeOH synthesis at 220 °C revealed that both products are formed over the same active sites.

As the mechanism of the alcohol-assisted reaction is altered compared to the gas-phase reaction, differences in the requirements for the catalyst were expected. To validate this assumption, selected samples derived from the LDH and malachite structure were applied in both processes and the MeOH yield was compared. The experiments shown in Section 3 already revealed that the present malachite-derived materials are more suitable for the gas-phase reaction. In the liquid phase however, a LDH-based catalyst calcined at 600 °C could overcome the malachite-derived ones in terms of MeOH production. This material had a higher amount of trivalent promoter, which was present in the form of crystalline spinel domains. The surplus of resulting acid/base sites showed to be advantageous for the alcohol-assisted process. Moreover, the MeOH formation rate normalized to the mass of catalyst was in the same order of magnitude for both processes. This illustrates that the alcohol-assisted process has the potential to compete with the industrially relevant gas-phase process.

Overall, the present results point out that there is no “best” MeOH synthesis catalyst in general. Instead, the catalyst preparation and process conditions need to be considered as an interdependent unity. The preparation of catalysts is a multidimensional matrix in which the metal ratio, precursor phase and calcination temperature can be varied, among others. Especially for LDH-derived materials in the alcohol-assisted synthesis, there is a lack on such a study. As the higher calcination temperature showed to have a positive effect on the material with 50 mol % Cu, it could also be applied to the materials with a higher Cu content. Moreover, a Ga-substituted series of the Cu content variation could be prepared or both Al and Ga could be incorporated in various ratios in order to find the most active catalyst.

To avoid a side product formation in the alcohol-assisted process by dehydrogenation of the solvent, MeOH itself could be applied as a solvent in an autocatalytic way. Firstly, MeOH would be dehydrogenated to formaldehyde. The corresponding analogue to the side product EA with C_1 building blocks is methyl formate. At the same time, this compound is the intermediate ester formed in the second mechanistic step. Hence, no additional compounds would be introduced to the reaction mixture by MeOH dehydrogenation, except formaldehyde. Yet the lab scale implementation is limited by the product analysis. The MeOH molecules produced by the reaction need to be distinguished from the ones added as a solvent. This requires e.g. the use of costly isotope-labeled materials, either in the solvent or syngas.

Finally, the study of the liquid-phase process can be extended to other catalyst classes. Aurichalcite, which is known to be another precursor phase of the commercial MeOH synthesis catalyst, was not yet dedicatedly employed in literature. Furthermore, materials which are not based on Cu as a reducing metal could be investigated. Herein, the lowered reaction temperature compared to the gas-phase process could be advantageous for the selectivity regarding the rWGS or methanation reaction. Promising candidates are, for example, promoted Ni-based catalysts for the CO_2 hydrogenation which are currently under development within the framework of the SPP2080.

8. References

[1] O. Hinrichsen, T. Genger, M. Muhler, *Chem. Eng. Technol.* **2000**, *23*, 956–959.

[2] R. Chatterjee, S. Kuld, R. van den Berg, A. Chen, W. Shen, J. M. Christensen, A. D. Jensen, J. Sehested, *Top. Catal.* **2019**, *62*, 649–659.

[3] D. Larcher, J.-M. Tarascon, *Nature Chemistry* **2015**, *7*, 19–29.

[4] A. Goeppert, M. Czaun, J.-P. Jones, G. K. S. Prakash, G. A. Olah, *Chemical Society Reviews* **2014**, *43*, 7957–8194.

[5] S. Solomon, G.-k. Plattner, R. Knutti, P. Friedlingstein, *Proceedings of the National Academy of Sciences* **2009**, *106*, 1704–1709.

[6] N. S. Lewis, D. G. Nocera, *Proceedings of the National Academy of Sciences* **2006**, *103*, 15729–15735.

[7] Directorate-General for Climate Action, 2050 long-term strategy, `https://climate.ec.europa.eu/eu-action/climate-strategies-targets/2050-long-term-strategy%7B%5C_%7Den` (visited on 07/31/2023).

[8] European Parliament, European Parliament resolution of 14 March 2019 on climate change, `https://www.europarl.europa.eu/doceo/document/TA-8-2019-0217%7B%5C_%7DEN.html` (visited on 07/31/2023).

[9] Bundesministerium für Wirtschaft und Klimaschutz, Abkommen von Paris, `https://www.bmwk.de/Redaktion/DE/Artikel/Industrie/klimaschutz-abkommen-von-paris.html` (visited on 07/31/2023).

[10] United Nations Framework Convention on Climate Change, The Paris Agreement, **2023**, `https://unfccc.int/process-and-meetings/the-paris-agreement` (visited on 09/01/2023).

[11] Nuclear Energy Agency, International Atomic Energy Agency, Uranium 2022: Resources, Production and Demand, tech. rep., **2023**.

[12] D. Lübbert, F. Lange, Uran als Kernbrennstoff: Vorräte und Reichweite, tech. rep., **2006**.

[13] Statistisches Bundesamt (Destatis), Stromerzeugung 2022: Ein Drittel aus Kohle, ein Viertel aus Windkraft, **2023**, `https://www.destatis.de/DE/Presse/Pressemitteilungen/2023/03/PD23_090_43312.html` (visited on 09/01/2023).

[14] Eurostat, Renewable energy statistics, **2023**, `https://ec.europa.eu/eurostat/statistics-explained/index.php?title=Renewable_energy_statistics#Share_of_renewable_energy_more_than_doubled_between_2004_and_2021` (visited on 09/01/2023).

[15] R. Roesch, M. Taylor, S. Al-Zoghoul, P. Ralon, O. Sorokina, Renewable Power Generation Costs in 2022, tech. rep., **2023**.

[16] A. H. Fathima, K. Palanisamy in *Hybrid-Renewable Energy Systems in Microgrids*, (Eds.: A. H. Fathima, N. Prabaharan, K. Palanisamy, A. Kalam, S. Mekhilef, J. J. Justo), Woodhead Publishing Series in Energy, Woodhead Publishing, **2018**, pp. 147–164.

[17] B. Dunn, H. Kamath, J.-m. Tarascon, *Science* **2011**, *334*, 928–936.

[18] NDR/ARD-aktuell (tagesschau.de), Spitzenrunde bekräftigt 2030-Ziel für E-Autos, **2023**, `https://www.tagesschau.de/inland/spitzenrunde-mobilitaet-e-autos-101.html` (visited on 08/29/2023).

[19] I. R. Skov, N. Schneider, *Energy policy* **2022**, *168*, 113121.

[20] F. Schüth, *Chemie Ingenieur Technik* **2011**, *83*, 1984–1993.

[21] M. A. Rosen, S. Koohi-Fayegh, *Energy Ecol. Environ.* **2016**, *1*, 10–29.

[22] A. Kovač, M. Paranos, D. Marciuš, *Int. J. Hydrogen Energy* **2021**, *46*, 10016–10035.

[23] The Royal Society, Ammonia: zero-carbon fertiliser, fuel and energy store, **2020**, `https://royalsociety.org/topics-policy/projects/low-carbon-energy-programme/green-ammonia/` (visited on 09/01/2023).

[24] P. H. Pfromm, *Journal of Renewable and Sustainable Energy* **2017**, *9*, 034702.

[25] Thyssenkrupp Steel Europe, Klimastrategie: Mit grünem Stahl in die Zukunft, `https://www.thyssenkrupp-steel.com/de/unternehmen/nachhaltigkeit/klimastrategie/` (visited on 07/31/2023).

[26] H2 Green Steel, We are H2 Green Steel, `https://www.h2greensteel.com/about-us` (visited on 07/31/2023).

[27] Y. S. Najjar, *Int. J. Hydrog. Energy* **2013**, *38*, 10716–10728.

[28] J. G. Chen, R. M. Crooks, L. C. Seefeldt, K. L. Bren, R. M. Bullock, M. Y. Darensbourg, P. L. Holland, B. Hoffman, M. J. Janik, A. K. Jones, M. G. Kanatzidis, P. King, K. M. Lancaster, S. V. Lymar, P. Pfromm, W. F. Schneider, R. R. Schrock, *Science* **2018**, *360*, DOI `10.1126/science.aar6611`.

[29] F. Schüth, R. Palkovits, R. Schlögl, D. S. Su, *Energy & Environmental Science* **2012**, *5*, 6278–6289.

[30] J. Martin, A. Neumann, A. Ødegård, *Renewable and Sustainable Energy Reviews* **2023**, *186*, 113637.

[31] S. Brynolf, J. Hansson, J. E. Anderson, I. R. Skov, T. J. Wallington, M. Grahn, D. A. Korberg, E. Malmgren, M. Taljegård, *Progress in Energy* **2022**, *4*, 042007.

[32] Z. Tian, Y. Wang, X. Zhen, Z. Liu, *Fuel* **2022**, *320*, 123902.

[33] G. Behrendt, B. Mockenhaupt, N. Prinz, M. Zobel, E. J. Ras, M. Behrens, *ChemCatChem* **2022**, *14*, 1–13.

[34] M. Behrens, *Recycl. Catal.* **2015**, *2*, 78–86.

[35] L. Plass, M. Bertau in *Methanol: The Basic Chemical and Energy Feedstock of the Future - Asinger's Vision Today*, (Eds.: M. Bertau, H. Offermanns, L. Plass, F. Schmidt, H. J. Wernicke), Springer, Berlin, Heidelberg, **2014**, pp. 13–18.

[36] The Methanol Institute, MMSA Global Methanol Supply and Demand Balance, **2022**, `https://www.methanol.org/methanol-price-supply-demand/` (visited on 04/28/2023).

[37] G. A. Olah, A. Goeppert, G. K. S. Prakash, *Beyond Oil and Gas: The Methanol Economy*, 2. Edition, Wiley-VCH Verlag GmbH & Co. KGaA, Weinheim, **2009**.

[38] G. A. Olah, *Angew. Chem. Int. Ed.* **2005**, *44*, 2636–2639.

[39] F. Asinger, *Methanol — Chemie und Energierohstoff*, 1. Ed., Springer-Verlag, Berlin Heiderberg New York, **1986**.

[40] T. Reed, R. Lerner, *Science* **1973**, *182*, 1299–1304.

[41] E. Kunkes, M. Behrens in *Chemical Energy Storage*, (Ed.: R. Schlögl), De Gruyter, Berlin, Boston, **2013**, pp. 413–442.

[42] J. B. Hansen, P. Erik, H. Nielsen in *Handb. Heterog. Catal.* (Eds.: G. Ertl, H. Knözinger, F. Schüth, J. Weitkamp), Wiley-VCH, Weinheim, **2006**, pp. 2920–2949.

[43] BASF, *German Patents 415 686 441 433 462 837* **1923**.

[44] C. Baltes, S. Vukojević, F. Schüth, *J. Catal.* **2008**, *258*, 334–344.

[45] B. Bems, M. Schur, A. Dassenoy, H. Junkes, D. Herein, R. Schlögl, *Chem. Eur. J.* **2003**, *9*, 2039–2052.

[46] M. Behrens, F. Girgsdies, A. Trunschke, R. Schlögl, *Eur. J. Inorg. Chem.* **2009**, 1347–1357.

[47] S. Natesakhawat, J. W. Lekse, J. P. Baltrus, P. R. Ohodnicki, B. H. Howard, X. Deng, C. Matranga, *ACS Catalysis* **2012**, *2*, 1667–1676.

[48] D. R. Palo, R. A. Dagle, J. D. Holladay, *Chem. Rev.* **2007**, *107*, 3992–4021.

[49] L. C. Grabow, M. Mavrikakis, *ACS Catal.* **2011**, *1*, 365–384.

[50] M. Behrens, *J. Catal.* **2009**, *267*, 24–29.

[51] M. Behrens, R. Schlögl, *Zeitschrift für Anorg. und Allg. Chemie* **2013**, *639*, 2683–2695.

[52] G. Fan, F. Li, D. G. Evans, X. Duan, *Chem. Soc. Rev.* **2014**, *43*, 7040–7066.

[53] M. Behrens, I. Kasatkin, S. Kühl, G. Weinberg, *Chem. Mater.* **2010**, *22*, 386–397.

[54] S. Kühl, A. Tarasov, S. Zander, I. Kasatkin, M. Behrens, *Chem. - A Eur. J.* **2014**, *20*, 3782–3792.

[55] S. Kühl, J. Schumann, I. Kasatkin, M. Hävecker, R. Schlögl, M. Behrens, *Catal. Today* **2015**, *246*, 92.

[56] J. Schumann, T. Lunkenbein, A. Tarasov, N. Thomas, R. Schlögl, M. Behrens, *ChemCatChem* **2014**, *6*, 2889–2897.

[57] S. Velu, C. Swamy, *J. Mater. Sci. Lett.* **1996**, *15*, 1674–1677.

[58] G. C. Chinchen, C. M. Hay, H. D. Vandervell, K. C. Waugh, *J. Catal.* **1987**, *103*, 79–86.

[59] M. B. Fichtl, J. Schumann, I. Kasatkin, N. Jacobsen, M. Behrens, R. Schlögl, M. Muhler, O. Hinrichsen, *Angew. Chem. Int. Ed.* **2014**, *53*, 7043–7047.

[60] M. Behrens, F. Studt, I. Kasatkin, S. Kühl, M. Hävecker, F. Abild-pedersen, S. Zander, F. Girgsdies, P. Kurr, B.-l. Kniep, M. Tovar, R. W. Fischer, J. K. Nørskov, R. Schlögl, **2012**, *759*, 893–898.

[61] T. Lunkenbein, J. Schumann, M. Behrens, R. Schlögl, M. G. Willinger, *Angew. Chem. Int. Ed.* **2015**, *54*, 4544–4548.

[62] S. Kannan, V. Rives, H. Knözinger, *J. Solid State Chem.* **2004**, *177*, 319–331.

[63] V. Rives, S. Kannan, *J. Mater. Chem.* **2000**, *10*, 489–495.

[64] I. Melián-Cabrera, M. López Granados, J. L. Fierro, *Phys. Chem. Chem. Phys.* **2002**, *4*, 3122–3127.

[65] M. J. Hernandez-Moreno, M. A. Ulibarri, J. L. Rendon, C. J. Serna, *Phys. Chem. Miner.* **1985**, *12*, 34–38.

[66] T. S. Stanimirova, I. Vergilov, G. Kirov, *J. Mater. Sci.* **1999**, *34*, 4153–4161.

[67] K. Sing, *Pure Appl. Chem.* **1982**, *54*, 2201–2218.

[68] M. Thommes, K. Kaneko, A. V. Neimark, J. P. Olivier, F. Rodriguez-Reinoso, J. Rouquerol, K. S. Sing, *Pure Appl. Chem.* **2015**, *87*, 1051–1069.

[69] A. Ota, E. L. Kunkes, I. Kasatkin, E. Groppo, D. Ferri, B. Poceiro, R. M. Navarro Yerga, M. Behrens, *J. Catal.* **2012**, *293*, 27–38.

[70] S. Kuld, C. Conradsen, P. G. Moses, I. Chorkendorff, J. Sehested, *Angew. Chem. Int. Ed.* **2014**, *53*, 5941–5945.

[71] S. Zander, E. L. Kunkes, M. E. Schuster, J. Schumann, G. Weinberg, D. Teschner, N. Jacobsen, R. Schlögl, M. Behrens, *Angew. Chem. Int. Ed.* **2013**, *52*, 6536–6540.

[72] J. Schumann, M. Eichelbaum, T. Lunkenbein, N. Thomas, M. C. Álvarez Galván, R. Schlögl, M. Behrens, *ACS Catal.* **2015**, *5*, 3260–3270.

[73] L. Pandit, A. Boubnov, G. Behrendt, B. Mockenhaupt, C. Chowdhury, J. Jelic, A. L. Hansen, E. Saraçi, E. J. Ras, M. Behrens, F. Studt, J. D. Grunwaldt, *ChemCatChem* **2021**, *13*, 4120–4132.

[74] B. Mockenhaupt, J.-L. Gieser, J. Jelic, L. Baumgarten, E.-J. Ras, J.-D. Grunwaldt, F. Studt, M. Behrens, On the secondary promotion effect of Al and Ga on Cu/ ZnO methanol synthesis catalysts, work in progress, **2023**.

[75] N. Ortner, D. Zhao, H. Mena, J. Weiß, H. Lund, S. Bartling, S. Wohlrab, U. Armbruster, E. V. Kondratenko, *ACS Catal.* **2023**, *13*, 60–71.

[76] Intergovernmental Panel on Climate Change, AR6 Synthesis Report: Climate Change 2023, `https://www.ipcc.ch/report/ar6/syr/resources/spm-headline-statements/` (visited on 07/31/2023).

[77] World Resources Institute, Tracking Progress of the 2020 Climate Turning Point, `https://wriorg.s3.amazonaws.com/s3fs-public/2020-turning-point-progress-infographic.png` (visited on 07/31/2023).

[78] Directorate-General for Communication of the European Comission, In focus: Hydrogen – driving the green revolution, `https://commission.europa.eu/news/focus-hydrogen-driving-green-revolution-2021-04-14%7B%5C_%7Den` (visited on 07/31/2023).

[79] M. Tahir, A. Batool in *Sustainable Materials and Green Processing for Energy Conversion*, (Eds.: K. Y. Cheong, A. Apblett), Elsevier, **2022**, pp. 97–130.

[80] O. Vozniuk, N. Tanchoux, J.-M. Millet, S. Albonetti, F. Di Renzo, F. Cavani in *Horizons in Sustainable Industrial Chemistry and Catalysis*, (Eds.: S. Albonetti, S. Perathoner, E. A. Quadrelli), Studies in Surface Science and Catalysis, Elsevier, **2019**, pp. 281–302.

[81] Fertilizers Europe, Green ammonia and low-carbon fertilizers, `https://www.fertilizerseurope.com/paving-the-way-to-green-ammonia-and-low-carbon-fertilizers/` (visited on 07/31/2023).

[82] Yara International ASA, Green fertilizers: everything you need to know, `https://www.yara.com/sustainability/transforming-food-system/green-fertilizers/what-you-need-to-know-about-green-fertilizers/` (visited on 07/31/2023).

[83] E. Shafiei, B. Davidsdottir, J. Leaver, H. Stefansson, E. I. Asgeirsson, *J. Clean. Prod.* **2017**, *141*, 237–247.

[84] T. Weimer, K. Schaber, M. Specht, A. Bandi, *Energy Convers. Manag.* **1996**, *37*, 1351–1356.

[85] F. Schorn, J. L. Breuer, R. C. Samsun, T. Schnorbus, B. Heuser, R. Peters, D. Stolten, *Advances in Applied Energy* **2021**, *3*, 100050.

[86] A. Baiker, *Appl. Organomet. Chem.* **2000**, *14*, 751–762.

[87] U.-D. Standt, F. Seyfried in *Methanol: The Basic Chemical and Energy Feedstock of the Future - Asinger's Vision Today*, (Eds.: M. Bertau, H. Offermanns, L. Plass, F. Schmidt, H. J. Wernicke), Springer, Berlin, Heidelberg, **2014**, pp. 410–419.

[88] M. Gassoumi, Z. Boutar, R. M. R. A. Shah, M. T. Aljarrah, M. Al Qubeissi, R. Ennetta, A. Onorati, H. S. Soyhan, *Energy Sources Part A: Recovery Utilization and Environmental Effects* **2023**, *45*, 9485–9497.

[89] A. B. Stiles, *AIChE Journal* **1977**, *23*, 362–375.

[90] K. Weissermel, H.-J. Arpe, *Industrial Organic Chemistry*, 4. Edition, Wiley-VCH GmbH & Co. KGaA, Weinheim, **2003**.

[91] V. Gronemann, L. Plass, F. Schmidt in *Methanol: The Basic Chemical and Energy Feedstock of the Future - Asinger's Vision Today*, (Eds.: M. Bertau, H. Offermanns, L. Plass, F. Schmidt, H. J. Wernicke), Springer, Berlin, Heidelberg, **2014**, pp. 234–266.

[92] M. M. Viitanen, W. P. Jansen, R. G. Van Welzenis, H. H. Brongersma, D. S. Brands, E. K. Poels, A. Bliek, *J. Phys. Chem. B* **1999**, *103*, 6025–6029.

[93] F. Studt, M. Behrens, E. L. Kunkes, N. Thomas, S. Zander, A. Tarasov, J. Schumann, E. Frei, J. B. Varley, F. Abild-Pedersen, J. K. Nørskov, R. Schlögl, *ChemCatChem* **2015**, *7*, 1105–1111.

[94] M. S. Spencer, *Top. Catal.* **1999**, *8*, 259–266.

[95] X. M. Liu, G. Q. Lu, Z. F. Yan, J. Beltramini, *Ind. Eng. Chem. Res.* **2003**, *42*, 6518–6530.

[96] M. Behrens, G. Lolli, N. Muratova, I. Kasatkin, M. Hävecker, R. N. D'Alnoncourt, O. Storcheva, K. Köhler, M. Muhler, R. Schlögl, *Phys. Chem. Chem. Phys.* **2013**, *15*, 1374–1381.

[97] M. Behrens, S. Zander, P. Kurr, N. Jacobsen, J. Senker, G. Koch, T. Ressler, R. W. Fischer, R. Schlögl, *J. Am. Chem. Soc.* **2013**, *135*, 6061–6068.

[98] T. Lorenz, M. Bertau, F. Schmidt, L. Plass in *Methanol: The Basic Chemical and Energy Feedstock of the Future - Asinger's Vision Today*, (Eds.: M. Bertau, H. Offermanns, L. Plass, F. Schmidt, H. J. Wernicke), Springer, Berlin, Heidelberg, **2014**, pp. 266–284.

[99] J. B. Joshi, *Chem. Eng. Res. Des.* **2014**, *92*, 2557–2567.

[100] E. Lam, G. Noh, K. W. Chan, K. Larmier, D. Lebedev, K. Searles, P. Wolf, O. V. Safonova, C. Copéret, *Chem. Sci.* **2020**, *11*, 7593–7598.

[101] J. Toyir, P. Ramírez De La Piscina, J. L. G. Fierro, N. Homs, *Appl. Catal. B Environ.* **2001**, *29*, 207–215.

[102] J. Toyir, P. R. De la Piscina, J. L. G. Fierro, N. Homs, *Appl. Catal. B Environ.* **2001**, *34*, 255–266.

[103] D. Laudenschleger, H. Ruland, M. Muhler, *Nat. Commun.* **2020**, *11*, 3898.

[104] O. Martin, J. Pérez-Ramírez, *Catal. Sci. Technol.* **2013**, *3*, 3343–3352.

[105] M. Peters, B. Köhler, W. Kuckshinrichs, W. Leitner, P. Markewitz, T. E. Müller, *ChemSusChem* **2011**, *4*, 1216–1240.

[106] L. Fan, Y. Sakaiya, K. Fujimoto, *Appl. Catal. A Gen.* **1999**, *180*, 13–15.

[107] R. Yang, Y. Fu, Y. Zhang, N. Tsubaki, *J. Catal.* **2004**, *228*, 23–35.

[108] N. Tsubaki, M. Ito, K. Fujimoto, *J. Catal.* **2001**, *197*, 224–227.

[109] P. Reubroycharoen, T. Yamagami, Y. Yoneyama, M. Ito, T. Vitidsant, N. Tsubaki, *Stud. Surf. Sci. Catal.* **2004**, *147*, 409–414.

[110] H. Nieminen, G. Givirovskiy, A. Laari, T. Koiranen, *J. CO2 Util.* **2018**, *24*, 180–189.

[111] P. Reubroycharoen, T. Vitidsant, Y. Yoneyama, N. Tsubaki, *Catal. Today* **2004**, *89*, 447–454.

[112] P. Reubroycharoen, T. Yamagami, T. Vitidsant, Y. Yoneyama, M. Ito, N. Tsubaki, *Energy and Fuels* **2003**, *17*, 817–821.

[113] Y. Jeong, I. Kim, J. Y. Kang, N. Yan, H. Jeong, J. K. Park, J. H. Park, J. C. Jung, *J. Mol. Catal. A Chem.* **2016**, *418-419*, 168–174.

[114] I. Kim, G. Lee, H. Jeong, J. H. Park, J. C. Jung, *J. Energy Chem.* **2017**, *26*, 373–379.

[115] J. Zeng, K. Fujimoto, N. Tsubaki, *Energy and Fuels* **2002**, *16*, 83–86.

[116] J. Thrane, S. Kuld, N. D. Nielsen, A. D. Jensen, J. Sehested, J. M. Christensen, *Angew. Chem. Int. Ed.* **2020**, *132*, 18346–18350.

[117] P. Schwiderowski, S. Stürmer, M. Muhler, *React. Chem. Eng.* **2022**, *7*, 2224–2230.

[118] S. Likhittaphon, R. Panyadee, W. Fakyam, S. Charojrochkul, T. Sornchamni, N. Laosiripojana, S. Assabumrungrat, P. Kim-Lohsoontorn, *Int. J. Hydrog. Energy* **2019**, *44*, 20782–20791.

[119] R. H. Höppener, E. B. Doesburg, J. J. Scholten, *Appl. Catal.* **1986**, *25*, 109–119.

[120] L. Anton Wein, H. Zhang, K. Urushidate, M. Miyano, Y. Izumi, *Appl. Surf. Sci.* **2018**, *447*, 687–696.

[121] N. Ahmed, M. Morikawa, Y. Izumi, *Catal. Today* **2012**, *185*, 263–269.

[122] D. Stoilova, V. Koleva, V. Vassileva, *Spectrochim. Acta A Mol. Biomol. Spectrosc.* **2002**, *58*, 2051–2059.

[123] A. V. Rodrigues, N. L. Sabino, *J. Mater. Sci. Mater. Electron.* **2019**, *30*, 16910–16916.

[124] U. Rambabu, N. R. Munirathnam, T. L. Prakash, B. Vengalrao, S. Buddhudu, *J. Mater. Sci.* **2007**, *42*, 9262–9266.

[125] M. M. Günter, T. Ressler, R. E. Jentoft, B. Bems, *J. Catal.* **2001**, *203*, 133–149.

[126] S. J. Gentry, N. W. Hurst, A. Jones, *J. Chem. Soc. Faraday Trans. 1* **1979**, *75*, 1688–1699.

[127] S.-i. Fujita, N. Iwasa, H. Tani, W. Nomura, M. Arai, N. Takezawa, *React. Kinet. Catal. Lett.* **2001**, *73*, 367–372.

[128] I. C. Freitas, S. Damyanova, D. C. Oliveira, C. M. Marques, J. M. Bueno, *J. Mol. Catal. A Chem.* **2014**, *381*, 26–37.

[129] Q. N. Wang, L. Shi, W. Li, W. C. Li, R. Si, F. Schüth, A. H. Lu, *Catal. Sci. Technol.* **2018**, *8*, 472–479.

[130] S. Amokrane, A. Boualouache, P. Simon, M. Capron, G. Otmanine, D. Allam, S. Hocine, *Catal. Letters* **2021**, *151*, 2864–2883.

[131] W. S. Putro, T. Kojima, T. Hara, N. Ichikuni, S. Shimazu, *Catal. Sci. Technol.* **2018**, *8*, 3010–3014.

[132] P. Vollhardt, N. Schore, *Organic Chemistry*, 6. Edition, W. H. Freeman and Company, New York, **2009**.

[133] J. Buddrus, B. Schmidt, *Grundlagen der Organischen Chemie*, 4. Edition, Walter de Gruyter GmbH & Co. KG, Berlin/New York, **2011**.

[134] R. Brückner, *Reaktionsmechanismen*, 3. Edition, Springer Spektrum Berlin, Heidelberg, **2004**.

[135] A. M. P. Koskinen, A. O. Kataja in *Organic Reactions*, John Wiley & Sons, Ltd, **2015**, Chapter 2, pp. 105–410.

[136] E. Santacesaria, G. Carotenuto, R. Tesser, M. Di Serio, *Chem. Eng. J.* **2012**, *179*, 209–220.

[137] S. V. Krivovichev, V. N. Yakovenchuk, E. S. Zhitova, A. A. Zolotarev, Y. A. Pakhomovsky, G. Y. Ivanyuk, *Mineralogical Magazine* **2010**, *74*, 833–840.

[138] T. Klein, Methanol: A Future-Proof Fuel. A Primer Prepared for the Methanol Institute, **2020**, `https://www.methanol.org/wp-content/uploads/2020/03/Future-Fuel-Strategies-Methanol-Automotive-Fuel-Primer.pdf` (visited on 08/03/2023).

[139] D. Waller, D. Stirling, F. S. Stone, M. S. Spencer, *Faraday Discuss. Chem. Soc.* **1989**, *87*, 107–120.

[140] S. Kattel, P. J. Ramírez, J. G. Chen, J. A. Rodriguez, P. Liu, *Science* **2017**, *355*, 1296–1299.

[141] K. Klier in (Eds.: D. Eley, H. Pines, P. B. Weisz), Advances in Catalysis, Academic Press, **1982**, pp. 243–313.

[142] M. Sahibzada, I. S. Metcalfe, D. Chadwick, *J. Catal.* **1998**, *174*, 111–118.

[143] Y. Yang, C. A. Mims, D. H. Mei, C. H. Peden, C. T. Campbell, *J. Catal.* **2013**, *298*, 10–17.

[144] S. N. Khadzhiev, N. V. Kolesnichenko, N. N. Ezhova, *Pet. Chem.* **2016**, *56*, 77–95.

[145] N. Khunathorncharoenwong, P. Charoensuppanimit, S. Assabumrungrat, P. Kim-Lohsoontorn, *Int. J. Hydrog. Energy* **2020**, *46*, 24591–24606.

[146] E. Riedel, C. Janiak, *Anorganische Chemie*, 7.Ed., Walter de Gruyter GmbH & Co. KG, Berlin, New York, **2007**.

[147] T. Ida, M. Nishida, Y. Hori, *J. Phys. Chem. A* **2019**, *123*, 9579–9586.

[148] X. Wang, Q. Meng, L. Gao, Z. Jin, J. Ge, C. Liu, W. Xing, *Int. J. Hydrogen Energy* **2018**, *43*, 7055–7071.

[149] M. S. Wainwright, T. Ahn, D. L. Trimm, N. W. Cant, *J. Chem. Eng. Data* **1987**, *32*, 22–24.

A. Appendix

List of Conference Contributions

08.2019	Europacat2019, Aaachen/Germany "Malachite-based catalyst precursors for methanol synthesis from CO_2-rich synthesis gas" (joint Poster with Gereon Behrendt)
03.2020	CENIDE Conference, Bergisch Gladbach/Germany "Malachite- and LDH-based catalyst precursors for methanol synthesis from CO_2-rich synthesis gas" (joint Poster with Gereon Behrendt)
09.2020	Online-Vortragstagung für Anorganische Chemie der Fachgruppen Wöhler-Vereinigung und Festkörperchemie und Materialforschung, online format "LDH-based Catalyst Precursors for Methanol Synthesis from CO_2-rich Synthesis Gas"
03.2021	54. Jahrestreffen Deutscher Katalytiker, online format "LDH-based Catalyst Precursors for Methanol Synthesis from CO_2-rich Synthesis Gas" (Additionally: presentation in the Virtual Poster Show)
05.2021	ExpReS 2021 conference, online format "LDH-based Catalyst Precursors for Methanol Synthesis from CO_2-rich Synthesis Gas"
02.2022	30th ATC 2022: Industrial Inorganic Chemistry - Materials and Processes, Frankfurt(Main)/Germany "Cu-based ex-LDH Catalysts for CO_2 Hydrogenation to Methanol" (honored with Best Poster Award)
03.2022	55. Jahrestreffen Deutscher Katalytiker, Weimar/Germany "CO_2 Reduction to Methanol by LDH-based Catalysts" (honored with Best Poster Award)
07.2023	PREPA13, Louvain-la-Neuve/Belgium "Vacuum-assisted Calcination of LDH-based Materials for Methanol Synthesis"

Declaration of Authorship

Hiermit bestätige ich, die vorliegende Arbeit mit dem Titel "Hydrogenation of Carbon Dioxide in the Gas- and Liquid-Phase over Cu-based Catalysts" eigenständig verfasst und nur die angegebenen Quellen und Hilfsmittel verwendet zu haben. Alle benutzten Quellen sind wörtlich oder sinngemäß als solche kenntlich gemacht. Diese Arbeit wurde in dieser oder ähnlicher Form bisher bei keinem Prüfungsausschuss oder einer anderen Universität eingereicht.

Duisburg, den 07. Dezember 2023, Jil-Lorean Gieser